INVESTIGATION OF SINGLE AND SPLIT INJECTION STRATEGIES IN AN OPTICAL DIESEL ENGINE

A thesis submitted for the degree of Doctor of Philosophy

By

Mohammad Reza Herfatmanesh

School of Engineering and Design
Brunel University
United Kingdom

October 2010

Abstract

This study investigates the effects of split injection strategy on combustion performance and exhaust emissions in a high speed direct injection optical diesel engine. The investigation is focused on the effects of injection timing, quantity and dwell angle using commercially available diesel fuel. Three different split injection strategies including 30:70, 50:50 and 70:30 have been investigated. Additionally, the effect of total injected fuel quantity using total fuel quantities of 10 mm^3 and 20 mm^3 has been investigated. Moreover, the effect of variable and fixed dwell angle in split injections has been examined for five different values between 5^o CA and 25^o CA in the case of variable and 10^o CA for the fixed dwell timing. The last parameter investigated was the injection timing, nine injection timings have been tested for each of the strategies.

A Ricardo Hydra single cylinder optical engine running at 1500 rpm was used in this investigation. Conventional methods such as direct in-cylinder pressure measurements and heat release rate analysis have been employed. In addition, optical techniques such as high speed video imaging and two-colour have been applied, aimed at in depth analysis of the effects of the aforementioned parameters on engine performance and emissions. Furthermore, a significant amount of effort was devoted to the development and application of Laser Induced Excipex Fluorescence (LIEF) technique for simultaneous visualisation of fuel liquid and fuel vapour distributions.

This investigation concludes that split injection strategy has the potential to reduce diesel exhaust emissions while maintaining a good level of fuel economy, provided that injection timings and the dwell angle between injections are appropriately selected. Further investigations are required in order to examine the effect of split injection under different engine operating conditions and speeds. In addition, the effect of alternative fuels must be considered. Moreover, the application of LIEF technique for quantitative fuel vapour concentration measurement should be considered through further optimisation and calibration of the LIEF system.

Acknowledgements

The financial and technical support provided by Delphi Diesel Systems UK is acknowledged.

I would like to thank Chief Technician, John Langdon, for his continual assistance during my study. I would also like to express my appreciation to Technicians, Andy Selway, Ken Anstiss and Clive Barrett for their incessant support, advice and assistance and all the other technical staff who have contributed to this work in many ways.

I would also like to thank Kiran Gill who unconditionally shared his invaluable knowledge of diesel engines, in particular the hydra engine, and my friends Roohollah Haghpanahan, Mansoor Salehi, Mohammad Reza Behjati, Vahid Pezeshki and in particular Sara Anjomani, with whom I have shared lots of unforgettable memories.

I would further like to thank my parents, aunt, brother and sister for their unconditional love and unwavering support in so many ways.

Finally, I extend my greatest respect, admiration and gratitude to Professor Hua Zhao for his encouragement, continual support and guidance over the last four years.

Abbreviations

ASOI	After the Start of Injection
ATDC	After Top Dead Centre
CA	Crank Angle
CARB	Californian Air Resource Board
CFD	Computational Fluid Dynamic
CI	Compression Ignition
CN	Cetane Number
CO	Carbon Monoxide
CO_2	Carbon Dioxide
CR	Compression Ratio
CRS	Common Rail System
CV	Calorific Value
CVC	Constant Volume Chamber
CVL	Copper Vapour Laser
DC	Direct Current
DCF	Dichroic Filter
DEF	Diesel Exhaust Fluid
DI	Direct Injection
DOC	Diesel Oxidation Catalyst
DPF	Diesel Particulate Filter
ECU	Electronic Control Unit
EGR	Exhaust Gas Recirculation
EPA	Environmental Protection Agency
Exciplex	Excited State Complex
FFT	Fast Fourier Transform
FID	Flame Ionisation Detector
FIE	Fuel Injection Equipment
FILE	Forward Illumination Light Extinction

fps	Frames per Second
FSN	Filter Smoke Number
H_2	Hydrogen
HCCI	Homogeneous Charge Compression Ignition
HR	Heat Release
HSDI	High Speed Direct Injection
IC	Internal Combustion
ICCD	Intensified Charge Coupled Device
ID	Ignition Delay
IMEP	Indicated Mean Effective Pressure
ISFC	Indicated Specific Fuel Consumption
IVC	Intake Valve Closure
LAS	Laser Absorption Scattering
LED	Light Emitting Diode
LIEF	Laser Induced Exciplex Fluorescence
LIF	Laser Induced Fluorescence
LII	Laser Induced Incandescence
LIS	Laser Induced Scattering
LLS	Laser Light Scattering
LPF	Longpass Filter
LRS	Laser Rayleigh scattering
LTC	Low Temperature Combustion
MK	Modulated Kinetics
N_2	Nitrogen
NDIR	Non-Dispersive Infrared
NEDC	New European Driving Cycle
NI	National Instruments
NO	Nitrogen Monoxide
NO_2	Nitrogen Dioxide

NOx	Nitrogen Oxides
O_2	Oxygen
O_3	Ozone
OH	Hydroxyl Radical
PCCI	Premixed Charge Compression Ignition
PIV	Particle Image Velocimetry
PM	Particulate Matter
ppm	Parts per Million
ppr	Pulse per Revolution
PREDIC	Premixed Lean Diesel Combustion
rpm	Revolutions per Minute
RS	Raman Scattering
SCR	Selective Catalytic Reduction
SI	Spark Ignition
SMD	Sauter Mean Diameter
SOC	Start of Combustion
SOI	Start of Injection
SPF	Shortpass Filter
TDC	Top Dead Centre
uHC	Unburned Hydrocarbons
UIS	Unit Injector System
UPS	Unit Pump System
UV	Ultra Violet
VCO	Valve Covered Orifice
VGS	Variable Geometry Spray
VVL	Variable Valve Lift
VVT	Variable Valve Timing

Contents

LIST OF FIGURES

LIST OF TABLES

1

CHAPTER 1

Introduction

1.1 Introduction

The invention of Internal Combustion (IC) engines dates back to 1876 through the introduction of a four stage engine cycle by Nicolaus Otto commonly known as the Otto cycle. This invention was then further developed; forming the current Spark Ignition (SI) engines also known as petrol or Otto engines. However, in 1892 the revolutionary design of the first Compression Ignition (CI) engine was established by Rudolph Diesel in Germany [1]. Subsequently the first diesel engine was manufactured and successfully tested at Augsburg Maschinenfabrik in 1894 [2]. Since then, diesel engines were manufactured as a more efficient replacement in industrial applications including stationary power plants, marine and public transport vehicles as well as being employed in locomotives and heavy duty vehicles. Despite the rapid market penetration of diesel cars in Europe, this trend does not hold true elsewhere whereby poor diesel quality, unfavourable emissions standards for diesel-engined cars as well as public perception issues are the prime factors for such shortcoming.

Although diesel engines are extremely robust and reliable, capable of producing outstanding torque at low speeds, inherent high levels of regulated and unregulated emissions and engine noise associated with conventional diesel engines have been the foremost reasons for such minimal market share until the late 1990s. This in turn incentivised SI engines as the prime choice in the passenger car market due to their higher power density, lower engine noise and manufacturing cost. However, recent developments in diesel engine technology, higher fuel prices as well as incentivising tax regimes based on CO_2 emission levels have led to a substantial shift in the

automotive market with diesel engines claiming approximately 50% of the European car market [3]. The diesel market is substantially dominant; reaching 80% of the market share in several European countries including Belgium, Luxembourg, France and Spain whereby lower tax on diesel fuel has led to such market penetration. Furthermore, recent technical improvements resulting in more refined and responsive diesel engines with exceptionally low pollutant emissions are perceived as principal contributors to such market success.

Concern over emission of exhaust pollutants has led to the introduction of emissions legislation since the 1960s by California Air Resource Board (CARB) and Environmental Protection Agency (EPA) in the United States and Euro 1-5 within the European Union since 1992. In order to meet the ever more stringent emission standards, significant efforts have been devoted to the research and development of cleaner IC engines.

Diesel combustion and the formation of pollutants are directly influenced by the spatial and temporal distributions of the injected fuel within the combustion chamber. Consequently, numerous research studies have been initiated aimed at more detailed investigation of fuel-air mixing and combustion processes as well as chemical/physical reactions involved in the production of pollutants, in particular Nitrogen Oxides (NOx) and Particulate Matter (PM), the most perilous emissions produced by diesel engines. The prime constituent of PM is identified as soot, formed in the presence of a rich combustion, while NOx formation takes place in high temperature zones mainly associated with the burned gas regions. In order to take advantage of the flexibility of electronically controlled common rail fuel injection systems, pilot and split injections as well as single injections are employed to minimise the emission of NOx and PM emissions from diesel engines. Nevertheless, diesel combustion and the associated mechanisms of pollutant formation are yet to be fully explored and require further investigation in order to meet future emissions legislation. Thus, conventional methods of engine measurement are no longer sufficient for further optimisation of diesel engines. Instead, nonintrusive laser based optical diagnostic techniques have been devised for in-depth analysis of fuel-air

mixing. The application of these techniques can serve as a qualitative and/or quantitative measure in the optimisation of diesel engines.

1.2 Aims and Objectives

The aim of this study was to characterise the Fuel Injection Equipment (FIE) and to investigate the effect of split injection strategies on diesel combustion and exhaust emissions through direct in-cylinder pressure measurements and heat release rate analysis in conjunction with the application of optical diagnostic techniques for detailed analysis of the results. The main objectives of this investigation were the:

- Characterisation of the FIE for the application of split injection strategies.
- Development, optimisation and implementation of optical techniques for in-cylinder spray and combustion studies.
- Implementation of a two-colour system using high speed video camera for in-cylinder soot and combustion temperature measurement.
- Investigation of the effect of injection timing and dwell angle using split injection strategies on mixture formation and the diesel combustion process aimed at reduction of exhaust emissions, mainly NOx and soot.
- Development, optimisation and implementation of Laser Induced Exciplex Fluorescence (LIEF) technique on the optical research engine, aimed at detailed analysis of fuel evaporation and mixing process during the preignition phase of combustion.

1.3 Outline of Thesis

Following a brief introduction in Chapter 1, Chapter 2 presents a review of the literature available surrounding diesel combustion and in-cylinder optical diagnostic techniques. The exhaust emissions from diesel engines are explained, detailing their respective mechanism of formation and diminution. The characteristics of conventional and alternative diesel combustion modes are outlined. The effect of

injection strategies on optimisation of diesel combustion, aimed at reduction of exhaust emissions while maintaining good levels of economy are discussed.

Chapter 3 gives a description of the experimental test facility, instrumentation and measurement equipment. The characteristics of the single cylinder optical diesel engine employed in this study are explained. The data analysis techniques employed in this study are discussed.

Chapter 4 details the principle of the two-colour method and its implementation on the single cylinder optical engine utilised in this study for in-cylinder flame temperature and soot concentration measurements.

Chapter 5 focuses on the characterisation of the FIE and the measurement of fuel injection rate using single and split injection strategies. The principle of the techniques employed and the results obtained are presented.

Chapter 6 outlines the effects of split injection strategies on diesel combustion and exhaust emissions using commercially available diesel fuel. The details of the operating conditions are given and the results are presented. The combustion characteristics are analysed through both direct in-cylinder pressure measurements and optical diagnostic techniques.

Chapter 7 describes the principle of the LIEF technique, its implementation and application in the optical diesel engine utilised in this study. The specification of the equipments, optical components, control systems and the data acquisition system are explained. The details of the operating conditions are given and the results are presented.

Chapter 8 details the conclusions drawn and recommendations for future work that can be performed in line with this investigation.

2

CHAPTER 2

Literature Review

2.1 Diesel Engine Emissions

A significant growth in the production of fossil fuel powered motor vehicles in the 20th century resulted in significant degradation of urban air quality, most famously the smog of Los Angles and London. Due to ever increasing concern over the environmental impacts of such levels of pollution, the first emission standard was introduced in 1966 by the California Motor Vehicle Pollution Control Board, currently known as California Air Resource Board, which stated maximum allowable exhaust emissions of unburned Hydrocarbons (uHC) and Carbon Monoxide (CO) for vehicles sold in the state of California [4]. Subsequently, the establishment of Environmental Protection Agency and the enforcement of Council Directive 70/220/EEC in 1970 in the United States and the European Union respectively, indicated the initiation of international evolution on emissions legislation. Since then, several directives have been passed by the United States and the European Union which resulted in the introduction of 'Tier' and 'Euro' standards respectively. Tier 1 was introduced in 1994 and the current Tier 2 in 2004 [5]. On the other hand, Euro 1 came into force in 1993, followed by Euro 2 in 1996, Euro 3 in 2000, Euro 4 in 2005 and the current Euro 5 in 2009. This will be followed by Euro 6 around 2014 [6]. Figure 2.1 illustrates the NOx and particulate matter emissions limits of light duty diesel vehicles for Euro 3-6.

The emissions testing ought to be carried out in accordance with the New European Driving Cycle (NEDC). The NEDC test consists of four urban driving conditions, replicating European city driving at low load and speed, followed by one extra urban assessment, simulating the high load and speed situation.

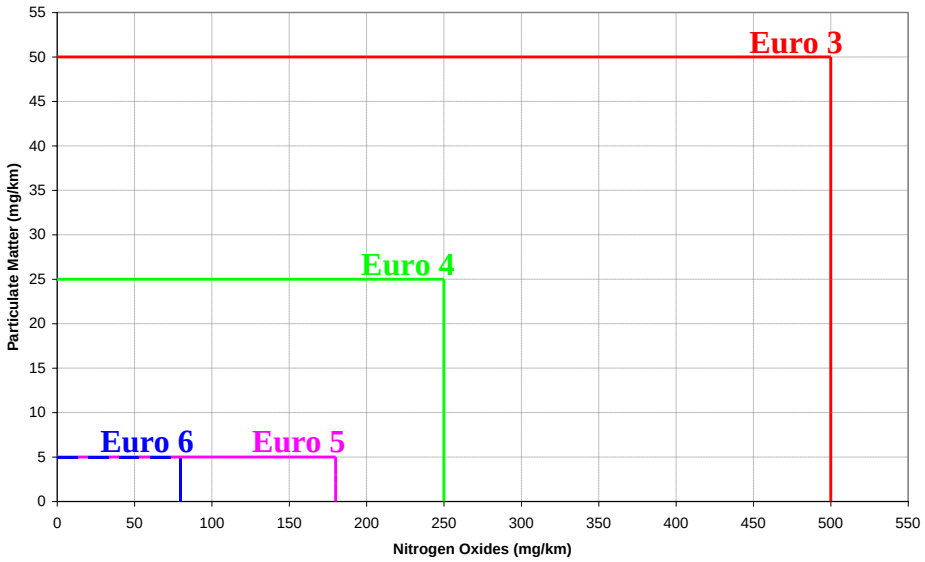

Figure 2.1 Euro 3-6 NOx and PM Emission Standards of Light Duty Diesel Vehicles

2.1.1 Particulate Matter

Particulate matter (PM) emission has been a major concern in the design and development of diesel engines. Diesel engines are one of the major sources of particulate emissions whereby approximately 0.2–0.5% of the fuel mass is emitted as small (~ 0.1 μm diameter) particulates [1]. Recent chemical and medical investigations have revealed the potential health risks associated with the suspension of such fine particles in ambient air [7].

The PM is composed of several constituents which can be divided into three categories, sulphate particles, soluble organic compounds and carbonaceous material, referred to as soot. A schematic diagram of diesel engine exhaust particles is presented in Figure 2.2 [8]. These individual particles of soot coated with adsorbed and condensed compounds are called spherules and agglomerate to form larger particulates [9]. The former is referred to as primary soot particles while the latter is known as secondary soot particles [10]. Soot formation involves different chemical and physical processes including formation and growth of large aromatic hydrocarbons to particles and the coagulation of such primary particles to larger aggregates [11]. The agglomerates are composed of collection of smaller particles that are spherical or nearly spherical [12] while the soluble organic compounds are

composed of aromatic compounds as well as various other unburned hydrocarbons [13].

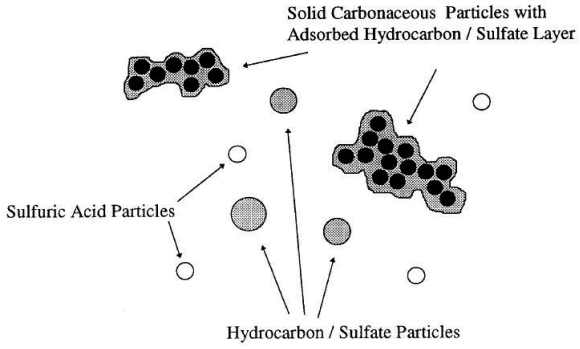

Figure 2.2 Schematic Diagram of Diesel Engine Exhaust Particles (Kittelson, [8])

Soot is formed in the presence of a rich combustion where fuel pyrolysis, the process of hydrocarbon chain decomposition at elevated temperatures in the absence of oxygen, is likely to take place [10]; while, lubricating oil on the cylinder walls is also reported as a contributing factor [1]. Although the majority of soot produced within the combustion chamber of diesel engines is oxidized during the combustion process, it remains the prime contaminant produced by diesel engines.

Soot formation has been extensively investigated with regard to combustion characteristics [14-18] and application of alternative fuels [19-21]. Studies of soot formation and oxidation mechanisms were carried out through the application of several optical techniques including luminosity measurements [17-20], elastic scattering [22-24], Laser Induced Scattering (LIS) [25] and Laser Induced Incandescence (LII) [22-24, 26, 27]. These nonintrusive techniques were implemented in optical diesel engines in order to identify the spatial and temporal distributions of soot particles formed during the combustion process.

Much in-cylinder diesel combustion research has been carried out by Dec and co-workers [22-24, 26, 27] in a heavy duty single cylinder diesel engine. Based on the results obtained surrounding soot formation characteristics through the application of various optical techniques, a phenomenological model of the soot formation and oxidation processes was proposed by Dec [28]. The schematic diagram of this conceptual model is depicted in Figure 2.3.

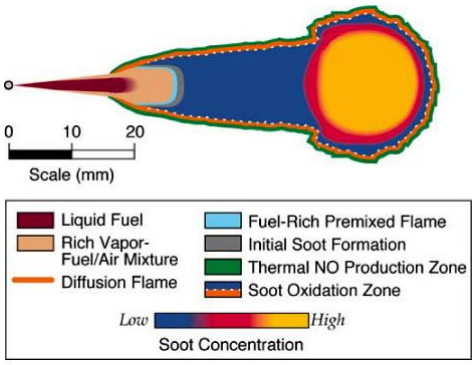

Figure 2.3 Schematic Diagram of the Conceptual Model for Quasi-Steady Burning Fuel Jet (Dec, [28])

This model predicts that primary soot particles initially form at the leading edge of the liquid fuel jet where rich premixed combustion takes place due to initial fuel mixing process. However, as the vapour jet progresses across the cylinder, secondary soot particles, accountable for the majority of soot emissions produced by diesel engines, form downstream of the jet particularly around the jet periphery where mixing controlled diffusion combustion occurs. Following the development of this fundamental model, several studies were conducted in order to examine its validity under different engine operating conditions. Senda et al. [29] applied a combination of Particle Image Velocimetry (PIV) and LIEF techniques in order to identify the dependency of soot formation on local fuel vapour distribution. The second harmonic of frequency-doubled Nd:YAG pulsed laser operating at the wavelength of 532nm was used as the excitation source. In addition, quantitative analysis of soot formation was carried out by Inagaki et al. [30] through the application of LII technique in an optically accessible diesel engine. The calibration procedure involved evaluation of the relationship between the LII signal, soot concentration and laser power using a flat flame burner. The results indicate that primary soot particles formed during premixed combustion are smaller in size in comparison to secondary particles formed during mixing controlled (i.e. diffusion) combustion. These findings were in good agreement with the conceptual model proposed by Dec [28], further supporting the validity of this model.

Xu and Lee [31-34] developed Forward Illumination Light Extinction (FILE) technique for soot measurements. The principle of this technique is based on the

attenuation of the light beam through both light scattering and absorption as the illumination source passes through the cloud of soot particles. The ratio of the final light beam intensity to that of the original, I/I_o, is used to evaluate the soot concentration within the measuring volume provided that the wavelength of the incident light and the refractive index of the soot particles are known. In this study, soot formation was studied in a Constant Volume Chamber (CVC) using the aforementioned technique. Based on their results the authors suggested that soot formation undergoes three stages. The first stage involves rapid soot formation at the end of premixed combustion, while the second stage involves a stable phase between soot formation and oxidation prior to the end of injection. The final stage mainly includes soot oxidation of fuel injected during the final stages of the fuel injection process.

Reitz et al. [21] have conducted several experiments in heavy duty diesel engines and developed a multi step model for soot formation in High Speed Direct Injection (HSDI) diesel engines. The simulated results indicated that soot particles formed during premixed combustion, many of which are subsequently oxidised by the increasing cylinder temperature from the diffusion combustion phase, are smaller in size. These results were in good agreement with the experimental results previously obtained by the authors and were also consistent with the data published by Xi and Zhong [10]. Senda et al. [35] and Choi et al. [36] also studied soot formation and oxidation mechanisms using various optical techniques. The experimental results presented by the authors followed the same trend as those published by Reitz et al. [21]. Since the development of the two step semi-empirical model of Hiroyasu and Kadota [37] and the model of Fusco et al. [38] and Kazakov and Foster [39], initial soot formation and autoignition have been thought to be strongly related to spatial and temporal distributions of fuel vapour. Kazakov and Foster [39] implemented their model in the KIVA-II Computational Fluid Dynamic (CFD) code. Their simulated results were consistent with the experimental data acquired using laser sheet imaging techniques. Recently, Tao et al. [40] developed a nine-step phenomenological soot model which was implemented into the KIVA-3V code in order to numerically evaluate the soot formation and oxidation processes within the combustion chamber of both heavy duty and light duty diesel engines over a wide range of operating

conditions. The results obtained by this model were more accurate than previously reported due to additional steps included in the model such as the effects of fuel pyrolysis, formation of soot precursors and OH-related soot oxidation.

Recent studies on soot formation involved detailed analysis of the effects of alternative fuels [41-44], fuel injector nozzle design [45], fuel injection pressure [46], fuel injection timing [47], injection strategy [48], in-cylinder water injection [49] and Exhaust Gas Recirculation (EGR) [50-52]. Modifications of engine operating parameters through the application of the aforementioned techniques resulted in significant reduction in soot emission.

2.1.1.1 Particulate Matter Effects

Although all types of exhaust emissions are of environmental concern, PM is of major concern due to the health risks associated with this type of emission. The effects of particulate matter on humans is yet to be fully understood, nevertheless enough evidence exists on negative effects of soot emission, indicating possible risks of causing or contributing to lung cancer, aggravated allergic responses, retarded lung growth, heart, liver and respiratory system damage [10, 53, 54]. The size of the particles is alleged to have an important bearing on the level of potential damage to human health. In initial investigations on the impact of PM emissions on human health, chronic lung disease, lung cancer, influenza, asthma and increases in daily mortality were associated with PM10 (diameter < 10 μm) [55]. However, recent studies suggest that these correlations are more closely linked with fine particulates (PM2.5: diameter < 2.5 μm) and ultra-fine particulates (PM0.1: diameter < 0.1 μm) [56, 57], since such fine particles can easily penetrate deep into the lungs [58]. Thus, although current PM emission limits are mass-based, future limits may be more effective, provided that stringent regulations are imposed on the particle size and number [9].

2.1.2 NOx Emission

Other major pollutants formed during diesel combustion are nitrogen oxides, commonly referred to as NOx, which consist of approximately 70-90% Nitrogen Monoxide (NO) and 10-30% Nitrogen Dioxide (NO_2) [59].

2.1.2.1 NOx Formation

Numerous investigations have been carried out on this topic; the results were consistent, indicating that formation of NOx is a function of high temperature and the availability of Oxygen (O_2) and Nitrogen (N_2). These conditions are experienced in premixed combustion where the mixture is close to stoichiometric as previously reported by many researchers [60-62]. The chemical process itself occurs via the extended Zeldovich mechanism which is highly temperature sensitive as described by Bowman [33] and Heywood [1]. The reversible reactions involved are depicted below:

$$O + N_2 \leftrightarrow NO + N \qquad \text{Equation 2.1}$$

$$N + O_2 \leftrightarrow NO + O \qquad \text{Equation 2.2}$$

$$N + OH \leftrightarrow NO + H \qquad \text{Equation 2.3}$$

NO is formed at high temperatures, provided that excess oxygen is exposed to nitrogen molecules. A by-product of this chemical reaction is an atom of nitrogen in an unstable state. This nitrogen atom reacts with oxygen to form more NO. Another source of NO formation is through the combination of Hydroxyl Radicals (OH), which appears during combustion, with atoms of nitrogen in an unstable state as shown in Equation 2.3.

In diesel combustion, NOx formation is related to local high temperatures that occur in the premixed combustion phase. Shundoh et al. [63] showed that a zero swirl ratio decreased NOx due to restricting air utilisation by limiting local mixture leaning. The reduction in NOx emission was due to reduction in the combustion temperature as well as limited availability of excess oxygen. Nehmer and Reitz [61] stated that premixed combustion, being approximately stoichiometric hence the charge being at high temperature and pressure as combustion takes place close to TDC, results in the local near-stoichiometric mixture providing sufficient excess oxygen and nitrogen, leading to significant NOx formation. Röpke et al. [62] showed that the amount of oxygen was the main parameter influencing the rate of NO formation. They also showed that NO formation was considerably reduced as the amount of inert gas in the intake was increased. Figure 2.4 illustrates the contour map of temperature versus equivalence ratio.

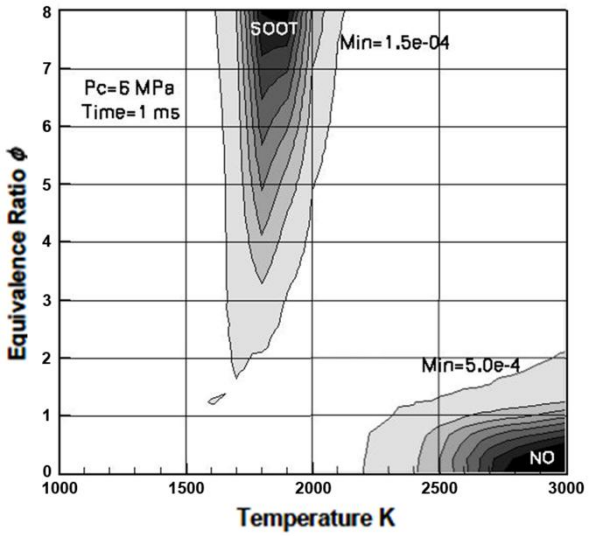

Figure 2.4 Φ- T Diagram (Alriksson et al., [64])

As previously state, soot is mainly formed in the presence of fuel rich mixture (i.e. high equivalence ratios) as shown in Figure 2.4. In addition, it is evident in Figure 2.4 that NOx forms at high temperatures, greater than 2000 K. Such high temperatures, which occur with slightly rich fuel mixtures, are required to break the strong N_2 molecular bond. In addition, NOx formation is dependent on the availability of O_2 and N_2, thus a lean or close to stoichiometric mixture promotes formation of this pollutant. However, one of the major difficulties in conventional diesel engines is the NOx-soot trade off. Premixed combustion, during which in-cylinder pressure and temperature are very high, plays an important role in NO formation. Techniques to control NOx formation are mainly linked to a reduction in combustion temperature during this phase of combustion. Unfortunately, reduction in combustion temperature leads to increase in PM emission. More recently, the effects of EGR [65, 66], alternative fuels [67], intake port water injection [68] and emulsified fuel with water [68] on NOx formation have been investigated. It was reported that although the use of such techniques yielded considerable reduction in NOx emission; the fuel consumption increased.

2.1.2.2 NOx Emission Effects

NO and NO_2 are toxic gasses [69]; therefore, their effects on the environment and human health are of major concern. Oxides of nitrogen react with oxygen in the atmosphere to form ground-level Ozone (O_3). Although the presence of ozone in the

stratosphere is favourable since it filters damaging shortwave radiation, at low-level, it is harmful to the respiratory system. Additionally, ozone is one of the primary factors in the formation of photochemical smog. Research on the effects of NOx has demonstrated the impact of this pollutant matter in the formation of nitric acid in the atmosphere and subsequently acid rain with its associated environmental damage, exacerbating asthmatic conditions as well as its influence on the nitrogen cycle resulting in water degradation [5].

2.1.3 Unburned Hydrocarbon

The unburned hydrocarbon (uHC) emission is mainly associated with exceptionally lean mixtures, due to over mixing, whereby autoignition is unlikely to occur and/or rich mixtures, due to under mixing, whereby sufficient oxygen is not available to initiate autoignition. In addition, flame quenching is presumed to be a contributing factor in production of uHC emissions. The hydrocarbons in the exhaust may condense to form white smoke during engine start-up and warm-up periods [1]. Amongst various propulsion systems, diesel engines are realised to produce minimal levels of uHC emissions. A trade-off between simultaneous reduction of NOx and soot through alternative combustion strategies and the level of uHC emission was observed, increasing as the level of NOx and soot emissions decreases [70, 71].

2.2 Aftertreatment

Aftertreatment devices allow further reduction of engine out emissions in the tailpipe. However, the implementation of such systems in production vehicles is accompanied by disadvantages in terms of weight, space, complexity, increased back pressure, lack of effectiveness at low load conditions and cost. Therefore, these systems are widely accepted as secondary measures in reducing exhaust emissions and not a replacement for reducing engine-out emissions through improvements in combustion efficiency. Current technologies are briefly discussed in the following sections.

2.2.1 Diesel Particulate Filter

A Diesel Particulate Filter (DPF) is designed for the removal of diesel particulate matter or soot from the exhaust gases produced by diesel engines. DPF incorporates a

honeycomb structure made of ceramic or metal fibre which limits the gas flow across the filter in order to maximise the efficiency of the PM deposition process. In such a configuration, exhaust gasses are forced through the walls between the channels of the DPF, depositing PM.

In this manner a large portion of PM can be removed, however the filter pores become blocked for which regeneration must be performed. However, diesel exhaust temperature is too low to oxidise the trapped PM so active regeneration methods are applied. Amongst various regeneration techniques, post fuel injection in the cylinder or low pressure fuel injection in the exhaust manifold are commonly used to activate the regeneration process. The use of a liquid catalyst additive is also employed by the PSA Group, whereby the additive is added to the fuel and its presence in the soot particle helps to lower the regeneration temperature of the soot particles. In addition, continuous catalytic regeneration through the use of catalytic coating is also available.

2.2.2 Selective Catalytic Reduction

Selective Catalytic Reduction (SCR) is a method of converting nitrogen oxides, by catalytic reaction, into nitrogen gas and water vapour. Since the SCR system does not alter the design of modern diesel engines, NOx emissions can be reduced without penalties in terms of fuel economy and engine durability. In a similar fashion to DPF, SCR provides aftertreatment in the tailpipe. The principle of SCR is based on the injection of Diesel Exhaust Fluid (DEF), such as ‘Adblue’, which comprises of approximately 60% Urea in water, into hot exhaust stack upstream of the SCR converter. In this setup, a separate tank is required for the storage of DEF. Consequently, this technique is less desirable for modern passenger cars where weight and size issues are of great concern. Other disadvantages include ammonia leakage, the need to refill and the lack of widespread additive availability.

2.2.3 NOx Trap

The NOx trap, also referred to as NOx adsorber, operates based on capturing and storing NOx and subsequently releasing and converting processes. During the capture phase, this system traps the nitrogen oxide in the exhaust gas in a porous carrier in the

catalytic converter coated with platinum, barium and rhodium. The platinum converts NO into NO_2 while the barium, which oxidises into barium oxide, traps and holds NO_2. In the release phase, a chemical process known as reductive elimination, the trapped oxides of nitrogen are purged and converted into nitrogen gas and water vapour. The release phase is carried out with the engine operating in rich-burn mode whereby CO and Hydrogen (H_2) emissions, the by-products of fuel-rich combustion, contribute to converting the stored NOx to carbon dioxide and nitrogen.

2.2.4 Diesel Oxidation Catalyst

A Diesel Oxidation Catalyst (DOC), which reduces uHC and CO emissions, is a flow through device that consists of a canister containing a honeycomb structure or substrate. The substrate has a large surface area which is coated with an active catalyst substance. This layer contains a small but well dispersed amount of precious metal catalyst such as platinum or palladium. As the exhaust gases flow through the catalyst, the CO, uHC and some soot particles are oxidized. DOCs are used on all diesel engines and they increasingly form part of catalytic regeneration of DPF systems whereby the reaction in the former increases the exhaust gas temperature to levels required for DPF regeneration.

2.3 Diesel Combustion

2.3.1 Conventional Diesel Combustion

The conventional diesel combustion process of four-stroke DI engines is well established as shown in Figure 2.5.

The engine cycle consists of induction, compression, combustion and exhaust strokes. During the induction stroke, air is drawn or blown into the cylinder. During the compression stroke, air is compressed to high pressure and temperature. Fuel is often injected close to Top Dead Centre (TDC) at high injection pressures directly into the cylinder. The combustion stroke comprises of two phases, premixed combustion and mixing controlled combustion. The former involves autoignition of fuel and air which has been mixed during the preignition phase of combustion while the latter involves

combustion of remnant fuel which has not been utilised during the first phase of combustion. During the exhaust stroke the gases are purged out of the combustion chamber due to the upward movement of the piston. The combustion process results in heat generation, the rate of which is used as a tool in characterising different phases of combustion as shown in Figure 2.5. The combustion process consists of several phases including Ignition Delay (ID), premixed combustion, mixing controlled combustion and late combustion.

Ignition Delay: This is the duration between the Start of Injection (SOI) and the Start of Combustion (SOC).

Premixed Combustion: The injected fuel evaporates and mixes with the surrounding air during the preignition phase of combustion (i.e. during the ignition delay). The fuel and air mix to a near stoichiometric ratio and auto-ignite due to the charge temperature being higher than the flash point of the fuel. The combustion associated with this phase is rapid and intense due to the mixture availability and occurs at high temperature due to the stoichiometric/slightly rich mixture. The resulting heat release rate spike is accompanied by sudden in-cylinder pressure rise which is responsible for the characteristic diesel engine noise. This phase is mainly responsible for NOx production due to high temperatures experienced.

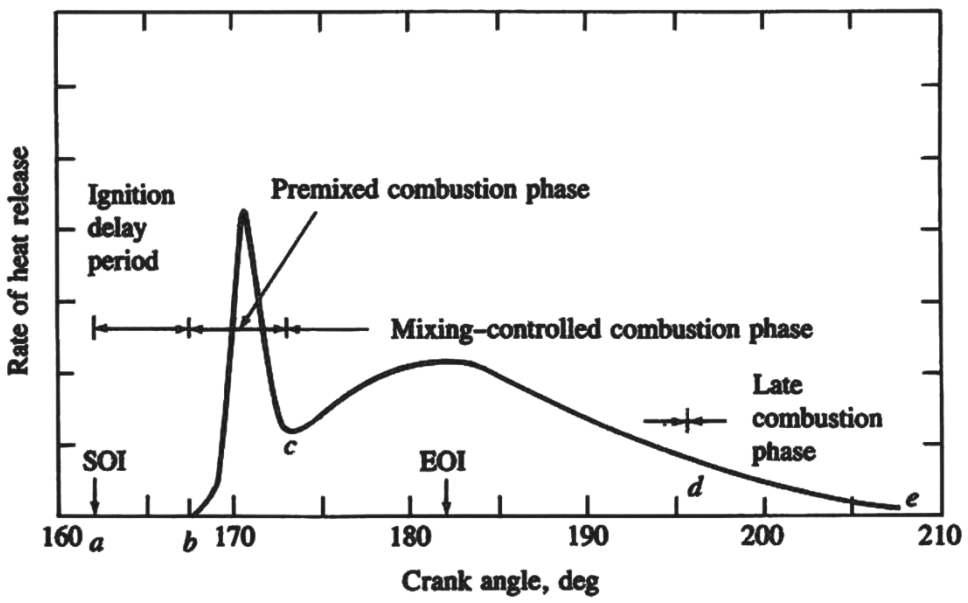

Figure 2.5 Diesel Combustion Heat Release Rate (Heywood, [1])

Mixing Controlled Combustion: Following the consumption of premixed fuel-air mixture, mixing controlled combustion, commonly referred to as diffusion combustion, commences. The remnant of the fuel and/or freshly injected fuel burns with a diffusion flame yielding rich combustion due to limited oxygen availability. This combustion is slower as it is limited by the mixing rate; hence combustion takes place at lower temperatures. This phase is responsible for the majority of soot production due to fuel rich combustion.

Late Combustion: After the bulk of diffusion combustion is completed, remaining fuel is partially oxidised. The in-cylinder temperature during this phase of combustion is relatively low which leads to the slowing and the termination of combustion.

2.3.2 Alternative Diesel Combustion Modes

Although exhaust gas emissions have been significantly reduced through the use of high pressure common rail fuel injection equipment and aftertreatment devices, further advancement in reducing such emissions through improvement of the combustion process is required in order to meet future legislations. Consequently, alternative methods of combustion have been developed and implemented in diesel engines during the past two decades aimed at simultaneous reduction of exhaust pollutants, mainly NOx and soot, while maintaining good levels of fuel economy and combustion efficiency. The following sections include detailed explanation of Homogeneous Charge Compression Ignition (HCCI), Premixed Charge Compression Ignition (PCCI) and Low Temperature Combustion (LTC).

2.3.2.1 Homogeneous Charge Compression Ignition

HCCI has been the subject of many investigations. The principle of this strategy lies on the combustion of a homogenous lean mixture aimed at simultaneous reduction of NOx and soot emissions. The former is achieved due to lower combustion temperature of the lean or diluted mixture, while the latter is accomplished due to the absence of fuel-rich burn. Figure 2.6 is a Φ-T diagram, illustrating the principle of NOx and soot reduction through the application of HCCI and PCCI combustion strategies in comparison to conventional diesel combustion.

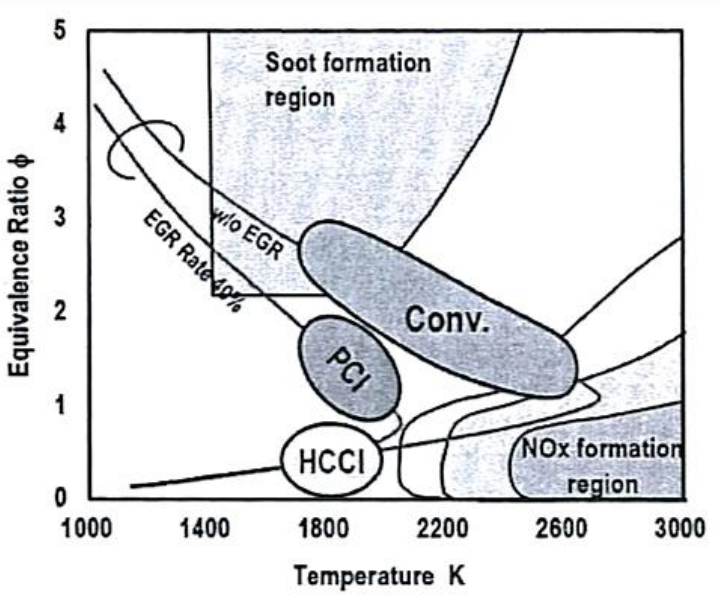

Figure 2.6 Φ-T Diagram of Conventional, HCCI and PCCI Combustion Strategies (Alriksson et al., [64])

In this strategy fuel is premixed in order to obtain a homogenous mixture, the subsequent combustion is characterised by multiple site initiation, rapid combustion and low soot and NOx emissions as reported by Hultqvist et al. [72]. The combustion of a premixed fuel and air is almost instantaneous causing high combustion rate, resulting in high in-cylinder peak pressures which can be regulated by dilution. HCCI combustion is dominated by local chemical-kinetic reactions [73]; thus the combustion process is highly sensitive to changes in in-cylinder temperature. This is mainly attributed to chemical reactions being highly sensitive. Consequently, it is extremely difficult to control SOC over a wide range of engine operating conditions as reported by Docquier and Bruneaux [74, 75]. However, ignition timing can be controlled by varying intake heating, EGR rate and intake manifold boost pressure. However, alterations in dilution ratio, intake heating and EGR rate limit the maximum power output.

Although simultaneous reduction of NOx and soot emissions can be achieved through the application of this technique, high CO and uHC emissions are reported. Stanglmaier and Roberts [76] related the rise in the aforementioned emissions to low charge temperature, limiting post combustion oxidation. The authors reported on the use of port injection, early and late direct injections in producing HCCI combustion.

HCCI combustion achieved through port injection resulted in high uHC and CO emissions with relatively higher fuel consumption. Oil dilution due to surface wetting was also observed. This configuration suffers from inadequate control of ignition timing by the injection system. Early injection, often during the intake stroke or early in the compression stroke, is ineffective for controlling the ignition timing. This is due to charge cooling effects as well as fuel spray wall impingement due to low in-cylinder charge density. Late injection, typically near or after TDC, requires high level of cooled EGR, a low compression ratio and a high swirl ratio to prolong the ignition delay in order to form a near homogenous mixture. They proposed that a dual mode combustion system with HCCI at part load and conventional diesel combustion at high load may provide the best overall solution.

Strålin et al. [77] reported on the use of advanced injection timing in achieving HCCI combustion which resulted in simultaneous reduction of NOx and soot emissions. However, high level of uHC emission and increased fuel consumption, due to wall wetting, were the drawbacks of achieving HCCI combustion through advanced injection timing. In order to reduce uHC emission in HCCI combustion, Ra et al. [78] applied Variable Geometry Spray (VGS) using injectors with a narrow cone angle aimed at avoiding wall wetting. The application of this technique led to significant reduction of uHC emission. Komminos et al. [79] developed a multi-zone model for detailed analysis of HCCI combustion where they showed that during the combustion process the fuel mass increased rapidly in the crevice area, resulting in the reduction of peak in-cylinder pressure as well as increase in uHC emission. Recent Studies have reported on the application of HCCI combustion using split injection, high EGR rate and late Inlet Valve Closure (IVC) or Variable Valve Lift (VVL) [80, 81]. The use of EGR resulted in sufficiently long ignition delay for the generation of premixed lean mixture. However, the control of injections proved challenging due to the short dwell angle required.

2.3.2.2 Premixed Charge Compression Ignition

Another alternative combustion strategy is PCCI, capable of simultaneous reduction of NOx and soot emissions but to a lesser extent in comparison to HCCI. In this setup,

the mixture is not fully homogenous due to mixing constraints encountered upon the application of this technique.

Initial investigation on this technique was carried out by Takeda et al. [82] using very advanced injection timings to allow thorough mixing to a locally lean state before premixed combustion was initiated, the authors referred to this alternative combustion technique as Premixed Lean Diesel Combustion (PREDIC). The early injection timing resulted in low temperature combustion, leading to reduction of NOx emissions, though uHC and CO emissions were increased due to mixture over-leaning. Subsequent work by Akagawa et al. [83] revealed that uHC and CO emissions can be significantly reduced by injector improvements and reduction of the piston top land crevice volume.

Kimura et al. [84] developed the concept of the Modulated Kinetics (MK) combustion strategy, benefiting from Low combustion temperature and the absence of diffusion combustion; thus, capable of lowering NOx and soot emissions respectively. Late injection timing, close to TDC, was used in this strategy for mixture formation, since early injection timing resulted in spray wall impingement and lack of control on ignition timing. The combustion rate was regulated through the use of high EGR rate which reduced the oxygen concentration, ignition delay was prolonged by low compression ratio and mixing was optimised by the combustion chamber geometry and high swirl ratio. Significant reductions in PM and NOx as well as uHC emissions, due to improved mixing and combustion chamber geometry, were made with this strategy which has since successfully been put into production by Nissan. However, the late injection MK combustion suffered from loss of fuel economy due to high swirl ratio used.

Simescu et al. [85, 86] applied the PCCI combustion technique on a heavy duty diesel engine where PCCI was achieved by using a port injection with injection quantities between 10% and 70% of the total fuel while the remaining fuel was directly injected into the cylinder. They reported reduction in NOx emissions except for low speed and high load conditions; though uHC and CO emissions were increased. However, CO emission was reduced with port injection quantities in excess of 60%, mainly due to

prolonged oxidation time. Kook and Bae [87] applied two-stage injection on a heavy duty engine with the main injection occurring around 100° CA BTDC and second injection close to TDC. Low temperature combustion was achieved due to early autoignition of the fuel mixture caused by the early injection timing of the main injection. Based on their result, 90% reduction in NOx emissions can be achieved with two-stage combustion in comparison to conventional diesel engines. However, uHC and CO emissions were increased.

An extensive study of PCCI was carried out by Hardy and Reitz [88-90] in a heavy duty diesel engine using early injection timing. It was reported that high level of EGR was required to control the combustion rate to lower NOx emission. The use of EGR also reduced the in-cylinder peak pressure responsible for knocking due to instantaneous combustion caused by early fuel injection. The soot emission was reduced by lowering the equivalence ratio through the use of intake air boosting. Kanda et al. [91] applied the same concept of early injection with a narrow cone injector. The compression ratio was reduced to avoid too advanced autoignition while EGR was used to retard the autoignition. Using an endoscope, they recorded combustion images. Although reduction in NOx emission was reported, uHC, CO and soot emissions increased due to the formation of a fuel wall-film on the piston wall as fuel evaporation was very poor at the time of injection. In a further study [92] they applied late injection timing, close to TDC. This injection timing produced levels of NOx very similar to PCCI with early injection, yet with the advantage of reducing the rest of the emissions due to the elimination of the fuel wall film phenomenon.

Lee and Reitz [93] investigated the effect of spray targeting in HSDI engines. It was reported that satisfactory NOx-soot trade off with low CO emission can be achieved, provided that spray was targeted to the edge of the piston bowl. Their results showed that soot emission was further lowered when the fuel spray was targeted to the bottom of the piston, though this resulted in higher CO emission. The applicability of this technique over a wide range of engine operating conditions was proven difficult. This was mainly due to the dependency of the onset of ignition on in-cylinder mixing which is a function of engine speed and intake manifold boost pressure.

Murata et al. [94], amongst others, used Variable Valve Timing (VVT) to adjust the effective compression ratio of the engine. Their results indicated improved control over ignition timing, allowing the application of PCCI to a wide range of engine operating conditions.

2.3.2.3 Low Temperature Combustion

The principle of LTC is similar to HCCI and PCCI strategies whereby low temperature combustion is achieved through the use of premixed fuel with relatively low equivalence ratio. Figure 2.7 is a Φ-T diagram, illustrating the principle of NOx and soot reduction through the application of LTC in comparison to HCCI, PCCI and conventional diesel combustion strategies.

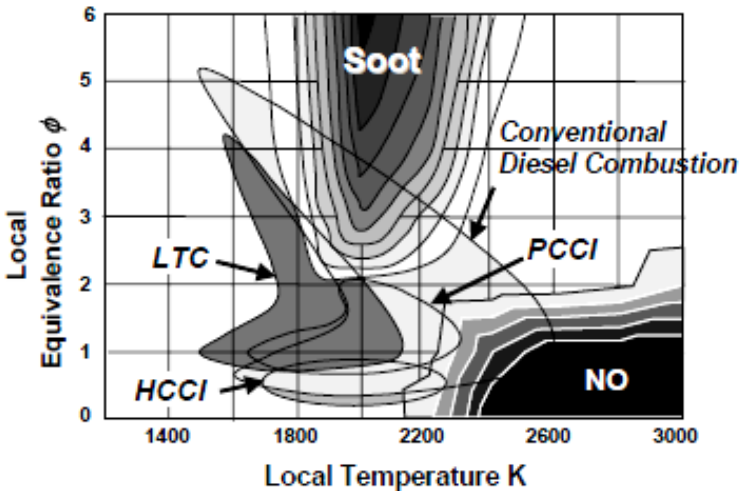

Figure 2.7 Φ- T Diagram of Conventional, LTC, HCCI and PCCI Combustion Strategies (Neely et al., [95])

Neely et al. [95] achieved LTC at low load by increasing the intake manifold temperature in conjunction with the use of hot EGR while LTC was realised at high loads through the use of cooled EGR, limiting the combustion temperature. Alriksson and Denbratt [96] applied the concept of LTC in a heavy duty engine using relatively high levels of EGR. It was reported that simultaneous reduction of NOx and soot emissions can be achieved with EGR rates less than 50%. However, this trend did not hold true when higher EGR rates, in excess of 50%, was used where increase in both fuel consumption and uHC emission was observed.

2.4 Injection Parameters

Characterisation and optimisation of the FIE has been the subject of a number of investigations. The effects of injector nozzle, injection pressure, injection timing, injection rate and alternative injection strategies on the characteristics of diesel combustion and emissions have been studied. Amongst these, injection timing, injection rate and alternative injection strategies are detailed in the following sections.

2.4.1 Injection Timing

The effect of injection timing on diesel combustion efficiency and the soot-NOx trade off is well established. Injection timing is referenced with respect to TDC where injections before and after this reference are referred to as being advanced and retarded respectively. Advancing injection timing increases the time available for fuel and air mixing during preignition phase of combustion since the in-cylinder pressure and temperature are lower than the autoignition temperature of fuel. Consequently, greater quantity of fuel and air can mix with such injection timing, resulting in increased premixed combustion and consequently higher NOx emission. However, soot emission is reduced due to lower quantity of fuel available for diffusion combustion which minimises soot formation as well as higher in-cylinder temperature due to rapid premixed combustion, improving the soot oxidation process. Nevertheless, there is an optimum timing beyond which further advancement of injection timing results in ignition and pressure rise occurring before TDC, opposing the rising piston and thus producing negative work. In addition, an increase in uHC emission can be a by-product of advanced injection timing; this is mainly due to lower charge density at the time of injection which leads to increased spray penetration and ultimately spray wall impingement, referred to as wall wetting. This is responsible for the increase in the level of unburned fuel. uHC emission can also increase due to the presence of very lean mixture caused by over-mixing due to prolonged ignition delay.

In contrast, retarding the injection timing results in fuel to be injected into the combustion chamber at higher in-cylinder pressure and temperature; thus, shortening the ignition delay. Consequently, less premixed combustion takes place with such injection timing, lowering NOx emission, though increase in diffusion combustion is

inevitably responsible for higher soot emission. Additionally, the reduction of premixed combustion and the associated rapid heat release rate and in-cylinder pressure rise is advantageous in reducing the combustion noise.

2.4.2 Injection Rate

The injection rate profile is a characteristic of a common rail diesel fuel injector which is almost rectangular in current diesel injectors. Though, recent developments in piezoelectric injectors led to improved injection rate profile due to faster opening and closing of the injector. The rate of fuel injection and its effect on engine noise, emission and performance has been extensively investigated since the early days of diesel engines. Figure 2.8 highlights the effects of injection rate profile on engine power, noise and exhaust emissions. The initial rapid increase in the rate of fuel injection promotes improved fuel atomisation leading to improved uHC emission. It is evident that further increase in the injection rate results in increase in engine power output and uHC emission, this is due to the introduction of high quantities of fuel at these stages. Additionally, increase in uHC emission is experienced during final stages of the fuel injection process; this is mainly attributed to fuel dribbling effect. It is therefore evident that the profile of rate of injection is one of the primary factors in the optimisation of engine performance and emissions.

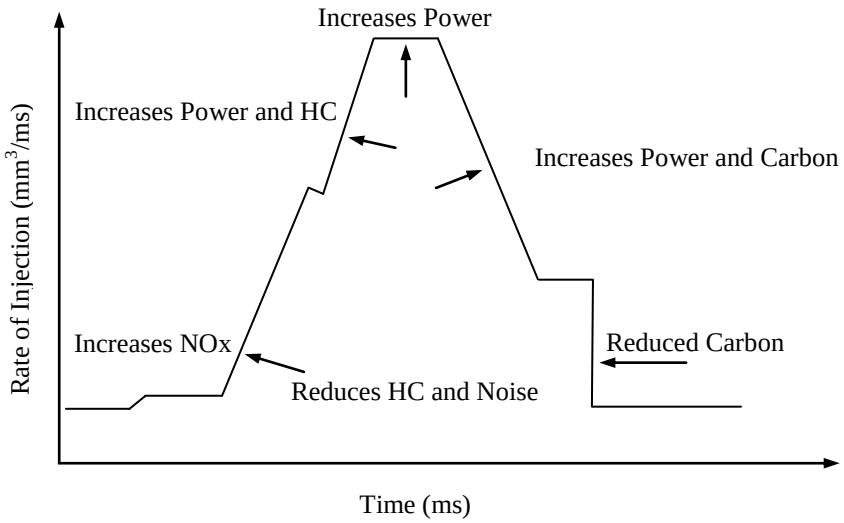

Figure 2.8 Influence of Injection Rate on Engine Power, Noise and Exhaust Emissions (Dolenc, [97])

Nehmer and Reitz [98] studied the effect of several injection rate profiles through modifying injectors. The combustion with injectors having slower rate profiles allowed the combustion to continue later in the expansion cycle. This resulted in lower soot emissions through improved oxidation process, though increase in fuel consumption was reported.

Zambare and Winterbone [99] used an optical engine in order to investigate the effect of injection rate profile of conventional and two-stage fuel injection systems. The results showed that NOx emission was reduced with the latter injection system in comparison to a conventional injection system, though soot emission was higher, particularly at low loads. Koyanagi et al. [100] also used an optical engine equipped with a common rail fuel injection system. They compared the effect of fuel injection rate using a conventional solenoid injector and a piezoelectric injector. The results indicated improvements in fuel and air mixing and soot emission due to higher fuel spray momentum caused by faster opening of piezoelectric injectors with a squarer injection rate profile. The fuel economy was also improved due to better fuel atomisation and mixing, though penalties in terms of engine noise and NOx emission were incurred.

Juneja et al. [101] investigated the effect of different injection rate profiles on liquid and vapour penetration, flame lift-off lengths and emissions. The injection rate profiles were defined based on extensive computational analysis of advanced fuel evaporation and primary jet breakup models which were further validated by experimental investigations. The results indicated that NOx and soot emissions were directly influenced by the equivalence ratio of the premixed fuel mixture prior to the onset of the combustion which can be controlled through modification of injection rate profile. Thus, it was reported that regulation of fuel distribution in the combustion chamber through modification of injection rate profile plays an important role in controlling exhaust emissions.

Tanabe et al. [102] developed a novel two-rail system comprising of a low and high pressure rail, feeding a single injector. The fuel injection rate was controlled by switching between the rails during fuel injection. The experiments were carried out in

a heavy duty diesel engine. Their results showed that fuel injection rate shaping resulted in simultaneous reduction of NOx and soot emissions, particularly at mid speed and high loads where control over combustion led to a more constant pressure combustion process similar to an ideal diesel cycle. Although alternative combustion strategies, explained in Section 2.3.2, are also capable of simultaneous reduction of NOx and soot emissions, fuel injection rate shaping allows simultaneous reduction of the aforementioned pollutants with no penalty in terms of fuel economy.

2.4.3 Injection Strategy

The introduction of the common rail fuel injection system in the 1990s allowed greater control over the fuel injection rate and timing over the entire operating range of diesel engines. The fuel injection pressure is independent of the engine speed; thus, capable of promoting improved fuel evaporation and mixture formation at low speeds and loads. Such control over fuel injection system resulted in the development of alternative injection strategies through the application of split or multiple injections aimed at the reduction of exhaust emissions while maintaining good level of fuel economy and combustion efficiency.

The initial investigations on using alternative injection strategies were primarily focused on the application of pilot and main injections or split injections with equal fuel demand per injection (50:50) [61, 103-105]. Their results were consistent and revealed that shorter ignition delay was achieved due to pilot injection, indicating less premixed combustion which in turn lowered the peak heat release rate. Therefore, combustion noise was considerably reduced in comparison to conventional diesel combustion due to shorter ignition delay. In addition, the effect of post injection on further reduction of soot emission has been examined by Han et al. [33] and Farrell et al. [106]. Their results showed that soot emission was reduced due to improved soot oxidation which was due to higher combustion temperature during mixing controlled combustion caused by the combustion of fuel injected during post injection.

However, further reduction of exhaust emissions produced by diesel engines was necessary in order to meet stringent emissions legislation. Consequently, the effect of EGR in conjunction with alternative injection strategies was investigated aimed at

simultaneous reduction of NOx and soot emissions while avoiding penalties in terms of engine noise and performance. Extensive research has been carried out including the work done by Montgomery and Reitz [107] and Shayler et al. [108]. The former study implemented this technique in a heavy duty diesel engine using 50:50, 55:45 and 70:30 split injection strategies with EGR levels varying between 10 to 25%. The 50:50 injection strategy involved two injections with equal quantities, the 55:45 strategy was based on the injection of 55% of total fuel quantity during the first injection and the remaining during the second and the 70:30 injection strategy was based on the injection of 70% of total fuel quantity during the first and the remnant during the second injection. Their investigation revealed the potential for simultaneous reduction of NOx and soot emissions when using split injection with EGR. The use of EGR decreased the NOx emission by limiting the peak heat release rate due to premixed combustion, thus lowering the in-cylinder temperature caused by limited availability of oxygen. The soot emission was reduced due to improved mixing in conjunction with the effect of late fuel injection which resulted in higher in-cylinder temperatures during diffusion combustion, maximising soot oxidation. The latter study compared the effect of split injection strategy to conventional single injection strategy. In this study all the split injection strategies were accompanied with a pilot injection whereby relatively small quantity of fuel was injected in order to improve fuel evaporation process during split-main injections. The results indicated that strategies with more fuel quantity during the first injection compared to the second injection resulted in less soot emission without affecting NOx emission.

Zhang et al. [109, 110] carried out a series of investigations involving detailed analysis of fuel and air mixing process in a constant volume vessel through the application of Laser Absorption Scattering (LAS). They investigated the mixing process using conventional single injection and compared their results with those obtained through split injection strategies 75:25, 50:50 and 25:75. They reported that the 75:25 split injection strategy resulted in maximum soot reduction under the tested engine operating conditions. This was mainly attributed to improved mixing due to increased in-cylinder turbulence caused by the combustion of fuel injected during the second injection. The same trend was observed by Shayler and Ng [111] who compared combustion and emission characteristics of their engine using single

injection and 90:10 and 60:40 split injection strategies. Their results also showed that soot emission was reduced as the quantity of the second injection increased. However, there is an optimum value beyond which further increase in the quantity of fuel injected during second injection results in the opposite.

More recently injection strategies have been investigated with up to 4 or 5 injections due to improved capability of modern fuel injection systems. Liu and Reitz [112] studied the effect of multiple injection strategy on diesel combustion and fuel efficiency. They reported that simultaneous reduction of exhaust emissions with no penalty can be achieved through the application of widely separated, two-stage combustion, consisting of early stage, pre-injection and late stage main injection. However, their result was limited to part load condition, thus further investigation of the effect of such fuel injection strategy over the entire operating range of diesel engines is required. Ricaud and Lavoisier [113] experimentally optimised HSDI diesel engine performance through the application of a multiple injection strategy consisting of pre-injection and main injection; two pre-injections and main injection; and two pre-injections, main injection and post injection. Their results indicated that there is virtually no advantage in using long pre-injection dwell timing, unless completely homogeneous combustion is desired. The authors concluded that the fuel quantity during each injection phase, the dwell angle between injections, the injection pressure and the start of injection timing as well as EGR ratio must be carefully selected to achieve optimised performance. In addition, Gill and Zhao [114] investigated the effects of multiple injection strategy on diesel combustion and emissions using commercially available diesel fuel and bio fuels. HCCI combustion was achieved through the use of multiple injection strategies which resulted in reduction of exhaust emissions. These results were further confirmed through the application of optical diagnostic techniques such as two-colour, chemiluminescence imaging and high speed video imaging.

Lee et al. [115] investigated the effect of split injection strategy in a diesel engine using CFD simulation. A multidimensional CFD application, Star-CD coupled with a modified 2-D flamelet was used to simulate multiple injection combustion. It was reported that the in-cylinder pressure and temperature were much lower than those of

normal injection conditions due to the advanced timing of the first injection, though poor fuel evaporation was reported. As a result, spray wall impingement occurred, resulting in increased level of uHC and CO emissions. They reported that spray wall impingement could be eliminated, provided that the timing of the first injection was retarded. In addition the effect of piston bowl geometry was investigated. The piston shape was designed such that fuel droplets were captured in the piston bowl. The combination of multiple injection strategy and optimised piston bowl geometry was proved to substantially lower NOx and soot emissions.

2.5 Exhaust Gas Recirculation

EGR is a widely adopted and understood method of NOx reduction whereby burned exhaust gases are recirculated and introduced into the intake manifold, the percentage of which is dependent on engine load and speed. The presence of exhaust gases lowers the in-cylinder charge temperature due to their higher specific heat capacity than air. Additionally, some of the excess oxygen in the pre-combustion mixture is replaced by the recirculated exhaust gases, reducing the combustion rate and peak temperature as the combustion takes place later in the expansion cycle. The reduction in in-cylinder temperature leads to lower NOx emissions since NOx formation is highly temperature sensitive, as explained in Section 2.1.2.1. The downsides of this technique are related to the issues of increased engine wear as well as increased CO and uHC emissions or even fuel economy penalty. In addition, one of the major drawbacks of using EGR is associated with the reduction of specific heat ratio of the mixture inside the cylinder which in turn lowers the amount of energy that can be extracted during the combustion process.

2.6 Optical Diagnostics

The combustion process and the level of exhaust emissions are directly related to spatial and temporal distributions of premixed fuel and air inside the combustion chamber of diesel engines. Diesel combustion is heterogeneous, unsteady and three dimensional, involving complex physical and chemical reactions. Optical techniques applied to IC engines can provide valuable insight into the mixture formation and combustion processes which could not be obtained either theoretically or

experimentally using conventional methods. There are numerous optical techniques, selection of which depends upon the specific parameter under investigation.

2.6.1 High Speed Imaging

Direct visualisation of diesel combustion has been performed since the 1930s. The application of this technique requires a camera with a high frame rate. This technique involves a simple setup with which flame luminosity, combustion initiation sites, swirl, extent of flame coverage, soot and combustion duration, intensity and rate can be qualitatively investigated. However, when implemented in conjunction with an illumination source such as a Copper Vapour Laser (CVL) light, visualisation of the fuel injection spray is also possible which can be useful for investigating spray penetration and wall impingement. This simplified technique has been utilised in numerous investigations [104, 116- 121].

2.6.2 Fuel Spray Visualisation Techniques

As previously stated, the spatial and temporal distributions of premixed fuel and air are amongst the primary factors influencing the efficiency of diesel combustion and the level of exhaust emissions produced. Therefore, detailed analysis of evaporating diesel fuel sprays is vital for better understanding of the processes involved during the preignition phase of the combustion process. However, conventional point measurement systems are not sufficient for in depth analysis of fuel evaporation and mixing processes. As a result, nonintrusive optical techniques were developed and implemented in diesel combustion studies due to their capability in providing detailed information on characteristics of fuel sprays.

2.6.2.1 Holography

Holography has many similarities with direct photography. The principle of this method is based on the illumination of moving droplets within the test volume through the use of lasers with very short pulses. Frozen flow images of the fuel spray can be obtained due to short duration of the laser beam. The resulting hologram provides three-dimensional information of the fuel spray in form of three-dimensional images

of the fuel spray on a holographic plate. This technique involves a complex setup requiring intricate manipulation of the light source. Although the application of this method requires no calibration, it is limited to the analysis of relatively less dense sprays. This technique is capable of measuring liquid droplets as small as 15 μm [122].

2.6.2.2 Shadowgraph Technique

The shadowgraph technique is amongst the primary visualisation techniques which projects the line of sight information onto a viewing screen or the camera focal plane [123]. The application of this technique involves the use of a light source and an optical lens with which the shadow created due to light reflection of fuel droplets are focused onto a screen or CCD camera. Figure 2.9 shows the schematic diagram of the Shadowgraph Technique.

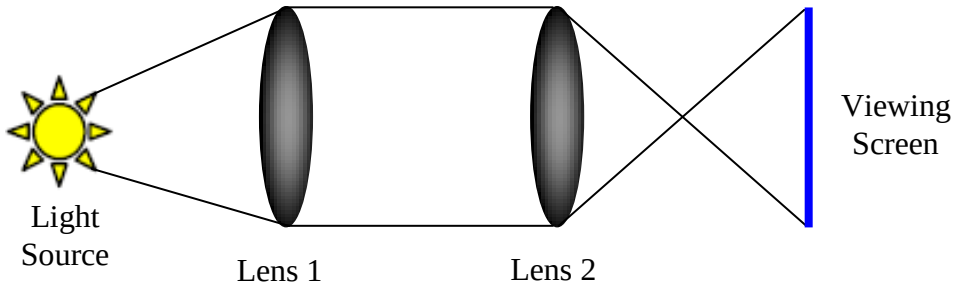

Figure 2.9 Schematic Representation of Shadowgraph Technique

2.6.2.3 Laser Rayleigh Scattering

The principle of Laser Rayleigh scattering (LRS) technique involves detection of scattered light at the same wavelength as the incident light, referred to as elastic scattering. This method is capable of providing detailed information on the vapour phase of fuel sprays in the absence of liquid droplets since the Mie scattering from fuel droplets in the test volume would otherwise be many orders of magnitude stronger than the LRS signal. This technique suffers from interference from Mie scattering due to solid particles and refection from the surrounding walls since the Rayleigh signal is at the same wavelength as that of the scattered light.

2.6.2.4 Mie Scattering

The principle of this technique is similar to LRS, it is based on elastic scattering of the test sample. This technique is capable of providing detailed information on liquid fuel droplets distribution. It is not sensitive to either molecular number density of the test sample or the ambient temperature. The scattered signal intensity is proportional to the size of liquid droplets; thus, liquid droplet size distribution measurements can be carried out using this method. Mie scattering signal is very strong since it involves no energy exchange and is merely based on elastic scattering of liquid droplets at the same wavelength as the light source.

2.6.2.5 Laser Induced Fluorescence

The principle of Laser Induced Fluorescence (LIF) is based on the excitation of the tracer molecules in a flow field with a monochromatic light source and the detection of fluorescence signal emitted by the dopants. The fluorescence signal intensity is proportional to fuel mass concentration, provided that the detection system is aptly calibrated. However, the detected signal contains fluorescence emission from both liquid and vapour phases and thus, incapable of providing discrete information on liquid and vapour phases. Although attempts were made to subtract Mie scattering signal from the LIF signal in order to segregate liquid and vapour signals, it resulted in the loss of vapour signal in the regions where liquid droplets were present.

2.6.2.6 Laser Induced Exciplex Fluorescence

In comparison with the normal LIF technique, Laser Induced Exciplex (*Exci*ted state com*plex*) Fluorescence (LIEF) technique is capable of discrete measurement of liquid and vapour phases at spectrally well separated wavelengths with potential for quantification. The LIEF technique was initially proposed by Melton [124]. It is based on the addition of organic dopants to the base fuel while maintaining similar chemical and physical properties in comparison to that of standard diesel fuel. This technique enables simultaneous and discrete measurement of liquid and vapour phases, provided that appropriate organic dopants are selected, as to be explained in detail in Chapter 7.

Melton and Verdieck [125] used tetramethyl-p-phenylene diamine (TMPD)/naphthalene exciplex system with the following concentration, 90% n-decane, 9% TMPD and 1% naphthalene. They reported on the potential of this exciplex system for quantitative analysis of fuel spray characteristics due to its proportionality to fuel mass concentration, provided that laser scattering and absorption effects as the laser light travels through the sampling volume is compensated for. More importantly, the quenching effects due to molecular oxygen were reported to significantly suppress the vapour phase signal intensity for which the use of an inert gaseous medium such as nitrogen was proposed. The first application of LIEF was first reported by Bardsley et al. [126, 127] where liquid and vapour portions of a fuel spray produced by a hollow cone injector were illuminated by an Nd:YAG laser which were recorded by an Intensified Charge Coupled Device (ICCD) camera. This technique was also implemented by Diwakar et al. [128] and Bower and Foster [129] in IC engines for simultaneous measurement of liquid and vapour portions of evaporating fuel sprays.

Melton [130] proposed a quantitative method based on the calibration of several photophysical parameters including light absorption and quantum yield of TMPD/naphthalene exciplex system. However, the accuracy of the calibration results depended on the accuracy of the individual calibration procedures involved. Subsequently, Rotunno et al. [131] presented a direct calibration procedure for the vapour phase concentration in the temperature range from 313 to 443 K. They have quantitatively illustrated the transient behaviour of the vapour and liquid phases in an evaporating spray. Felton et al. [132] also applied the technique to a hollow-cone spray in a two-stroke diesel engine. However, the vapour phase concentration obtained by Rotunno et al. [131] exhibited a considerable disparity when compared to the results obtained through direct-pressure measurement by Felton et al. [132]. This was attributed to highly temperature dependent nature of the TMPD absorption as the temperature exceeded 500 K. Yeh et al. [133] also carried out quantitative analysis of fuel vapour concentration in a rapid compression machine. They calibrated the TMPD fluorescence intensity in a range from 500 to 800 K. Their result showed that the absorbance of TMPD was minimally affected by the surrounding temperature, contrary to the results reported by Felton. Senda et al. [134] applied the exciplex

method to an impinging spray in a CVC with the ambient temperature and pressure of 700 K and 25 bar respectively. The authors used the Lambert-Beer's law to measure the TMPD concentration from measured fluorescence intensity and subsequently correcting the intensity for the effects of fluorescence quenching, the ambient temperature and fuel mixture concentration. The fuel temperature was estimated based on two assumptions: the mixing between the fuel and air was adiabatic and occurred at constant pressure. Ghandhi and Kim [135] also carried out a series of LIEF experiments in a CVC whereby they developed a technique for quantitative analysis of vapour concentration in evaporating fuel sprays.

More recent work using this technique involved quantitative analysis of fuel vapour concentration by Yamashita et al. [136]. The effect of ambient pressure from 30 to 50 bar and temperature between 550 to 900 K on TMPD fluorescence intensity and ultimately fuel vapour concentration was intensively investigated. The authors utilised this technique for detailed investigation of the influence of nozzle hole diameter, injection pressure and ambient conditions on fuel spray characteristics. Bruneaux and Maligne [137] applied the LIEF technique aimed at detailed investigation of fuel evaporation and mixing processes using a single hole common rail diesel injector, allowing high injection pressure up to 1200 bar. The experiments were carried out in a high pressure, high temperature CVC that replicated the thermodynamic conditions similar to those experienced in diesel engines at the time of injection. The tested injection strategies included a single short injection serving as a reference and two double short injections with short and long dwell timings.

2.6.3 Two-colour Method

The two-Colour Method was developed in 1932 by Hottel [138] aimed at flame temperature measurement in industrial furnaces. However, Matsui et al. [139-141] further developed and implemented this technique for flame temperature and soot concentration measurements in diesel engines. The principle of the two-colour method is based on the detection of the radiation from soot particles during combustion. Plank's law was applied in order to estimate the flame temperature and soot concentration. However, this equation is based on the radiation of a black body which

is a theoretical concept. As a result, the radiation emitted by a black body and a non-black body were linked by introducing the concept of apparent temperature, T_a, which is defined as the temperature at which the radiation emitted by a black body is equal to that of a non-black body at a temperature T. Thus, the soot radiation was measured at two different wavelengths from which two apparent temperatures were calculated. Based on the measured apparent temperatures, the flame temperature and soot concentration were estimated using the calibration data obtained through the use of a tungsten lamp. The theoretical background surrounding the application and calibration of this technique is outlined in Chapter 4.

Zhao and Ladommatos [142, 143] presented a guide for the application of the two-colour method, from which the theory of this technique is adopted. The two-colour method has been implemented in diesel engines with "Bowditch" design using various optical configurations [139-141, 144]. In these investigations an ICCD camera was utilised for the measurement of soot concentration and flame temperature, however, due to inherent long data acquisition time of this type of camera system, only one image per cycle was taken. Thus, previous results suffered from cyclic variations even though ensemble averaged images at each engine crank angle were obtained. However, the in-cylinder thermodynamic conditions are considerably different in optical engines compared to standard all-metal diesel engines; this is due to excessive heat loss and air leakage in optical engines. In order to overcome such hurdles, this technique was applied in standard production diesel engines through the use of fibre optics [145, 146] and endoscopes [147, 148]. More recently, Tominaga et al. [149] applied this method in a two-stroke optical diesel engine. In this study a high speed video camera was used which allowed cyclically resolved in-cylinder measurement of soot concentration and flame temperature. However, the experiments were carried out at very low engine speed of 345 rpm which did not replicate any typical operating condition of a modern HSDI diesel engine.

2.7 Summary

This chapter has presented the background, current and future state of emissions legislation. The exhaust emissions from diesel engines were outlined, detailing their

respective mechanism of formation and diminution. The significant amount of research carried out on conventional and modern alternative diesel combustion modes have been extensively discussed. The experimental investigations detailing the effects of injection parameters including injection timing, rate and strategies were explicated. Finally, various optical diagnostic techniques were explained and the techniques employed in this study were outlined.

The review of the previous experimental studies has shown that few in-cylinder studies were carried out on the fuel injection and combustion processes with split injections. This is mainly due to the introduction of alternative combustion processes such as HCCI and PCCI combustion modes involving multiple injection strategies. However, recent studies are focused on exposing the true potential of split injection strategy due to the simplified nature of the combustion process using this mode of fuel injection in comparison to multiple injection strategies. In this study, a single cylinder optical research engine of "Bowditch" design was used to carry out systematic investigations of split fuel injections, their interactions and the subsequent autoignition and combustion processes. The present study involves detailed investigation of split injection strategy using 30:70, 50:50 and 70:30 injection strategies through the application of different optical techniques as well as conventional heat release analysis and emission measurements. The fuel injection process was characterised through high speed laser illuminated imaging. The LIEF technique has been developed and implemented for the analysis of fuel spray evaporation and mixing processes during preignition phase of combustion. The combustion process and soot formation was then quantified through the application of a high speed two-colour system. The results were subsequently compared with a conventional single injection strategy. The combination of these techniques were utilised in this study in order to allow detailed analysis of the effect of split injection strategies and the fuel injection system on diesel combustion and emissions.

3

CHAPTER 3

Experimental Facilities, Method and Data Analysis

3.1 Introduction

This chapter includes detailed explanation of the experimental setup, test facilities, data acquisition system and the data analysis techniques employed in this study. The characteristics of the optical single cylinder engine utilised in this study are presented. The optical techniques and their implementation are subsequently explicated. Methods for heat-release analysis and emission measurements are included as they were routinely used.

3.2 Ricardo Single Cylinder Research Engine with Optical Access

3.2.1 General Description

All experimental testing in this study was carried out in a single cylinder Ricardo Hydra engine, designed to be representative of a typical modern HSDI diesel engine. The engine specifications are depicted in Table 3.1. The engine consists of a Ricardo Hydra crankcase, extended cylinder block with a standard production cylinder head and common rail fuel injection system. The engine is mounted on a Cussons Technology single cylinder engine test bed comprising of a seismic mass engine mounting, 30 kW DC dynamometer and engine coolant and oil circuits, as shown in Figures 3.1 and 3.2.

The extended engine cylinder block has upper and lower portions which are connected to the cylinder head and the engine crankcase respectively; such a configuration was implemented in order to accommodate the installation of the extended piston. The

cylinder block was machined with three cylinder wall cut-outs where glass windows can be fitted to gain optical access through the side.

Table 3.1 Ricardo Hydra Engine Specifications

Ricardo Hydra Single-Cylinder Engine	
Bore	86 mm
Stroke	86 mm
Swept Volume	499 cm^3
Compression Ratio	16:1
Piston Bowl Diameter/Depth	43.4/11.6 mm
	Re-entrant bowl with flat bottom
Swirl Ratio	1.4
Engine Speed for Testing	1500 rpm

The mechanical and thermal stresses the optical components are exposed to during firing cycles are substantial, thus the operating time of optical engines is extremely limited. As a result, both the coolant and lubricating oil are heated prior to use to ensure reasonable engine temperature was achieved. The engine coolant was preheated to 90^{o}C while the lubricating oil was preheated to 80^{o}C. The coolant system consists of a test bed mounted electric water pump and a thermostat controlled immersion heater. The lubrication system consists of a wet sump, test bed mounted gravity-fed pressure pump driven by an electric motor and two immersion heaters in the sump. Oil is drawn from the sump and pumped through an oil filter before being fed to the main oil gallery in the crankcase which provides the required level of lubrication to the crankshaft and big end bearing in the crankcase and to the camshaft in the cylinder head. The lower piston and piston rings are lubricated by splash lubrication whereby oil thrown up by the upward motion of the piston onto the cylinder wall facilitates the lubrication.

The 30 kW DC dynamometer motors the engine which acts as a brake when the engine is firing. The dynamometer control system allows a set engine speed point to be set and automatically maintained by driving or braking the engine as necessary.

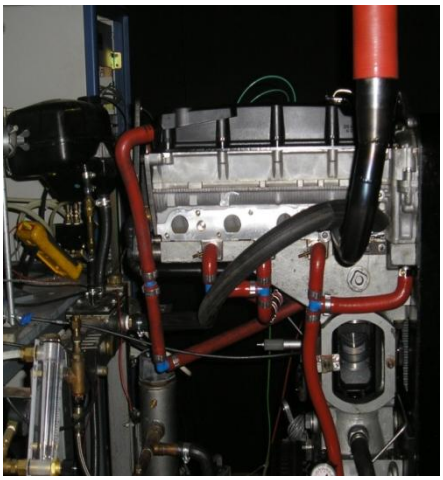

Figure 3.1 Front View of the Ricardo Hydra Engine

Figure 3.2 Side View of the Ricardo Hydra Engine

3.2.2 Cylinder Head

The Ricardo Hydra engine utilised in this study was designed to allow the use of a standard production four-cylinder head. In order to accommodate mounting of such a cylinder head on the single cylinder block, a platform visible in Figure 3.1 was designed and manufactured. The cylinder head is from a production Ford 2.0 litre ZSD 420 Duratorq turbocharged engine. The aluminium cylinder head consists of double overhead camshafts, four valves, a centrally located injector and a glow plug. The valve train of the unused cylinders is deactivated through the removal of the rocker arms. The corresponding oil feed holes on the rocker shafts are blocked off in order to prevent the squirting of unnecessary oil which could result in drop in oil pressure. As previously mentioned, the engine is preheated prior to the use, thus problems associated with the cold start are eliminated. Therefore, the glow plug in this study is replaced by a Kistler 6125 piezoelectric pressure transducer for in-cylinder pressure measurement.

3.2.3 Optical Configuration

3.2.3.1 Extended Piston and Cylinder Block

Optical access is provided by the Bowditch piston design which allows for the visualisation of the combustion chamber through the axis of the cylinder via a glass window, made from fused silica, mounted in the crown of the piston. An extended

piston and cylinder block are required in order to accommodate such an optical configuration which consists of lower and upper parts with a 45^{o} angled mirror, made of glass with aluminized front surface, between the sections. Thus, the combustion chamber and cylinder walls can be fully visualised through such an optical setup, Figure 3.3. The lower part of the piston consists of a standard type piston, modified such that the upper piston can be bolted on. Conventional oil scraper rings are utilized to control the excess oil in the lower cylinder wall while the elongated piston has a large through-slot allowing the mounting of the 45^{o} mirror around which the piston reciprocates.

The extended cylinder block and elongated piston cannot be lubricated by oil due to rapid contamination of the optical surfaces. Thus, the upper piston is lubricated by two carbon graphite rings made of Le Carbone Lorraine grade 5890 carbon. Additionally, two conventional steel compression rings are fitted for sealing, lubricated by the carbon particles deposited on the cylinder walls by the carbon rings. In order to provide additional lubrication between the piston and the cylinder block, high performance dry film lubricant, manufactured by Rocol, is applied to the upper cylinder block during each rebuild.

3.2.3.2 Optical Windows

The upper cylinder block has three rectangular cut-outs which can be fitted with glass

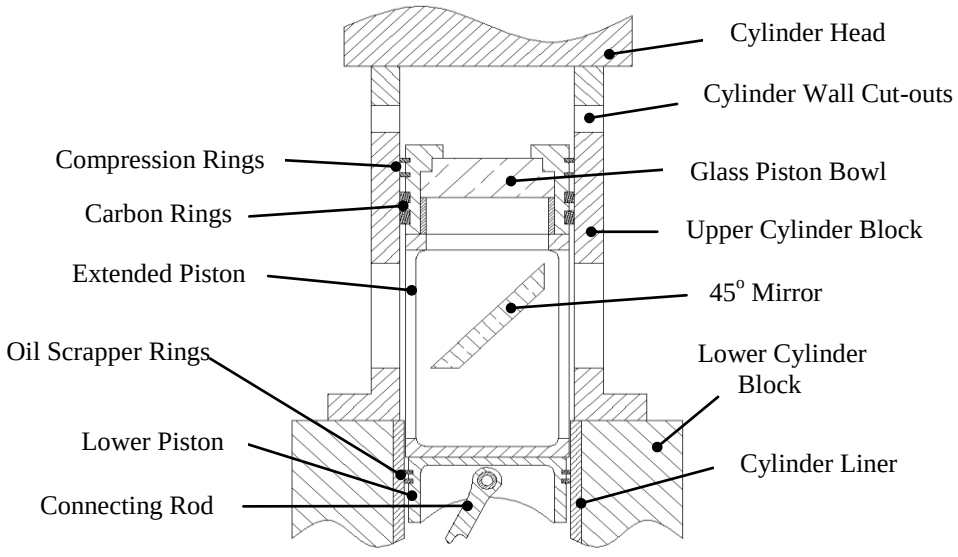

Figure 3.3 Sectional Schematic View of the Optical Layout

windows made of fused silica for side optical access. Two of these windows which can be seen in Figure 3.4, are in the same plane allowing laser sheet imaging while the third window is positioned at 90^{o}, premeditated for imaging and detection purposes.

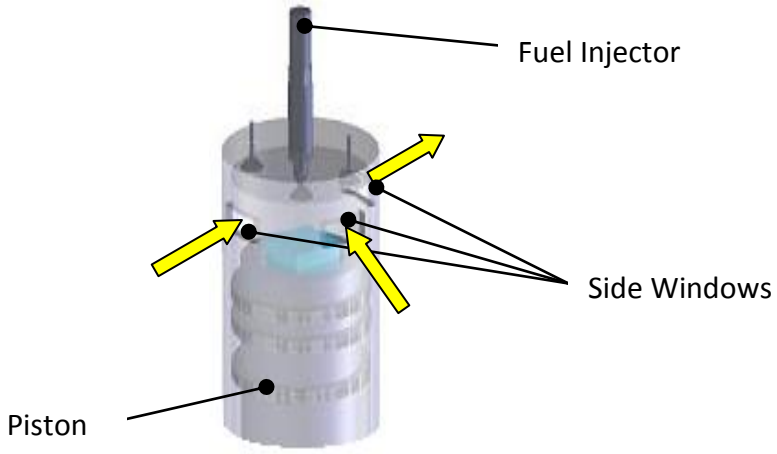

Figure 3.4 Schematic View of Side Windows

The optical access in this study was through the crown of the elongated piston. The piston has an internal diameter of 43.4mm in which the optical window is mounted. However, it is extremely difficult to seal a combination of glass and metal surfaces; therefore achieving a reasonable in-cylinder pressure with minimum cylinder leakage is difficult. Figure 3.5 is a schematic diagram of the upper part of the piston detailing the sealing arrangement.

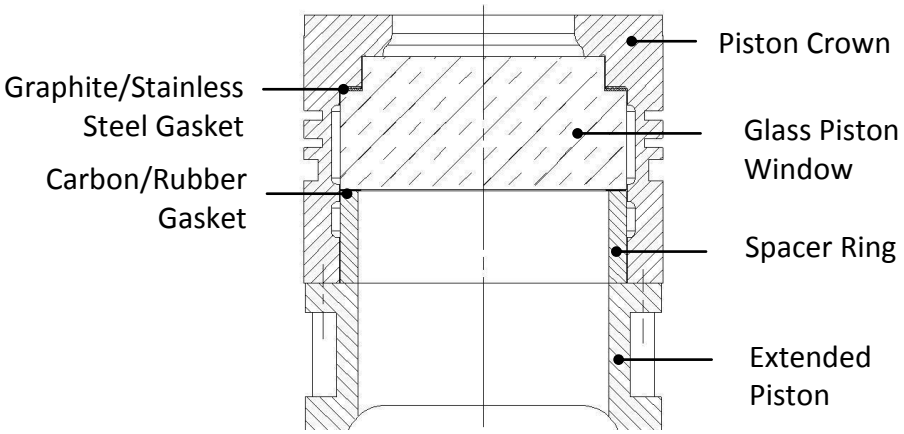

Figure 3.5 Schematic View of the Piston Assembly

A steel spacer ring is machined and fitted between the upper piston and the lower piston ensuring a snug fit of the glass and gaskets. The spacer ring cannot be tightly clamped against the carbon gasket and the glass window due to brittle nature of the optical window. This is mainly due to stress concentrations encountered by the optical window while the engine is running. In order to overcome this difficulty, three raised edges were machined on the surface of the spacer ring where it was in contact with the carbon gasket, creating high pressure points to assist sealing. In addition, an O-ring was fitted on the inner surface of the piston where it is in contact with the glass piston in order to further prevent gas leakage through this gap. The schematic diagram of the modified piston assembly is shown in Figure 3.6. Consequently, the cylinder leakage was greatly reduced in comparison to the previous studies carried out by Gill [150] and Diez [151] at Brunel University; explained in detail in Chapter 6.

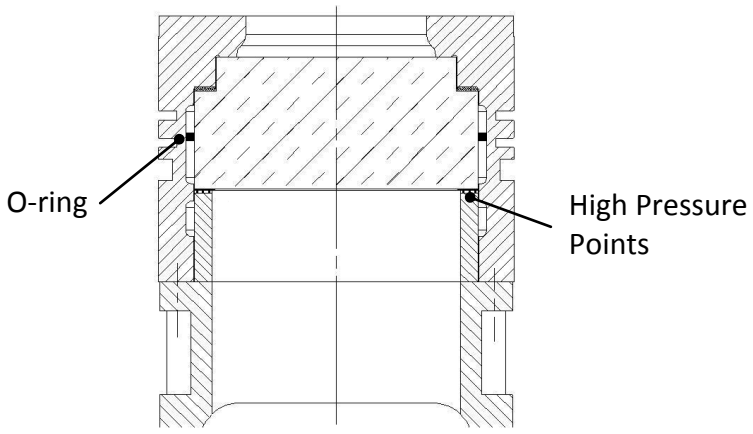

Figure 3.6 Schematic View of the Modified Piston Assembly

Furthermore, the force exerted on the glass piston due to the increase in the in-cylinder pressure during the compression stroke forces the glass down against a Klingersil gasket made of carbon and rubber to further assist the sealing on the underside of the piston. On the other hand, a Klinger graphite-laminate SLS gasket, consisting of graphite with a reinforcing stainless steel mesh core, is placed on top of the optical window to dampen the impact with the piston crown due to directional changes and/or vibrational forces encountered.

The piston window is replaced by a metal piston blank to avoid excessive thermal stress on the optical components during emissions test. The blank is held in the extended piston by a spacer ring and has a copper ring for sealing purposes. This configuration allows for continuous operation of the engine for longer periods of time.

3.2.4 Crank Shaft Position System

In order to establish the angular position of the crankshaft, a shaft encoder is fitted to the crankshaft. The shaft encoder generates two signals: one Pulse per Revolution (ppr) and 1800 ppr. These signals are sent to the Electronic Control Unit (ECU) which controls the fuel injection and data acquisition systems. The single pulse is used to illuminate a Light Emitting Diode (LED) which represents the thermodynamic TDC position on the appropriate high-speed movie frames as shown in Figure 3.7.

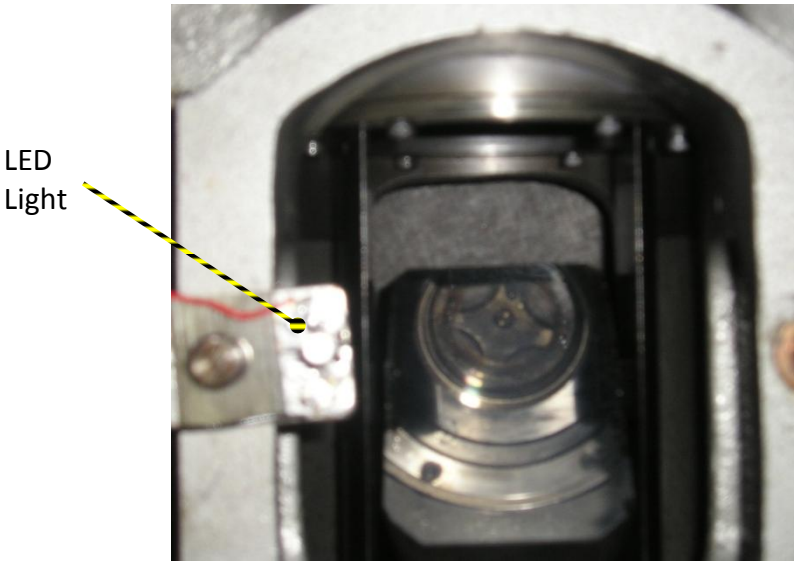

Figure 3.7 LED Position

The single pulse signal is generated on every revolution, hence generating two signals per engine cycle. In order to identify the TDC corresponding to the compression stroke, a hall-effect sensor, operating with a metal disc mounted on the high pressure pump driven at half the engine speed is utilised. The presence or absence of the signal from the hall-effect sensor allows the fuel injection system to determine which part of the cycle each TDC signal refers to.

3.2.5 Fuel Injection System

The fuel injection system is designed to promote high level of atomization aimed at maximizing fuel evaporation and mixture formation over a short period of time. The fuel injection system must be capable of precise supply of fuel into the combustion chamber of an engine at a specific time and rate over the entire engine loads and speeds.

The common rail fuel injection system employed in this study was capable of producing maximum injection pressure of 1350 bar. This system is commonly used for HSDI diesel engines as the injection pressure is independent of the engine speed, promoting improved mixture formation and greater flexibility in terms of injection rate and timing over the entire operating range of the engine, explained in detail in Chapter 5. The fuel supply system consists of a fuel filter and a 12V low pressure pump which draws the filtered fuel from the fuel tank. A first generation Bosch high pressure pump is employed for the generation of pressurised fuel to one of the injectors, Figure 3.8.

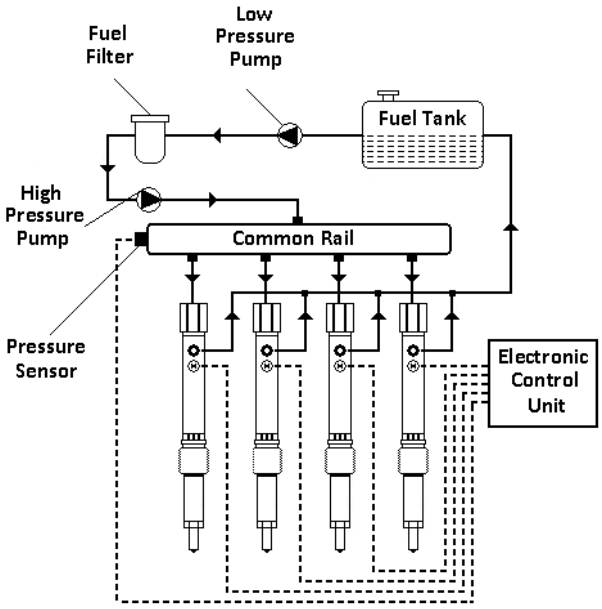

Figure 3.8 Schematic Diagram of Common Rail Fuel Injection System

The fuel is supplied to a Delphi common rail through a single thick-wall steel pipe. The Common Rail System (CRS) is fitted with a Delphi rail pressure sensor whose

signal is fed to the ECU to regulate the injection pressure. The common rail employed in this investigation consists of four outlets, one of which was used to connect the rail to the injector through a high pressure pipe while the other three were blanked off. In this configuration, the high pressure pump continuously supplies the common rail with pressurised fuel. The volume of the rail is large enough to suppress pressure waves due to injections; however, the high pressure pipes between the common rail system and the injectors reduce the peak injection pressure due to losses encountered inside the pipe.

The injector utilised in this study was a Delphi multi-hole Valve Covered Orifice (VCO) injector capable of injecting up to 1600 bar. However, the high pressure pump limits the maximum system pressure to 1350 bar as previously mentioned. The specifications of the fuel injection system are shown in Table 3.2.

Table 3.2 Fuel Injection System Specifications

Injection System	
1st Generation Common Rail System	
Maximum Injection Pressure	1350 bar
Delphi Standard Injector	
Number of Holes	6
Hole Size	0.154 mm
Cone Angle	154^{o}
Flow Rate	0.697 l/min
Type	VCO

The high pressure pump is designed to operate with diesel fuel whereby the mechanical parts of the pump are well lubricated through the circulation of fuel inside the pump. The use of low lubricity fuels could lead to premature failure of the pump, yet, as part of this investigation LIEF technique was implemented for in depth analysis of evaporating diesel fuel sprays whereby special blend of low lubricity single component dopants were utilised, discussed in detail in Chapter 7. Thus, in order to retain the fuel injection characteristics throughout the entire investigation, a pneumatic high pressure pump was employed instead which required no lubrication. Therefore,

the first generation Bosch high pressure pump outlet was blanked off and the pneumatic pump outlet was directly connected to the common rail.

The injection system was controlled by the use of an EC-GEN 500 ECU supplied by EmTroniX. The injection system is controlled through the use of computer based software called EC-Lab. The input signals from the shaft encoder, hall-effect sensor and rail pressure are detected by the ECU. Subsequently, the injection pressure, number of injections, timing and quantity can be set in EC-Lab. The schematic diagram of the fuel injection control system is depicted in Figure 3.9.

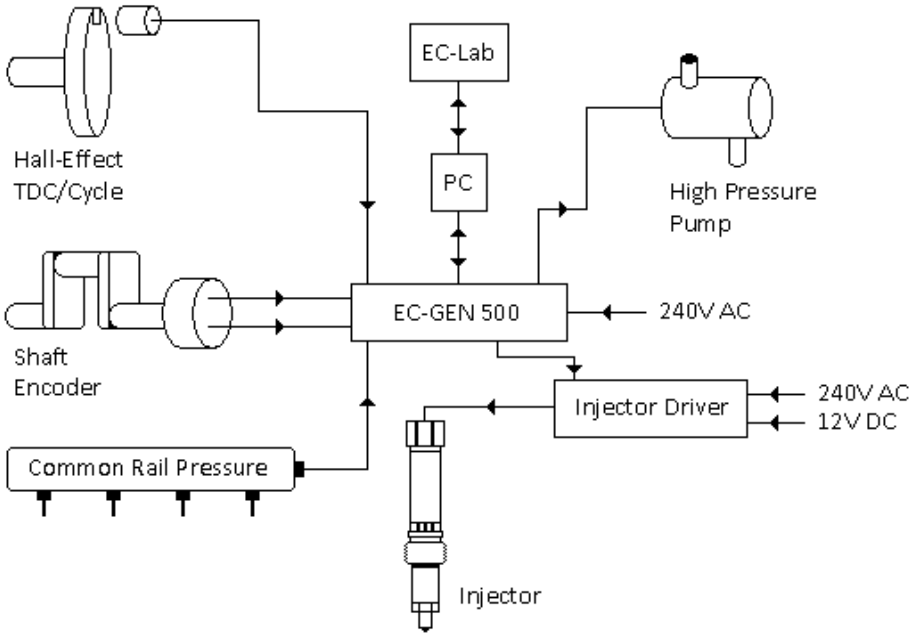

Figure 3.9 Schematic Diagram of Fuel Injection Control System

The ECU generates two output signals; the first is fed to the high pressure pump to control the injection pressure while the second is sent to the injector driver. Subsequently, the injector driver generates a current signal which is then transmitted to the injector. A screenshot of the user interface is shown in Appendix A.

3.2.6 Intake System

The single cylinder Hydra engine used for the purpose of this investigation was setup such that it could operate based on two principles; naturally aspirated and

supercharged. The changeover valve was utilised in order to switch between the two modes. It is also possible to simulate the effect of EGR on combustion characteristics and exhaust emissions through the injection of nitrogen into the intake system as illustrated in Figure 3.10.

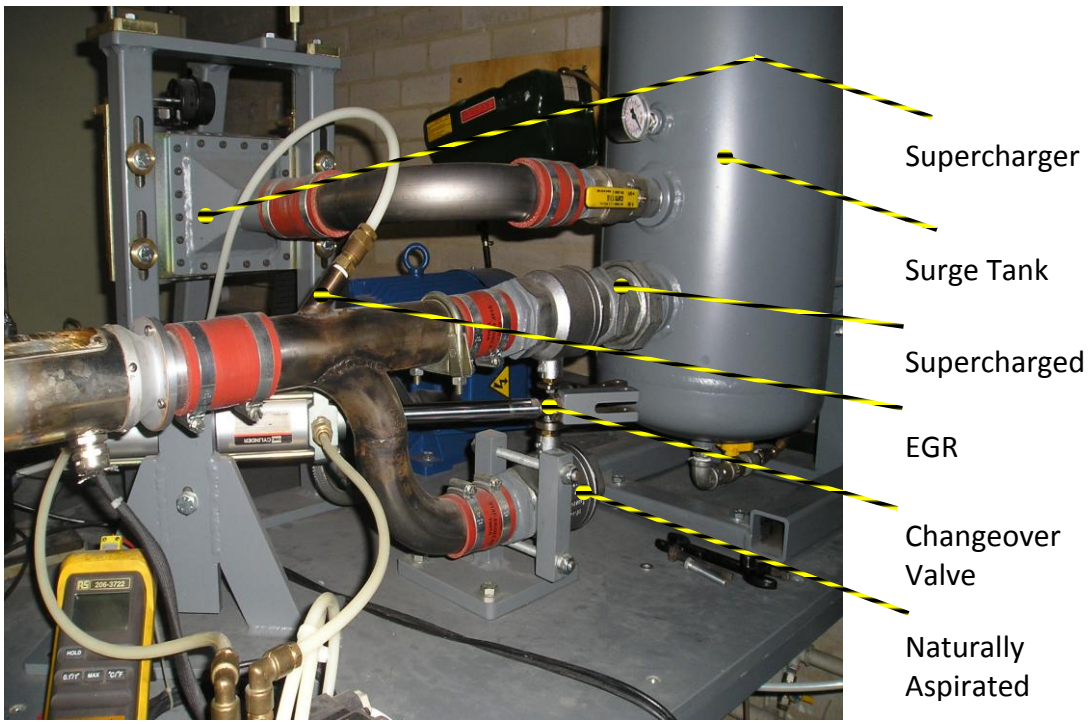

Figure 3.10 Ricardo Hydra Engine Intake System

The principle of this setup is based on the injection of nitrogen into the intake manifold aimed at replication of the effect of EGR on combustion characteristics and exhaust emissions. However, the effect of EGR has not been investigated in this study.

3.2.6.1 Forced Induction

The intake system of the engine is equipped with a forced induction system to allow boosting of the intake pressure when required. A positive displacement roots type blower, Eaton M45 supercharger, with three lobes and helical rotors driven with an AC motor rotating at 2600 Revolutions per Minute (rpm) is used. The supercharger is capable of producing maximum boost pressure of 0.5 bar, though it incorporates a bypass valve allowing the boost pressure to be manually controlled by opening and closing the bypass valve. The maximum boost pressure is achieved when the bypass

valve is fully closed. Figure 3.11 shows the supercharger, drive motor and bypass valve.

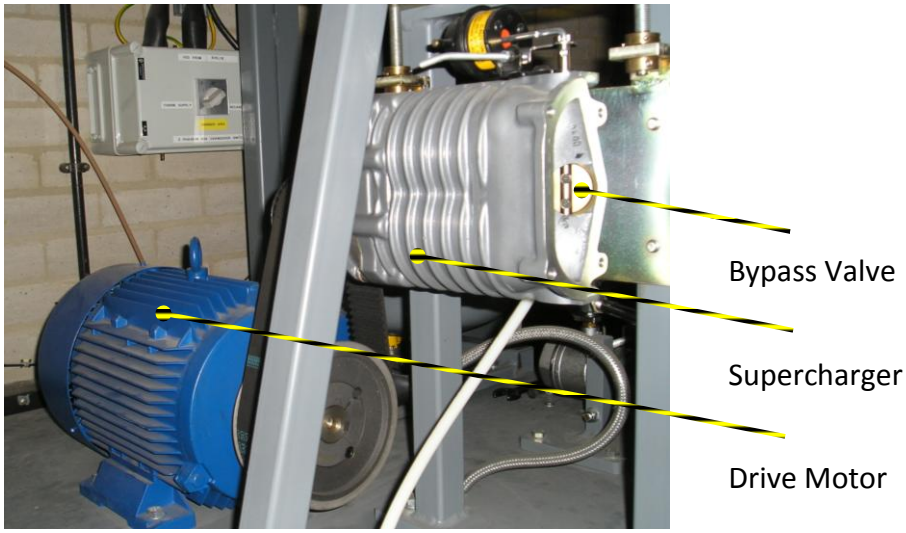

Figure 3.11 Supercharging System

A Kistler 4045A5 piezo-resistive pressure transducer, shown in Figure 3.12, is mounted in the intake manifold which is equipped with a Kistler 4618A2 piezo-resistive amplifier. The signal from the charge amplifier is connected to a digital oscilloscope from which the intake manifold pressure can be determined and recorded.

3.2.6.2 Intake Heating

In order to replicate typical operating conditions of HSDI diesel engines, intake air was heated by a 3kW heater installed upstream of the intake manifold which can be used in both naturally aspirated and forced induction modes as shown in Figure 3.12.

A thermocouple was installed in the intake manifold whose signal was fed to a custom built heater control box allowing closed-loop control of the air temperature. The control box turns the heater on and off continuously in order to maintain the air temperature at the preset value. Intake air temperature of 100^{o}C was set on the heater box for the purpose of this study.

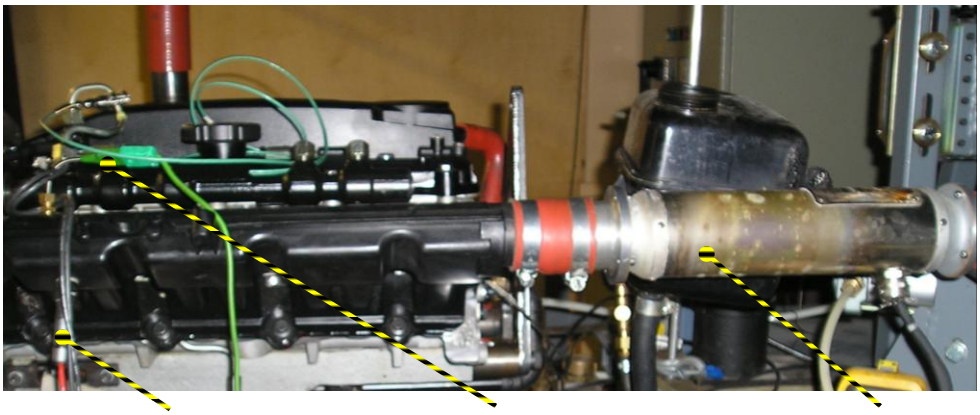

Figure 3.12 Intake Heating System

3.3 In-Cylinder Pressure Data Acquisition System

The in-cylinder pressure measurement, through which heat release rate is estimated, is a powerful tool in the analysis of diesel combustion. Additionally, the motoring in-cylinder peak pressure is a useful measure in assessing the condition of piston window seals. Reduction in the peak pressure is typically an indication of cylinder leakage. The principle and implementation of the in-cylinder pressure measurement and heat release analysis are detailed in the following sections.

3.3.1 In-Cylinder Pressure Measurement

As previously stated in Section 3.2.2, A Kistler 6125A piezoelectric pressure transducer, mounted in place of the glow plug, is connected to a Kistler 5011 charge amplifier in order to measure the in-cylinder pressure. The transducer is un-cooled with a range of 0-250 bar and a sensitivity of -15 pC/bar. The charge from the transducer is passed through the charge amplifier which converts and amplifies the signal into an output voltage. The output signal is subsequently fed to the data acquisition system.

The pressure transducer and charge amplifier were calibrated using a deadweight tester. The amplifier was calibrated over a range of 0-200 bar and was set to give the maximum output voltage of 10V at 200 bar in order to prevent the risk of overloading the charge amplifier.

3.3.2 Data Acquisition System

The data acquisition system employed in this study consists of an interface board on which a National Instruments (NI) data acquisition card is assembled. The data is recorded using a data acquisition program written in LabVIEW by John Williams, formerly at Brunel University. The signals from the shaft encoder and the in-cylinder pressure transducer amplifier are connected to the NI BNC-2110 board which itself is connected to the NI OCI-MIO-16E data acquisition board. The signals from the shaft encoder, the 1800 ppr and 1 ppr signals are used by the software as the clock and reference for the start of recording cycles respectively. Hence the data is recorded at 0.2^{o} CA intervals. The software records and displays in real-time the in-cylinder pressure as a function of crank angle. It is also capable of calculating and recording IMEP, p-V diagram, heat release rate and mass fraction burned. However, the data acquisition system was used only to record the pressure data, subsequent data analysis including the evaluation of IMEP and heat release rate were carried out in Microsoft Excel. A screenshot of the LabVIEW program is presented in Appendix A.

3.3.3 Experimental Procedure

The engine was heated by means of electrical heaters fitted on the cooling water and lubricating oil circulation systems prior to engine operation for approximately one hour in order to replicate typical operating conditions of a HSDI diesel engine as stated earlier in Section 3.2.1. The low pressure pump was turned on before motoring the engine in order to ensure that the high pressure pump was well lubricated. The engine was then motored to 1500 rpm and the intake heater was switched on. The heater could only be switched on when the engine is running to avoid overheating. When the intake air temperature reaches 100^{o}C, testing can commence. In order to fire the engine, a button in the EC-Lab software was pressed to start the injection. The reverse procedure was followed when the test was completed. To record the in-cylinder motoring pressure, the “Run” button in the LabVIEW data acquisition program was pressed which was set to record and save the in-cylinder pressure of 20 consecutive cycles. To record the combustion pressure, the engine was fired for a few cycles to improve the combustion stability before the data acquisition system was triggered. In practice in-cylinder pressure data is averaged over few hundred engine

cycles, however, this is not possible with optical engines due to excessive window fouling even at low load conditions. Thus, the in-cylinder motoring and combustion pressures were acquired for 20 consecutive engine cycles which was identified to be the optimum value for the tested conditions in this study. The glass piston and the cylinder head were thoroughly cleaned prior to the onset of each optical test in order to improve the accuracy and quality of the collected data. For the purpose of this investigation, both the in-cylinder motoring and combustion pressure data were recorded with the engine being in an optical configuration.

At the start of every test, and regularly during optical measurements, the motoring pressure was recorded and inspected in order to ensure that identical in-cylinder conditions were maintained throughout the experiments. As previously mentioned in Section 3.3, the motoring pressure was also periodically monitored to detect possible cylinder leakage due to worn piston window seals. The engine was rebuilt once reduction of 1 bar in the peak in-cylinder motoring pressure was detected.

3.4 Optical Setup

The optical techniques applied in this study involve high speed imaging, two-colour method and LIEF. The two-colour method was initially developed with ICCD cameras, capable of recording a single shot per engine cycle hence suffering from cycle to cycle variations. However, the two-colour method used in this study has been further developed, capable of operating with high speed cameras thus allowing continual measurement of required combustion characteristics over several engine cycles. The LIEF technique is a unique technique capable of simultaneous visualisation of liquid and vapour portions of fuel sprays through the use of special blend of single component dopants. The principle of the two-colour method and LIEF techniques and their implementation are explained in Chapters 4 and 7 respectively.

3.4.1 Combustion High Speed Imaging

High speed video imaging was employed to record colour video images of fuel spray during the injection period and subsequent combustion process. In order to visualise

the fuel sprays a CVL, CU15 Oxford Lasers, was utilised. The specifications of the CVL are listed in Table 3.3.

Table 3.3 Copper Vapour Laser Specifications

Copper Vapour Laser Type: CU15 Oxford Laser	
Wavelength (nm)	511
Average Power (W)	8.5
Pulses Width (ns)	10-40
Pulse Repetition Frequency (kHz)	10

An optical fibre was used to direct the beam onto the 45^{o} angled mirror which was then directed into the combustion chamber to illuminate the chamber during the initial stages of the fuel injection process. As stated in Section 3.2.4, an LED indicating the TDC position which is triggered by the shaft encoder reference signal was used to determine the TDC position. The light emitted by the LED was recorded on the captured videos thus allowing the TDC position to be easily determined from which the crank position for all the other frames were determined. Figure 3.13 shows the optical fibre, optical fibre holder and the high speed camera.

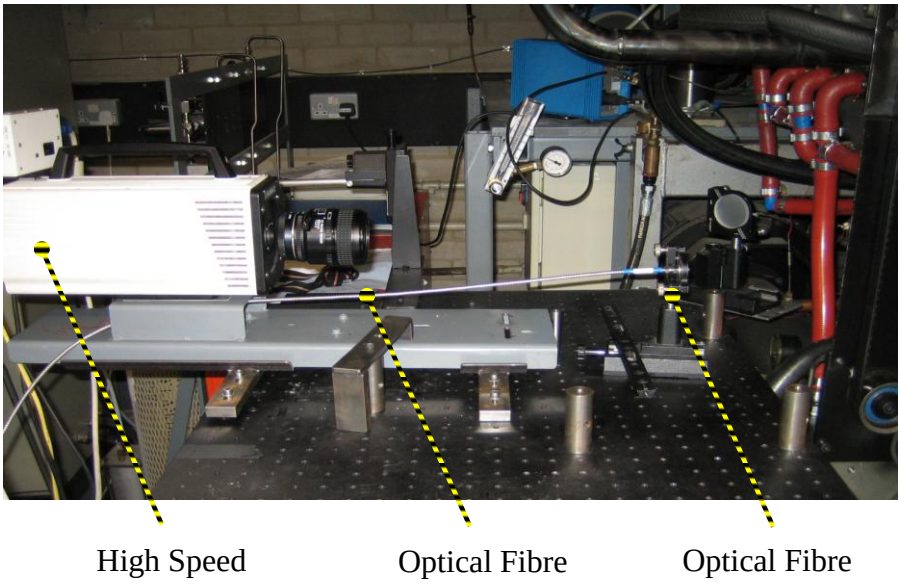

Figure 3.13 High Speed Video Imaging Optical Arrangement

A NAC Memrecam FX6000 high speed video camera was used which was equipped with a high speed colour CMOS sensor. The high speed camera was set to capture videos at 10,000 frames per second (fps), thus one frame equates to 0.9 degree crank angle at the engine speed of 1500 rpm. The image resolution is dependent on the frame rate, at 10,000 fps the image resolution was 512 x 248 pixels. A Nikon 50mm f.1.4 lens was used.

The camera was connected to a monitor via a VGA convertor allowing real-time visualisation of the recorded videos stored on the camera's internal memory, while it can also be used to visualise the combustion chamber during focusing. The selected frames were downloaded through a PC which was connected to the camera via an Ethernet cable.

3.5 Exhaust Emissions Measurement

Exhaust emissions of CO, Carbon Dioxide (CO_2), O_2, uHC and NOx were measured through the use of a Horiba MEXA-7170DEGR analyser while the soot emission was measured using an AVL 415 smoke meter.

3.5.1 Horiba MEXA-7170DEGR Emissions Analyser

The Horiba MEXA-7170DEGR was used to measure the aforementioned exhaust emissions. The unit consists of four analyser modules controlled by a PC acting as the main control unit. Each module operates based on a different measurement principle, explained in detail in the subsequent sections. The interface includes a touch screen which displays instantaneous emissions values in both graphical and numerical formats.

3.5.1.1 Horiba AIA-72X: CO and CO_2 Measurement

A Horiba AIA-72X analyser module operating based on Non-Dispersive Infrared (NDIR) method was used for the measurement of CO and CO_2 concentrations. Its measuring principle is based on the fact that different molecules absorb infrared radiation at different wavelengths whereby the concentration of each molecule is

proportional to the level of absorption. The schematic diagram of such an analyser is illustrated in Figure 3.14.

The analyser consists of a chamber which is divided into two sealed cells, sample cell and comparison cell. The latter is filled with nitrogen gas while the sample gas is pumped through the former. An infrared light source is projected into both cells. The comparison cell containing nitrogen does not absorb radiation in the infrared region thus the beam remains unattenuated. However, the gas in the sample cell absorbs radiation at specific wavelengths depending on the species present and their corresponding concentration. The infrared lights are subsequently passed through the detector cells which contain two sealed cells filled with the sample gas separated by a membrane. The difference in the radiation in the cells results in the change in the sample gas temperature leading to a differential expansion. The movement of the membrane is detected as an electrical signal proportional to the gas concentration.

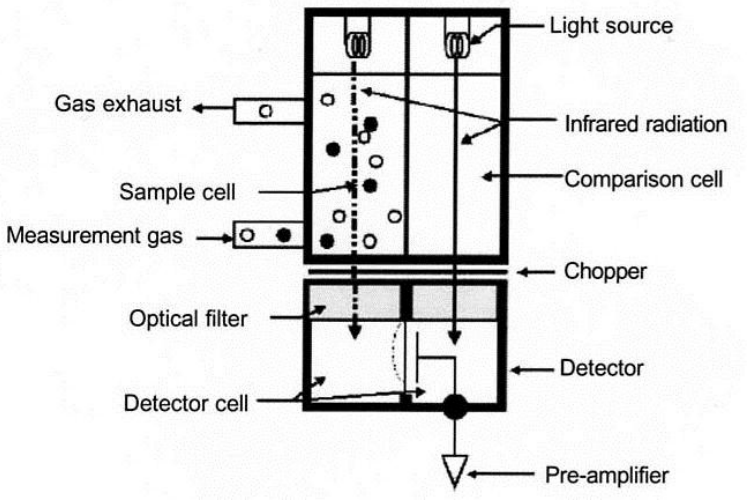

Figure 3.14 Schematic Diagram of NDIR Analyser (Horiba Instruments Ltd)

A light chopper is employed allowing intermittent transmission of infrared light to enable the detection of the changes in the species concentration in the sample cell. In order to ensure that the transmitted signal to the detector cell is merely generated by the species of interest, an optical filter is placed upstream of the detector cell to block the transmission of wavelengths absorbed by other species.

3.5.1.2 Horiba MPA-720: O_2 Measurement

The Horiba MPA-720 magneto-pneumatic analyser was used to measure the oxygen concentration. This analyser module operates based on the principle of paramagnetism, whereby certain materials are magnetic when an external magnetic field is applied upon them. Amongst all common exhaust gas components, oxygen and oxides of nitrogen namely NO and NO_2 are the only species affected in the presence of an external magnetic field while the influence of oxides of nitrogen is negligible in comparison. Figure 3.15 shows a schematic diagram of a magneto-pneumatic oxygen analyzer.

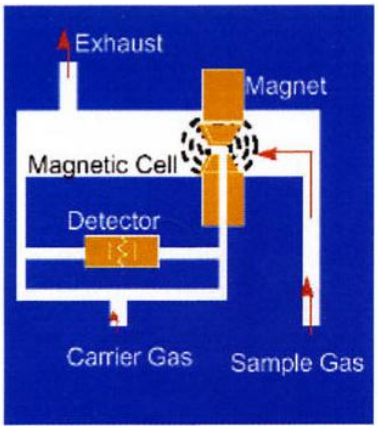

Figure 3.15 Schematic Diagram of a Magneto-Pneumatic Analyser (Horiba Instruments Ltd)

The sample gas flows through the magnetic cell whereby an electromagnetic field is created around the poles by flowing AC current through the electromagnet. The altering magnetic field attracts the oxygen molecules which creates a rise in pressure around the poles proportional to the oxygen concentration. The analyser is equipped with a condenser microphone which generates an output electrical signal upon the detection of a change in pressure.

3.5.1.3 Horiba FIA-720: Unburned Hydrocarbon Measurement

The Horiba FIA-720 Flame Ionisation Detector (FID) was used to measure the uHC concentration. The analyser module operates based on the principle that when a gas

containing hydrocarbons is burned, ions are produced. The rate of ion production is directly proportional to the hydrocarbon concentration. A schematic diagram of a FID detector is depicted in Figure 3.16. Hydrogen, employed as the fuel gas, is burned in the detector using high purity oxygen since minimal ionisation occurs during its combustion. The sample gas is mixed with the hydrogen in order to promote thermal dissociation of hydrocarbons present in the mixture; ions are produced during this process. A high DC voltage is applied between the burner jet and a collector around the flame which results in ions migrating into one and the electrons to the other which creates an electrical current proportional to the level of ionisation which is directly proportional to the number of carbon atoms present. As a result, this method is only capable of measuring the total hydrocarbons with no specific information available on specific hydrocarbon components present.

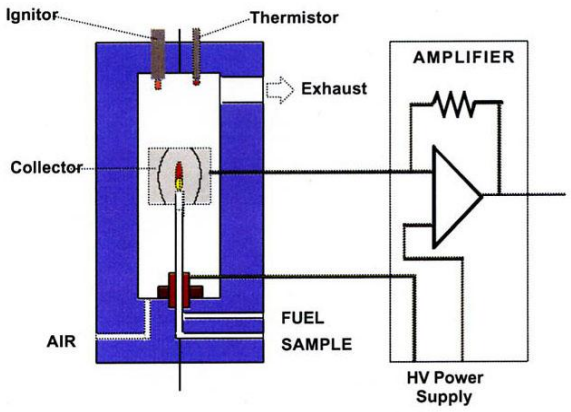

Figure 3.16 Schematic Diagram of a FID Analyser (Horiba Instruments Ltd)

3.5.1.4 Horiba CLA-720A: NOx Measurement

The Horiba CLA-720A chemiluminescence analyser was used for the measurement of NO and NO_2 concentrations. This analyser module operates based on the reaction between NO and ozone (O_3) resulting in the oxidation of NO to NO_2. However, some of the NO_2 produced through this process are in an excited state at elevated energy level (NO_2^*) as shown below:

$$NO + O_3 \rightarrow NO_2^* + O_2$$

$$NO_2^* \rightarrow NO_2 + h\nu$$

The excited molecules decay to the ground state through the emission of a photon, the process referred to as chemiluminescence. The intensity of the light emitted is proportional to the concentration of NO molecules present in the sample gas.

The sample gas enters the reaction chamber where it mixes and reacts with the ozone. The light emitted through the chemiluminescence process is passed through a bandpass filter placed in front of a light detector which outputs a voltage signal upon the detection of light. Figure 3.17 shows a schematic diagram of a chemiluminescence detector.

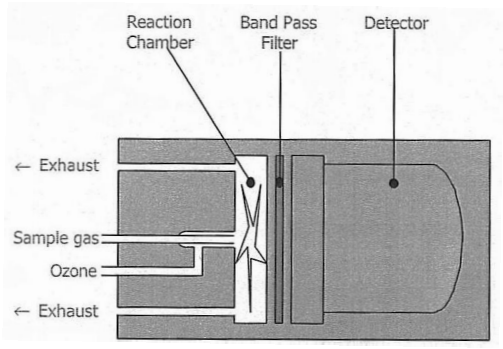

Figure 3.17 Schematic Diagram of a Chemiluminescence Detector (Horiba Instruments Ltd)

Although the majority of the excited molecules emit light by returning to the ground state, some loose their energy through collision with other molecules such as CO_2 and H_2O molecules which are present in the exhaust gas. In order to minimise such interference, the sample gas is diluted with nitrogen prior to entering the detector.

3.5.2 AVL 415: Soot Measurement

The AVL 415 smoke meter was used to measure the soot concentration. The analyser is equipped with a diaphragm type pump which sucks the exhaust gas into the sampling line. The exhaust gas is passed through a paper filter and a flow meter respectively. The measuring principle is based on the use of a reflectometer which measures and compares the reflectance of the clean and the blackened filter papers as depicted in Figure 3.18.

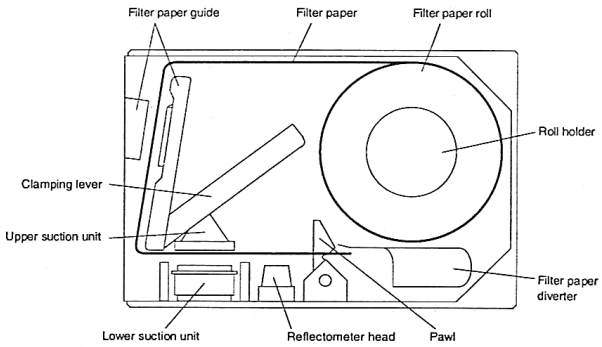

Figure 3.18 Schematic Diagram of AVL 415 Smoke Meter (AVL LIST GmbH)

This process yields the level of paper blackening where a clean white filter paper has the value of zero and a completely blackened paper has the value of 10 which corresponds to soot concentration of 0 and 32000 mg/m^3 respectively. The governing equation is given by:

$$P_B = 10 \times \left(1 - \frac{R_B}{R_W} \right) \qquad \text{Equation 3.1}$$

Where P_B Paper blackening

R_B Reflection power of blackened filter paper

R_W Reflection power of white filter paper

The soot concentration is measured in Filter Smoke Number (FSN) throughout this investigation whereby FSN is defined as FSN = P_B when L_{eff} = 405 mm, based on ISO 10054 standards, and L_{eff} is given by:

$$L_{eff} = \frac{V_{eff}}{A} \qquad \text{Equation 3.2}$$

Where L_{eff} Effective length of the gas column drawn through the filter

V_{eff} Effective volume of gas drawn through the filter

A Area of the blackened filter paper

Further, V_{eff} is defined by the following expression:

$$V_{eff} = V_S - V_D - V_L \qquad \text{Equation 3.3}$$

Where V_S Sample volume

V_D Dead volume, the volume of clean air between the filter paper and the end of the sampling line sucked through prior to the sample gas

V_L Leak volume, the volume of clean air and sample gas lost due to minor leaks

The measurement procedure is carried out automatically by the smoke meter with the FSN number displayed on a digital display. For the purpose of this investigation, the sample volume was automatically determined; the smoke meter performs an initial test to calculate the required sample volume. The meter was set to perform three consecutive sample measurements where the average was displayed.

3.6 Data Analysis

The in-cylinder pressure data was used to determine the heat release rate, mean effective pressure and ignition delay. Additionally, two-colour results and emissions data were analysed quantitatively while the high speed video images served as a qualitative measure in analysing the combustion characteristics.

3.6.1 Cylinder Volume Calculation

The cylinder volume is calculated based on the engine geometry for any crank angle using the following equations:

$$V = V_c + \frac{\pi B^2}{4}(l + a - s)$$ Equation 3.4

Where V Cylinder volume

V_c Clearance volume

B Cylinder bore

l Connecting rod length

a Crank radius

s Distance between crankshaft and piston pin axes

Further s is given by:

$$s = a\cos\theta + \sqrt{(l^2 - a^2 \sin^2\theta)}$$ Equation 3.5

The following equation defines compression ratio through the following expression:

$$r_c = \frac{V_d + V_c}{V_c}$$ Equation 3.6

Where r_c Compression ratio

V_d Displacement volume

Further, the ratio of connecting rod length to crank radius is given by:

$$R = \frac{l}{a}$$ Equation 3.7

Where R Ratio of connecting rod length to crank radius

Thus, Equation 3.4 can be rearranged to:

$$V = V_c\{1 + \frac{1}{2}(r_c - 1)[R + 1 - \cos\theta - \sqrt{(R^2 - \sin^2\theta)}]\}$$

3.6.2 Engine Combustion and Heat Release Analysis

From the in-cylinder pressure data, engine output and combustion characteristics under various operating conditions can be calculated using Microsoft Excel.

3.6.2.1 Indicated Mean Effective Pressure

Indicated Mean Effective Pressure (IMEP) is a theoretical measure of the effectiveness of the engine in producing work as a function of the displacement volume of the engine with respect to the maximum pressure produced in the cycle. It is equal to the enclosed areas on the pressure versus volume graph, referred to as p-V diagram. The p-V diagram of a four-stroke diesel engine is shown in Figure 3.19.

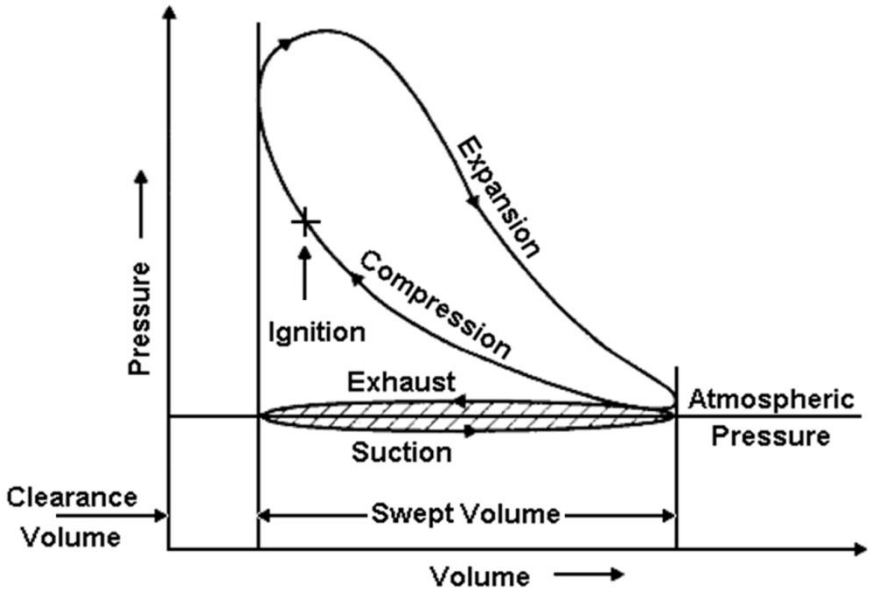

Figure 3.19 Four-Stroke Engine p-V Diagram (Joel, [152])

A four-stroke engine consists of four-strokes, induction, compression, expansion and exhaust. The p-V diagram of this type of engine consists of two loops, the work loop outlined by the lines of compression and expansion strokes and the pumping loop bounded by the lines of induction and exhaust strokes. The combustion process takes place in the work loop thus positive work is done during this period while work is done on the engine during the pumping loop hence negative work is done. The area enclosed by the work loop represents the Gross IMEP. However, net IMEP takes into account of the work done during induction and exhaust strokes and is determined by subtracting the area of the pumping loop from the work loop.

Thus, IMEP is calculated by numerical integration of the p-V diagram:

$$IMEP = \frac{1}{V_d} \int_y^x p.dV \qquad \text{Equation 3.9}$$

Where p In-Cylinder pressure

The in-cylinder pressure sampling rate serves as the step interval in Equation 3.9, 0.2^o CA in this case. The limits of integration, x and y, are zero to 720^o CA which includes the whole engine cycle, representing the Net IMEP as calculated for this study.

3.6.2.2 Indicated Specific Fuel Consumption

Indicated Specific Fuel Consumption (ISFC) is calculated based on the fuel flow rate and the engine work output:

$$ISFC = \frac{\dot{m}_f \times rpm}{IMEP \times V_d} \qquad \text{Equation 3.10}$$

Where $\dot{m}_f$ Mass flow rate of fuel

3.6.2.3 Combustion Efficiency

The combustion efficiency is evaluated from the cumulative heat release and the heating value of the fuel:

$$\eta_c = \frac{\sum \frac{dQ_n}{dt}}{\dot{m}_f \, Q_{HV}} \qquad \text{Equation 3.11}$$

Where $\frac{dQ_n}{dt}$ Heat release rate

Q_{HV} Lower heating value of fuel

3.6.2.4 Heat Release Rate

Apparent heat release rate is calculated based on the in-cylinder pressure and volume which is a measure of the amount of heat added, or subtracted, to the cylinder contents in order to achieve the same in-cylinder pressure. This method is incapable of accurate measurement of the heat release rate due to in-cylinder charge leakage in optical engines caused by the optical components utilised, hence termed “apparent”. In order to calculate the heat release rate, one-zone thermodynamic model is employed which considers the cylinder as an open system, the first law of which is:

$$\frac{dQ}{dt} - p\frac{dV}{dt} + \sum_i \dot{m}_i h_i = \frac{dU}{dt} \qquad \text{Equation 3.12}$$

Where $\frac{dQ}{dt}$ Rate of heat transfer into system across boundary

$p\frac{dV}{dt}$ Rate of work transfer by system

$\dot{m}_i$ Mass flow rate into system at location i

h_i Enthalpy of flux i

U Internal energy of cylinder contents

The mass flow across the system boundary, while both intake and exhaust valves are closed, includes the mass of fuel injected into the combustion chamber and the mass of air lost due to crevice flow. However, in the case of optical engines cylinder leakage due to window sealing is to be considered which is extremely difficult to compute. The effects of cylinder leakage are neglected due to intricate calculations involved and the fact that heat release is used as an approximate measure. Therefore, Equation 3.12 becomes:

$$\frac{dQ}{dt} - p\frac{dV}{dt} + \dot{m}_f h_f = \frac{dU}{dt} \qquad \text{Equation 3.13}$$

U is taken as the sensible internal energy of the in-cylinder charge, U_s, and h_f as the sensible enthalpy of the injected fuel. Thus, dQ/dT becomes the net heat release rate, while dQ_n/dT is the difference between the heat release rate due to the combustion of fuel and the heat transfer from the system. Since $h_{s,f} \approx 0$, Equation 3.13 can be written as:

$$\frac{dQ_n}{dt} = p\frac{dV}{dt} + \frac{dU_s}{dt} \qquad \text{Equation 3.14}$$

Assuming that the in-cylinder charge can be considered as an ideal gas, Equation 3.14 can be written as:

$$\frac{dQ_n}{dt} + p\frac{dV}{dt} + m c_v \frac{dT}{dt} \qquad \text{Equation 3.15}$$

Where c_v Specific heat at constant volume

T Absolute temperature

Based on the ideal gas law, $pV = mRT$, with R assumed constant:

$$V\frac{dp}{dt} + p\frac{dV}{dt} = m\,R\frac{dT}{dt} \qquad \text{Equation 3.16}$$

Where R Ideal gas constant

Further, T, the gas temperature, can be eliminated by combining Equation 3.15 and Equation 3.16 as shown below:

$$\frac{dQ_n}{dt} = \left(1 + \frac{c_v}{R}\right)p\frac{dV}{dt} + \frac{c_v}{R}V\frac{dp}{dt} \qquad \text{Equation 3.17}$$

Considering $\gamma = \frac{c_p}{c_v}$, ratio of specific heat, Equation 3.17 can be written as:

$$\frac{dQ_n}{dt} = \frac{\gamma}{\gamma - 1}\,p\frac{dV}{dt} + \frac{1}{\gamma - 1}V\frac{dp}{dt} \qquad \text{Equation 3.18}$$

Equation 3.18 is a simplified form of Equation 3.12 employed for the calculation of the heat release rate data presented in this study. The value of γ is not constant through different stages of the engine cycle, however for diesel heat release analysis it is common practice to take a single appropriate value, for this study $\gamma = 1.3$.

3.6.2.5 Cumulative Heat Release

The cumulative heat release can be calculated from the heat release rate by the following expression:

$$CHR_n = HR_{n-1} + \left(HR_n \times \Delta\theta\right)$$

Where HR Heat release rate

$\Delta\theta$ Change in crank angle, 0.2^o CA in this case

3.6.2.6 Ignition Delay

ID is defined as the delay between the SOI and the SOC. The SOI is considered as the timing of the first injection while the SOC is established from the heat release rate as the point where the rate initially begins to increase. The rate of heat transfer during initial stages of combustion is more dominant than the first positive heat release prior to onset of more substantial heat release, yet the start of combustion is taken as the point when the first combustion occurs.

3.7 Summary

This chapter has detailed the specification of the optical research engine and its components, the control system and the data acquisition system. The equipments used for the in-cylinder pressure and the exhaust emission measurements have been described. The optical setups and techniques utilised in this study were explicated. The experimental procedure utilised has been described. The fundamental techniques used for the analysis of the recorded data have been explained.

4

CHAPTER 4

The Two-colour Method and System

4.1 Introduction

The two-colour method is a technique capable of estimating the flame temperature and soot concentration within the combustion chamber of diesel engines. This technique is based on the principle of flame luminosity. Diesel combustion is rather luminous due to the radiation of soot particles at elevated temperatures. Therefore, the flame temperature and soot concentration in terms of *KL* factor can be estimated from the radiation emitted during the combustion process.

This chapter includes detailed explanation of the principle of the two-colour method, its implementation and calibration in an optical diesel engine. As stated in Chapter 3, this technique has been previously used with ICCD cameras, incapable of simultaneous measurement of flame temperature and soot concentration over the whole engine cycle due to long data acquisition time of this type of camera. However, the setup employed in this study allows for the use of high speed cameras, thus having the advantage of simultaneous measurement of the flame temperature and soot concentration during the entire engine cycle.

4.2 Principle of the Two-colour Method

The two-colour method is based on the measurement of radiation emitted by soot particles during the combustion process at two different wavelengths to estimate the flame temperature and soot concentration. Although this technique is commonly used for the estimation of flame temperature, it can be used to estimate the in-cylinder gas temperature since the difference between the soot particles and the surrounding gaseous medium is approximately 1 K [139-141].

The radiation intensity emitted by a black body at a given wavelength is dependent on the body temperature where the emissivity remains constant at ε = 1. Therefore, a black body can be defined as an object that absorbs the entire incident light and emits radiation over a range of wavelengths. A body with constant spectral emissivity is referred to as a "grey body", however, soot particles cannot be categorised as grey bodies since their emissivity varies with wavelength.

Plank's law describes the radiation of a black body as a function of its emitted wavelength:

$$E_{b,\lambda}(T) = \frac{C_1}{\lambda^5\left[e^{\left(\frac{C_2}{\lambda T}\right)} - 1\right]} \qquad \text{Equation 4.1}$$

Where $E_{b,\lambda}$ Monochromatic emission power of a black body at temperature T

T Temperature

C_1 1st Plank's constant, 3.7510 x 10^{-16} Wm^2

C_2 2nd Plank's constant, 1.4210 μmK

λ Wavelength

However, black body is just a theoretical concept while all real bodies have an emissivity less than one. Therefore, the definition of emissivity appears as:

$$\varepsilon_\lambda = \frac{E_\lambda(T)}{E_{b,\lambda}(T)} \qquad \text{Equation 4.2}$$

Where ε_λ Monochromatic emissivity

E_λ Non-black body radiation intensity

4.2.1 Flame Temperature Estimation

The radiation emitted by a black body and a non-black body can be linked

by introducing the concept of apparent temperature, T_a, which is defined as the temperature at which the radiation emitted by a black body is equal to that of a non-black body at a temperature T. Thus, apparent temperature is given by:

$$E_{b,\lambda}(T_a) = E_{\lambda}(T) \qquad \text{Equation 4.3}$$

As stated earlier, the emissivity of a non-black body is always less than one, hence the apparent temperature is always less than the temperature of the black body, $T > T_a$. Therefore, Equation 4.2 and Equation 4.3 can be combined:

$$\varepsilon_{\lambda} = \frac{E_{b,\lambda}(T_a)}{E_{b,\lambda}(T)} \qquad \text{Equation 4.4}$$

With which Equation 4.1 can be rearranged as:

$$\varepsilon_{\lambda} = \frac{e^{\left(\frac{C_2}{\lambda T}\right)} - 1}{e^{\left(\frac{C_2}{\lambda T_a}\right)} - 1} \qquad \text{Equation 4.5}$$

ε_{λ} is estimated using an empirical correlation developed by Hottel and Broughton [138] as shown below:

$$\varepsilon_{\lambda} = 1 - e^{\left(\frac{-KL}{\lambda^{\alpha}}\right)} \qquad \text{Equation 4.6}$$

Where K Absorption coefficient proportional to soot density

L Geometrical thickness of the flame along the optical axis of the detection system

α Spectral range constant

The parameter α is a constant which depends on the physical and optical properties of the soot particles, the selection of which is discussed in Section 4.3.1.1. The product of K and L is referred to as the KL factor which is proportional to soot concentration. The combination of Equation 4.5 and Equation 4.6 yields:

$$KL = -\lambda^{\alpha} \ln\left[1 - \left(\frac{e^{\left(\frac{C_2}{\lambda T}\right)} - 1}{e^{\left(\frac{C_2}{\lambda T_a}\right)} - 1}\right)\right] \qquad \text{Equation 4.7}$$

The unknown KL factor can be eliminated from Equation 4.7 provided that this expression is applied for two apparent temperatures at distinct wavelengths λ_1 and λ_2 as shown below:

$$\left[1 - \left(\frac{e^{\left(\frac{C_2}{\lambda_1 T}\right)} - 1}{e^{\left(\frac{C_2}{\lambda_1 T_{a1}}\right)} - 1}\right)\right]^{\lambda_1^{\alpha 1}} = \left[1 - \left(\frac{e^{\left(\frac{C_2}{\lambda_2 T}\right)} - 1}{e^{\left(\frac{C_2}{\lambda_2 T_{a2}}\right)} - 1}\right)\right]^{\lambda_2^{\alpha 2}} \qquad \text{Equation 4.8}$$

Thus, the flame temperature, T, can be estimated from the above equation provided that the apparent temperatures T_{a1} and T_{a2} are known and an appropriate value of α is selected. The apparent temperature can be evaluated through a calibration process using a tungsten lamp, explained in detail in Section 4.6.

4.2.2 *KL* Factor and Soot Concentration Estimation

The KL factor can be evaluated by Equation 4.7 following successful estimation of the flame temperature through Equation 4.8.

Further, the volumetric density of the soot particles, C_V, can be estimated by the following expression:

$$C_V = \frac{KL}{6\pi L I m\left(\frac{m^2 - 1}{m^2 + 1}\right)\lambda^{\alpha}} \qquad \text{Equation 4.9}$$

Where m Complex refractive index of soot particles

I Obtained through Lambert-Beer law

The value of I can be calculated by the following expression:

$$I = I_0 \exp\left(\int_0^L K_{ext}\, dx\right) \qquad \text{Equation 4.10}$$

Where I_0 Incident light intensity (Wm^{-2})

K_{ext} Extinction coefficient

L Path length of light beam

Furthermore, the gravimetric soot concentration, C_m, which represents the mass of soot particles per unit gas volume can be estimated through the following equation:

$$C_m = \rho C_V \qquad \text{Equation 4.11}$$

Where ρ Soot density

However, the estimation of gravimetric soot concentration requires successful evaluation of soot density which is dependent on the composition of the soot particles.

4.3 Implementation

As stated in Section 4.2.1, the flame temperature is dependent on the value of α and the apparent temperatures T_{a1} and T_{a2}. The selection procedure employed in this study involves the estimation of the parameter α and the calculation of the apparent temperatures at two distinct wavelengths, λ_1 and λ_2.

4.3.1 Selection Procedure

4.3.1.1 Parameter α

It is evident from Equation 4.7 and Equation 4.8 that successful estimation of the flame temperature and the KL factor are dependent on the selection of a suitable value of α. The parameter α is dependent on the light wavelength and the size and refractive index of the soot particles. The effect of parameter α on the flame

temperature is less critical, provided that the two selected wavelengths are in the visible region as illustrated in Figure 4.1.

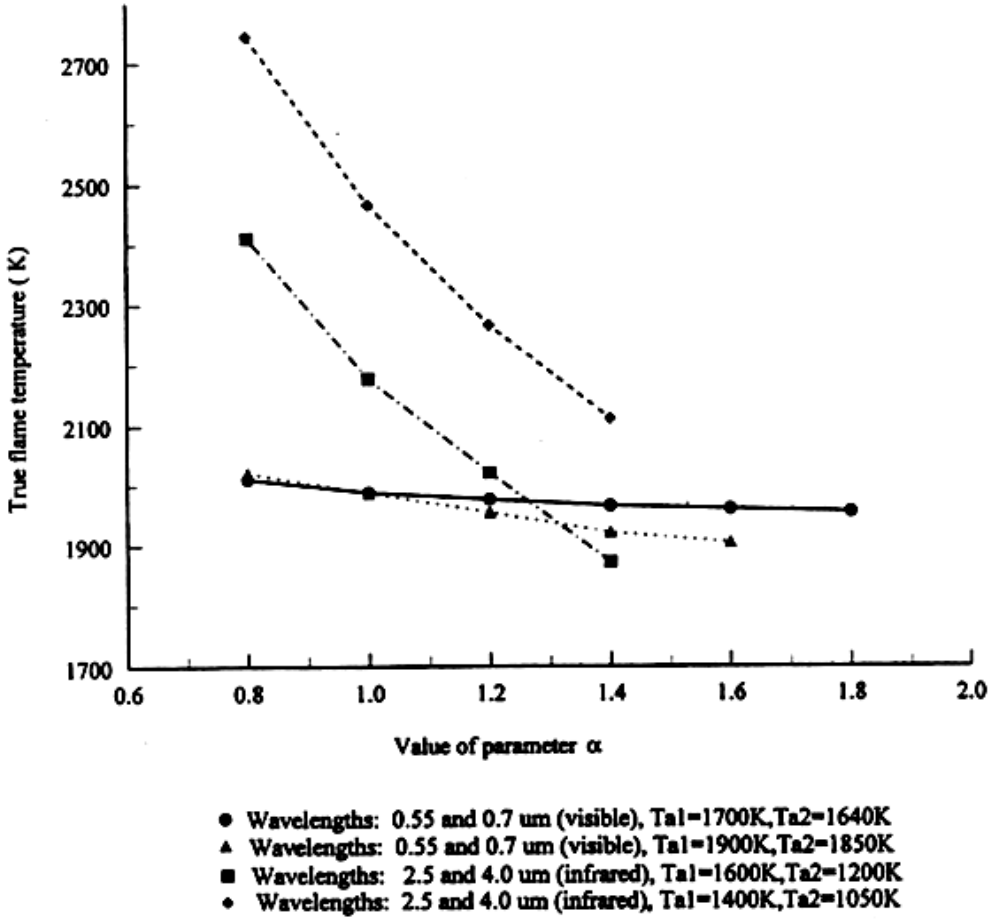

Figure 4.1 The Effect of the Value of α on the Estimated Flame Temperature (Zhao and Ladommatos, [153])

The value of α was selected based on the data presented by Zhao and Ladommatos [153], listed in Table 4.1. This data includes a compilation of values of α in the Hottel and Broughton [138] correlation for soot emissivity.

From the data present in Table 4.1, it is evident that for a selection of wavelengths in the visible region, the value of $\alpha = 1.39$ is recommended which is suitable to be used for various fuels. This value has been widely used for the estimation of the flame temperature in diesel engines using two-colour method [154-156], thus the same value is employed in this study.

Table 4.1 Compilation of Values of the Parameter α in the Hottel and Broughton Correlation for Soot Emissivity (Zhao and Ladommatos, [153])

Value of Parameter α				
Visible Wavelengths	**Infrared Wavelengths**		**Fuel or Flame Type**	**Reference**
1.39	0.95	λ>0.8 μm	Steady luminous flame	Hottel and Broughton (1932)
1.38	0.91 – 0.97	λ = 2-4 μm	Diesel engine soot	Matsui et al. (1980)
1.39	-		Diesel engine soot	Yan and Boreman (1988)
-	0.94 – 0.96	λ>0.8 μm		Libert and Hibbard (1970)
-	0.89 , 1.00	λ>1-7 μm	Amyl acetylene	Siddel and McGrath (1963)
-	0.77	λ>1-7 μm	Kerosene	
-	0.94 , 0.95	λ>1-7 μm	Benzene	
-	0.93	λ>1-7 μm	Candle	
-	0.96 , 1.14 , 1.25	λ>1-7 μm	Furnace samples	
-	1.06	λ>1-7 μm	Petrotherm	
-	1.00	λ>1-7 μm	Propane	
-	α = 0.91+0.28lnλ	λ>1-7 μm	Various fuels	
1.43	-		Acetone	Rossler and Behrens (1950)
1.39	-		Amyl acetate	
1.29	-		Coal gas/air	
1.23	-		Benzene	
1.14	-		Nitrocellulose	
0.66 – 0.75	-		Acetylene/air	

4.3.1.2 Wavelengths

Equation 4.8 includes two unknowns λ_1 and λ_2 , thus an auxiliary equation must be generated in order to solve this equation. This is achieved by performing the detection process at two distinct wavelengths. The flame luminosity can be detected in both visible and infrared regions [157, 158]; however, visible wavelengths are preferred. This is mainly attributed to the greater sensitivity of the detection system to changes in flame temperature within the temperature range of 1000 to 2000 K in the visible region. Figure 4.2 confirms this theory, indicating larger rate of change of spectral

radiance with respect to temperature, dI_λ / dT, in the visible region. In addition, interference due to radiation from other gaseous species such as CO, CO_2, water vapour and fuel vapour during the combustion process is likely in the infrared region but not experienced in the visible range which further confirms the use of wavelengths in the visible region.

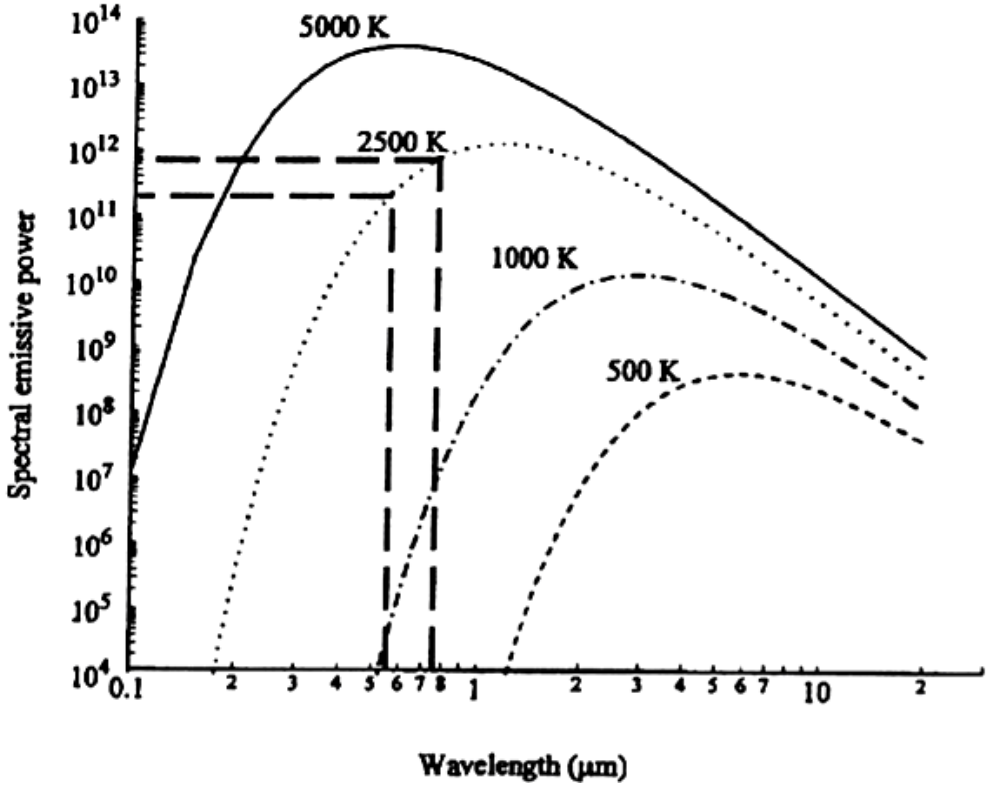

Figure 4.2 The Spectral Radiance of a Black Body as a Function of Temperature (Zhao and Ladommatos, [153])

The two-colour method was initially implemented by Sison [159] and Gill [150] at Brunel University using an ICCD camera. The selected wavelengths were 550nm and 750nm due to the spectral response of the ICCD camera utilised. The same wavelengths were chosen for this investigation, though modifications were made to the experimental setup and the instrumentation to allow for the use of the technique with a high speed video camera as explained in the following section.

4.4 Experimental Setup

This section includes detailed explanation of the experimental setup employed in this study, outlining the characteristics of the detection system utilised.

4.4.1 High Speed Camera System

As mentioned in Section 4.1, the setup employed in this study allows for the application of two-colour method with high speed camera which has the advantage of continuous data acquisition over the entire engine cycle. The high speed camera system is capable of recording a maximum of 12 consecutive engine cycles at the engine speed of 1500 rpm. The optical access through the glass piston and the 45^{o} angled mirror was used for this technique as shown in Figure 4.3.

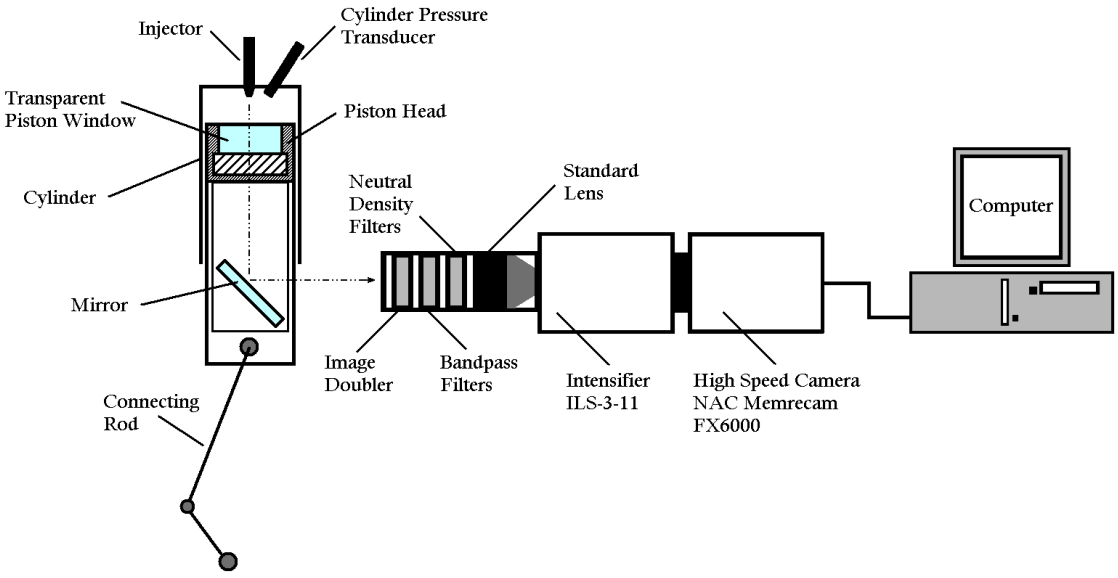

Figure 4.3 Schematic Diagram of the Two-Colour Experimental Setup

The optical setup consisted of a NAC Memrecam FX6000 high speed camera, a DRS intensifier ILS-3-11 and a standard Nikon 60mm f2.8 lens in front of which a custom built optical holder was fabricated to house an image doubler and a set of neutral density and bandpass filters at 550nm and 750nm.

The spectral sensitivity of the system is determined by the spectral response of the detection system, the high speed camera and the intensifier, as shown in Figures 4.4 and 4.5 respectively.

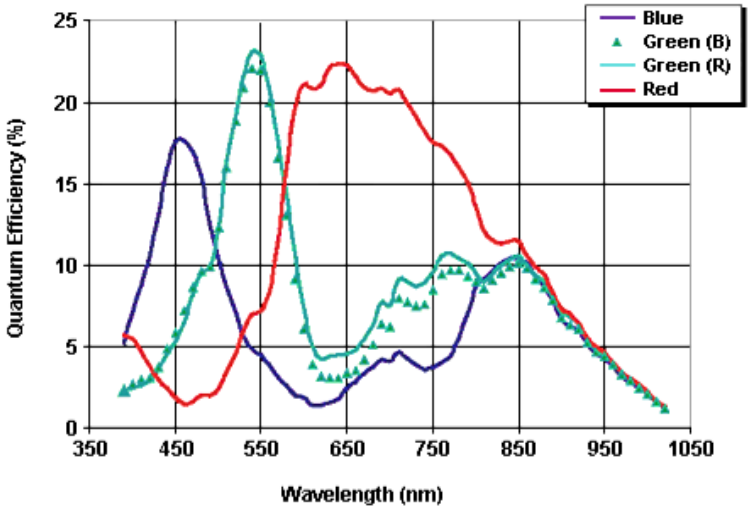

Figure 4.4 Spectral Response of NAC Memrecam FX6000 High Speed Camera

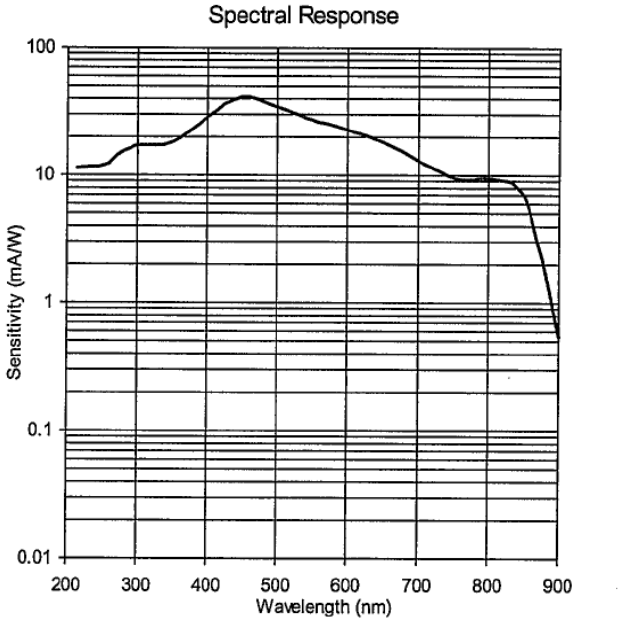

Figure 4.5 Spectral Response of DRS ILS-3-11 Intensifier

As evident from Figures 4.4 and 4.5, the total spectral response of the system at 750nm is very low compared to 550nm, thus neutral density filters were utilised in order to equalise the radiation intensities recorded at 550nm and 750nm.

4.4.2 Intensifier Lens System

As previously stated in Section 4.4.1, a DRS ILS3-11 intensifier lens system was utilised in this study. This type of intensifier is designed to provide light intensification, high speed shuttering and Ultra Violet (UV) to visible conversion for use with a range of high speed video camera systems. The intensifier is compatible with a range of Nikon lenses since it is equipped with an F-mount Nikon lens adaptor. It allows high speed imaging up to approximately 100,000 fps. The intensifier is triggered externally with a TTL input pulse which comes from the high speed camera.

4.4.3 Optical Components

As previously mentioned in Section 4.4.1, the optical setup consists of an image doubler and a set of neutral density and bandpass filters at 550nm and 750nm. The specification of each optical element is detailed in the following sections.

4.4.3.1 Image Doubler

The principle of the two-colour method involves the measurement of the flame luminosity at two distinct wavelengths, thus two images of the combustion is required. A Hoya Vari-Multivision image doubler was used for the purpose of this investigation, Figure 4.6.

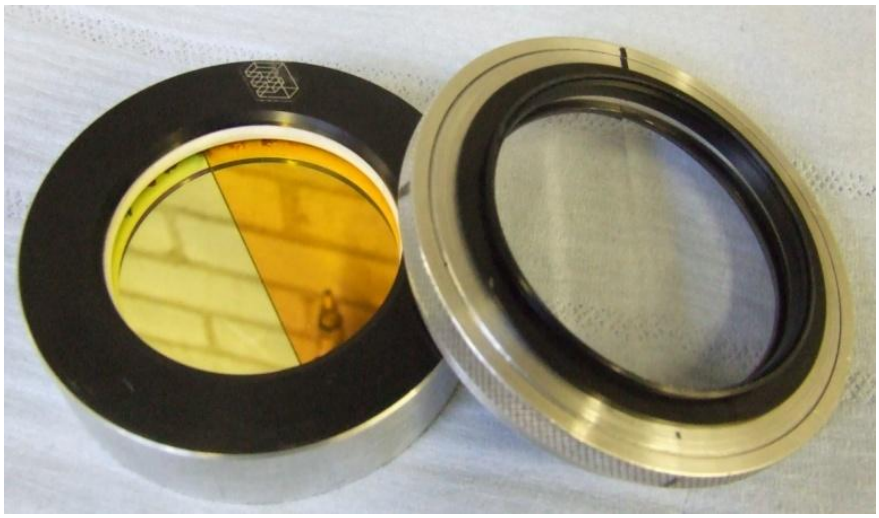

Figure 4.6 Image Doubler (Right) and Bandpass Filters (Left)

4.4.3.2 Bandpass Filter

Two TFI Technologies Inc. bandpass filters were used in this study which were cut into semi-circles in order to conform to the shape of the image doubler as shown in Figure 4.6. The specifications of the bandpass filters are listed in Table 4.2.

Table 4.2 The Specifications of TFI Bandpass Filters

	TFI Bandpass filter 550-40	**TFI Bandpass filter 750-40**
CWL	550 +/- 8nm	750 +/- 8nm
FWHM	40 +/- 8nm	40 +/- 8nm
Transmission	>70% @peak	>=75% @peak
Blocking Bandwidth	>=OD4, UV-1150nm (dielectric blocking)	>=OD4, UV-1150nm (dielectric blocking)
Size	50mm diam. +0/-0.25mm	50mm diam.+0/-0.25mm
Thickness	<6.3mm	<6.3mm
AOI	0 degrees	0 degrees

4.4.3.3 Neutral Density Filter

As stated in Section 4.4.1, the spectral response of the system at 750nm is considerably lower in comparison to 550nm, thus neutral density filters were utilised so that the intensity at 550nm and 750nm were of the same magnitude. This was achieved by the use of Kodak Wratten neutral density filters, two with 50% transmission response at 550nm and one with 10% transmissivity at 750nm.

4.5 Experimental Procedure

The two-colour data was recorded three cycles after the start of injection in order to allow the combustion to stabilise. This was the optimum delay period whereby minimum window fouling was experienced prior to the onset of data acquisition. The high speed camera was triggered externally through a TTL input pulse generated by a custom built synchronisation unit. The timing diagram of the control system employed for the synchronisation of the two-colour method is shown in Figure 4.7.

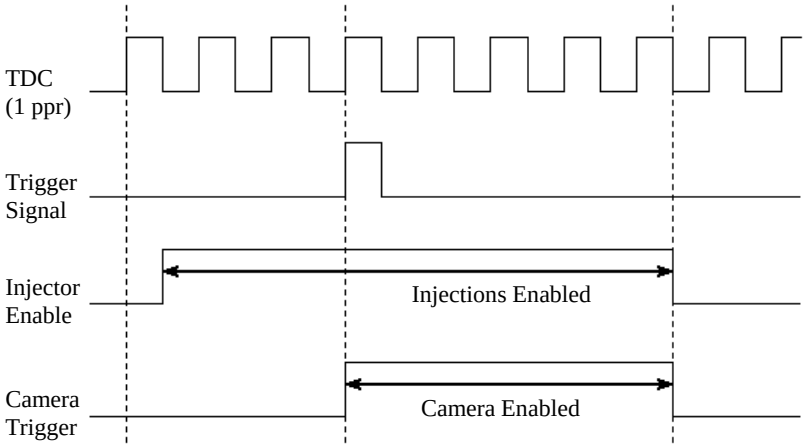

Figure 4.7 Two-Colour Control System Timing Diagram

The engine was run in skip-fire mode to prevent excessive window fouling and to prolong the running time between engine rebuilds. The engine was fired for eight cycles, after three of which the high speed camera was triggered by a TTL output pulse generated by the synchronisation unit. The intensifier was subsequently triggered by the high speed camera as explained in Section 4.4.2. The high speed camera and the intensifier are shown in Figure 4.8.

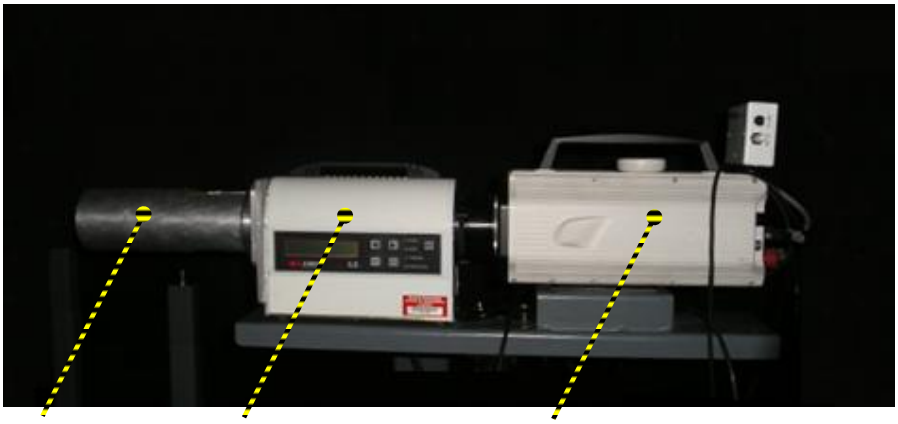

Figure 4.8 The Experimental Setup for the Two-Colour Method

The high speed camera recorded the combustion luminosity at 10,000 fps. The *KL* factor and the flame temperature were estimated for every frame, the data analysis technique employed is explained in Section 4.7. The data extracted from the

individual frames were put together to create the *KL* factor and flame temperature contour maps.

4.6 Calibration

The principle of the two-colour method is based on the estimation of the *KL* factor and the flame temperature through Equations 4.7 and 4.8 respectively. This is achieved by generating an auxiliary equation through the application of the technique for two apparent temperatures at two distinct wavelengths. Thus, flame temperature and *KL* factor can be estimated, provided that the apparent temperatures at their corresponding wavelengths are evaluated. This is achieved by obtaining the intensity values at each pixel through pixel by pixel analysis of every recorded frame. However, the system must be calibrated such that the intensity value at each pixel can be converted into flame temperature and *KL* factor.

The calibration process must be ideally carried out using a black body at two distinct wavelengths; however, a tungsten lamp, Figure 4.9, was used in this project instead since a black body was not available.

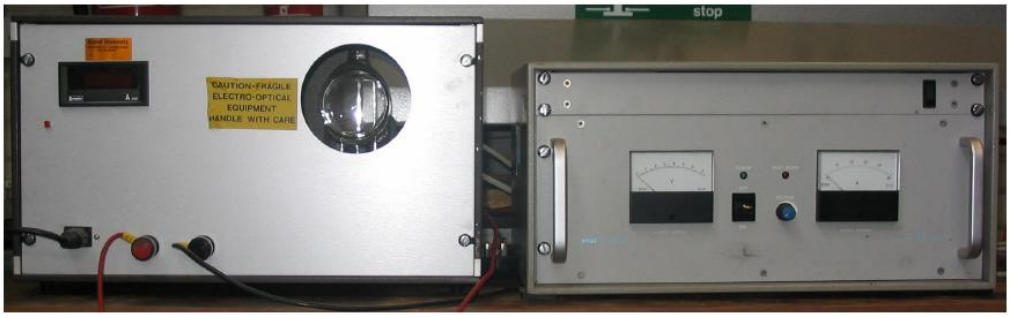

Figure 4.9 Tungsten Ribbon Lamp Unit (Left), Power Supply (Right)

The tungsten lamp was calibrated by the manufacture against a black body whereby the black body radiance temperature was accurately measured as a function of the current supplied to the lamp filament as shown in Figure 4.11, the calibration table based on which Figure 4.11 is plotted is presented in Appendix B. However, the calibration process was carried out at 660nm; though, the data obtained at this

wavelength can be used at wavelengths near 660nm with reasonable accuracy [142]. The schematic diagram of the calibration setup is depicted in Figure 4.10.

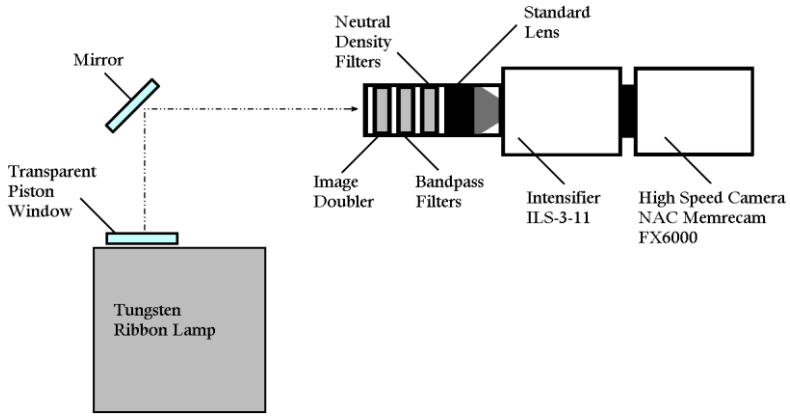

Figure 4.10 Schematic Diagram of the Two-Colour Calibration Setup

As evident from Figure 4.10, the setup employed for the calibration process is identical to the optical arrangement used for in-cylinder soot concentration and flame temperature measurements in the single cylinder optical engine. All the optical elements are identical to those used on the engine, including the 45^{o} angled mirror and the transparent glass piston, to improve the accuracy of the calibration data.

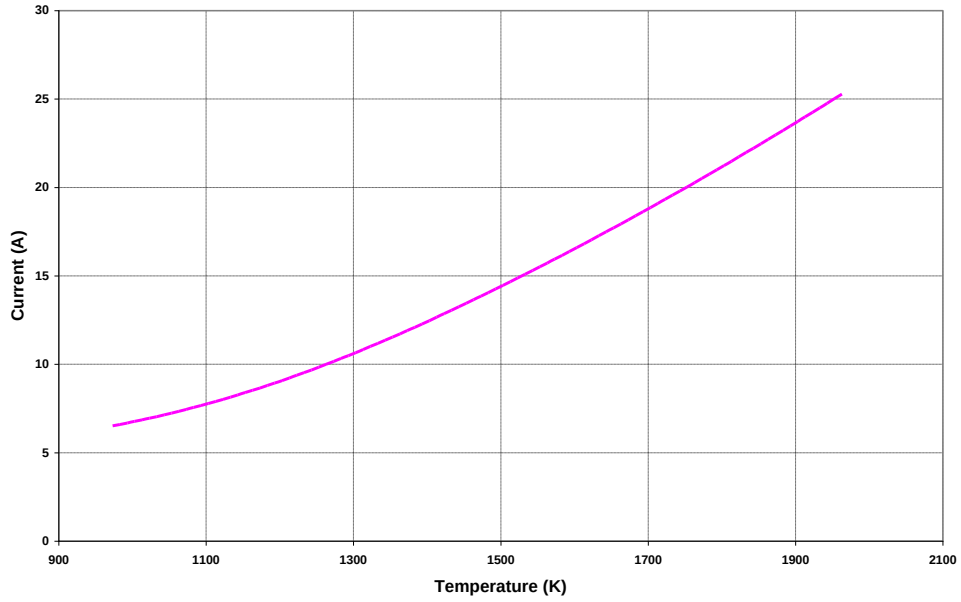

Figure 4.11 Tungsten Ribbon Lamp Calibration Curve

As mentioned earlier, the tungsten lamp was calibrated at 660nm, thus the estimation of apparent temperatures at 550nm and 750nm requires the information on the emissivity values at these wavelengths. The relationship between emissivity and apparent temperature developed by Larrabee et al. [160] was used to calculate the emissivity at the selected wavelengths. The emissivity values at 550nm and 750nm were calculated through interpolating the results presented by Larrabee et al. [160]. The emissivity values at 550nm were calculated from the results presented at 540nm and 560nm while values at 750nm were calculated based on the results at 740nm and 760nm. The emissivity values at the selected wavelengths are listed in Table 4.3.

Table 4.3 Emissivity Values at Different Wavelengths

Wavelength (nm)	Temperature (K)				
	1600	**1800**	**2000**	**2200**	**2400**
540	0.453	0.451	0.448	0.446	0.443
550	**0.4525**	**0.4500**	**0.4470**	**0.4445**	**0.4420**
560	0.452	0.449	0.446	0.443	0.441
740	0.430	0.426	0.422	0.419	0.415
750	**0.4285**	**0.4245**	**0.4210**	**0.4175**	**0.4140**
760	0.427	0.423	0.420	0.416	0.413
660	**0.441**	**0.436**	**0.432**	**0.428**	**0.424**

The apparent temperatures can be calculated based on the emissivity values presented in Table 4.3 by the following expressions:

$$T_{a1} = \frac{\varepsilon_{550}}{\varepsilon_{660}} T_{660}$$ Equation 4.12

$$T_{a2} = \frac{\varepsilon_{750}}{\varepsilon_{660}} T_{660}$$ Equation 4.13

The calibration process was carried out for one aperture position of the Nikon lens. The calibration procedure was performed at the intensifier gain shown in Table 4.4. The calibration data can be used to measure the flame temperature and soot concentration under various engine operating conditions.

Table 4.4 Calibration Matrix

Aperture Position	Intensifier Gain (%)
f 4	90

A relationship between the RGB colour intensity values of the pixels and the apparent temperature for every frame can be obtained following successful calibration of the system. In order to obtain such a relationship, the tungsten lamp was set at different temperatures and movies were taken at 550nm and 750nm using the detection system described previously. Furthermore, to obtain the RGB intensity values at a specific temperature, 20 frames were selected from the high speed movie recorded at that temperature. The pixel values from the selected frames were averaged to improve the accuracy of the calibration results. However, variations in the pixel intensity values at low apparent temperatures between different frames were considerably high due to low signal to noise ratio. The variation in the intensities lessened as the apparent temperature increased. Therefore, a cut-off pixel value was adopted below which the apparent temperature was considered zero. The error generated in the averaged intensity values was less than 5% due to the introduction of such a cut-off value. Thus, the first few frames just after the start of combustion and the last few frames towards the end of combustion were not analysed, hence flame temperature and *KL* factor at the initial and final stages of the combustion were not estimated. The final correlation between the pixel intensity values and the apparent temperatures are presented in Appendix B.

4.7 Data Analysis

The recorded high speed movies contained two images of combustion, one recorded at 550nm and the other at 750nm. Therefore *KL* factor and flame temperature can be estimated through Equations 4.7 and 4.8 respectively. This was achieved by saving every frame of the high speed movies in bitmap (.bmp) format and processing them in a LabVIEW program. Two programs were written by Sison [159], formerly of Brunel University, one to allow the alignment and resizing of the selected frames called "align and crop.vi" and the other to calculate the flame temperature and *KL* factor at

every pixel of each frame called “two-colour.vi”. The program requires two apparent temperatures as an input at each pixel in order to estimate the flame temperature. Nevertheless, Equation 4.8 cannot be solved analytically as it is highly nonlinear, thus a numerical method based on the Newton-Raphson method was used. However, this method does not always obtain convergent solutions, particularly when the two apparent temperatures are similar, i.e. when the monochromatic emissivities are close to unity. Therefore, a method developed by Yan [161] is used in this study where the calculation involves estimation of the apparent temperature at the first wavelength T_{a1} for an assumed T, where T is taken as the adiabatic flame temperature T=3500 K and a measured apparent temperature at the second wavelength T_{a2}. The temperature T_{a1} is calculated iteratively until the difference between the calculated T_{a1} and the measured is less than 0.1 K. Each iteration was calculated for a new estimated T, determined by linear interpolation as explained in the following section.

4.7.1 Calculation of Flame Temperature and Soot Concentration

This section details the iterative method developed by Yan [161] which is based on the fact that the variation of T_{a1} with T at a given T_{a2} is approximately linear for a short temperature range as shown in Figure 4.12. Therefore, Equation 4.8 can be rearranged as:

$$\frac{1}{T_{a1}} = \frac{\lambda_1}{C_2} ln\left[1 + \left(\frac{e^{\left(\frac{C_2}{\lambda_1 T}\right)} - 1}{A}\right)\right] \qquad \text{Equation 4.14}$$

Where,

$$A = 1 - \ln\left[1 - \left(\frac{e^{\left(\frac{C_2}{\lambda_2 T}\right)} - 1}{e^{\left(\frac{C_2}{\lambda_2 T_{a2}}\right)} - 1}\right)^{\frac{\alpha_2}{\alpha_1}}\right] \qquad \text{Equation 4.15}$$

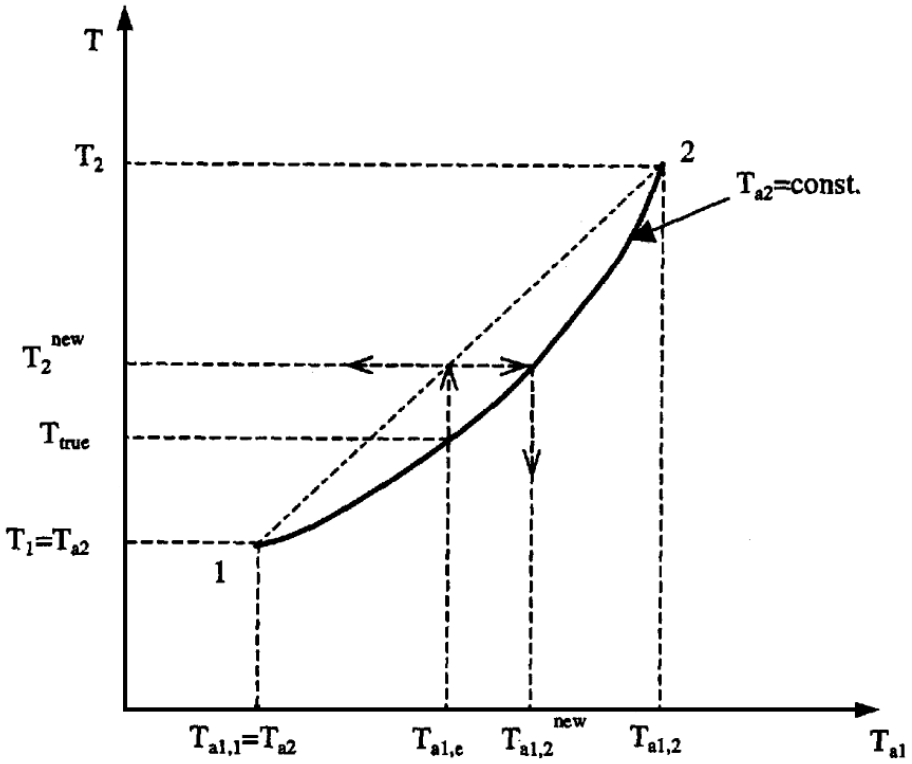

Figure 4.12 Schematic of the Numerical Scheme for Solving Equation 4.8 (Zhao & Ladommatos, [153])

As stated earlier, Equation 4.8 cannot be directly solved due to nonlinear nature of the function. As a result, an iterative method was used to estimate the true flame temperature. This solution technique involves several iterative steps which are listed below.

1. True flame temperature is assumed to be between points 1 and 2 in Figure 4.12 whereby point 1 is assigned to the measured apparent temperature, which is the apparent temperature T_{a2} at the longer wavelength and point 2 is selected to be greater than the true temperature.

    a. T_1 is assigned to the measured temperature T_{a2} at the longer wavelength and $T_{a1,1}$ is the apparent temperature $T_{a1,1} = T_{a2}$

    $$T > T_1 = T_{a2}$$

2. The true flame temperature is assumed to be T_2. The flame temperature in a diesel engine is around 3000 K, thus T_2 is assumed to be 3500 K at the start of the iteration, $T_2 = 3500K > T$

   Where, the flame temperature is higher than its apparent temperature.

   $T > T_{a1} > T_{a2}$

3. Through Equation 4.14, the initial value of the apparent temperature at shorter wavelength $T_{a1,2}$ is calculated using the known values of T_{a2} and T_2.

   $T_{a1,2} > T_{a1,m}$

4. The new flame temperature at point 3 can be estimated based on the calculated value of $T_{a1,2}$ by linear interpolation. Therefore, the new flame temperature is given by:

$$T_2^{new} = T_1 + \frac{(T_2 - T_1)(T_{a1,m} - T_{a2})}{(T_{a1,2} - T_{a2})} \qquad \text{Equation 4.16}$$

5. The flame temperature at point 4, $T_{a1,2}^{new}$, can be estimated through Equation 4.16 using the newly calculated flame temperature T_2^{new} and the constant value T_{a2}.

6. The newly calculated flame temperature on the ordinate axis $T_{a1,2}^{new}$ is compared with the measured temperature T_{a1}. If the difference between the two temperatures is less than 0.1 K, then T_2^{new} is the solution to the true flame temperature for the two measured apparent temperatures. If not, then $T_{a1,2}$ is replaced with $T_{a1,2}^{new}$ and steps 3-5 are repeated until a convergent solution is found.

7. The *KL* factor can be calculated upon successful estimation of the true flame temperature T_2^{new}.

4.7.2 LabVIEW Programs

As previously stated, two programs written by Sison [159] in LabVIEW were used for image post-processing purposes with the ICCD camera. However, the programs had to be modified so that image post-processing could be done for images obtained with the high speed camera. The programs were modified by Diez [151], formerly of Brunel University.

4.7.2.1 Align and Crop

The two combustion images at 550nm and 750nm must be thoroughly aligned in order to allow accurate pixel by pixel analysis. The "Align and Crop.vi" program was developed based on the use of a correlation coefficient to indicate the accuracy of the alignment. This correlation coefficient could vary between zero and one where the latter is achieved when the images were absolutely identical. However, as the RGB values for each image were slightly different due to the filters, the maximum value was less than one. The correlation coefficient was calculated by the following expression:

$$r = \frac{\sum_x \sum_y \left(A_{xy} - \overline{A}\right)\left(B_{xy} - \overline{B}\right)}{\sqrt{\sum_x \sum_y \left(A_{xy} - \overline{A}\right)^2 \times \sum_x \sum_y \left(B_{xy} - \overline{B}\right)^2}} \qquad \text{Equation 4.17}$$

There are two cursors that could be moved on the intensity graph to locate the centre of each image as shown in Figure 4.13. Each movement of the cursors results in a different correlation coefficient. The program would automatically crop and save two images, one at 550nm and the other at 750nm, provided that the value of the correlation factor is equal or greater than 0.93. The error encountered due to the introduction of such a correlation factor was below 5%. However, the original program was intended for use with pictures taken by the ICCD camera which were in greyscale 8-bit, however, the frames recorded by the high speed camera were in RGB 32-bit format. Thus, minor modification was made to the original program so that the images in RGB 32-bit format could be aligned and saved.

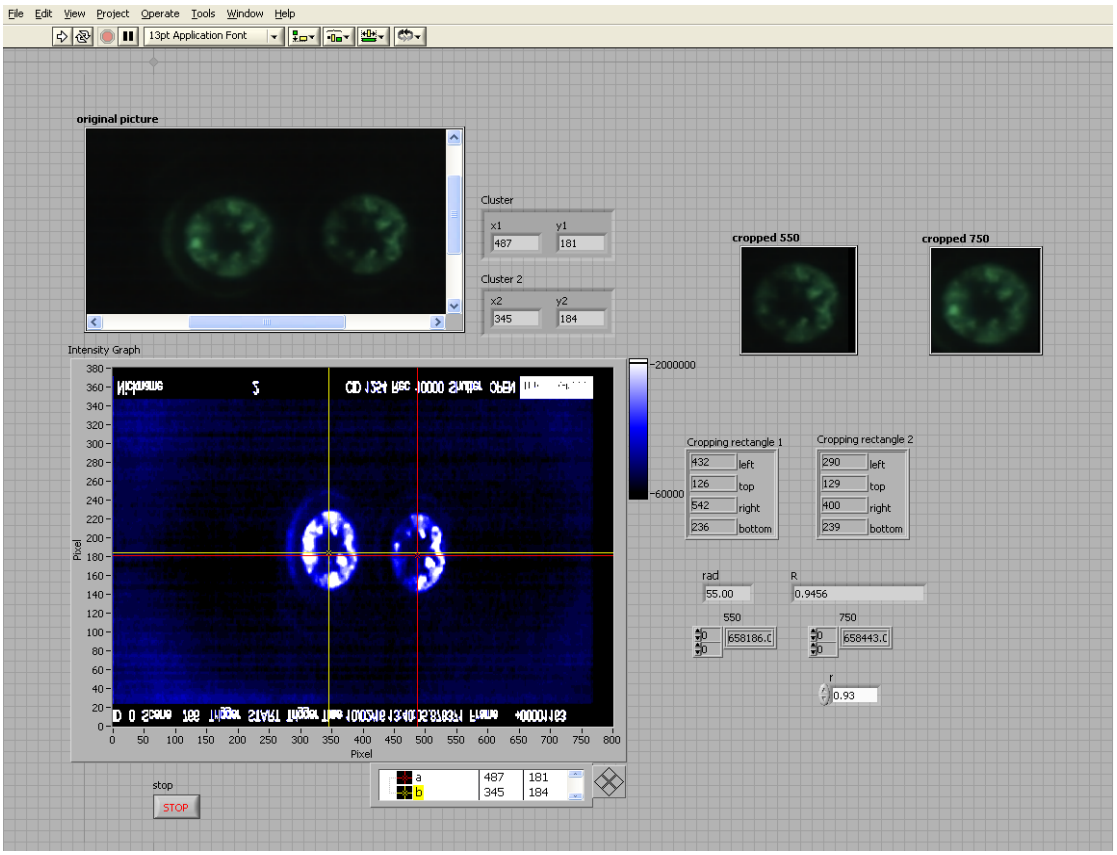

Figure 4.13 Front Panel of Align and Crop.vi Program

4.7.2.2 Determination of Temperature and *KL* Factor

The "Two-colour.vi" program was developed to perform the required iterative steps in the calculations on a pixel by pixel basis on the images produced by align and crop program. This program outputs the contours of the flame temperature and soot concentration in terms of the *KL* factor. It was modified so that the calibration equations and the cut-off pixel values were implemented in the program. The "two-colour.vi", screenshot of which is shown in Figure 4.14, is run by clicking on the white arrow. The program instantaneously compiles and displays the flame temperature and soot concentration contour maps as illustrated in Figure 4.14. The program automatically allows various images and data files to be saved which were used for in depth combustion analysis.

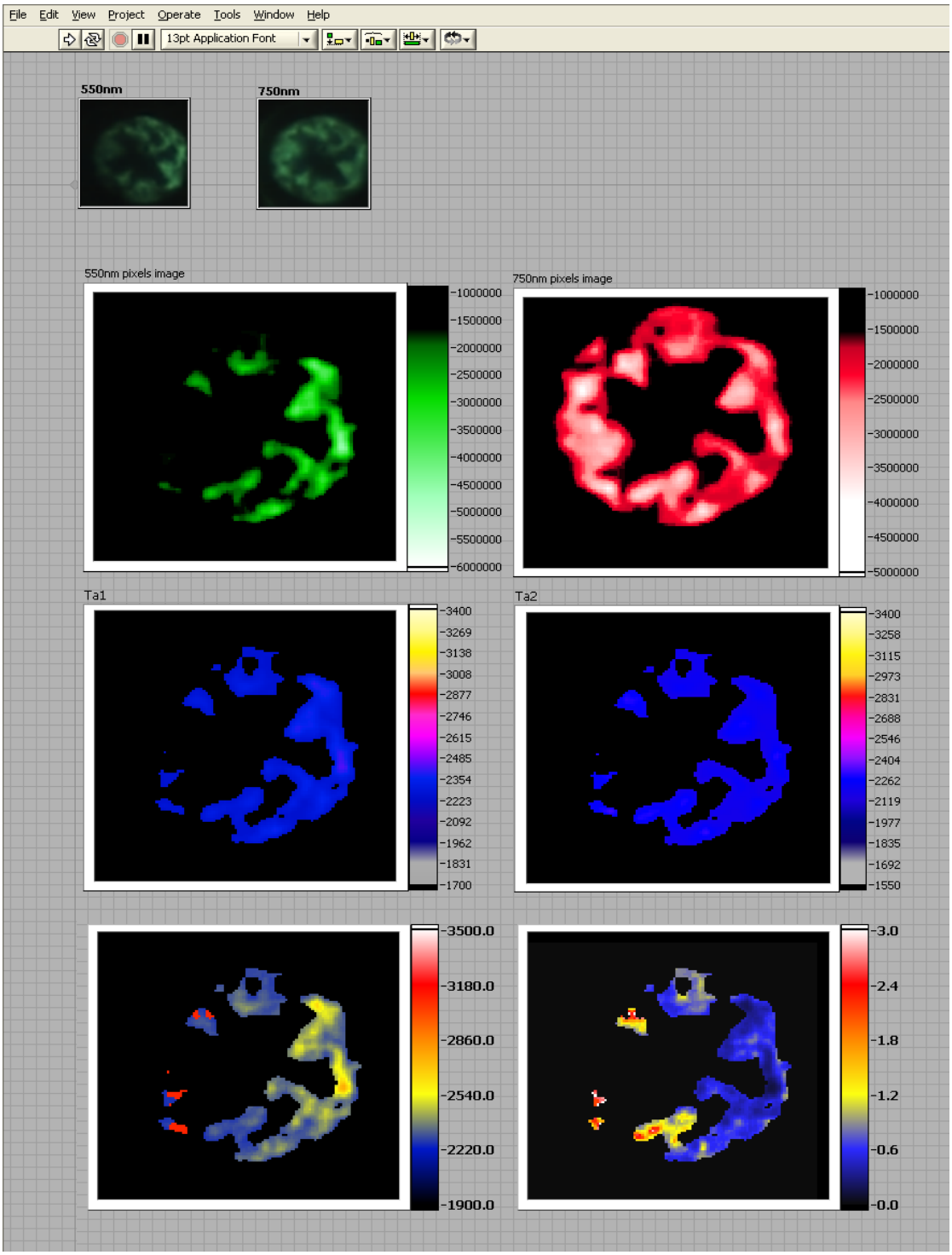

Figure 4.14 Front Panel of Two-Colour.vi Program

4.8 Summary

This chapter detailed the principle of the two-colour method as well as its implementation using a high speed intensified imaging system for the estimation of

the flame temperature and soot concentration in diesel engines. The experimental setup and procedures involved in both the calibration process and direct flame luminosity measurements were comprehensively explained. The numerical solution employed for the estimation of the flame temperature was discussed. In addition, the importance of obtaining cyclically resolved in-cylinder soot and combustion temperature measurements in a single cylinder optical engine using a high speed video camera was outlined. Furthermore, the custom-written programs employed for image post-processing purposes were described.

5

CHAPTER 5

Fuel Injection Characterisation Equipment and Application

5.1 Introduction

Ever more stringent emission standards have led to the development of high pressure FIE aimed at improving the combustion efficiency through improved fuel atomisation and mixture formation [162]. Thus, a fuel injection system capable of controlling the injection timing, quantity and rate of injection over the entire engine operating conditions is essential.

The combustion efficiency is directly influenced by the characteristics of the fuel sprays injected into the combustion chamber. Therefore, the effects of fuel injection rate on combustion efficiency and exhaust emissions have been the focus of numerous studies. The effects of this phenomenon on fuel spray formation and atomisation are widely established. The injection rate profile is also perceived as the regulating factor in pollutant formation including uHC, NOx and PM [163].

However, it is not yet possible to control the injection rate profile over the entire range of loads and speeds, mainly due to the cavitation erosion and parasitic losses experienced by the fuel injectors and pumps at high and low injection pressures respectively. The cyclic variations of diesel engines are mainly attributed to the aforementioned shortcomings of the fuelling system.

5.2 Fuel Injection System

The fuel injection system was briefly described in Chapter 3; further detailed information on the fuel injection equipment is presented in the following sections.

5.2.1 Fuel Injector

There are two main diesel injector nozzle types, VCO and the sac hole nozzle as shown in Figure 5.1.

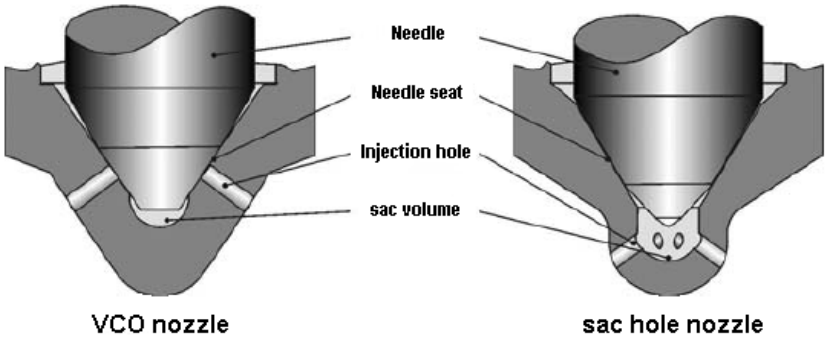

Figure 5.1 Schematic Diagram of Different Types of Diesel Injector Nozzles (Baumgarten, [164])

The difference between the two nozzle types lies on the sac volume size and the position of the needle seat relative to the sac volume. The VCO nozzles suffer from uneven distribution of fuel spray through different nozzle holes due to eccentric or radial motion of the needle tip. Bae et al. [165] investigated the asymmetry of the fuel sprays at the initial stages of injection (i.e. the initial stages of the needle opening) through high speed imaging as shown below, Figure 5.2. This inherent characteristic of such nozzle geometry was also evident in the high speed images presented in Section 5.3.5.3.

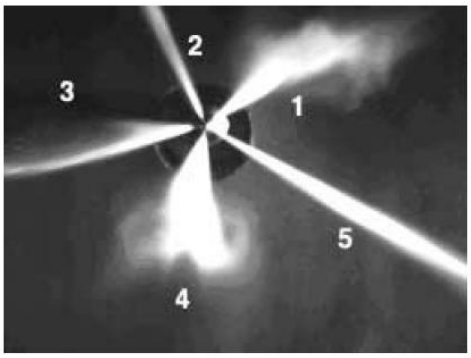

Figure 5.2 Initial Development of Fuel Sprays From a VCO Nozzle Under Atmospheric Conditions (Bae et al., [165])

This is mainly attributed to close proximity of the needle seat to the nozzle holes. However, such asymmetry is suppressed with sac hole nozzles whereby the needle tip is sufficiently distant from the nozzle holes. However, the excess fuel retained in the sac volume, following the closure of the needle, enters the combustion chamber at low pressures; commonly referred to as dribbling. Consequently, the uHC and soot emissions increase as a result of late introduction of such poorly atomised fuel. Thus, minimisation of the sac volume is highly desirable for the control of the combustion characteristics and pollutant formation. The VCO nozzles do not exhibit such characteristic since the nozzle holes are fully shut at the time of needle closure.

A Delphi multi-hole VCO injector capable of injecting up to 1600 bar was employed in this investigation, the specifications of which were explained in detail in Chapter 3.

5.2.2 Fuel Delivery System

As previously stated in Chapter 3, the fuel injection system is designed to promote high level of atomisation aimed at maximising fuel evaporation and mixture formation over a short period of time. Modern high pressure fuel injection systems can be divided into three main categories; Unit Injector System (UIS), Unit Pump System (UPS) and Common Rail System (CRS) [164].

In unit fuel injection systems, the high pressure pump and injection nozzle are combined into a single unit, accordingly, each cylinder of an engine is equipped with a UIS. In these systems, the generation of injection pressure and the onset of injection take place synchronously. The high pressure pump is driven by the engine camshaft, thus leading to the dependence of injection pressure on the engine speed. This inherent feature is a major drawback of such systems whereby poor atomisation at low engine speeds and excessive cavitation at high speeds are to be experienced.

The characteristics of unit pump fuel injection systems are identical to UIS, though the high pressure pump is decoupled from the injection nozzle. In such systems, fuel at elevated pressures is imparted to the fuel injectors through high pressure pipes. As a result, lower peak injection pressures are expected due to losses in the connecting

pipes. The assembly of these fuel injection systems on the engine cylinder head are greatly simplified compared to UIS due to their compact size.

Recent developments in diesel FIE have resulted in the development of common rail fuel injection system. As previously described in Chapter 3, this system consists of a fuel filter, a 12V low pressure pump which draws the filtered fuel from the fuel tank and a high pressure pump which is employed for the generation of pressurised fuel to all of the injectors. In this configuration, the high pressure pump continuously supplies the common rail with pressurised fuel. As a result, the injection pressure is independent of the engine speed, promoting improved mixture formation at low engine speeds and loads. More importantly, the CRS injector has much greater flexibility over injection rate and timing over the entire operating range of the engine.

5.2.3 Fuel Injection Rate

The injection rate profile of unit injector systems has a triangular shape due to the large feed rate of the plunger which considerably increases the injection pressure during injection. On the contrary, common rail fuel injection systems have a rectangular injection rate profile since the injection pressure remains constant in the rail throughout the injection event when the injector is fully opened, as shown in Figure 5.3.

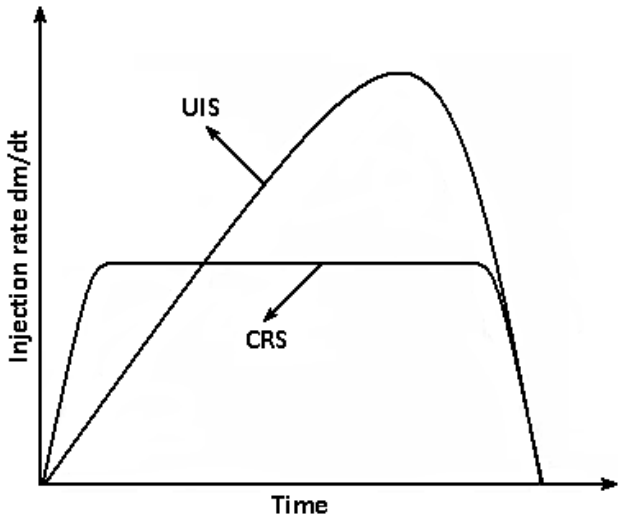

Figure 5.3 Typical Injection Rate Profiles of Common Rail and Unit Injector Systems (Baumgarten, [164])

In common rail fuel injection systems, optimum atomisation and mixing could be achieved upon the onset of injection since maximum injection pressure is achieved over a short period. Although fuel atomisation and mixing is poor at the start of injection in unit injector systems, much more refined fuel atomisation at peak injection pressures is achieved compared to the common rail fuel injection systems. Nevertheless, the new generation of common rail systems capable of generating injection pressures of up to 2500 bar, promote much greater fuel atomisation and mixing in comparison to unit injection systems even at peak injection pressures [166].

5.2.3.1 Measurement Principle of the Fuel Injection Rate Equipment

In this study, a fuel injection rate characterisation rig was commissioned in order to study the effects of multiple injections and alternative diesel fuels on the performance of high pressure fuel injectors. As mentioned in Chapter 3, standard production Delphi VCO injectors were employed to study the effect of split injection and fuel properties. It is presumed that such a solenoid injector is capable of generating up to five injections per cycle, allowing a high degree of flexibility and control on the injection rate, quantity and timing over the entire operating conditions of a diesel engine. This level of performance is habitually achievable with piezo type injectors whereby fast needle response is attainable. Nevertheless, Delphi injectors used in this study are capable of providing high level of economy and performance expected of piezo systems without the complexity and expense of the latter system [167]. However, as is to be shown later, the injector design will limit the availability of injection strategies that can be implemented in practice.

Comprehensive studies on the rate measurements and its effect on the emission and combustion characteristics have been carried out by several researchers including Ishikawa et al. [168], Desantes et al. [169], Arcoumanis et al. [170], Banisad [163], Kohketsu et al. [171] and Bower and Foster [162]. The evaluation method employed in this study is based on Zeuch's method presented by Ishikawa et al. [168].

The principle of this technique is based on the injection of fuel into a CVC filled with the selected fuel for the measurements, in this case commercially available diesel fuel. Consequently, the pressure inside the chamber increases, this augmentation is

proportional to the quantity of fuel injected. Therefore, the fuel injection quantity can be measured based on the change in CVC pressure. The pressure rise ΔP through the change in volume ΔV transpired due to the injection of fuel into the CVC with volume V can be determined from the following equation,

$$\Delta P = k \frac{\Delta V}{V} \qquad \text{Equation 5.1}$$

Where k Bulk modulus of fuel

The fuel injection rate can be determined by differentiating Equation 5.1 with respect to time (t) as depicted below,

$$\frac{dV}{dt} = \frac{V}{k} \times \frac{dP}{dt} \qquad \text{Equation 5.2}$$

In the case of single injection, fuel quantity and injection duration as a function of injection pulse width could be measured through the application of this technique. In addition, interference between injections could also be identified for split or multiple injections, whereby substantial variations in the quantity and rate of fuel injection could be experienced.

The bulk modulus of a fluid changes with pressure, thus accurate measurement of fuel injection rate requires evaluation of bulk modulus as a function of CVC pressure.

5.2.4 Bulk Modulus Measurement

The bulk modulus of elastitsity of a liquid is a measure of its compressibility upon the application of pressure. Thus, the bulk modulus of a fluid is directly proportional to the pressure of the measuring volume; hence, the bulk modulus of fuel, in this case commercially available diesel, is directly proportional to the internal pressure of the working fluid, in this case, the pressure rise due to the injection of diesel fuel into the CVC. In this section, the bulk modulus of commercially available diesel fuel as a function of pressure is evaluated.

5.2.4.1 Evaluation of Bulk Modulus

The bulk modulus of elasticity of the diesel fuel is measured through the application of known forces upon a constant volume of fuel. A compression machine was used to apply the force to the fuel while recording the movement of the compression head, Figure 5.4.

Figure 5.4 Instron Compression Test Machine

Therefore, the plot of strain versus the applied force is obtained from which the bulk modulus of the fuel could be computed. The schematic diagram of the device employed for the compressibility measurements is depicted in Figure 5.5.

The bottom pin is positioned on the fixed head of the compression machine while the force is applied to the top pin through the top crosshead of the machine (i.e. the mobile crosshead). The pins are made of hardened steel to prevent buckling under high compressive loads. In order to eliminate fuel leakage from the sides of the pin, due to the pressure rise inside the chamber, two Viton grade A o-rings are placed at the tip of both pins.

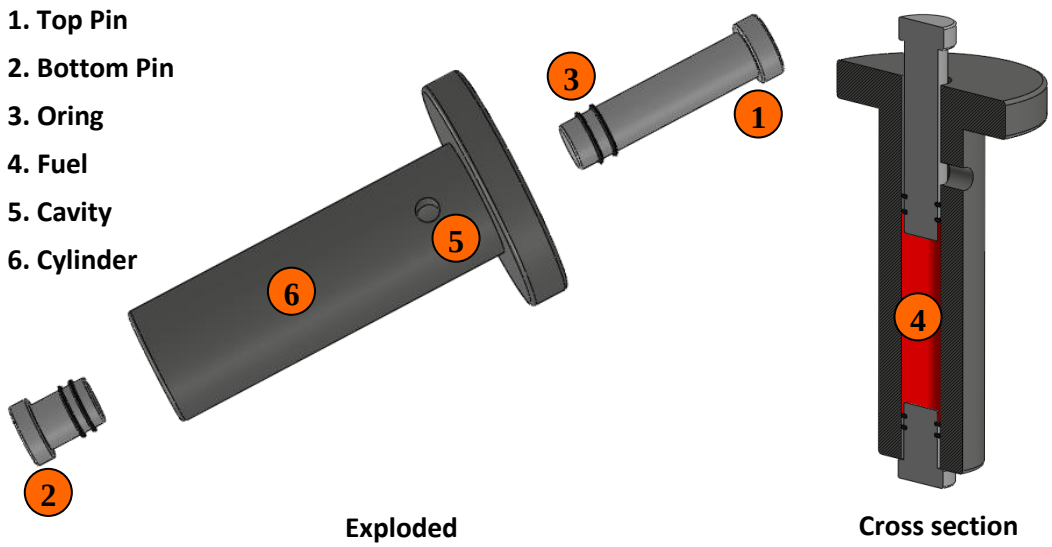

Figure 5.5 Schematic Drawing of the Bulk Modulus Measurement Device

The internal volume of the cylinder, made of tool steel, is dependent on the relative distance between the top and the bottom pins prior to the application of force. Hence, the bottom pin is made detachable such that the internal volume of the chamber could be easily adjusted. The cavity on the side of the cylinder is premeditated so that the trapped air could be discharged upon the initial movement of the top pin without any force being exerted on the fuel (i.e. eliminating the compressibility effects of the trapped air inside the piston).

The bulk modulus of elasticity of a fluid is defined as shown below,

$$K = \frac{Normal\ \ Stress}{Volumetric\ \ Strain} \qquad \text{Equation 5.3}$$

Where normal stress can be defined in the following manner,

$$Normal\ \ Stress = \frac{Force}{Area} \qquad \text{Equation 5.4}$$

While the volumetric strain can be expressed as:

$$Volumetric\ Strain = \frac{\Delta V}{V} \qquad \text{Equation 5.5}$$

Therefore, the bulk modulus of the working liquid can be calculated, provided that the volume of the chamber, the applied force, the area upon which the force is applied to and the strain data (i.e. ΔV) are known. In the current setup the applied force was known, the strain values were recorded by the Instron compression machine, the top pin area was computed (i.e. the area upon which the force is applied to) and the volume of the CVC was measured. Therefore, the bulk modulus of the fuel was calculated from the force versus strain graph produced by the compression machine.

5.2.4.2 Data Acquisition System

An onboard data acquisition system supplied by the manufacturer of the compression machine was utilised to record the data during the measurements. The data was transferred and saved to a computer via a network cable.

5.2.4.3 Result

The bulk modulus of commercially available diesel fuel was experimentally evaluated at Wolfson research centre for materials processing, Brunel University. The bulk modulus of standard diesel fuel in terms of the applied pressure is shown in Figure 5.6.

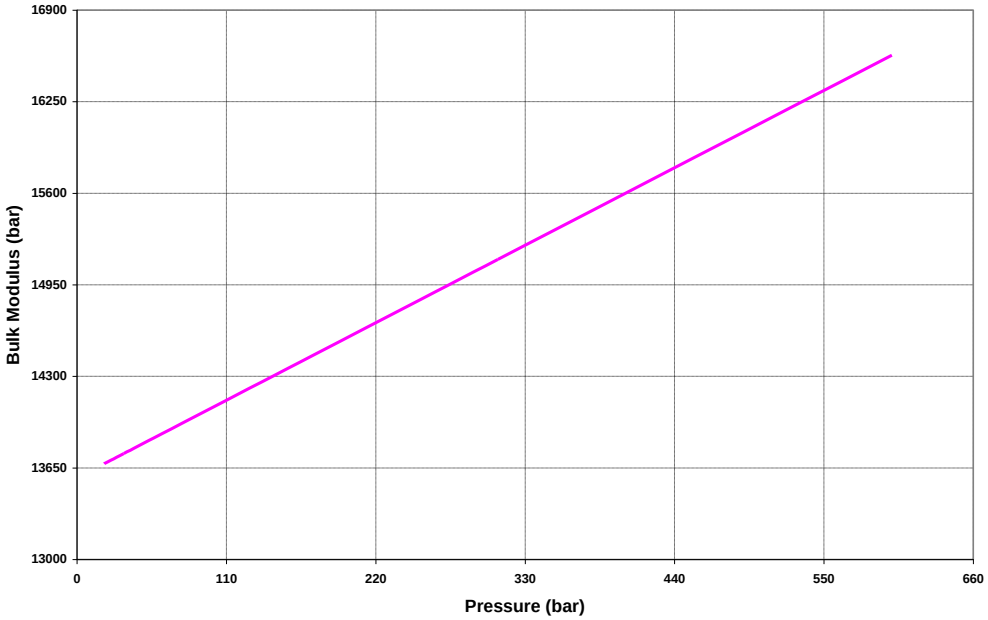

Figure 5.6 Bulk Modulus of Commercially Available Diesel Fuel

The results were obtained through the use of the aforementioned experimental setup. As previously stated, the force was applied to the top pin; thus, the pressure applied to the working fluid was proportional to the cross sectional area of the pin. Consequently, the CVC was manufactured at Brunel University with the bore diameter of 10 mm and volume of 20 cm^3 (measured), allowing bulk modulus measurements up to 600 bar. The thickness of the piston was designed to be 10 mm so that the effect of piston wall expansion under the maximum applied force was negligible. The test at a given pressure reading was repeated 20 times ensuring the repeatability of the results.

5.3 Fuel Injection Equipment

In the following sections, the experimental setup of the fuel injection rate measurement and the corresponding results are presented.

5.3.1 Experimental Setup

A first generation Delphi common rail fuel injection system, incorporating a VCO standard production solenoid injector was used in this study. These common rail systems are commonly equipped with a high pressure diesel pump capable of generating high injection pressures. These pumps are designed to operate with diesel fuel whereby the mechanical parts of the pump are well lubricated through the circulation of fuel inside the pump. Thus, the use of low lubricity fuels could lead to premature failure of the pump. However, a special blend of single component dopants with considerably low lubricity was used for the LIEF measurements which could lead to premature failure of the mechanical high pressure pump, thus, a high pressure pneumatic pump was employed instead whereby no lubrication was required, detailed explanation is presented in Chapter 7. In order to retain the fuel injection characteristics throughout the subsequent investigations, the same fuel injection system was employed.

A CVC, of approximately 50 cm^3, equipped with three pressure sensors; measuring background pressure, pilot injection and main injection was employed in this study. The first sensor, Kistler 4043A50 piezo-resistive absolute pressure transducer,

measured the pressure inside the chamber prior to the onset of fuel injection (i.e. back pressure) while the second and the third sensors, Kistler 701A piezoelectric pressure transducers with high and low sensitivities, were installed for the measurement of small and large fuel quantities (i.e. pilot and main injections) respectively. The piezoelectric pressure transducers were adopted in this setup since their accuracy is often not affected by the size or the volume of the quartz, but the geometry and material used, enabling acquisition of accurate data even at absolute pressures ten times higher than their dynamic measuring full scale range. The detailed characteristics of the pressure transducers are depicted below, Table 5.1. The pressure signal from the former transducer (i.e. Kistler 4043A50) was connected to a piezo-resistive charge amplifier, Kistler 4618A2; while the output signals from the latter transducers (i.e. Kistler 701A) were connected to digital charge amplifiers, Kistler 5001.

Table 5.1 Characteristic Features of Kistler Pressure Transducers

Type	Measuring Range (bar)	Overload (bar)	Sensitivity		Natural Frequency kHz	Operating Temperature Range ^{o}C
			pC/bar	mV/bar		
4043A10	0…50	125	-	10	>180	-20…50
710A	0…250	400	82.9	-	≈ 70	-150…200
710A	0…250	400	82.4	-	≈ 70	-150…200

A combination of a pressure relief valve and a solenoid actuator were located on top of the CVC. A schematic diagram of the experimental setup is depicted in Figure 5.7. A high pressure direct acting coaxial solenoid valve, manufactured by co-ax valves, was positioned directly on top of the CVC. A Swagelok R series proportional relief valve was utilised in order to regulate the back pressure. The relief valve consists of a spring mechanism inside the valve assembly, opens gradually when system pressure reaches the set pressure and closes when system pressure falls below the set pressure. The desired pressure could be set by screwing the spring mechanism cap which in turn adjusts the compression of the spring mechanism. A lock nut system is used in order to maintain the cap position. A high precision positive displacement fuel flow meter, ONO SOKKI FP-200 series, was mounted after the pressure relief valve, measuring

the quantity of the injected fuel. The resultant fuel quantities calculated based on the application of Zeuch's method were further validated by the fuel quantities measured by the flow meter. The fuel injector is positioned horizontally opposite the pressure sensors such that the pressure rise inside the CVC could be accurately measured.

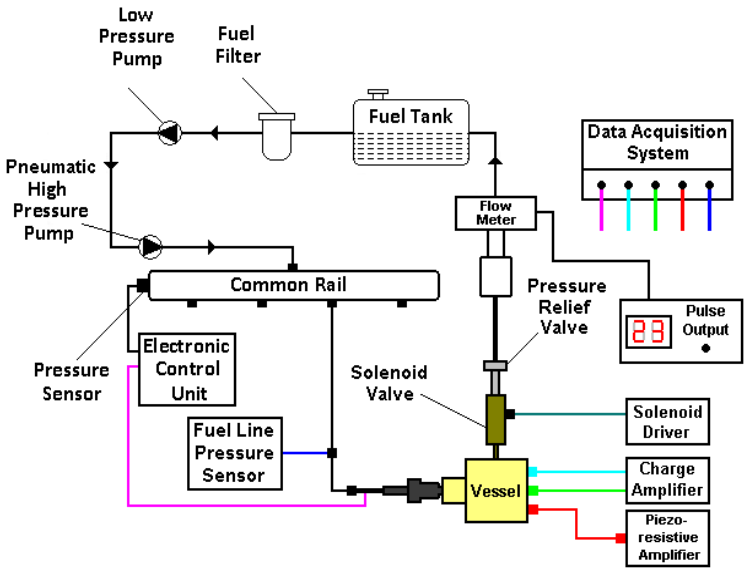

Figure 5.7 Schematic Diagram of the Experimental Setup Based on Zeuch's Method

Although the solenoid valve is normally open, it could be triggered to the closed mode by a TTL pulse prior to the onset of measurements. The injection signal was used as a trigger input while a custom-built synchronisation unit was used to control the duration of the solenoid valve closing time, the timing diagram is shown below, Figure 5.8.

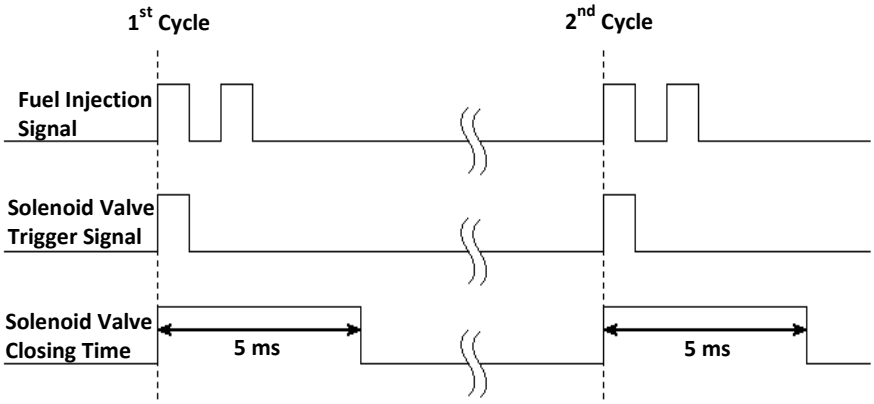

Figure 5.8 Timing Diagram of the Injection Rate Test Rig

5.3.2 Data Acquisition System

The data acquisition system consisted of a National Instruments SCB-68 E series board and a National Instruments PCI-MIO-16E data acquisition card. A LabVIEW program written by the author was utilised in order to synchronise the system and to record the data. The injection signal was used as the trigger for the data acquisition software. This signal and the signals from the charge amplifiers were acquired by the data acquisition system and subsequently recorded by a computer. The connections from the data acquisition system can be found in Table 5.2.

Table 5.2 National Instruments Data Acquisition System Configuration

Channel Inputs	Channel Description
Channel 1	Injection Signal (Trigger)-Current Clamp Signal
Channel 2	High Sensitivity Pressure Amplifier Output
Channel 3	Low Sensitivity Pressure Amplifier Output
Channel 4	Back Pressure Amplifier Output
Channel 5	Fuel Line Pressure Amplifier Output

The software generated an internal clock signal based on the preselected sampling number and rate. The software recorded the pressure signals from the charge amplifiers which were thereafter exported to Microsoft Excel for further analysis. A screenshot of the LabVIEW program is shown in Appendix C.

5.3.3 Data Analysis

As previously stated, the pressure signals form the pressure transducers were passed through the charge amplifiers and subsequently recorded by the data acquisition system. The collected data was imported into "Origin", a software package designed for data analysis, where further data manipulation was carried out. The pressure signals were filtered using Fast Fourier Transform (FFT) function as depicted below.

$$f_{Cutoff} = \frac{1}{n\Delta t} \qquad \text{Equation 5.6}$$

Where n is the number of data points considered in every filtering region and Δt is the time (or commonly the abscissa) spacing between two adjacent data points. Therefore,

larger values of *n* result in lower cut-off frequencies, hence a greater degree of smoothing. Further data analysis was carried out in Microsoft Excel using the filtered pressure signals. The cut-off frequency of 5 kHz was used in this study.

5.3.4 Evaluation Method

The bulk modulus of the diesel fuel was determined from Figure 5.6 based on the internal pressure of the CVC. Subsequently, the rate of change in pressure with respect to time (i.e. *dp*/*dt*) was calculated from which the injection rate, Equation 5.2, was determined. This investigation was carried out to analyse the injection characteristics of single and split injection strategies as depicted in Table 5.3.

Table 5.3 Fuel Injection Quantities for Single and Split Injection Strategies

Strategy	Dwell Angle	Quantity (mm^3)			
Single Injection	N/A	10		20	
Split Injection (30:70)	Variable Fixed	3	7	6	14
Split Injection (50:50)	Variable Fixed	5	5	10	10
Split Injection (70:30)	Variable Fixed	7	3	14	6

Thus, the fuel demand corresponding to each injection strategy must be evaluated as a function of the injection duration which is generated by the ECU. In order to identify the correct injection duration, several injection durations were tested and their corresponding quantities were identified. The injection rate profiles of the quantities of interest are only presented in the following section.

5.3.5 Results

5.3.5.1 Leak Test

The system was leak tested prior to the onset of the measurements in order to ensure that no fuel leakage occurred during the measurements. This was achieved by real time data acquisition of the CVC absolute pressure using the piezo-resistive pressure

transducer. The solenoid valve was triggered by the data acquisition system to the closed mode and fuel was injected into the chamber.

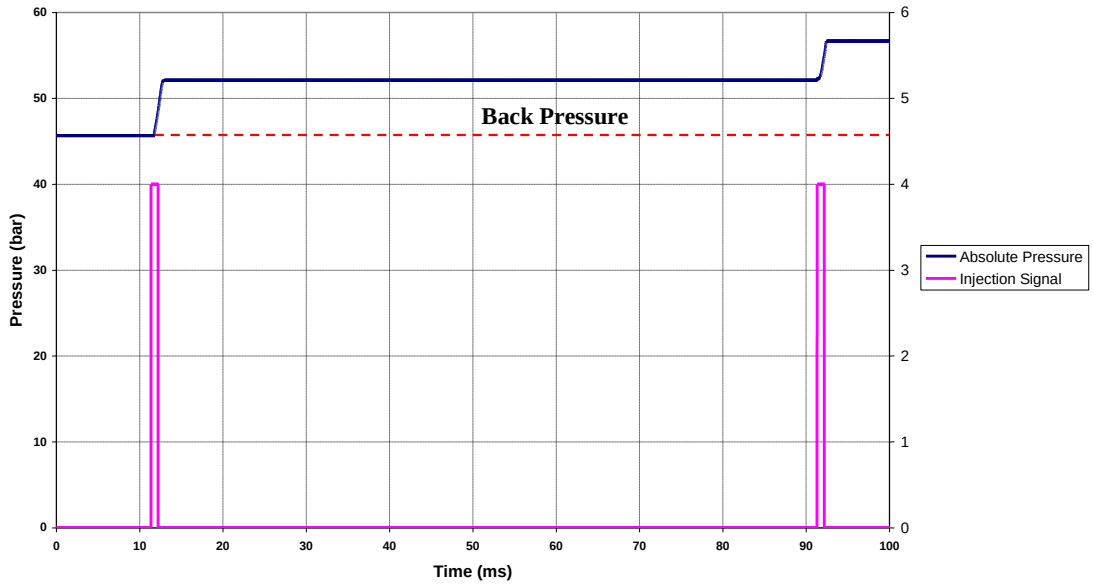

Figure 5.9 Constant Volume Chamber Absolute Pressure

The pressure data presented in Figure 5.9 demonstrates that the absolute pressure inside the CVC remained constant prior and after the injection events, indicating no fuel leakage. The red dotted line represents the back pressure prior to the onset of the fuel injection.

5.3.5.2 Single Injection

The injection rate results corresponding to single injection strategies are depicted in Figure 5.10. The fuel quantity for each injection strategy could be obtained by taking the area under the injection rate profile. The fuel quantities obtained were validated by the flow meter to ensure the accuracy of the results. The ECU was set to the simulation mode whereby the engine speed and the fuel injection pressure were controlled manually. The engine speed and the fuel injection pressure were set at 1500 rpm and 1200 bar respectively throughout the experiments.

As evident in Figure 5.10, there is a 205 µs delay between the start of injection (i.e. the rising edge of the injection signal) and the start of the injection rate plot. This is

mainly attributed to three primary reasons; first, the internal delay of the injector driver, secondly, particularly in the case of mini-sac or micro-sac injectors, the time required for the pressure build up in the sac volume as well as the acceleration time of fuel through the nozzle and finally the position of the pressure transducers relative to the tip of the injector [163, 170]. The pressure build up time can be neglected in the current study since VCO injectors were employed. However, the relative position of the injector to the pressure transducers is significant; the pressure transducer was positioned 250 mm away from the nozzle tip.

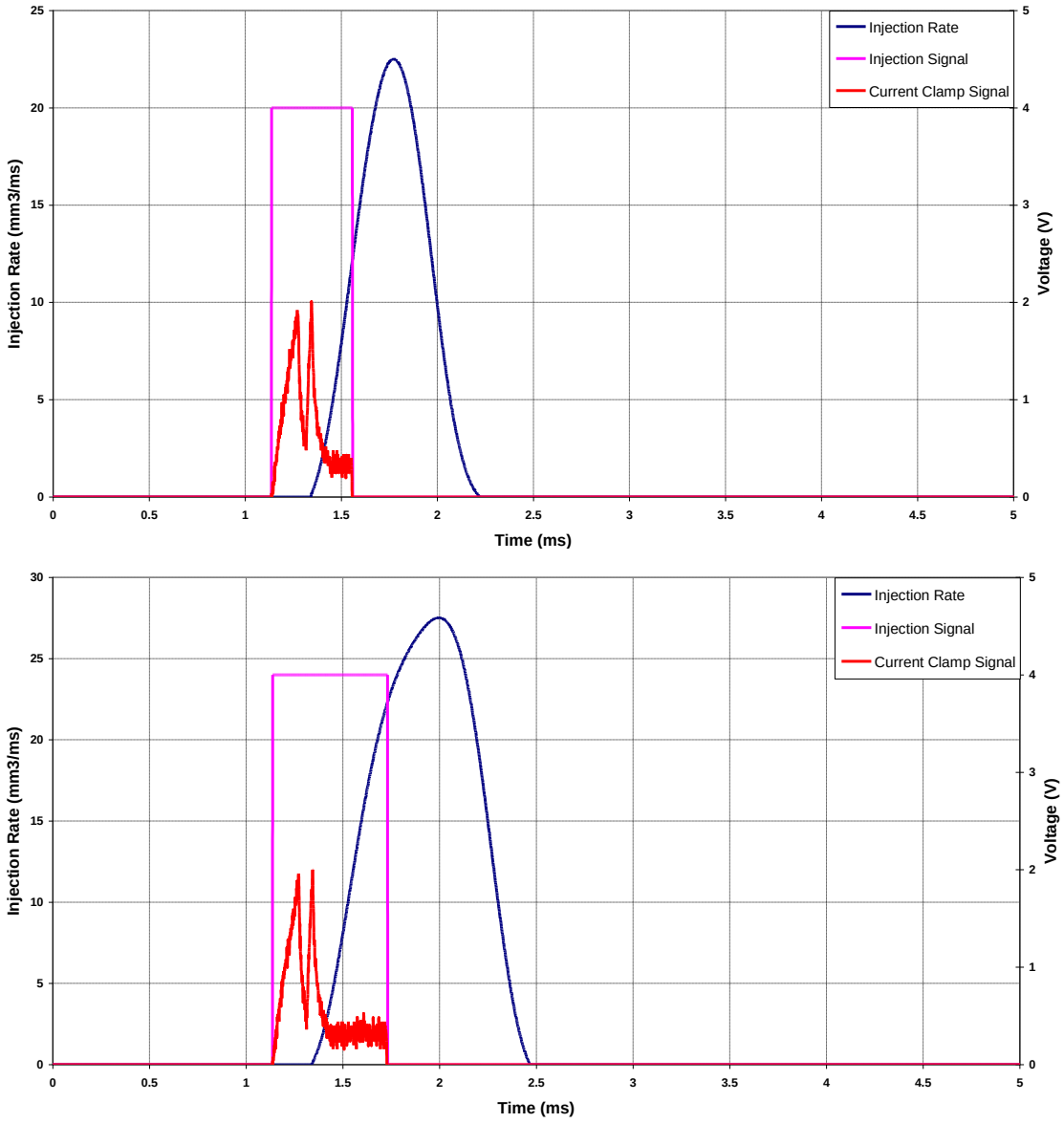

Figure 5.10 Injection Rate Profile for Single Injection Strategies; 10 mm^3 (Top), 20 mm^3 (Bottom)

5.3.5.3 Split Injection

As depicted previously, Table 5.3, the following split injection strategies were selected for the purpose of this investigation, 30:70, 50:50 and 70:30. The injection quantities corresponding to the quantity of each injection event for the aforementioned strategies must therefore be identified as shown in Figure 5.11.

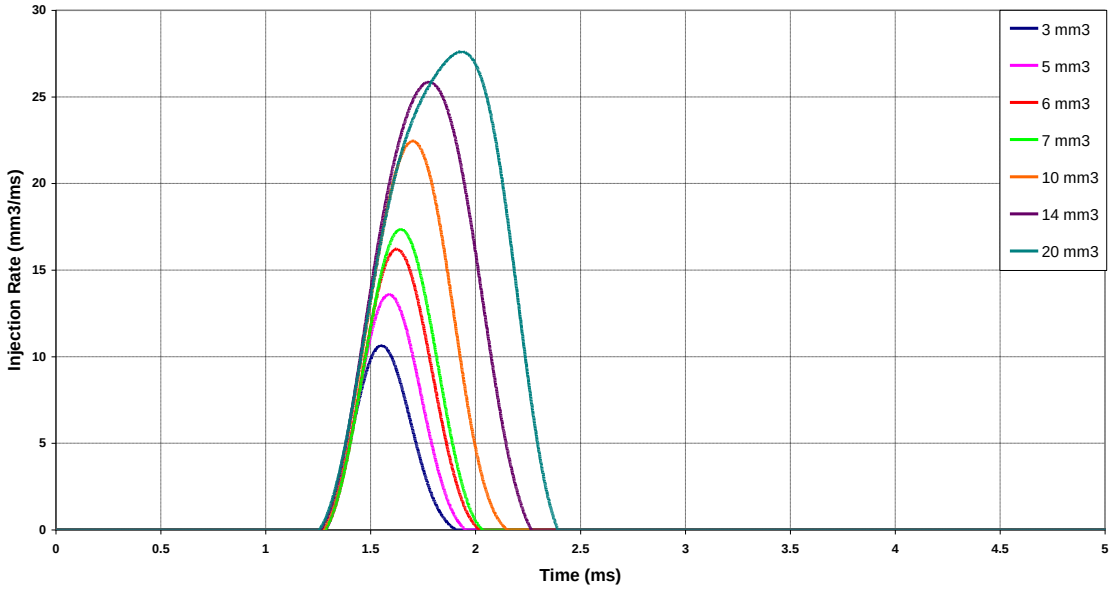

Figure 5.11 Injection Rate Profile for Single Injection Quantities

As evident in Figure 5.11, the start of fuel injection (i.e. the point at which pressure rise was detected) is identical for all measurements, indicating a constant time lag between the start of injection signal and the onset of fuel injection as discussed in the previous section.

In order to select an appropriate dwell angle (i.e. the timing between the two injections) for the split injection strategies, different dwell angles were studied. Figure 5.12 shows the injection rate profiles for 50:50 split injection strategies with total fuel demand of 10 mm^3 per cycle.

As evident in Figure 5.12, the dwell angle of 5^o CA was not sufficient for the injector needle to fully close prior to the start of the second injection, thus the injected fuel quantity was more than anticipated. It is apparent that the time lag between the first

and the second injection is approximately 230 µs as opposed to 555.5 µs (i.e. 5^{o} CA at 1500 rpm). This phenomenon was further validated through high speed imaging, Figure 5.13. The 50:50 split injection strategy with 10 mm^{3} fuel demand per cycle was studied where the first and the second fuel injections took place at 5^{o} CA BTDC and TDC respectively. The injection pressure and engine speed were set at 1200 bar and 1500 rpm respectively.

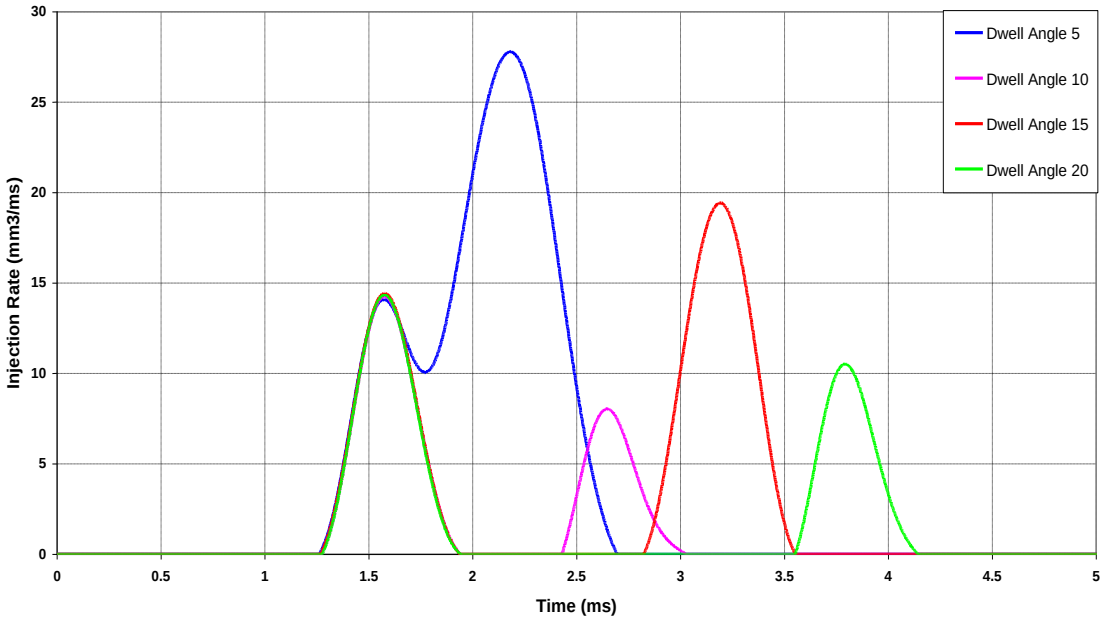

Figure 5.12 Injection Rate Profile for 50:50 Split Injection Strategies, 10 mm^{3}

Although the start of the first and the second injections are marked as 5^{o} CA BTDC and TDC respectively, it is conspicuous from the high speed images that the fuel spray in both cases is not at the initial stages of development; this is mainly attributed to the limitation of the high speed camera in terms of the maximum number of frames per second it can capture while maintaining an acceptable image size.

Based on the image sequence presented in Figure 5.13, it is evident that, there exists a time lag of approximately 2^{o} CA, 256µs at 1500 rpm, between the end of the first injection and the start of the second. This finding is in good agreement with the results obtained from the CVC measurements. As previously explained in Section 5.2.1, the asymmetry of the fuel spray at the initial stages of the injection event is a major drawback of VCO injector nozzles; this phenomenon is perceptible in the high speed

images obtained from the optical hydra engine. It is also important to note that although the injection duration was identical for both injections, the second injection took place over 2.7^{o} CA whereas the first injection took place over 1.8^{o} CA. This finding is also in good agreement with the data presented in Figure 5.12 for 5^{o} CA dwell timing whereby the magnitude of the second injection rate peak was significantly larger compared to the first peak.

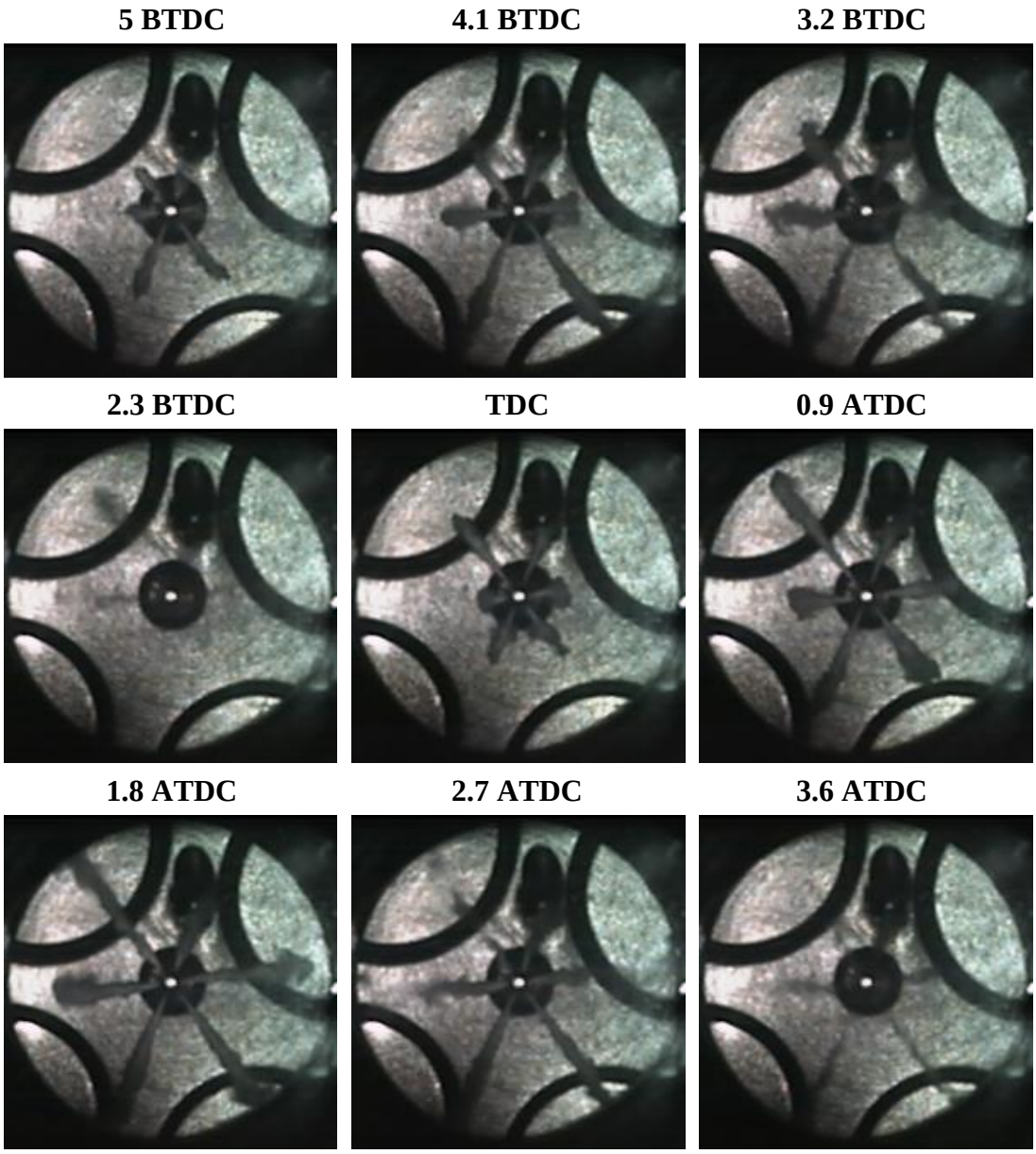

Figure 5.13 Fuel Spray Image Sequence at 1200 bar

The same explanation holds true for the 50:50 split injection strategies with 20 mm^3 fuel demand per cycle, Figure 5.14.

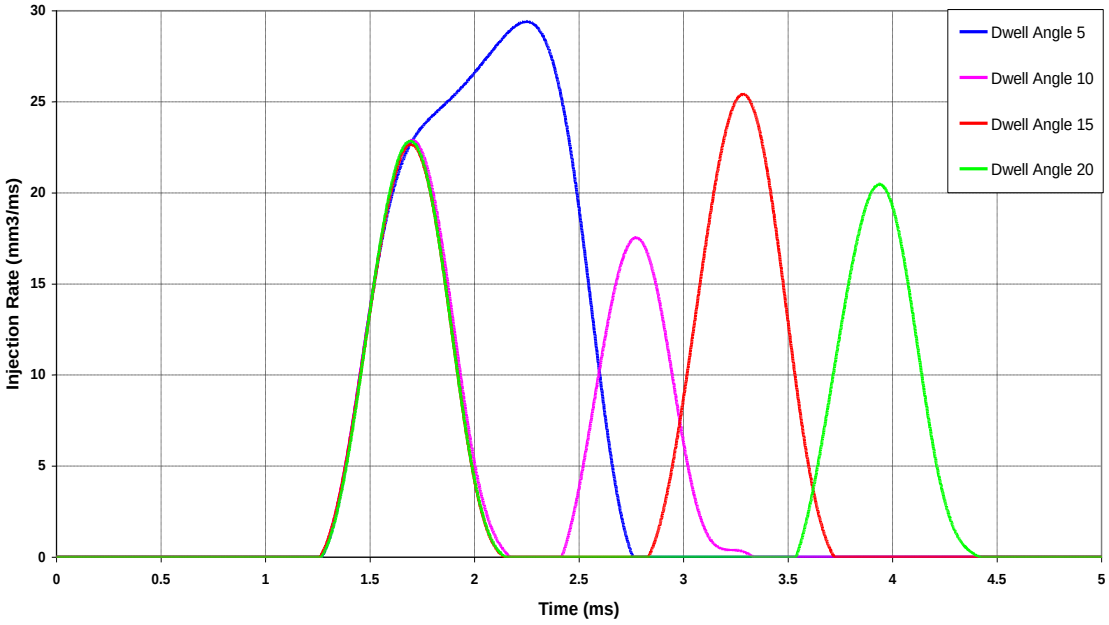

Figure 5.14 Injection Rate Profile for 50:50 Split Injection Strategies, 20 mm^3

As evident in Figure 5.14, the dwell angle of 5^o CA was not sufficient to separate the two injection events. The injection rate profile shows that the two injections acted as a single injection with a total fuel quantity of approximately 28 mm^3 which was substantially more than the desired quantity. This is due to the fact that the needle was fully open during the middle of the first injection when the second injection pulse was transmitted to the injector, thus maintaining the full needle opening position at the start of the second injection, resulting in excess fuel being injected into the engine. However, longer dwell angles between the two injections, similar to 10 mm^3 injection strategies, minimised the interference between the two injections.

The same explanation holds true for 30:70 and 70:30 split injection strategies with 10 mm^3 fuel demand per cycle whereby the dwell angle of 5^o CA between the two injections resulted in interference between the two injections, Figure 5.15. However, this phenomenon was less paramount in the case of 30:70 strategy since the first injection duration was significantly shorter compared to the second injection, thus minimum interference took place.

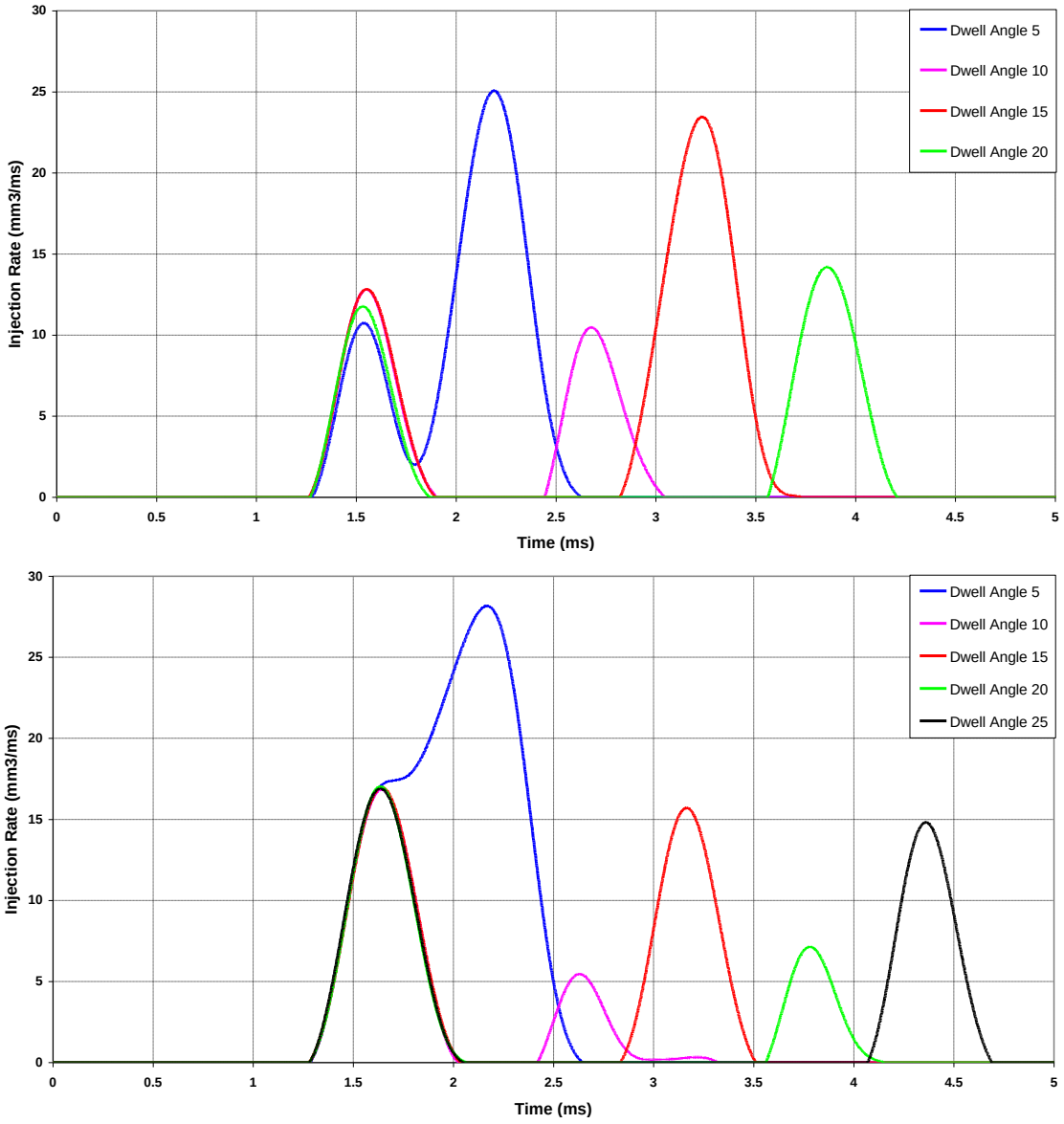

Figure 5.15 Injection Rate Profile for Split Injection Strategies, 10 mm^3, 30:70 (Top), 70:30 (Bottom)

Similar results were also obtained for 30:70 and 70:30 split injection strategies with 20 mm^3 fuel demand per cycle, Figure 5.16. In the same manner as previously described, the dwell angle of 5^o CA between the two injection events resulted in interference. It is evident that in the case of 70:30 split injection strategy, the split injection almost acted as a single injection. In other words, the first injection event was long enough such that the start of the second injection took place during the first injection event. Therefore, the expected fuel quantity in this case was exceedingly larger than desired, approximately 29 mm^3.

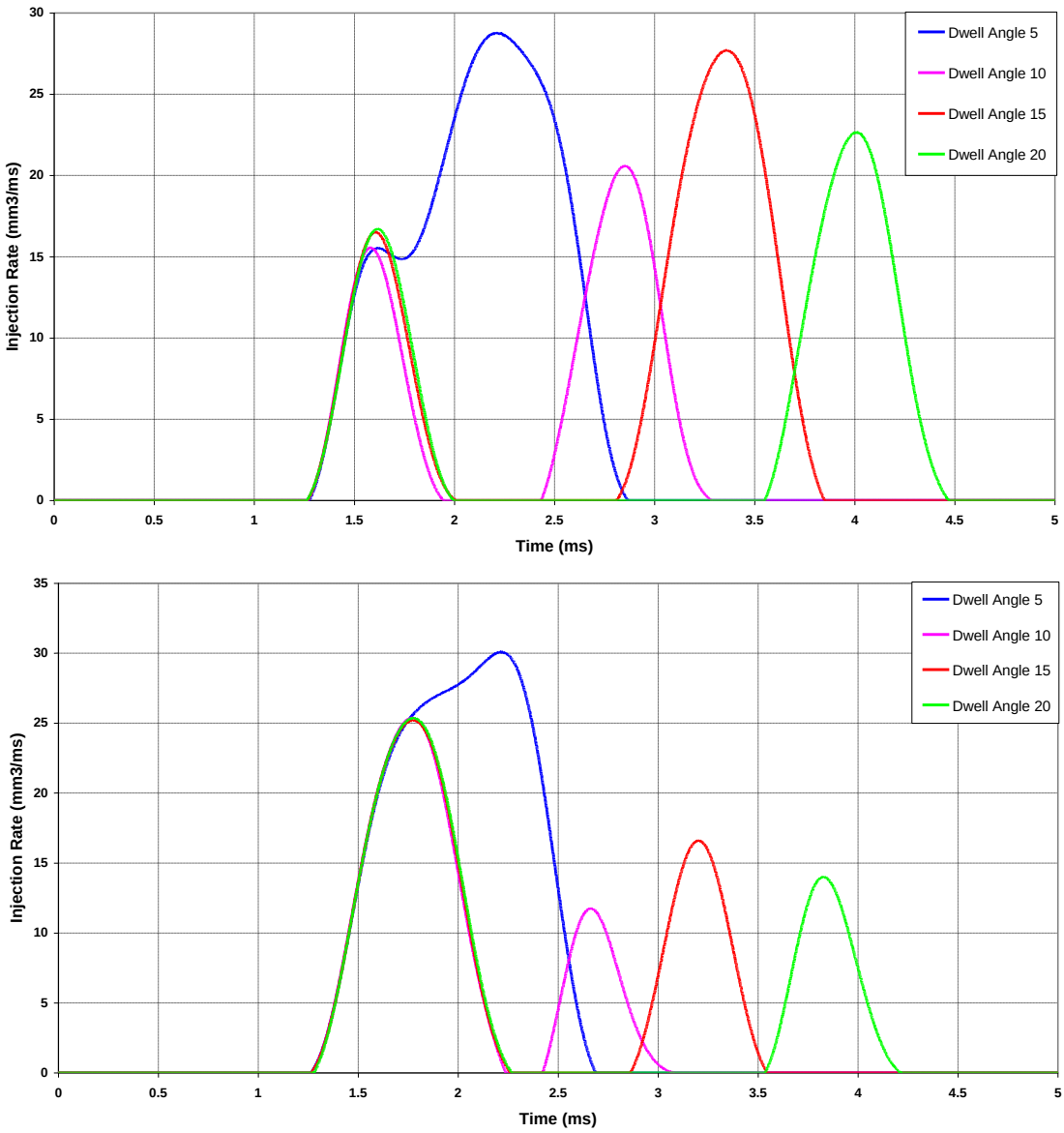

Figure 5.16 Injection Rate Profile for Split Injection Strategies, 20 mm^3, 30:70 (Top), 70:30 (Bottom)

In the case of 10^o CA, 15^o CA, 20^o CA and 25^o CA dwell timings, the injection quantity of the first injection remained almost constant for all the tested strategies, though the quantity of the second injection varied depending on the dwell timing used. This was mainly attributed to the adverse effect of pressure waves, due to first injection, in the high pressure fuel line connecting the injector to the common rail as shown in Figure 5.17. In this Figure the first injection is shown in gray which is fixed for all the strategies and the second injections use the same colour coding as the fuel line pressure traces.

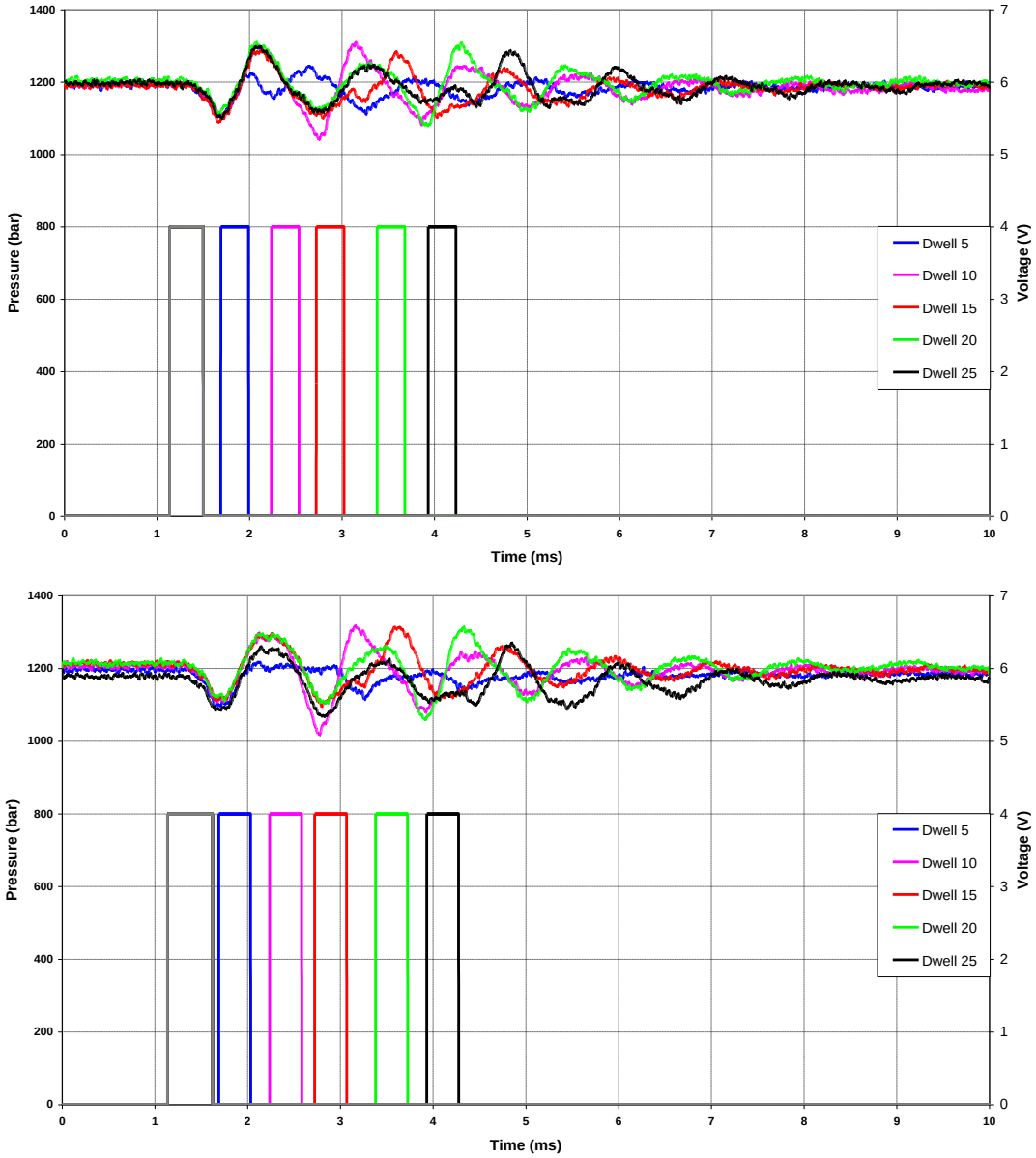

Figure 5.17 Fuel Line Pressure Traces, 10 mm^3 (Top); 20 mm^3 (Bottom)

The fuel line pressure traces presented in Figure 5.17 correspond to 70:30 split injection strategies, though the same trend held true for 30:70 and 50:50 strategies. Moreover, the same pattern in fuel line pressure fluctuations was observed for both cases of 10 mm^3 and 20 mm^3 fuel demand. This was mainly due to identical hydraulic properties of the tested fuel in both cases which led to similar patterns in the detected pressure waves in the high pressure fuel line.

In the case of 10^o CA, fuel line pressure was declining at the start of the second injection which resulted in lower fuel injection quantity during the second injection. Although fuel line pressure was lower than set in the case of 15^o CA, it was higher in comparison to the former case at the start of the second injection which justifies the increase in the injected fuel quantity. In the case of 20^o CA, the fuel quantity during the second injection was lower than expected, however its effect was less paramount in comparison to 10^o CA case since the fuel line pressure was relatively higher at the start of the second injection. The same trend held true in the case of 25^o CA, though the reduction in fuel line pressure due to the pressure waves was less in comparison to the former case; hence more fuel quantity was injected.

5.4 Summary

This chapter has detailed the process of FIE characterisation through Zeuch's method. Single and split injection strategies were employed in order to identify the fuel injection system characteristics under both conditions while the total injected fuel quantity per cycle remained constant. In order to improve the accuracy of the fuel injection rate results, an Instron compression rig has been modified and adapted to measure the bulk modulus of diesel fuel. The results confirmed that the VCO nozzles suffer from uneven distribution of the fuel spray through different nozzle holes. Furthermore, the injection rate profiles for single injection strategies were obtained at different fuel quantities. Subsequently, 30:70, 50:50 and 70:30 split injection strategies with different dwell timings were studied. In all cases, single and split injection strategies, the total fuel quantities of 10 and 20 mm^3 per cycle were investigated. The dwell timing of 5^o CA resulted in interference between the two injections replicating single injection characteristics while well separated injection rate profiles were obtained under longer dwell timings. Nevertheless, it was observed that the quantity of fuel injected during the second injection was influenced by the first injection. This was mainly attributed to the mechanical limitations of the fuel injector utilised in this study as well as pressure fluctuations in the fuel line pressure caused by the first injection.

6

CHAPTER 6

Investigation of the Effects of Single and Split Injection Strategies on Diesel Combustion and Emission

6.1 Introduction

This chapter details the investigation that was carried out on the use of single and split injection strategies aimed at detailed analysis of mixture formation, combustion and exhaust emissions by means of various optical techniques and in-cylinder pressure and exhaust emissions measurements.

The following sections describe the combustion strategies, experimental techniques, test conditions, injection strategies and the test plan utilised in this study followed by the presentation and discussion of the results.

The conventional main injection and split injection combustion concepts were investigated. These combustion systems were extensively studied in order to identify the combustion and emissions characteristics under different operating conditions. For all the strategies presented in this section the in-cylinder pressure data was recorded from which heat release rate was calculated. The exhaust emissions and soot concentration were also measured to assess the effect of different injection strategies on the level of emissions produced. In addition, optical techniques including high speed video imaging and two-colour techniques were applied to the better performing strategies which were selected based on the IMEP values and the level of exhaust and soot emissions.

Although high speed imaging and two-colour techniques produce crank angle resolved information on the combustion characteristics, flame temperature and soot

concentration, only few frames are presented for each test condition at particular points of interest based on the heat release rate data.

6.2 Experiments

6.2.1 Test Conditions

High cylinder leakage was experienced during motoring and combustion cycles due to the use of glass piston. The peak motoring pressure with the metal piston was approximately 32 bar while the peak pressure with the glass piston was substantially lower at 23 bar. In order to overcome such pressure loss, three raised edges were machined on the surface of the spacer ring where it was in contact with the carbon gasket, creating high pressure points to assist sealing. In addition, an o-ring was fitted on the inner surface of the piston where it is in contact with the glass piston in order to further prevent gas leakage through this gap, as previously stated in Section 3.2.3.2. The peak motoring pressure of approximately 32 bar was achieved when operating in naturally aspirated mode using the improved piston assembly as illustrated in Figure 6.1.

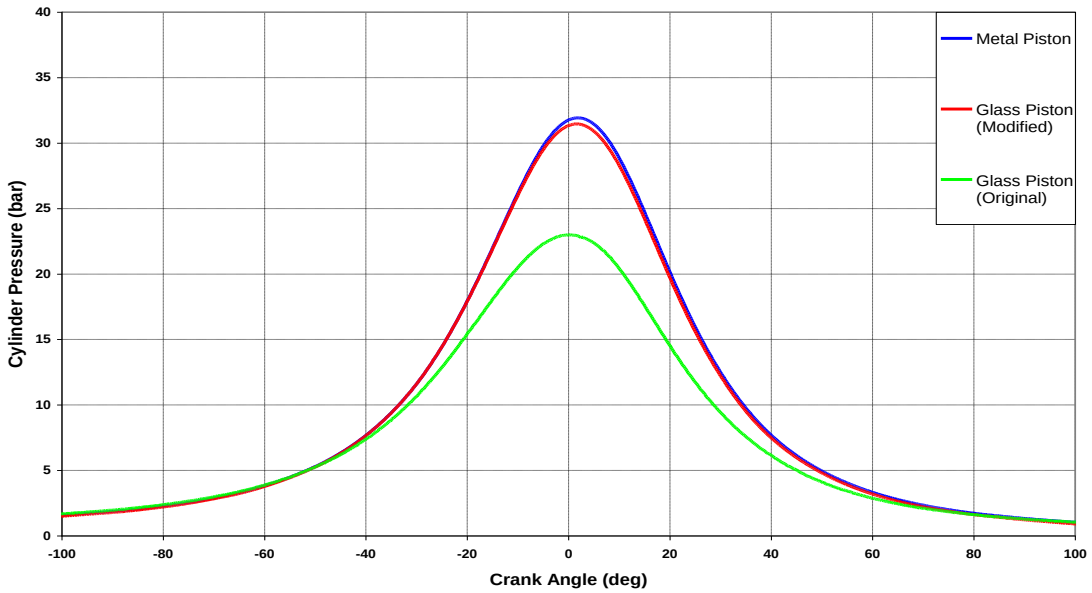

Figure 6.1 In-Cylinder Motoring Pressure

Thus, the in-cylinder conditions were almost identical with both metal and glass pistons which is crucial when comparing the high speed images, in-cylinder pressure

traces and emissions data. Nevertheless, it is important to note that the in-cylinder pressure traces, rate of heat release and emissions data obtained with metal piston is slightly different from the those obtained with a glass piston as demonstrated by Aronsson et al. [172] and Kashdan and Thirouard [173].

In previous investigations [150, 151] the difference in the in-cylinder pressure between the metal and glass pistons was compensated for by boosting the intake air through the use of a supercharger.

The test conditions for the experimental work carried out in this chapter are listed in Table 6.1.

Table 6.1 Test Conditions

Intake Air	100°C Naturally Aspirated, ≈ 0 bar Gauge
Engine Speed	1500 rpm
Fuel	Commercially Available 49.1 CN Diesel
Fuelling Demand	10, 20 mm^3/cycle
Load	≈ 36% and 72% of full load
Injection Pressure	1200 bar
Piston Bowl	Glass – Pressure, High Speed Imaging, 2-Colour Technique Metal – Soot, Emissions

Intake Air: Intake air temperature was set and sustained at approximately 100^oC in order to replicate typical diesel engine operating condition and to compensate for relatively low engine temperature of optical engines compared to standard all-metal diesel engines where the engine reaches considerably higher temperatures. As stated earlier, since the in-cylinder motoring pressure with the glass piston was almost identical to the motoring pressure with the metal piston, all the experiments were carried out with the engine running in the naturally aspirated mode. The intake pressure under this operating condition equates to 1 bar (Absolute).

Engine Speed: Engine speed was set and maintained at 1500 rpm through the use of a dynamometer as explained in Section 3.2.1. This speed is selected in order to replicate typical low/medium speed HSDI diesel engine operation.

Fuelling: All the experiments were performed with total fuel demand of 10 mm^3 and 20 mm^3. The fuel utilised was standard commercially available diesel with a Cetane Number (CN) of 49.1.

Load: Diesel engine load is determined by the quantity of fuel injected. The load on the engine was estimated based on the percentage of maximum fuelling (27.69 mm^3/cycle), intake air temperature of 100^oC and engine speed of 1500 rpm, at lambda 1.0 (AFR 20) with natural aspiration and they equated to approximately 36% and 71% of the full load at 10 mm^3 and 20 mm^3 fuel demand respectively.

Injection Pressure: The FIE utilised in this study was capable of operating at the maximum fuel injection pressure of 1600 bar, however injection pressure of 1200 bar was selected for the purpose of this investigation as being typical of current injection pressures for optical diesel engines.

Piston Bowl: As previously stated in Section 3.2.3.1, a flat glass window, fitted in the crown of the piston, was utilised for in-cylinder pressure measurements and all the optical techniques employed in this study instead of current ω-shaped piston design in order to minimise the effect of optical aberration. Thus, the in-cylinder flow conditions were different than those present in all-metal production type diesel engines. Consequently, the mixing process, combustion characteristics and exhaust emissions were affected in this study, yet the trend obtained in most cases is presumed to hold true in real life applications. A metal piston blank was utilised for exhaust emissions measurement so as to preserve the glass window. A shallow ball was machined in the crown of the metal piston so that the effective compression ratios with metal and glass pistons were comparable.

6.2.2 Injection Strategies

The strategies are divided into two categories, single and split, as listed in Table 6.2. The former is utilised as a benchmark when analysing the combustion and emissions characteristics of strategies under the latter injection mode. All the strategies were carried out with total injection pulse width corresponding to total fuel demand of 10 mm^3 and 20 mm^3 based on the results presented in Chapter 5.

The single strategies were formulated based on the following criteria:

- All individual injections to occur within the second half of the compression stroke to avoid low fuel evaporation.

The split injection strategies were formulated on the following basis:

- Equal fuel injection pulse width for the first and second injections. In the ideal case when the injection process is identical during the first and second injections, 50% of the total fuel quantity would be injected during the first injection and the other 50% during the second injection.
- Variable fuel injection pulse width for the first and second injections, 30:70 and 70:30 split injection strategies. In the former case, the pulse widths of the first and the second injections were set respectively to 30% and 70% of the total fuel injection duration based on the single fuel injection calibration curves. In the latter case, 70% and 30% duration were set for the first and second injections respectively.
- Constant dwell angle between the first and second injections while altering the timing of the first injection event.
- Variable dwell angle between the first and the second injections while keeping the timing of the second injection constant.
- In case of the 70:30 injection strategies, the timing of the second injection was altered while keeping the timing the first injection constant in order to investigate the effect of late injection on soot emission.

As reported by Hardy and Reitz [89], optimisation and refinement of modern internal combustion engines has become exceedingly more difficult, something which is further exacerbated in this investigation due to the limited running time of the optical engine utilised. Therefore, the strategies selected and tested should be considered as a starting point upon which further detailed investigation and optimisation is expected to exist.

Table 6.2 Injection Strategies

Strategy	Test Number		SOI (^{o} CA ATDC)		Dwell Angle
Single Injection	10 mm^3	20 mm^3	Main		
	A1	AA1	-15		N/A
	A2	AA2	-10		
	A3	AA3	-5		
	A4	AA4	TDC		
Split Injection 50:50			1st Injection	2nd Injection	Variable
	B1	BB1	-20	TDC	
	B2	BB2	-15	TDC	
	B3	BB3	-10	TDC	
	B4	BB4	-5	TDC	
	C1	CC1	-20	-10	Fixed (10^{o} CA)
	C2	CC2	-15	-5	
	C3	CC3	-10	TDC	
	C4	CC4	-5	5	
Split Injection 30:70	D1	DD1	-20	TDC	Variable
	D2	DD2	-15	TDC	
	D3	DD3	-10	TDC	
	D4	DD4	-5	TDC	
	E1	EE1	-20	-10	Fixed (10^{o} CA)
	E2	EE2	-15	-5	
	E3	EE3	-10	TDC	
	E4	EE4	-5	5	
Split Injection 70:30	F1	FF1	-20	TDC	Variable
	F2	FF2	-15	TDC	
	F3	FF3	-10	TDC	
	F4	FF4	-5	TDC	
	G1	-	-10	5	
	G2	-	-10	10	
	G3	-	-10	15	
	H1	HH1	-20	-10	Fixed (10^{o} CA)
	H2	HH2	-15	-5	
	H3	HH3	-10	TDC	
	H4	HH4	-5	5	

6.2.3 Test Plan

All the strategies were tested with the optical configuration at an injection pressure of 1200 bar in order to obtain the in-cylinder pressure data and high speed videos. The IMEP and heat release data were subsequently calculated based on the methods described in Sections 3.6.2.1 and 3.6.2.4 respectively. In addition, exhaust and soot emissions were measured for all the strategies. Analysis of the in-cylinder pressure, heat release rate, IMEP and high speed videos led to the selection of the better performing strategies for the two-colour measurements. Table 6.3 details the testing performed for each strategy.

The optical techniques including high speed imaging and two-colour techniques required extended engine running time thus these techniques have been performed for selected strategies in order to minimise the engine wear and rebuilds with the associated labour and parts costs.

6.2.4 Data Processing and Analysis

Table 6.4 summarises the calculated and measured data for injection and combustion characteristics. Injection duration for each individual injection strategy was determined based on the injection rate profiles obtained through Zeuch's method, described in detail in Chapter 5. IMEP values and SOC timings were calculated from the in-cylinder pressure and heat release rate data respectively. Ignition delay was determined from the heat release rate data as the time between the start of the first injection and the onset of combustion, described in Section 3.6.2.6.

The soot and exhaust emissions were measured for all the strategies. The soot concentration was measured in terms of FSN, while the NOx and uHC emissions were measured in Parts per Million (ppm). The results for each injection strategy with total fuel demand of 10 mm^3 and 20 mm^3 are discussed and compared. Furthermore, the soot concentration for better performing strategies were further investigated by the two-colour technique in order to identify the effect of injection timing and quantity on the formation and oxidation of soot particles.

Table 6.3 Test Plan

Test Number		Cylinder Pressure	High Speed Imaging	Soot & Emissions	2-colour
A1	AA1	√	-	√	-
A2	AA2	√	-	√	-
A3	AA3	√	-	√	-
A4	AA4	√	√	√	-
B1	BB1	√	-	√	-
B2	BB2	√	√	√	-
B3	BB3	√	-	√	-
B4	BB4	√	-	√	-
C1	CC1	√	-	√	-
C2	CC2	√	-	√	-
C3	CC3	√	-	√	-
C4	CC4	√	-	√	-
D1	DD1	√	-	√	-
D2	DD2	√	√	√	-
D3	DD3	√	-	√	-
D4	DD4	√	-	√	-
E1	EE1	√	-	√	-
E2	EE2	√	-	√	-
E3	EE3	√	-	√	-
E4	EE4	√	-	√	-
F1	FF1	√	-	√	-
F2	FF2	√	√	√	√
F3	FF3	√	-	√	-
F4	FF4	√	-	√	-
G1	-	√	√	√	√
G2	-	√	-	√	-
G3	-	√	-	√	-
H1	HH1	√	-	√	-
H2	HH2	√	-	√	-
H3	HH3	√	-	√	-
H4	HH4	√	-	√	-

Table 6.4 Injection and Combustion Characteristics

Test Number		Injection Pressure (bar)	Total Injection Duration (^{o} CA)		IMEP (bar)		Start of Combustion (^{o} CA ATDC)		Ignition Delay (^{o} CA)	
A1	**AA1**	1200	3.8	5.4	1.20	3.06	-6.8	-6.6	8.2	8.4
A2	**AA2**	1200	3.8	5.4	1.31	3.17	-2.8	-2.6	7.2	7.4
A3	**AA3**	1200	3.8	5.4	1.41	3.46	1.8	2.6	6.8	7.6
A4	**AA4**	1200	3.8	5.4	2.27	4.43	9.4	12.6	9.4	12.6
B1	**BB1**	1200	5.9	7.6	0.86	2.65	-15.2	-11.2	4.8	8.8
B2	**BB2**	1200	5.9	7.6	2.60	4.24	-9.4	-7.4	5.6	7.6
B3	**BB3**	1200	5.9	7.6	0.79	1.98	-4.6	-3.8	5.4	6.2
B4	**BB4**	1200	5.9	7.6	2.82	5.43	3.4	3.2	8.4	8.2
C1	**CC1**	1200	5.9	7.6	0.53	1.74	-16.4	-6.8	3.6	13.2
C2	**CC2**	1200	5.9	7.6	0.67	1.84	-12.8	-3.4	2.2	11.6
C3	**CC3**	1200	5.9	7.6	0.79	1.98	-6.6	-4.2	3.4	5.8
C4	**CC4**	1200	5.9	7.6	0.76	2.12	1.4	1.4	6.4	6.2
D1	**DD1**	1200	5.9	7.6	0.96	3.56	-16.2	-16.4	3.8	3.6
D2	**DD2**	1200	5.9	7.6	3.17	4.28	-7.6	-7.8	7.4	7.2
D3	**DD3**	1200	5.9	7.6	0.79	2.86	-8.2	-5.4	1.8	4.6
D4	**DD4**	1200	5.9	7.6	2.26	5.42	-4.0	3.6	1.0	8.6
E1	**EE1**	1200	5.9	7.6	0.64	2.51	-15.2	-16.2	4.8	3.8
E2	**EE2**	1200	5.9	7.6	0.74	2.73	-11.6	-12.4	3.4	2.6
E3	**EE3**	1200	5.9	7.6	0.79	2.86	-7.6	-4.6	2.4	5.4
E4	**EE4**	1200	5.9	7.6	0.82	2.98	-4.2	0.6	0.8	5.6
F1	**FF1**	1200	5.9	7.6	1.01	1.54	-12.2	-9.8	7.8	10.2
F2	**FF2**	1200	5.9	7.6	2.33	3.71	-7.8	-6.8	7.2	8.2
F3	**FF3**	1200	5.9	7.6	0.84	2.62	-5.6	-3.4	4.4	6.6
F4	**FF4**	1200	5.9	7.6	3.06	5.74	2.2	3.8	7.7	8.8
G1	**-**	1200	5.9	-	2.61	-	-3.6	-	6.4	-
G2	**-**	1200	5.9	-	1.24	-	-3.6	-	6.4	-
G3	**-**	1200	5.9	-	1.68	-	-3.6	-	6.4	-
H1	**HH1**	1200	5.9	7.6	0.80	2.75	-12.6	-10.8	7.4	9.2
H2	**HH2**	1200	5.9	7.6	0.78	2.76	-8.2	-7.4	6.8	7.6
H3	**HH3**	1200	5.9	7.6	0.84	2.62	-4.2	-3.2	5.8	6.8
H4	**HH4**	1200	5.9	7.6	0.85	3.40	1.4	2.8	6.4	7.8

6.3 Single Injection Strategy Results

The effect of injection timing and quantity on the combustion characteristics and emissions are reported in this section based on the in-cylinder pressure, heat release rate, high speed videos, soot concentration and exhaust emissions for single injection strategies with total fuel demand of 10 mm^3 and 20 mm^3 corresponding to strategy A and AA respectively.

6.3.1 Strategy A (Low load, single fuel injection)

6.3.1.1 In-Cylinder Pressure and Heat Release Rate Analysis

The in-cylinder pressure data for strategies A1, A2, A3 and A4 averaged over 20 consecutive cycles are shown in Figure 6.2. The in-cylinder pressure trace for A1 strategy, SOI at -15^o CA BTDC, followed the line of motoring pressure until -7.8^o CA ATDC. It gradually increased until -2.4^o CA ATDC where it rapidly increased and reached its peak value of 38.9 bar at 6.4^o CA ATDC and steadily decreased from this point during the expansion stroke. This strategy resulted an IMEP value of 1.2 bar.

The in-cylinder pressure trace for A2 strategy, SOI at -10^o CA ATDC, followed the line of motoring pressure until -3.2^o CA ATDC. It progressively increased until -1.4^o CA ATDC where it experienced a rapid pressure rise and reached its peak value of 38.3 bar at 8.8^o CA ATDC, 2.4^o CA after A1 strategy. The peak in-cylinder pressure value was almost identical to A1 strategy since the in-cylinder conditions during the premixed and combustion phases were nearly the same even though the combustion process was initiated later as shown in Table 6.4. The in-cylinder pressure steadily decreased from this point during the expansion stroke, through it remained higher compared to A1 strategy. The IMEP value was 1.31 bar.

The fuel injection timing was further retarded for A3 strategy, -5^o CA ATDC, which delayed the onset of the in-cylinder pressure rise compared to the previous strategies. The in-cylinder pressure followed the trend of motoring pressure until 5.6^o CA ATDC, 13.4^o CA after A1 strategy, since the in-cylinder conditions were almost identical to those of motoring up to this point. The first increase in in-cylinder pressure took place at 5.6^o CA ATDC due to late initiation of the combustion process. The in-cylinder

pressure reached its maximum value of 34.2 bar at 13.2^{o} CA ATDC, 6.8^{o} CA after A1 strategy. The peak in-cylinder pressure was lower compared to the previous strategies. This was mainly attributed to late initiation of the combustion process in the expansion stroke where the piston was descending after TDC due to retarded fuel injection timing used for this strategy. The in-cylinder pressure gradually decreased during the expansion stroke but remained higher than A1 and A2 strategies which led to an IMEP value of 1.41 bar.

The fuel injection event was further retarded for A4 strategy in comparison to the other strategies. The in-cylinder pressure followed the trend of motoring pressure until 13.2^{o} CA ATDC since the thermodynamic conditions under this strategy were almost identical to those of motoring up to this point. The in-cylinder pressure gradually increased until 19.2^{o} CA ATDC where the rate of change in pressure rapidly increased. The in-cylinder pressure reached its maximum value of 24 bar at 23.6^{o} CA ATDC. The peak in-cylinder pressure was considerably lower compared to the previous strategies; this was mainly due to late initiation of the combustion process during the expansion stroke as previously stated for A3 strategy. The in-cylinder pressure progressively decreased and remained higher compared to A1, A2 and A3 strategies. This strategy resulted an IMEP value of 2.27 bar.

The heat release rate for strategies A1, A2, A3 and A4 are presented in Figure 6.3. The heat release rate for A1 strategy exhibited a sudden decrease at -10.6^{o} CA ATDC due to charge cooling shortly after the onset of the fuel injection and also heat transfer effects during the compression stroke which lasted until -6.8^{o} CA ATDC. After this point, the rate of heat release rapidly increased, reaching its peak value at 2.2^{o} CA ATDC, due to premixed combustion, where the premixed fuel and air burned rapidly resulting in high temperature combustion. This phase of combustion lasted until 10.6^{o} CA ATDC. Subsequently, the second phase of combustion due to mixing controlled or diffusion combustion took place which was controlled by the rate of fuel and air mixing. The heat release rate profile experienced a second peak at 13.2^{o} CA ATDC which was considerably lower compared to the peak experienced during the premixed combustion and gradually decreased from this point onwards during the expansion stroke.

The heat release rate for A2 and A3 strategies followed a similar trend to that of A1 strategy. In the same manner, the rate of heat release decreased at -6.4^{o} CA ATDC and -0.8^{o} CA ATDC due to charge cooling effects, 3.6^{o} CA and 4.2^{o} CA after the start of the injection respectively. This reduction in the heat release lasted until -2.8^{o} CA ATDC and 1.8^{o} CA ATDC respectively. Subsequently, the heat release rate rapidly increased, reaching its peak value at 5.4^{o} CA ATDC and 10.6^{o} CA ATDC respectively, due to premixed combustion, which was higher in comparison to A1 strategy. This was mainly attributed to improved fuel evaporation and mixing effects given that fuel injection took place closer to TDC where the in-cylinder temperature was higher. This phase of combustion lasted until 12.2^{o} CA ATDC and 18.6^{o} CA ATDC respectively. In the case of A2 strategy, the second phase of combustion through mixing controlled started at 12.2^{o} CA ATDC, 1.6^{o} CA after A1 strategy. The maximum heat release rate through this phase of combustion occurred at 15.8^{o} CA ATDC and gradually decreased afterwards. The second phase of combustion for A3 strategy started at 18.4^{o} CA ATDC, 7.8^{o} CA after A1 strategy, with its peak at 20.8^{o} CA ATDC and gradually decreased from this point onwards during the expansion stroke. The majority of A2 and the entire A3 combustion processes took place during the expansion stroke due to the retarded injection timing; this was further confirmed by the lower in-cylinder peak pressures shown in Figure 6.2. Moreover, the diffusion combustion was weaker for A2 and A3 strategies compared to A1 strategy duel to the limited time available for the combustion process to complete.

The heat release rate for A4 strategy experienced a sudden decrease at 4.2^{o} CA ATDC due to charge cooling effect shortly after the onset of the fuel injection which lasted until -9.4^{o} CA ATDC. After this point, the rate of heat release rapidly increased, reaching its peak value at 21.8^{o} CA ATDC, due to premixed combustion. The maximum heat release rate during the first phase of combustion was the highest for this strategy in comparison to A1, A2 and A3 strategies. This was due to longer ignition delay for this strategy, indicating prolonged premixed phase. Consequently, more fuel and air was mixed which led to greater heat release due to premixed combustion. In this case, the end of premixed combustion and the start of the diffusion combustion were mixed and difficult to distinguish. The heat released during the second phase of combustion was relatively lower in comparison to A1, A2

and A3 strategies since fuel injection timing was further retarded for this strategy, thus limiting the time available for the combustion process to complete.

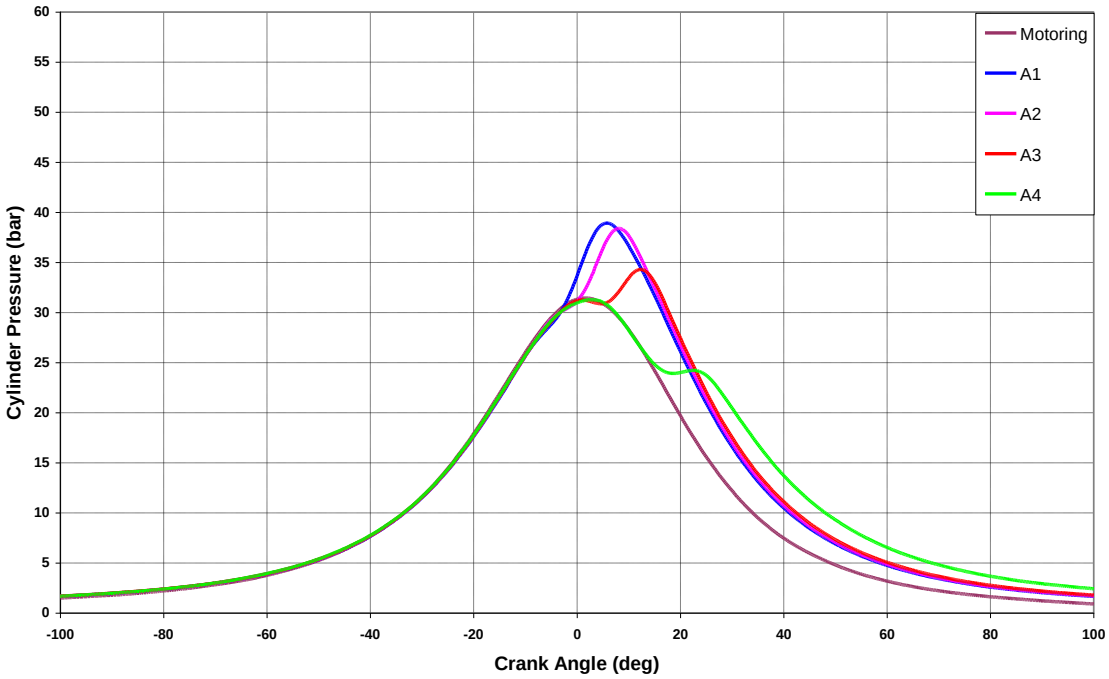

Figure 6.2 In-Cylinder Pressure Data for Strategy A at 1200 bar

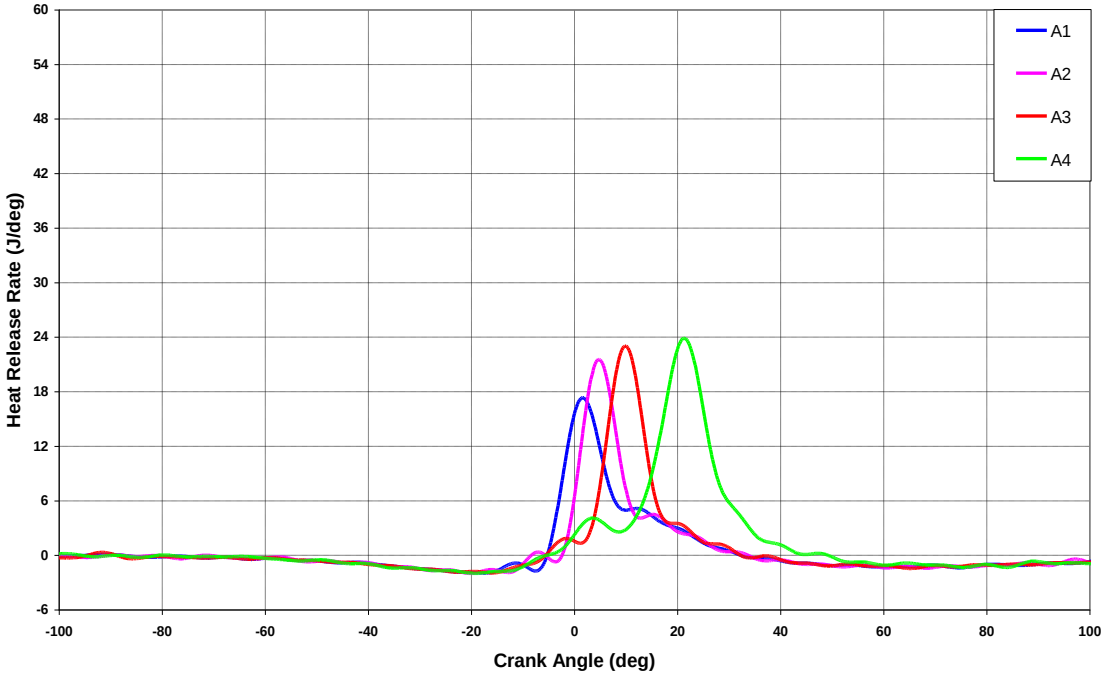

Figure 6.3 Heat Release Rate Traces for Strategy A at 1200 bar

6.3.1.2 Fuel Injection and Combustion Visualisation

Figure 6.4 shows the image sequence obtained for A4 strategy through high speed video imaging technique, described in Section 3.4.1.

The first six frames in Figure 6.4 show the fuel spray development from the start to the end of the fuel injection event where in the last frame fuel sprays were almost fully evaporated. From the images presented at 1.8^{o} CA ATDC and 2.7^{o} CA ATDC, it is evident that the fuel sprays almost reached the piston wall. The asymmetric spray jets seen in the first three frames are typical of VCO type injector nozzles due to uneven pressure distribution between the nozzle holes. The first combustion phase apparent from the heat release rate data at 9.4^{o} CA ATDC, Figure 6.3, resulted in no visible combustion until 19.8^{o} CA ATDC where the first visible combustion was observed. The next frame presented at 21.6^{o} CA ATDC shows more visible flame which corresponded to the peak heat release rate due to premixed combustion. The frame at 29.7^{o} CA ATDC shows the point at which both premixed and diffusion combustion were present. Minor bright spots are present in the subsequent frames at 33.3^{o} CA ATDC and 37.8^{o} CA ATDC respectively, indicating the presence of some diffusion combustion corresponding to the second phase of combustion, as evident in Figure 6.3. Flame was moved in the clockwise direction due to the swirl motion as the combustion process evolved. The flame luminosity is due to the radiation of soot particles, thus the luminous regions in the high speed images were mainly responsible for the production of soot particles during the combustion process.

6.3.1.3 Soot and Exhaust Emissions

The soot and gaseous exhaust emissions results for strategy A are depicted in Figures 6.5 and 6.6 respectively.

The soot level produced by the engine progressively decreased for all the strategies. This was mainly due to retarded injection timing used for A2, A3 and A4 strategies whereby less time was available during the premixed and combustion phases. This was further validated by heat release rate traces shown in Figure 6.3 where diffusion combustion associated with A2, A3 and A4 strategies were relatively weaker

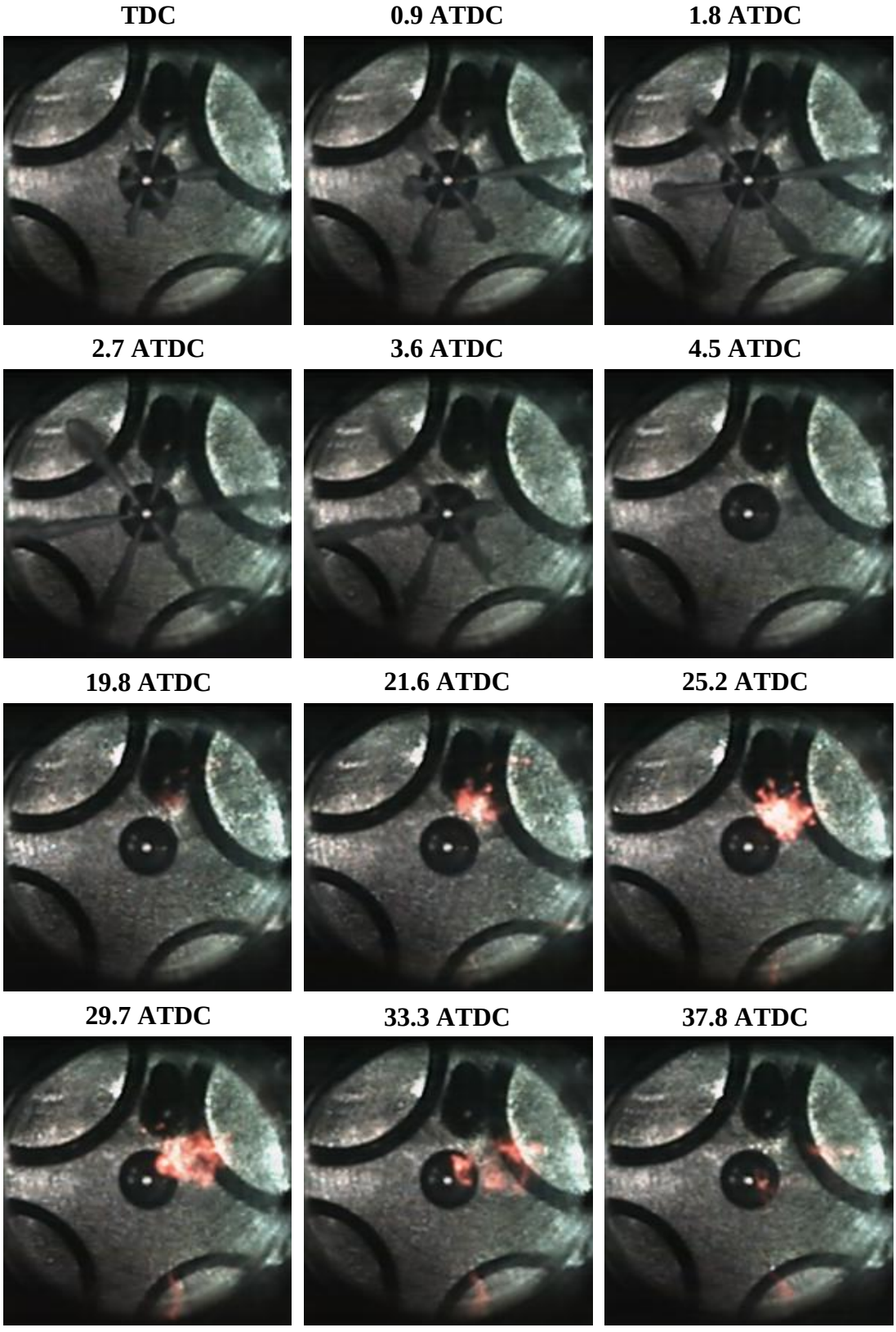

Figure 6.4 Combustion Image Sequence for A4 Strategy at 1200 bar

compared to A1 strategy. In general, soot particles are formed due to fuel oxidation and/or pyrolysis; typically at temperatures above 1300 K. Soot particles are initially formed during the premixed combustion which are small in size and density. The soot particles rapidly grow larger in size and density during the diffusion combustion, thus, weaker diffusion combustion leads to lower soot concentration.

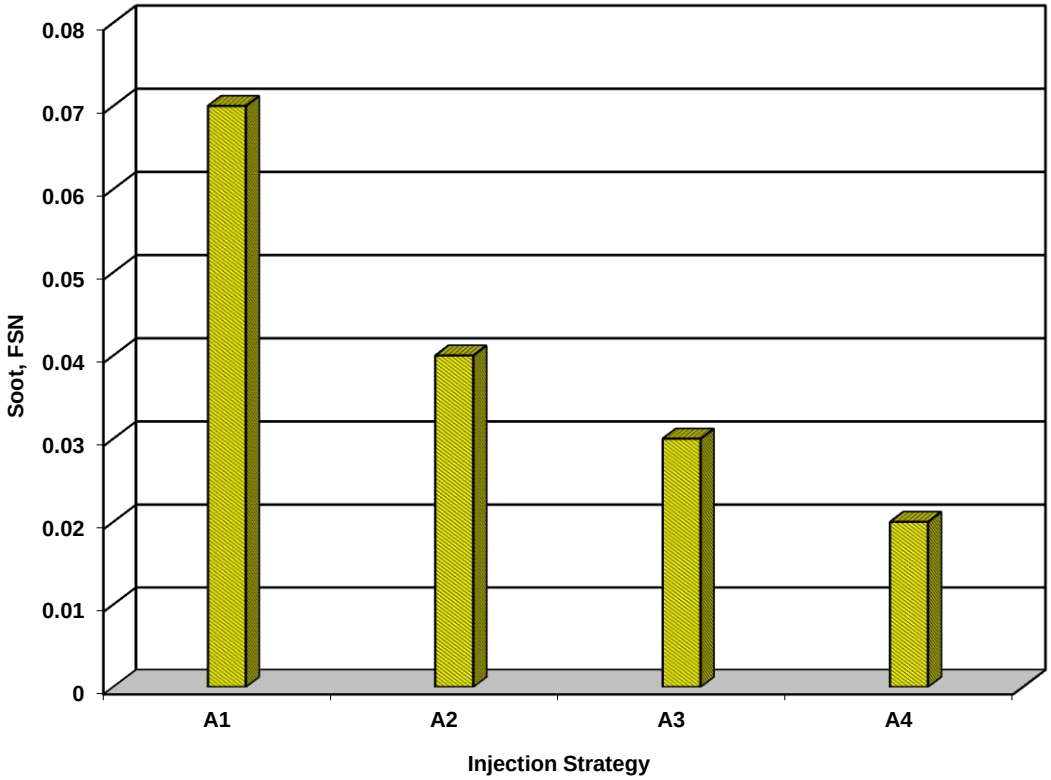

Figure 6.5 Soot Concentration for Strategy A at 1200 bar

NOx production is dependent on the surrounding temperature whereby increase in the in-cylinder temperature leads to higher NOx levels. The NOx emission progressively decreased as shown in Figure 6.6; this was due to lower combustion temperature with retarded fuel injection timing for A2, A3 and A4 strategies.

Poor fuel evaporation and mixing processes promote high levels of uHC emissions. A2 strategy produced less uHC emission in comparison to A1 strategy due to improved fuel evaporation since fuel was injected closer to TDC where the in-cylinder temperature was higher. The A3 strategy produced the same level of uHC emission

since the in-cylinder conditions were similar to those of A2 and there was yet enough time available for the fuel evaporation and mixing processes. On the contrary, A4 strategy resulted in considerably higher uHC emissions even though fuel injection timing occurred at TDC where in-cylinder temperature was relatively higher. This was mainly due to lower combustion temperature and hence lower oxidation rate as the combustion was delayed further into the expansion stroke.

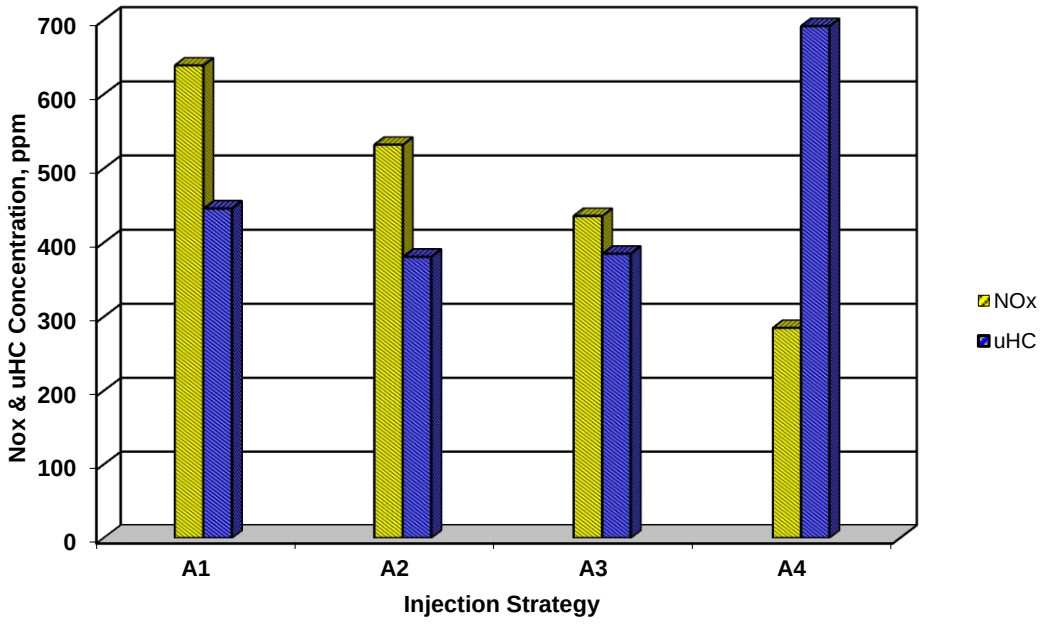

Figure 6.6 NOx and uHC Concentration for Strategy A at 1200 bar

6.3.2 Strategy AA (High load, single fuel injection)

6.3.2.1 In-Cylinder Pressure and Heat Release Rate Analysis

The in-cylinder pressure data averaged over 20 consecutive cycles for strategies AA1, AA2, AA3 and AA4 of 20 mm^3 single fuel injection are shown in Figure 6.7. The in-cylinder pressure traces followed the same pattern as those of strategy A with 10 mm^3 single fuel injection.

The in-cylinder pressure trace for AA1 strategy with SOI at -15^o CA BTDC followed the line of motoring pressure until -10.8^o CA ATDC. It gradually increased until -4.4^o CA ATDC where it rapidly increased and reached its peak value of 52.8 bar at 5.6^o

CA ATDC and steadily decreased from this point during the expansion stroke. This strategy resulted an IMEP value of 3.06 bar.

The in-cylinder pressure trace for AA2 strategy followed the line of motoring pressure until -7.2^{o} CA ATDC. It progressively increased until -1.2^{o} CA ATDC where the in-cylinder pressure rose rapidly and reached its peak value of 49.5 bar at 8.8^{o} CA ATDC, 3.2^{o} CA after AA1 strategy. The peak in-cylinder pressure value was almost identical to AA1 strategy since the in-cylinder conditions during the premixed and combustion phases were nearly the same even though the combustion process was initiated later as shown in Table 6.4. The in-cylinder pressure steadily decreased afterwards during the expansion stroke, through remained higher compared to AA1 strategy. The fuel was injected at -10^{o} CA ATDC which resulted an IMEP value of 3.17 bar.

In a similar manner to that of strategy A, the fuel injection timing was retarded for AA3 strategy, -5^{o} CA ATDC, which delayed the onset of the in-cylinder pressure rise compared to the previous strategies. The in-cylinder pressure followed the trend of motoring pressure until -3.2^{o} CA ATDC, 7.6^{o} CA after AA1 strategy. The first increase in in-cylinder pressure occurred at 4.8^{o} CA ATDC due to late initiation of the combustion process. The in-cylinder pressure reached its maximum value of 44.5 bar at 13.6^{o} CA ATDC, 8.0^{o} CA after AA1 strategy. The peak in-cylinder pressure was lower in comparison to the previous strategies. This was mainly attributed to late initiation of the combustion process in the expansion stroke where the piston was descending after TDC due to retarded fuel injection timing used. The in-cylinder pressure gradually decreased during the expansion stroke but remained higher than AA1 and AA2 strategies which led to an IMEP value of 3.46 bar.

The fuel injection event was further retarded for AA4 strategy in comparison to the other strategies. The in-cylinder pressure almost followed the line of motoring pressure until 17.6^{o} CA ATDC since the thermodynamic conditions under this strategy were almost identical to those of motoring up to this point. The in-cylinder pressure rapidly increased at 17.8^{o} CA ATDC and reached its maximum value of 24 bar at 26.6^{o} CA ATDC, 21^{o} CA after AA1 strategy. The peak in-cylinder pressure was

considerably lower compared to the previous strategies; this was due to late initiation of the combustion process during the expansion stroke as previously explained for AA3 strategy. The in-cylinder pressure progressively decreased during the expansion stroke, yet remained higher compared to AA1, AA2 and AA3 strategies. This strategy resulted an IMEP value of 4.43 bar.

The heat release rate for strategies AA1, AA2, AA3 and AA4 are presented in Figure 6.8. The heat transfer rates for strategy AA of 20 mm^3 fuel demand followed the same trend as those of strategy A of 10 mm^3 fuel demand. The heat release rate for AA1 strategy exhibited a sudden decrease at -10.6^o CA ATDC due to charge cooling shortly after the onset of the fuel injection and the heat transfer effects during the compression stroke which lasted until -6.6^o CA ATDC. After this point, the rate of heat release rapidly increased and reached its peak value at 0.6^o CA ATDC, due to premixed combustion. This phase of combustion lasted until 7.8^o CA ATDC at which point diffusion combustion started. The heat release rate profile experienced a second peak, due to diffusion combustion, at 12.6^o CA ATDC which was considerably lower compared to the peak experienced during the premixed combustion and gradually decreased from this point onwards.

The heat release rates for AA2 and AA3 strategies followed a similar trend to that of AA1 strategy. In the same manner, the rate of heat release decreased at -6.2^o CA ATDC and -0.6^o CA ATDC due to charge cooling effects, 3.8^o CA and 4.4^o CA after the start of injection for AA2 and AA3 strategies respectively. This reduction in the heat release lasted until -2.6^o CA ATDC and 2.6^o CA ATDC respectively. Subsequently, the rate of heat release rapidly increased and reached its peak value at 4.8^o CA ATDC and 10.2^o CA ATDC, 4.2^o CA and 9.6^o CA after AA1 strategy respectively, due to premixed combustion. The rate of heat release during this phase of combustion increased as the fuel injection timing was further retarded. This was mainly due to improved fuel evaporation and mixing effects given that fuel injection took place closer to TDC where the in-cylinder temperature was higher. This phase of combustion lasted until 11.8^o CA ATDC and 17.4^o CA ATDC respectively. In the case of AA2 strategy, the second phase of combustion started at 11.8^o CA ATDC, 4.0^o CA after AA1 strategy. The maximum heat release rate through this phase of

combustion occurred at 15.8^{o} CA ATDC and gradually decreased afterwards. The second phase of combustion for AA3 strategy started at 17.4^{o} CA ATDC, 9.6^{o} CA after AA1 strategy; with its peak value at 21.6^{o} CA ATDC. After this point, the heat release rate gradually decreased during the expansion stroke. The majority of AA2 and the entire AA3 combustion processes took place during the expansion stroke due to the retarded injection timing used; this was further confirmed by the lower in-cylinder peak pressures shown in Figure 6.7. Moreover, diffusion combustion was weaker for AA2 and AA3 strategies compared to AA1 strategy due to limited time available for the combustion process to complete.

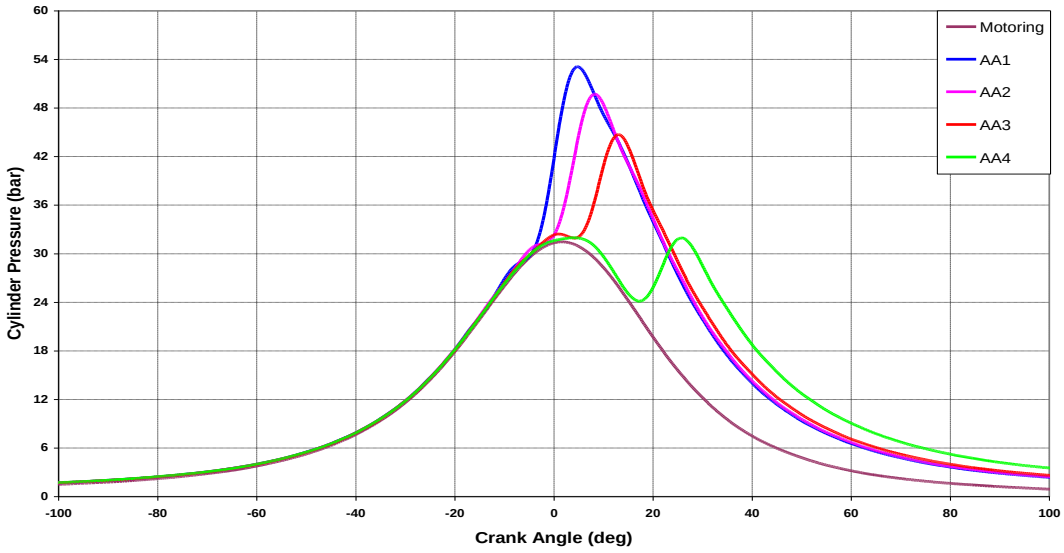

Figure 6.7 In-Cylinder Pressure Data for Strategy AA at 1200 bar

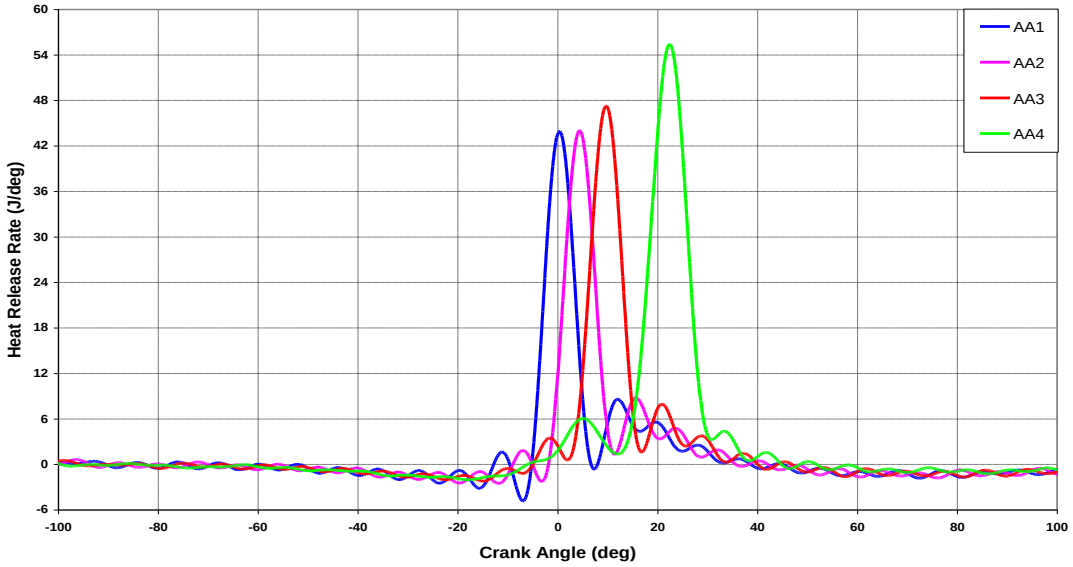

Figure 6.8 Heat Release Rate Traces for Strategy AA at 1200 bar

The heat release rate for AA4 strategy exhibits a sudden decrease at 5.6^{o} CA ATDC due to charge cooling effect shortly after the onset of the fuel injection, 5.6^{o} CA after the start of injection, which lasts until 12.6^{o} CA ATDC. After this point, the rate of heat release rapidly increases, reaching its peak value at 22.8^{o} CA ATDC, 22.2^{o} CA after AA1 strategy, due to premixed combustion. The maximum heat release rate during the first phase of combustion is the highest for this strategy in comparison to AA1, AA2 and AA3 strategies. This is due longer ignition delay for this strategy as shown in Table 6.4, indicating prolonged premixed phase. Consequently, more fuel and air can be mixed which leads to greater heat release due to premixed combustion. The first phase of combustion lasts until 31.4^{o} CA ATDC at which point diffusion combustion starts. The end of premixed combustion and the start of diffusion combustion are discrete in this strategy unlike A4 strategy. The heat release through the second phase of combustion peaks at 34.2^{o} CA ATDC but is relatively lower in comparison to AA1, AA2 and AA3 strategies. This is due to limited time available for the combustion process to complete since fuel injection timing was further retarded for this strategy. The same explanation for the maximum in-cylinder peak pressure as that of A4 strategy holds true, the lowest in-cylinder peak pressure was obtained with AA4 strategy since the combustion process took place late in the expansion stroke.

6.3.2.2 Fuel Injection and Combustion Visualisation

Figure 6.9 shows the image sequence obtained for AA4 strategy through high speed video imaging technique.

The first five frames in Figure 6.9 show the fuel sprays development from the start to the end of the injection where in the last frame fuel sprays were almost fully evaporated. The initial fuel jets were asymmetrically distributed. From the images presented at 3.6^{o} CA ATDC and 5.4^{o} CA ATDC, it is evident that the fuel sprays impinged on the piston wall which resulted in the tip of the sprays spreading outwards. The first combustion phase apparent from the heat release rate data at 12.6^{o} CA ATDC, Figure 6.8, resulted in no visible combustion until 20.7^{o} CA ATDC where the first visible combustion was observed. The next frame presented at 22.8^{o} CA ATDC shows more visible flame which corresponded to the peak heat release

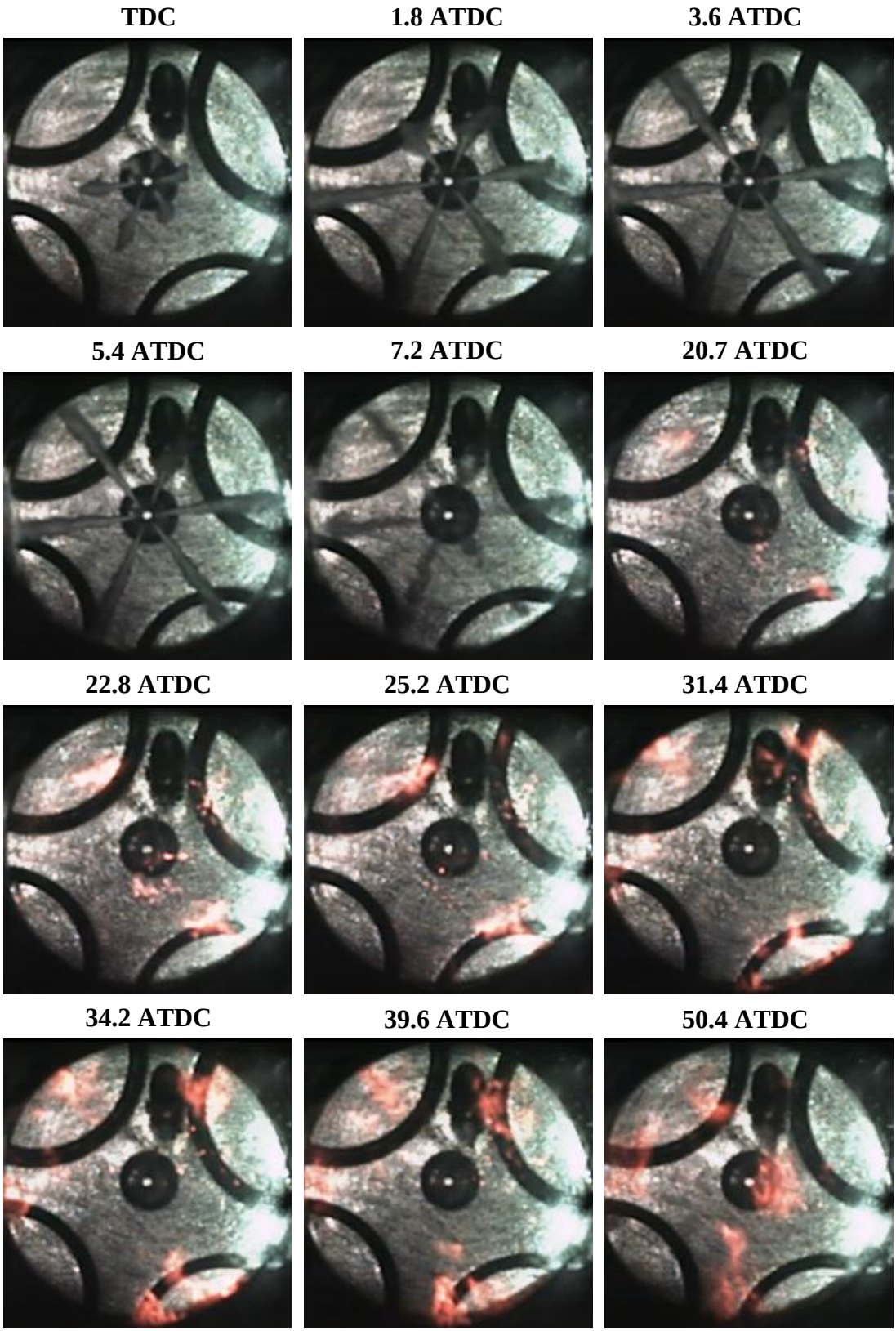

Figure 6.9 Combustion Image Sequence for AA4 Strategy at 1200 bar

rate due to premixed combustion. The frame at 25.2^{o} CA ATDC shows flame propagation during this phase of combustion. In the subsequent frames at 31.4^{o} CA ATDC, 34.2^{o} CA ATDC, 39.6^{o} CA ATDC and 50.4^{o} CA ATDC several combustion sites are present, indicating the presence of some diffusion combustion corresponding to the second phase of combustion as shown by the heat release rate data, Figure 6.8. Flame was moved in the clockwise direction due to the swirl motion as the combustion process evolved.

6.3.2.3 Soot and Exhaust Emissions

The soot and gaseous exhaust emissions results for strategy AA are depicted in Figures 6.10 and 6.11 respectively.

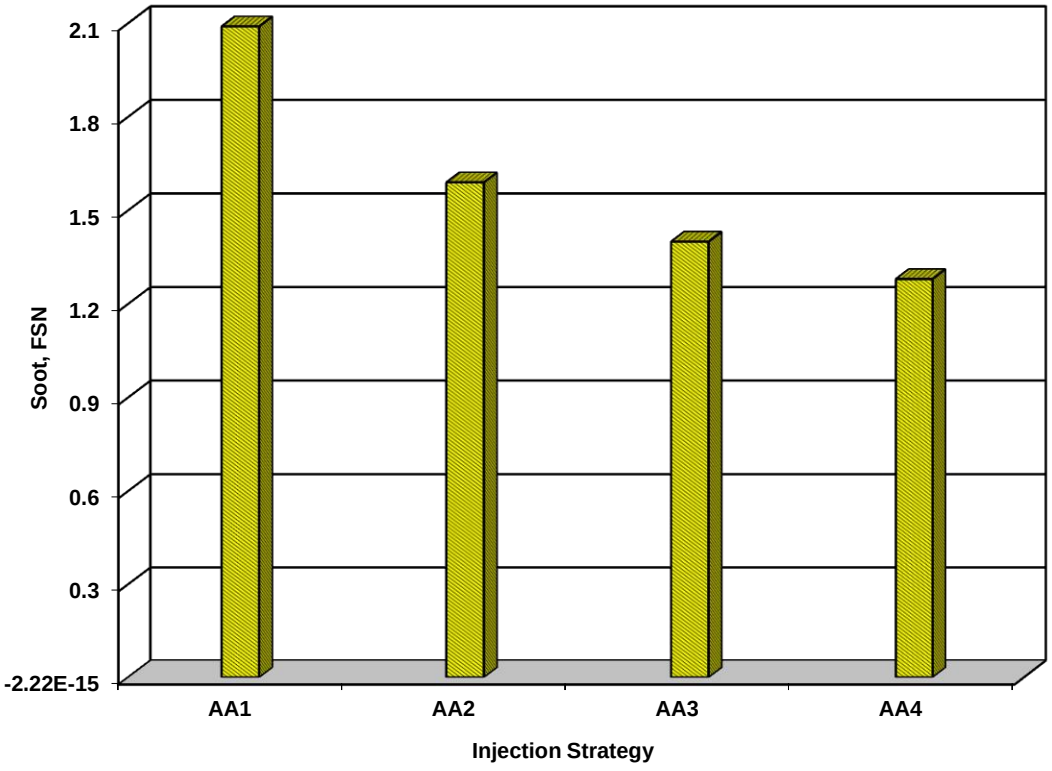

Figure 6.10 Soot Concentration for Strategy AA at 1200 bar

The same trend as that of strategy A exists for strategy AA, the soot level produced by the engine progressively decreased for all the strategies. This was mainly due to retarded injection timing used for AA2, AA3 and AA4 strategies whereby less time

was available during the premixed and combustion phases. This was further validated by heat release rate traces shown in Figure 6.8 where diffusion combustion associated with AA2, AA3 and AA4 strategies were relatively weaker.

As previously stated in Section 6.3.1.3, NOx production is dependent on the surrounding temperature whereby increase in the in-cylinder temperature leads to higher NOx levels. The NOx emission progressively decreased as shown in Figure 6.11. This was mainly due to late initiation of the combustion process due to retarded fuel injection timing which resulted in lower in-cylinder pressures and temperatures.

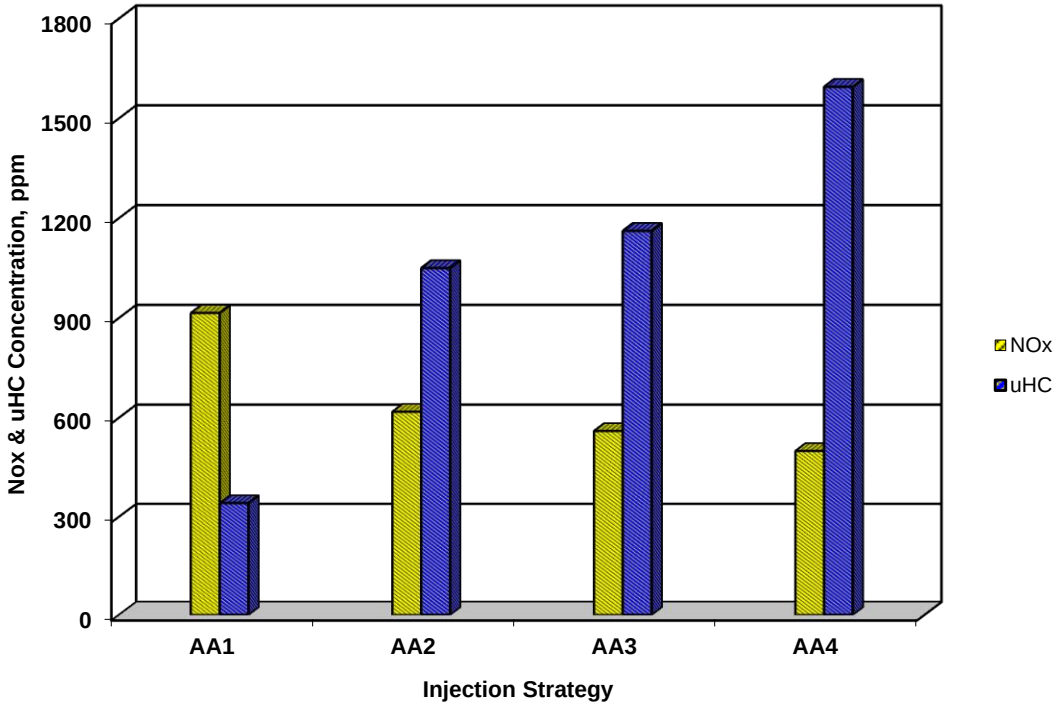

Figure 6.11 NOx and uHC Concentration for Strategy AA at 1200 bar

The uHC emission progressively increased as shown in Figure 6.11 with retarded fuel injection timing for AA2, AA3 and AA4 strategies. This was due to the limited time available for the fuel evaporation and mixing processes during the premixed phase of combustion which resulted in high levels of unburned fuel remaining inside the cylinder upon the completion of the combustion process.

6.4 Results of 50:50 Split Injection Strategy

6.4.1 Strategy B (Low load, 50:50 split injection with fixed 2nd injection at TDC)

This section involves analysis of injection timing with variable dwell angle between injections on the combustion and emissions characteristics through 50:50 split injection strategies with the second injection fixed at TDC. The total fuel demand is 10 mm^3.

6.4.1.1 In-Cylinder Pressure and Heat Release Rate Analysis

The in-cylinder pressure data for strategies B1, B2, B3 and B4 averaged over 20 consecutive cycles are shown in Figure 6.12. The in-cylinder pressure trace for B1 strategy followed the line of motoring pressure until -3.8^o CA ATDC where it progressively increased and reached its peak value of 33.5 bar at 6.6^o CA ATDC. The in-cylinder pressure steadily decreased from this point during the expansion stroke. The fuel injections took places at -20^o CA BTDC and TDC which resulted an IMEP value of 0.86 bar.

The in-cylinder pressure trace for B2 strategy followed the line of motoring pressure until -3.6^o CA ATDC where it progressively increased and reached its peak value of 40.5 bar at 10.8^o CA ATDC, 4.2^o CA after B1 strategy. The peak in-cylinder pressure value was considerably higher in comparison to B1 strategy. This was mainly attributed to the difference in the fuel quantity injected as the dwell angle between the two injections changed as shown in Figure 5.12. Thus, the increase in in-cylinder pressure was not solely due to the fuel injection timing, a phenomenon which was not taken into account in most previous investigations. The in-cylinder pressure steadily decreased after the peak during the expansion stroke, though remained higher compared to B1 strategy. The fuel was injected at -15^o CA ATDC and TDC which led to an IMEP value of 2.6 bar.

The in-cylinder pressure trace for B3 strategy followed the line of motoring pressure until -5.4^o CA ATDC and progressively increased until 1.4^o CA ATDC where it rapidly increased and reached its maximum value of 33.6 bar at 8.8^o CA ATDC, 2.2^o

CA after B1 strategy. This delay was due to retarded injection timing of the first injection whereby the combustion process took place late in the expansion cycle. The peak in-cylinder pressure was considerably lower than B2 strategy since the fuel quantity injected with 10^o CA dwell timing was considerably lower in comparison to B2 strategy where the dwell angle between the injections was 15^o CA as shown in Figure 5.12. The in-cylinder pressure after the peak steadily decreased following almost the same line as B1 strategy. The fuel was injected at -10^o CA ATDC and TDC which resulted an IMEP value of 0.79 bar.

The in-cylinder pressure trace for B4 strategy followed the line of motoring pressure until 5.8^o CA ATDC since the thermodynamic conditions under this strategy were almost identical to those of motoring up to this point. After this point, the in-cylinder pressure sharply increased and reached its maximum value of 38.9 bar at 15.2^o CA ATDC, 8.6^o CA after B1 strategy. The dwell angle between the two injections for this strategy was 5^o CA which was not sufficient for the injector to fully close prior to the onset of the second injection, due to mechanical limitations of the injector utilised in this study. Consequently, the second injection took place while the needle was partially open which resulted in much greater fuel quantity injected than intended as depicted in Figure 5.12. The peak in-cylinder pressure was higher than B1 and B3 strategies due to the greater fuel quantity injected, yet remained lower than B2 strategy since the time available during the premixed and combustion phases was limited for B4 strategy. The in-cylinder pressure after the peak steadily decreased but remained higher than all the other strategies. The fuel was injected at -5^o CA ATDC and TDC which led to an IMEP value of 2.82 bar.

The heat release rate for strategies B1, B2, B3 and B4 are presented in Figure 6.13. The heat release rate for B1 strategy exhibited a sudden decrease at -18.8^o CA ATDC due to charge cooling shortly after the onset of the first fuel injection and the heat transfer effects during the compression stroke which lasted until -15.2^o CA ATDC. After this point, the rate of heat release progressively increased until 0.8^o CA ATDC where it rapidly increased following the start of the second injection at TDC. The maximum heat release rate occurred at 9.4^o CA ATDC, due to premixed combustion. This phase of combustion lasted until the end of the combustion process with no

evidence of diffusion combustion taking place for this strategy based on the heat release rate trace presented in Figure 6.13. The heat release gradually decreased after the peak during the expansion stroke.

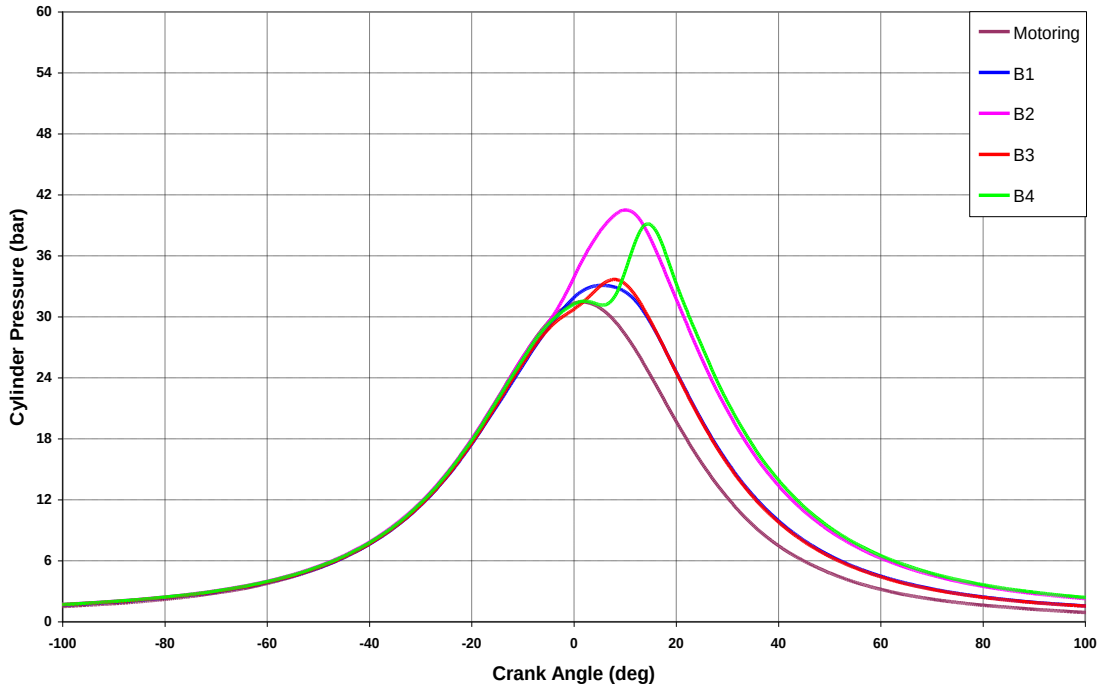

Figure 6.12 In-Cylinder Pressure Data for Strategy B at 1200 bar

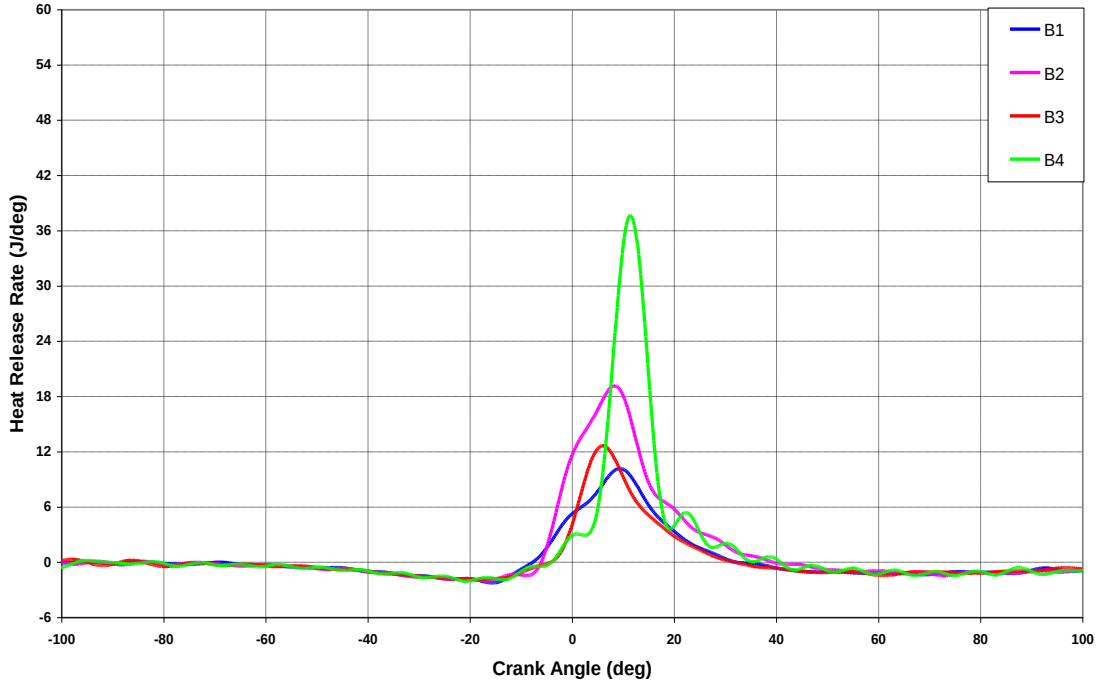

Figure 6.13 Heat Release Rate Traces for Strategy B at 1200 bar

The heat release rate for B2 strategy experienced a sudden decrease at -11.2^{o} CA ATDC due to charge cooling shortly after the onset of the first fuel injection and the heat transfer effects during the compression stroke which lasted until -9.4^{o} CA ATDC. After this point, the rate of heat release sharply increased until 1.8^{o} CA ATDC due to the first fuel injection. At this point the heat release rate rapidly increased for the second time following the onset of the second fuel injection at TDC. The maximum heat release rate due to premixed combustion occurred at 7.6^{o} CA ATDC, 1.8^{o} CA before B1 strategy, which was higher than B1 strategy. This was mainly attributed to improved fuel evaporation and mixing processes given that the first fuel injection took place closer to TDC where the in-cylinder temperature was higher. In addition, the ignition delay was longer in comparison to B1 strategy due to the greater fuel quantity injected for this strategy. Therefore, more fuel and air was mixed during the premixed phase of combustion which resulted in greater heat release rate during the first phase of combustion. In this case the end of premixed combustion and the start of diffusion combustion were mixed and difficult to distinguish.

The heat release rate for B3 strategy rapidly increased after the start of the first injection and reached its peak value at 6.6^{o} CA ATDC, 2.8^{o} CA before B1 strategy, due to premixed combustion. The peak heat release rate was lower than B2 strategy since the time available for the combustion process was more limited due to further retarded injection timing of the first injection. In addition, less fuel was injected due to the dwell angle used as shown in Figure 5.12. After this point, the heat release rate steadily decreased during the expansion stroke with no noticeable signs of diffusion combustion taking place based on the heat release rate data shown in Figure 6.13.

As previously stated in Chapter 5, 5^{o} CA dwell timing between the two injections was not sufficient for the injector to fully close prior to the onset of the second injection, thus the two injections interfered with each other and replicated a single injection strategy with total fuel injected quantity considerably higher than intended. The heat release rate for B4 strategy experienced a sudden decrease at 1.2^{o} CA ATDC due to charge cooling shortly after the onset of the first and second injections which lasted until 3.4^{o} CA ATDC. After this point, the rate of heat release rapidly increased and

reached its maximum value at 11.8^{o} CA ATDC, 2.4^{o} CA after B1 strategy, due to premixed combustion. This strategy produced the maximum heat release rate due to premixed combustion in comparison to the other strategies as shown in Figure 6.13. This was due to the greater fuel quantity injected as a consequence of the dwell angle used as shown in Figure 5.12 as well as longer ignition delay which prolonged the premixed phase, Table 6.4. Consequently, more fuel and air was mixed which resulted in greater heat release during the first phase of combustion. This phase of combustion lasted until 19.6^{o} CA ATDC where the second phase of combustion started. The maximum heat release rate due to diffusion combustion occurred at 22.8^{o} CA ATDC and gradually deceased afterwards during the expansion stroke.

6.4.1.2 Fuel Injection and Combustion Visualisation

Figure 6.14 shows the image sequence obtained for B2 strategy through high speed video imaging technique.

Although B4 strategy produced the maximum heat release rate, high speed imaging was carried out for B2 strategy since the actual fuel quantity injected for B4 strategy was much greater than 10 mm^{3}. The first three frames in Figure 6.14 show the fuel spray development from the start to the end of the first injection where in the last frame fuel sprays are almost fully evaporated. The subsequent five frames show the image sequence from the start to the end of the second injection. Although the same injection duration was used for both injections, the second injection lasted longer which indicated more fuel was injected during the second injection. This finding was in good agreement with the results obtained through Zeuch's method as shown in Figure 5.12. From the image sequence presented during the first and second injections, it is evident that the fuel sprays did not reach the piston wall due to shorter injection duration used with 50:50 split injection strategies since the same total fuel quantity as that of strategy A was injected but in two stages.

The first combustion phase apparent from the heat release rate data at -9.4^{o} CA ATDC, Figure 6.13, resulted in no visible combustion. The first visible combustion was detected at 1.8^{o} CA ATDC. Flame propagation started at the tip of the fuel sprays where fuel vapour was highly concentrated and spread along the periphery of the

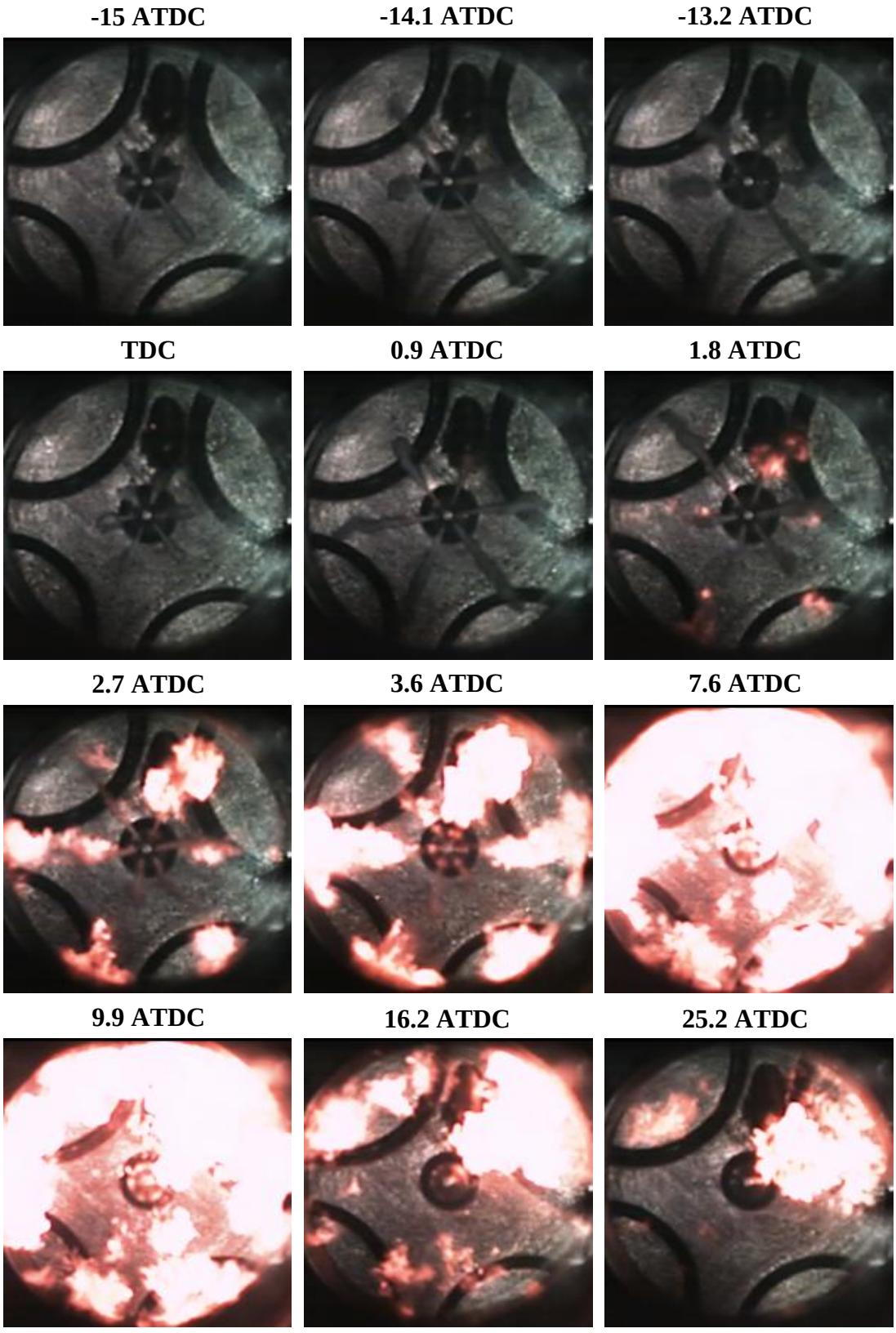

Figure 6.14 Combustion Image Sequence for B2 Strategy at 1200 bar

fuel sprays where fuel evaporation rate was considerably higher than the core region where liquid fuel droplets were the dominating constituents as shown in frames seven and eight at 2.7^{o} CA ATDC and 3.6^{o} CA ATDC respectively. In these frames flame spread to the outer regions of the sprays tip due to the fuel sprays impingement on the piston wall, creating a mushroom like structure. In the next frame at 7.6^{o} CA ATDC, where the maximum heat release rate occurred during the premixed combustion, intense flame propagation took place which spread to the periphery of the piston bowl where the majority of premixed fuel and air was concentrated. The same trend exists at 9.9^{o} CA ATDC where fuel was burning in the same manner during the first phase of combustion. Although the end of premixed combustion and the start of the diffusion combustion for this strategy were mixed as shown in Figure 6.13, several combustion sites are present indicating the presence of some diffusion combustion corresponding to the second phase of combustion at 16.2^{o} CA ATDC and 25.2^{o} CA ATDC. Flame was moved in the clockwise direction due to the swirl motion as the combustion process evolved.

6.4.1.3 Soot and Exhaust Emissions

The soot and gaseous exhaust emissions results for strategy B are depicted in Figures 6.15 and 6.16 respectively.

The soot level produced by B2 strategy was considerably higher in comparison to B1 strategy; this was mainly due to the greater fuel quantity injected for this strategy as a result of the interaction of the two injection events. The soot concentration for B3 strategy was similar to that of B1 strategy since similar fuel quantities were injected as shown in Figure 5.12. B4 strategy produced high levels of soot since dwell timing between the two injections was not sufficient for the injector to fully close prior to the onset of the second injection, thus replicating a single injection strategy with the total fuel injection quantity considerably higher than intended. However, the soot produced by B4 strategy remained lower than B3. As shown by images in Figure 6.14, the start of combustion coincided with the second injection. Consequently, fuel was injected into burning regions before it had time to mix with air. Therefore, more soot was produced due to fuel pyrolysis as indicated by the brighter regions in the images.

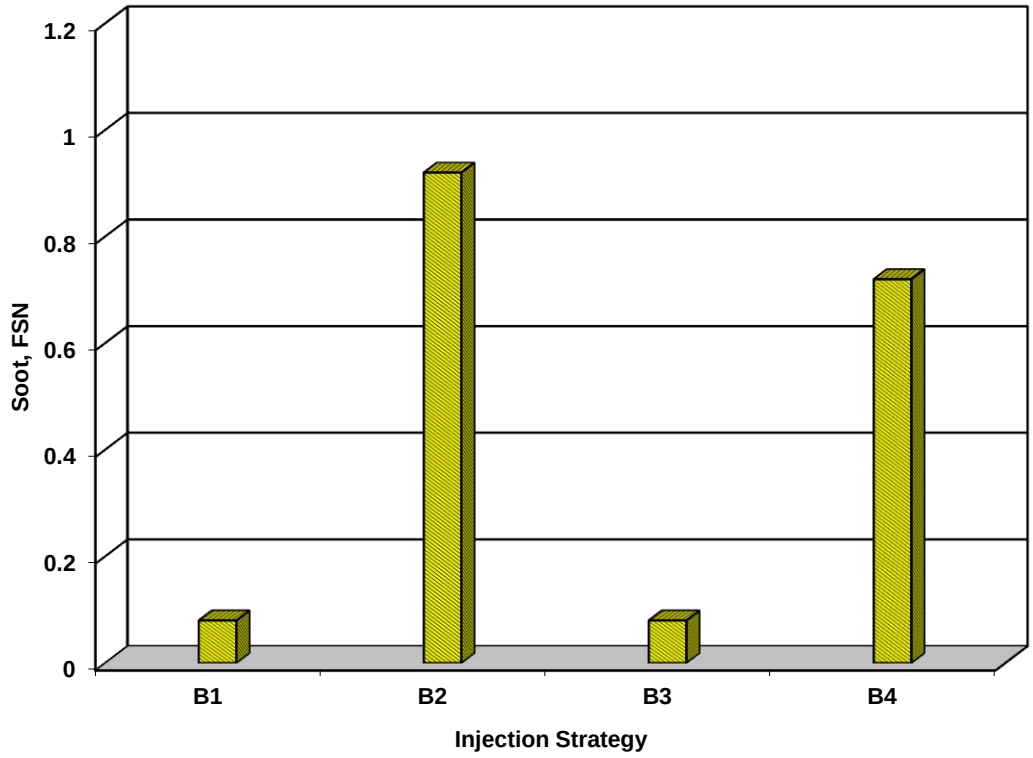

Figure 6.15 Soot Concentration for Strategy B at 1200 bar

The NOx emission produced by B2 strategy was considerably higher than B1 strategy since greater fuel quantity was injected for B2 strategy due to the injection timing used as shown in Figure 5.12 which resulted in higher temperature combustion. In contrast, B3 strategy produced lower NOx emission compared to B2 strategy since the injected fuel quantity was less for B3 strategy as shown in Figure 5.12. Nevertheless, NOx emission produced by B3 was higher than B1 since the first injection was retarded. The NOx emission produced by B4 strategy was substantially higher than the other strategies due to greater total fuel injection quantity than intended, Figure 5.12, as well as longer ignition delay which resulted in prolonged premixed phase as shown in Table 6.4.

The uHC emission for B2 strategy was lower compared to B1 strategy, this was due to improved fuel evaporation and mixing processes since the first injection took place closer to TDC. In addition, the ignition delay for this strategy was longer in comparison to B1 strategy thus greater fuel and air mixing took place during the premixed phase of combustion which in turn led to lower uHC emission. B3 strategy

produced higher uHC emission in comparison to B2 strategy; this was mainly due to the limited time available during the premixed and combustion phases as the injection timing of the first injection was further retarded. The uHC emission produced by B4 strategy was further increased due to the greater fuel quantity injected as a result of the dwell angle used as shown in Figure 5.12.

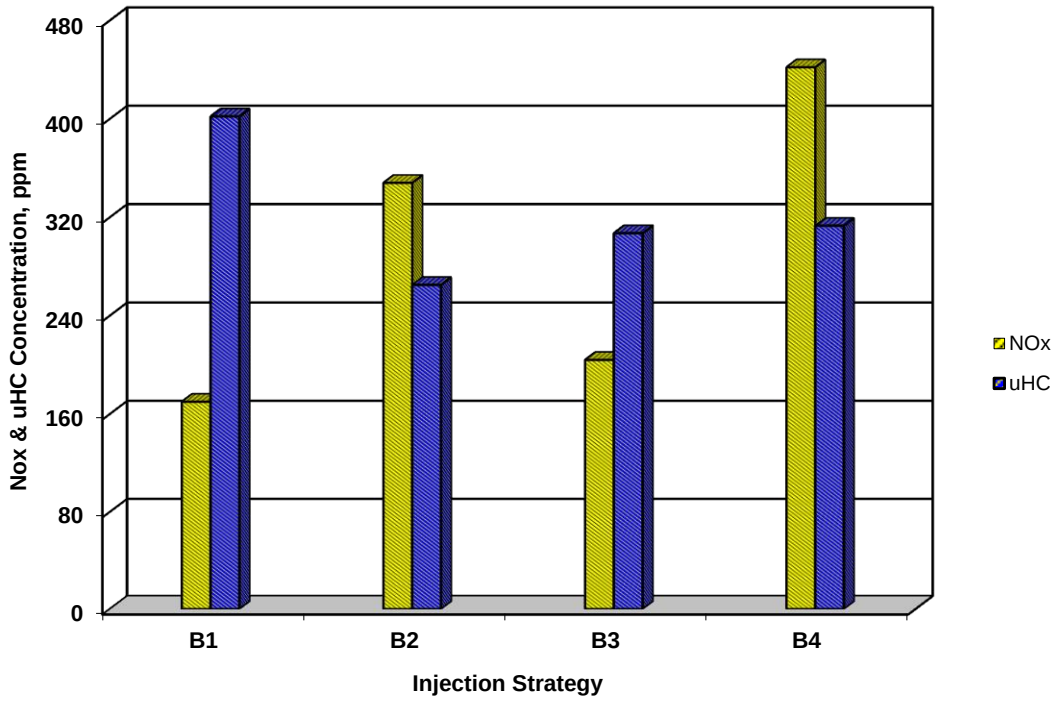

Figure 6.16 NOx and uHC Concentration for Strategy B at 1200 bar

6.4.2 Strategy BB (High load, 50:50 split injection with fixed 2nd injection at TDC)

This strategy is similar to Strategy B but with 20 mm^3 total fuel demand. It involves analysis of injection timing with variable dwell angle between injections on the combustion and emissions characteristics of a four-stroke HSDI diesel engine through 50:50 split injection strategies with the second injection fixed at TDC.

6.4.2.1 In-Cylinder Pressure and Heat Release Rate Analysis

The in-cylinder pressure data for strategies BB1, BB2, BB3 and BB4 averaged over

20 consecutive cycles are shown in Figure 6.17. The in-cylinder pressure trace for BB1 strategy followed the line of motoring pressure until -7.4^{o} CA ATDC where it progressively increased and reached its peak value of 41.6 bar at 2.2^{o} CA ATDC, due to the first injection. The in-cylinder pressure experienced its second peak value of 40.5 bar at 8.4 2^{o} CA ATDC, due to the second injection. The in-cylinder pressure steadily decreased from this point during the expansion stroke. The fuel injections took places at -20^{o} CA ATDC and TDC which resulted an IMEP value of 2.65 bar.

The in-cylinder pressure trace for BB2 strategy followed the line of motoring pressure until -4.2^{o} CA ATDC where it rapidly increased and reached its peak value of 45.9 bar at 9.4^{o} CA ATDC, 7.2^{o} CA after BB1 strategy. The peak in-cylinder pressure value was considerably higher in comparison to BB1 strategy. This was mainly due to the difference in the fuel quantity injected as the dwell angle between the two injections changed as shown in Figure 5.14. The in-cylinder pressure steadily decreased after the peak during the expansion stroke, though remained higher than BB1 strategy. The fuel was injected at -15^{o} CA ATDC and TDC which led to an IMEP value of 4.24 bar.

The in-cylinder pressure trace for BB3 strategy followed the line of motoring pressure until -1.4^{o} CA ATDC and rapidly increased and reached its maximum value of 40.5 bar at 8.2^{o} CA ATDC, 6.0^{o} CA after BB1 strategy. This delay was due to retarded injection timing of the first injection whereby the combustion process took place later in the expansion stroke. The peak in-cylinder pressure was considerably lower than BB2 strategy since the total fuel injection quantity with 10^{o} CA dwell timing between the two injections was considerably lower in comparison to BB2 strategy where the dwell angle between the injections was 15^{o} CA as shown in Figure 5.14. The in-cylinder pressure after the peak steadily decreased but remained lower than BB1 and BB2 strategies. The fuel was injected at -10^{o} CA ATDC and TDC which led to an IMEP value of 1.98 bar.

The in-cylinder pressure trace for BB4 strategy followed the line of motoring pressure until 4.8^{o} CA ATDC where it experienced a rapid increase in pressure and reached its maximum value of 43.7 bar at 15.6^{o} CA ATDC, 13.4^{o} CA after BB1 strategy. This delay was attributed to late initiation of the combustion due to retarded injection

timing of the first injection. The dwell angle between the two injections for this strategy was 5^{o} CA which was not sufficient for the injector to fully close prior to the onset of the second injection as previously stated. Thus, the second injection took place while the needle was partially open which resulted in much greater total fuel injection quantity than intended as depicted in Figure 5.14. The peak in-cylinder pressure was higher than BB1 and BB3 strategies due to greater fuel quantity injected but remained lower than BB2 strategy since the combustion process took place further into the expansion stroke. The in-cylinder pressure after the peak steadily decreased but remained higher than all the other strategies. The fuel was injected at -5^{o} CA ATDC and TDC which resulted an IMEP value of 5.43 bar.

The heat release rate for strategies BB1, BB2, BB3 and BB4 are presented in Figure 6.18. The heat release rate for BB1 strategy exhibited a sudden decrease at -15.8^{o} CA ATDC due to charge cooling shortly after the onset of the first injection and the heat transfer effects during the compression stroke which lasted until -11.2^{o} CA ATDC. After this point, the rate of heat release rapidly increased and reached its peak value at -2.6^{o} CA ATDC, due to premixed combustion. This phase of combustion lasted until 3.4^{o} CA ATDC where the second phase of combustion started. The maximum heat release rate due to diffusion combustion occurred at 9.8^{o} CA ATDC and gradually deceased after this point during the expansion stroke.

The heat release rate for BB2 strategy experienced a sudden decrease at -11.2^{o} CA ATDC due to charge cooling shortly after the onset of the first fuel injection and the heat transfer effects during the compression stroke which lasted until -7.4^{o} CA ATDC. After this point, the rate of heat release rapidly increased until 1.2^{o} CA ATDC where the maximum heat release due to premixed combustion occurred, 3.8^{o} CA after BB1 strategy, which was higher than BB1 strategy. This was mainly attributed to improved fuel evaporation and mixing effects given that the first fuel injection took place closer to TDC where the in-cylinder temperature was higher. Consequently, the ignition delay was shorter in comparison to BB1 strategy due to faster fuel evaporation. This phase of combustion lasted until 6.2^{o} CA ATDC where the second phase of combustion started. The maximum heat release rate due to diffusion combustion

occurred at 10.6^{o} CA ATDC following the onset of the second injection and gradually decreased after the peak during the expansion stroke.

The heat release rate for BB3 strategy experienced a sudden decrease at -7.4^{o} CA ATDC due to charge cooling shortly after the onset of the first fuel injection and the heat transfer effects during the compression stroke which lasted until -3.8^{o} CA ATDC. After this point, the rate of heat release rapidly increased until 4.2^{o} CA where the maximum heat release due to premixed combustion occurred, 6.8^{o} CA after BB1 strategy. The peak heat release rate was lower than BB2 strategy since the time available for the combustion process to complete was more limited due to retarded injection timing of the first injection. In addition, less fuel was injected due to the dwell angle used as shown in Figure 5.14. This phase of combustion lasted until 11.6^{o} CA ATDC where the second phase of combustion started. The maximum heat release rate due to diffusion combustion occurred at 14.6^{o} CA ATDC following the onset of the second injection and gradually decreased after this peak during the expansion stroke.

As previously stated for B4 strategy, dwell timing of 5^{o} CA between the two injections was not sufficient for the injector to fully close prior to the onset of the second injection, thus replicating a single injection strategy with total fuel injection quantity considerably higher than intended. The heat release rate for BB4 strategy experienced a sudden decrease at 0.6^{o} CA ATDC due to charge cooling shortly after the onset of the second injection which lasted until 3.2^{o} CA ATDC. After this point, the rate of heat release rapidly increased and reached its maximum value at 11.4^{o} CA ATDC, 14.0^{o} CA after BB1 strategy, due to premixed combustion. This strategy produced the maximum heat release rate due to premixed combustion in comparison to the other strategies as shown in Figure 6.18. This was due to the greater fuel quantity injected as a consequence of the dwell angle used as shown in Figure 5.14, as well as longer ignition delay which resulted in prolonged premixed phase, Table 6.4. Consequently, more fuel and air was mixed which led to greater heat release during the first phase of combustion. This phase of combustion lasted until 18.6^{o} CA ATDC where the second phase of combustion started. The maximum heat release rate due to

diffusion combustion occurred at 23.2^{o} CA ATDC and progressively decreased after this point during the expansion stroke.

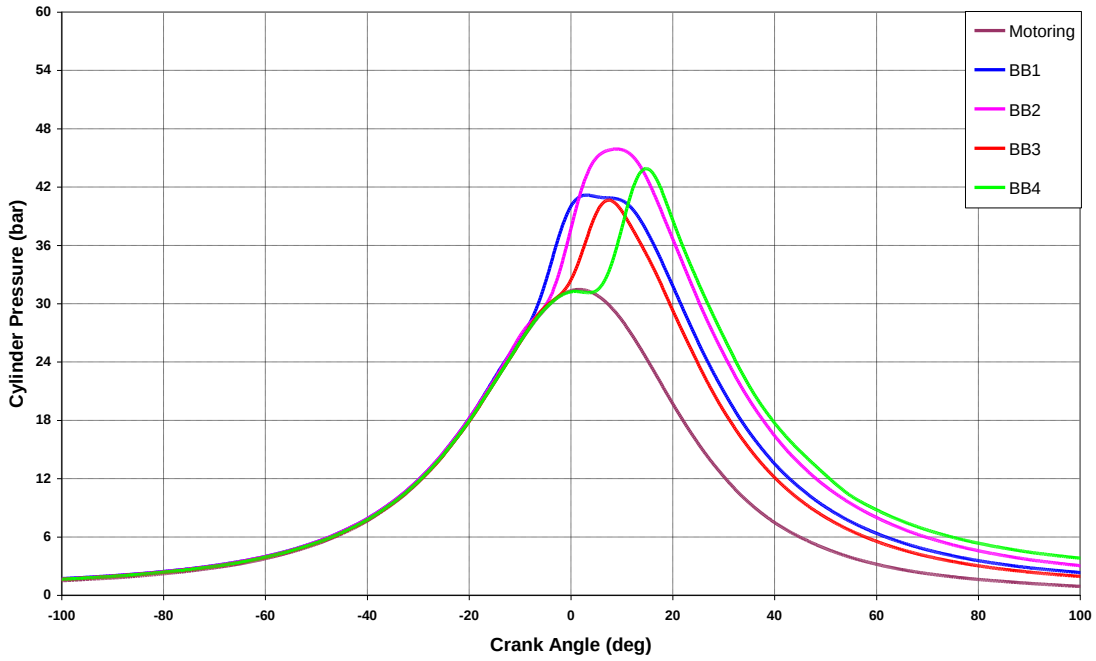

Figure 6.17 In-Cylinder Pressure Data for Strategy BB at 1200 bar

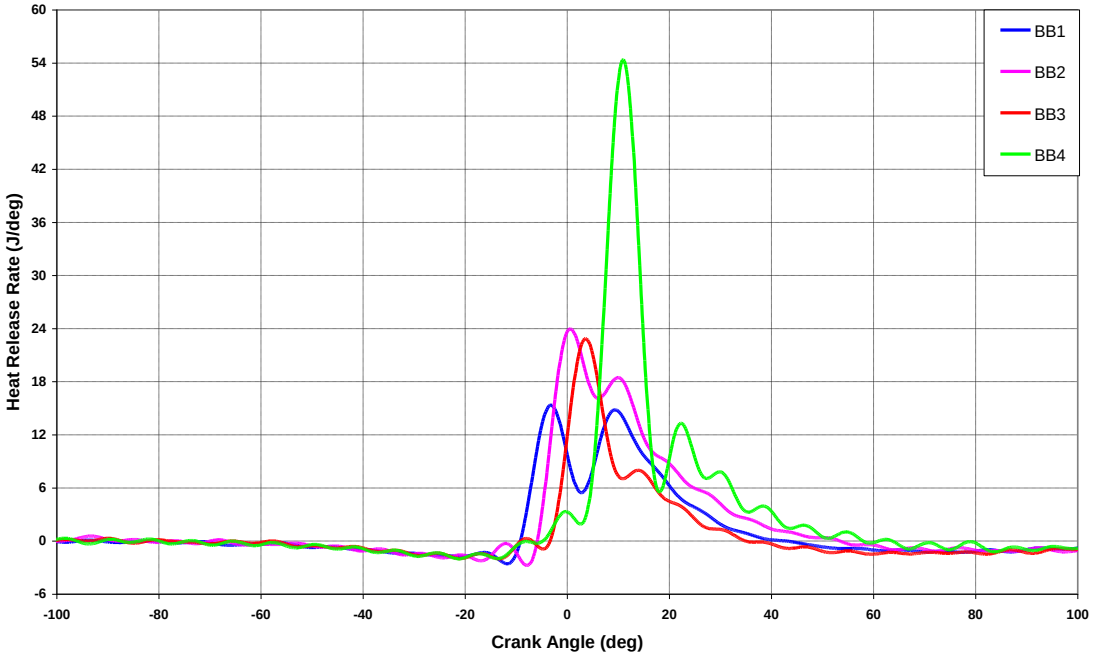

Figure 6.18 Heat Release Rate Traces for Strategy BB at 1200 bar

6.4.2.2 Fuel Injection and Combustion Visualisation

Figure 6.19 shows the image sequence obtained for BB2 strategy through high speed video imaging technique.

Although BB4 strategy produced the maximum heat release rate, high speed imaging was carried out for BB2 strategy since the actual total fuel injection quantity for BB4 strategy was much greater than 20 mm^3. The first three frames in Figure 6.19 show the fuel spray development from the start to the end of the first injection where in the last frame fuel sprays impinged on the piston wall on the left hand side. As previously stated in Chapter 5, the fuel spray asymmetry is an inherent characteristic of VCO nozzles. The subsequent five frames show the image sequence from the start to the end of the second injection. Although the same injection duration was used for both injections, the second injection lasted longer which indicated that more fuel was injected during the second injection. This finding was in good agreement with the results obtained through Zeuch's method as shown in Figure 5.14. Unlike B2 strategy where the fuel sprays did not reach the piston wall due to shorter injection duration, fuel sprays in BB2 strategy did reach the piston wall even though half the total fuel quantity was injected during each injection event since the total fuel injection quantity was twice that of B2 strategy.

The first combustion phase apparent from the heat release rate data at -7.4^o CA ATDC, Figure 6.18, resulted in no visible combustion until -4.2^o CA ATDC where the first visible combustion was observed. Flame propagation started at the tip of the fuel sprays where fuel vapour was highly concentrated and spread along the periphery of the fuel sprays where fuel evaporation rate was considerably higher than the core region where liquid fuel droplets were the dominating constituents as shown in frame seven at 2.7^o CA ATDC. In the next frame at 3.6^o CA ATDC, the flame was propagated at the tip of the sprays, spreading to the outer regions of the sprays tip due to fuel sprays impingement on the piston wall, creating a mushroom like structure. In the subsequent frame at 6.3^o CA ATDC, intense flame propagation took place, spreading to the periphery of the piston wall where the majority of premixed fuel and air was concentrated. The same trend existed at 10.8^o CA ATDC where fuel was burning in the same manner but spreading to the central regions of the piston,

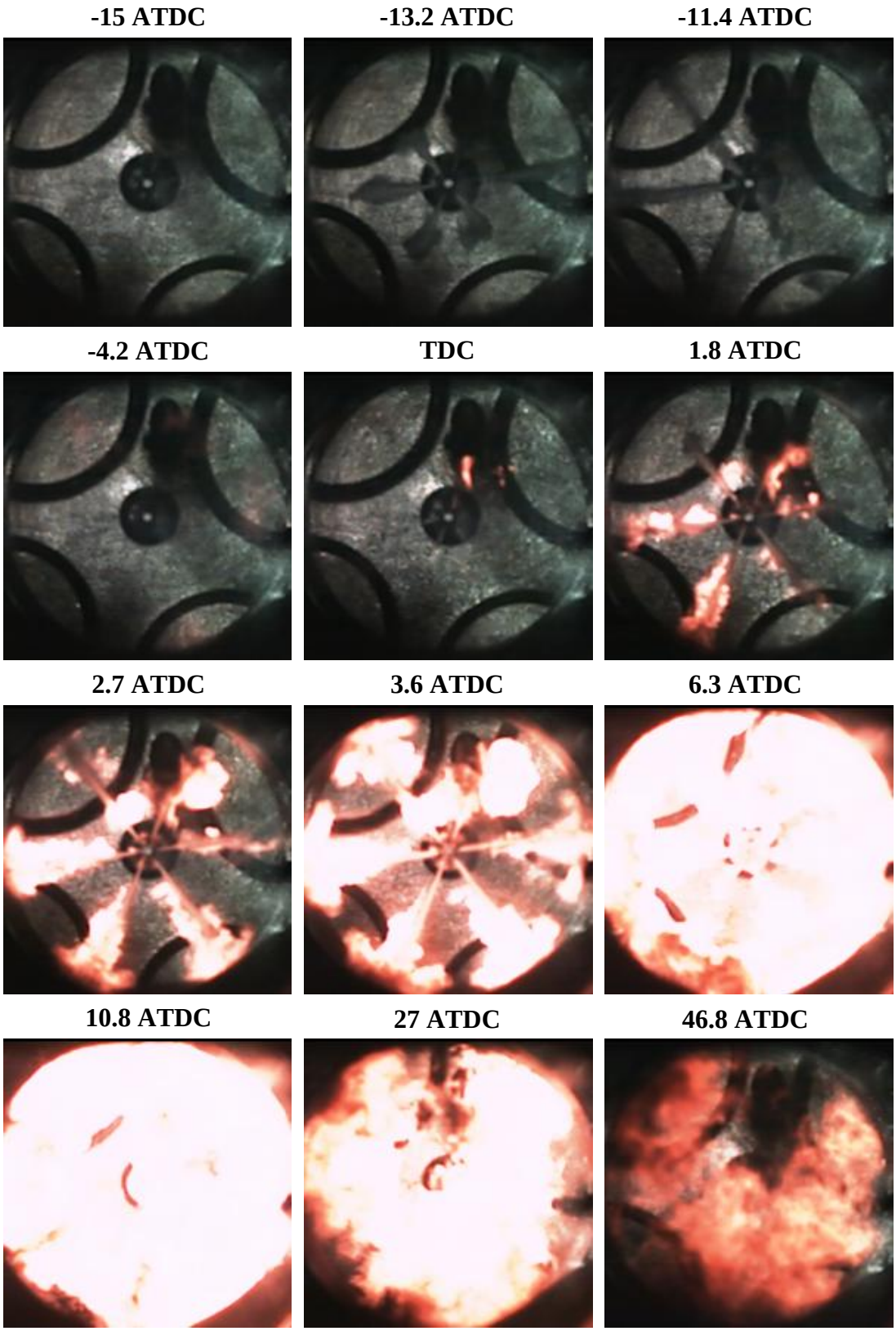

Figure 6.19 Combustion Image Sequence for BB2 Strategy at 1200 bar

due to diffusion combustion. In the next two frames several combustion sites are present, indicating the presence of diffusion combustion at 27.0^{o} CA ATDC and 46.8^{o} CA ATDC. Flame was moved in the clockwise direction due to the swirl motion as the combustion process evolved.

6.4.2.3 Soot and Exhaust Emissions

The soot and gaseous exhaust emissions results for strategy BB are depicted in Figures 6.20 and 6.21 respectively.

The soot level produced by BB2 strategy was considerably higher compared to BB1 strategy; this was mainly due to the greater fuel quantity injected for this strategy as a result of the dwell angle used. The soot concentration for BB3 strategy was substantially lower, this was due to lower fuel quantity injected as a consequence of the dwell angle used as shown in Figure 5.14 as well as shorter ignition delay which indicated curtailed premixed phase, Table 6.4.

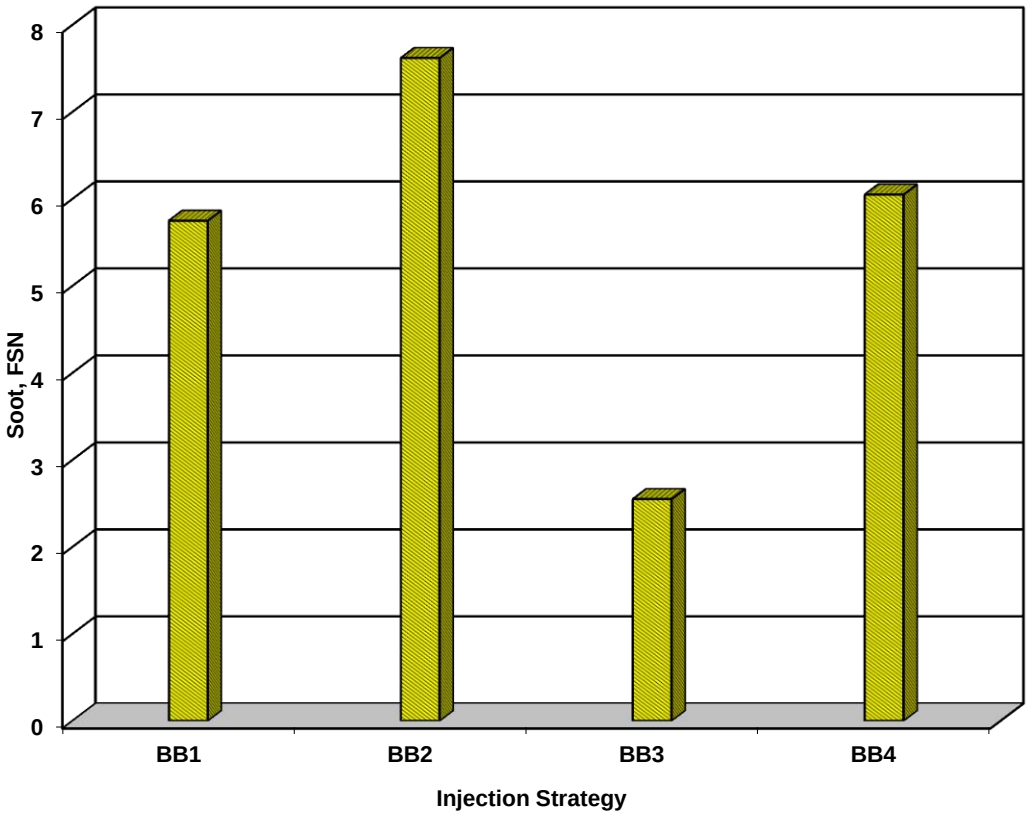

Figure 6.20 Soot Concentration for Strategy BB at 1200 bar

BB4 strategy produced high levels of soot since the dwell timing between the two injections was not sufficient for the injector to fully close prior to the onset of the second injection as previously stated for B4 strategy. Thus, the total fuel injection quantity was considerably higher than intended.

The NOx emission for BB2 strategy was less than BB1 due to delayed combustion phasing, as well as shorter ignition delay for this strategy whereby less fuel and air was mixed prior to the onset of the combustion in comparison to BB1 strategy as shown in Table 6.4. The NOx emission produced by BB3 strategy was almost identical to BB1 strategy. BB4 strategy produced the lowest NOx emission compared to all the other strategies since combustion took place during the expansion stroke as shown in Figure 6.18; thus, the maximum combustion temperature was limited even though the ignition delay was longer than BB2 and BB3 strategies.

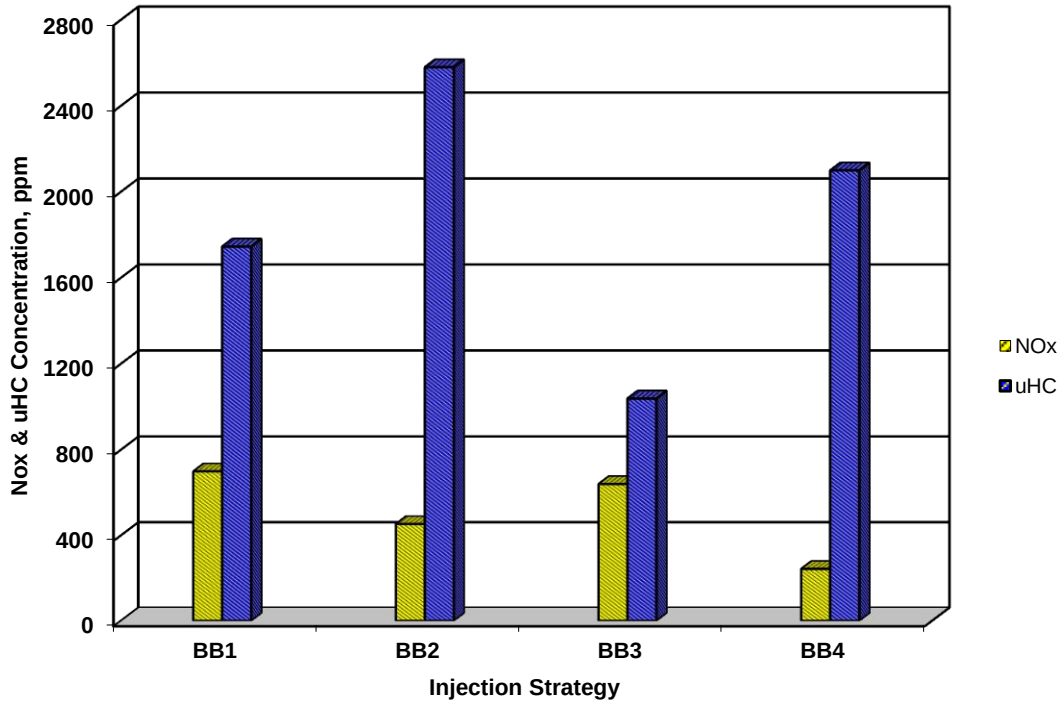

Figure 6.21 NOx and uHC Concentration for Strategy BB at 1200 bar

The uHC emission was higher for BB2 and lower for BB3 strategies in comparison to BB1 strategy since higher and lower quantities of fuel was injected respectively, due to the dwell timings used for these strategies as shown in Figure 5.14. In addition, the

first fuel injection took place closer to TDC for BB3 strategy where the in-cylinder temperature was higher which led to improved fuel evaporation and mixing processes. Thus, less unburned fuel remained inside the cylinder upon the completion of the combustion process. BB4 strategy produced high level of uHC emission; this was due to the greater total fuel injection quantity as a result of the dwell angle used as shown in Figure 5.14, as well as the limited time available during the premixed and combustion phases as the injection timing was further retarded.

6.4.3 Strategy C (Low load, 50:50 split injection with fixed dwell angle of 10^o CA)

This strategy involves analysis of Injection timing with fixed dwell angle between injections on the combustion and emissions characteristics of a four-stroke HSDI diesel engine through 50:50 split injection strategies. The total fuel demand is 10 mm^3.

6.4.3.1 In-Cylinder Pressure and Heat Release Rate Analysis

The in-cylinder pressure data for strategies C1, C2, C3 and C4 averaged over 20 consecutive cycles are shown in Figure 6.22. The in-cylinder pressure trace for C1 strategy followed the line of motoring pressure until -5.4^o CA ATDC where it sharply increased and reached its peak value of 35.5 bar at 4.8^o CA ATDC. The in-cylinder pressure steadily decreased from this point during the expansion stroke. The fuel injections took place at -20^o CA ATDC and -10^o CA ATDC which resulted an IMEP value of 0.53 bar.

The in-cylinder pressure trace for C2 strategy followed the line of motoring pressure until -2.2^o CA ATDC where it rapidly increased and reached its peak value of 35.7 bar at 6.2^o CA ATDC, 1.4^o CA after C1 strategy. This delay was due to retarded injection timing of the second injection for this strategy compared to C1 strategy. The fuel was injected at -15^o CA ATDC and -5^o CA ATDC which led to an IMEP value of 0.67 bar. The peak in-cylinder pressure value was almost identical to C1 strategy since the dwell angle between the two injections remained constant which resulted in equal total injected fuel quantities for all the strategies tested in this section. The in-cylinder

pressure steadily decreased after the peak during the expansion stroke and remained approximately the same as that of C1 strategy.

The in-cylinder pressure trace for C3 strategy followed the line of motoring pressure until -5.6^{o} CA ATDC and gradually increased and reached its maximum value of 33.6 bar at 8.6^{o} CA ATDC, 3.8^{o} CA after C1 strategy. This delay was due to retarded injection timing of the second injection for this strategy in comparison to C1 strategy. The peak in-cylinder pressure was lower than C1 and C2 strategies since injection timings were further retarded. The in-cylinder pressure after the peak steadily decreased and remained almost identical to those of C1 and C2 strategies. The fuel was injected at -10^{o} CA ATDC and TDC which resulted an IMEP value of 0.79 bar.

The in-cylinder pressure trace for C4 strategy followed the line of motoring pressure until 4.2^{o} CA ATDC at which point the peak in-cylinder pressure with the value of approximately 31 bar was reached. The peak in-cylinder pressure was lower than C1, C2 and C3 strategies since the first fuel injection timing was further retarded. The in-cylinder pressure remained almost constant until 10.2^{o} CA ATDC where it steadily decreased and remained almost identical to those of C1, C2 and C3 strategies. The fuel was injected at -5^{o} CA ATDC and 5^{o} CA ATDC which resulted an IMEP value of 0.76 bar.

The heat release rate for strategies C1, C2, C3 and C4 are presented in Figure 6.23. The heat release rate for C1 strategy exhibited a sudden decrease at -19.2^{o} CA ATDC due to charge cooling shortly after the onset of the first fuel injection and the heat transfer effects during the compression stroke which lasted until -16.4^{o} CA ATDC. The charge cooling effect was less evident with these strategies since the injected quantities with 10^{o} CA dwell timing resulted in the least total fuel injection quantity as shown in Figure 5.12. After this point, the rate of heat release gradually increased until -8.6^{o} CA ATDC where it suddenly increased and reached its peak value at 1.6^{o} CA ATDC, due to premixed combustion. The end of premixed combustion and the start of diffusion combustion were mixed and difficult to distinguish from the heat release rate data. The heat release gradually decreased during the expansion stroke.

The heat release rate for C2 strategy experienced a minor decrease at -14.2^{o} CA ATDC due to charge cooling effect shortly after the onset of the first fuel injection and the heat transfer effects during the compression stroke which lasted until -12.8^{o} CA ATDC. As previously stated for C1 strategy, the charge cooling effect was less paramount due to lower fuel injection quantity. After this point, the rate of heat release gradually increased until -7.2^{o} CA ATDC where it rapidly increased until 2.8^{o} CA ATDC where the maximum heat release due to premixed combustion occurred,

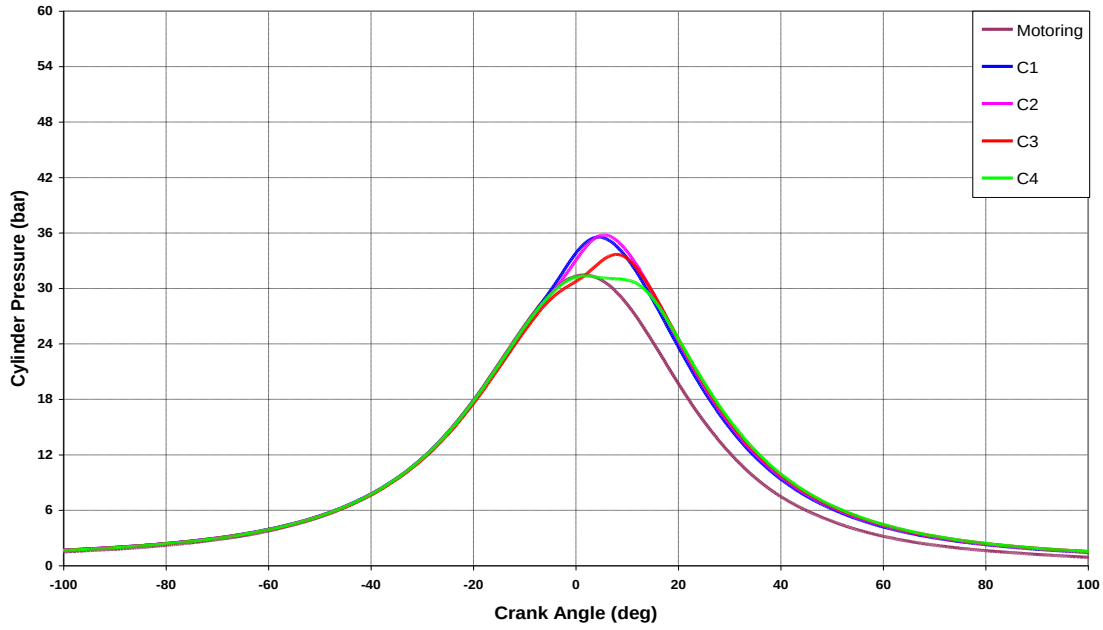

Figure 6.22 In-Cylinder Pressure Data for Strategy C at 1200 bar

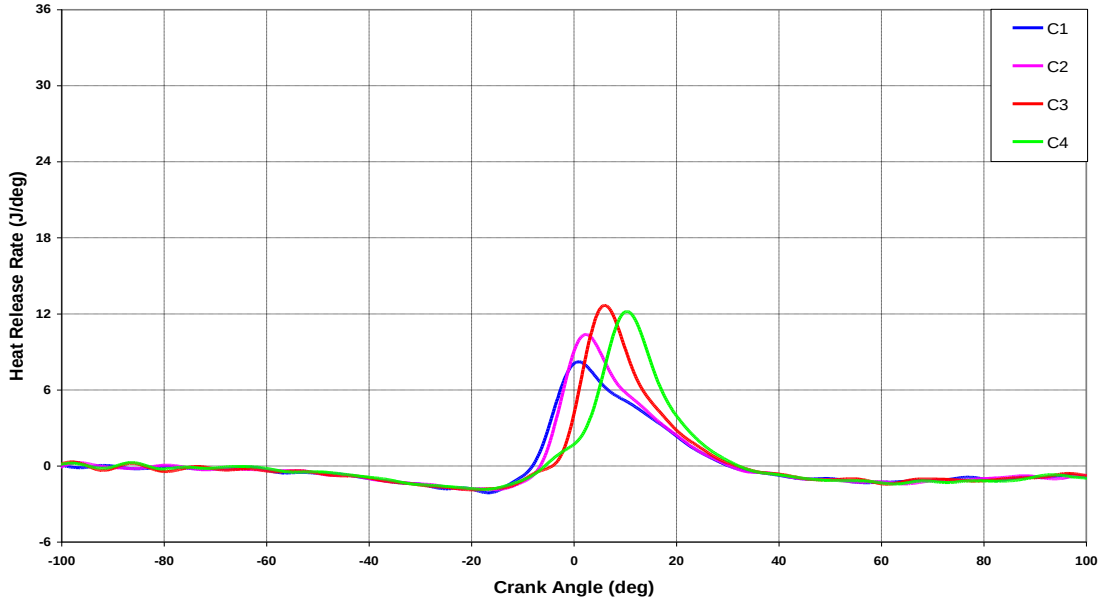

Figure 6.23 Heat Release Rate Traces for Strategy C at 1200 bar

1.2^{o} CA after C1 strategy, which was higher than C1 strategy. This was due to improved fuel evaporation since the first injection took place closer to TDC where the in-cylinder temperature was higher. The end of premixed combustion and the start of diffusion combustion were mixed and difficult to distinguish from the heat release rate data. The heat release gradually decreased during the expansion stroke.

The heat release rate for C3 strategy experienced a small decrease at -7.2^{o} CA ATDC due to charge cooling effect shortly after the onset of the first fuel injection and the heat transfer effects during the compression stroke which lasted until -6.6^{o} CA ATDC. Since fuel was injected closer to TDC where the in-cylinder temperature was higher, the cooling effects were further diminished. After this point, the rate of heat release gradually increased until -4.2^{o} CA ATDC where it sharply increased and reached its maximum value at 6.8^{o} CA ATDC due to premixed combustion, 5.2^{o} CA after C1 strategy. The maximum heat release rate was higher than C1 and C2 strategies due to further retarded injection timing of the first injection whereby fuel evaporation process was further improved. The heat release rate trace for C3 strategy steadily decreased after the peak during the expansion stroke with no noticeable signs of diffusion combustion from the heat release rate data.

The heat release rate for C4 strategy experienced no reduction due to charge cooling, it gradually increased following the onset of the first injection until 1.4^{o} CA ATDC where it suddenly increased and reached its peak value at 11.2^{o} CA ATDC, 9.6^{o} CA after C1 strategy, due to premixed combustion. The maximum heat release rate for this strategy was higher than C1 and C2 strategies; this was due to improved fuel evaporation and mixing processes caused by further retarded injection timings used. The heat release rate trace for C4 strategy steadily decreased after the peak during the expansion stroke with no detectable signs of diffusion combustion from the heat release rate data.

6.4.3.2 Soot and Exhaust Emissions

The soot and emissions results for strategy C are depicted in Figures 6.24 and 6.25 respectively.

The soot level produced by C2 and C3 strategies are lower than C1 strategy since diffusion combustion was less intense for C2 strategy and was not present for C3 strategy based on the heat release rate traces. B4 strategy produced more soot in comparison to C3 strategy even though no diffusion combustion was detected for this strategy. The increase in soot emission was mainly due to the limited time available for the soot particles to oxidise during the expansion stroke.

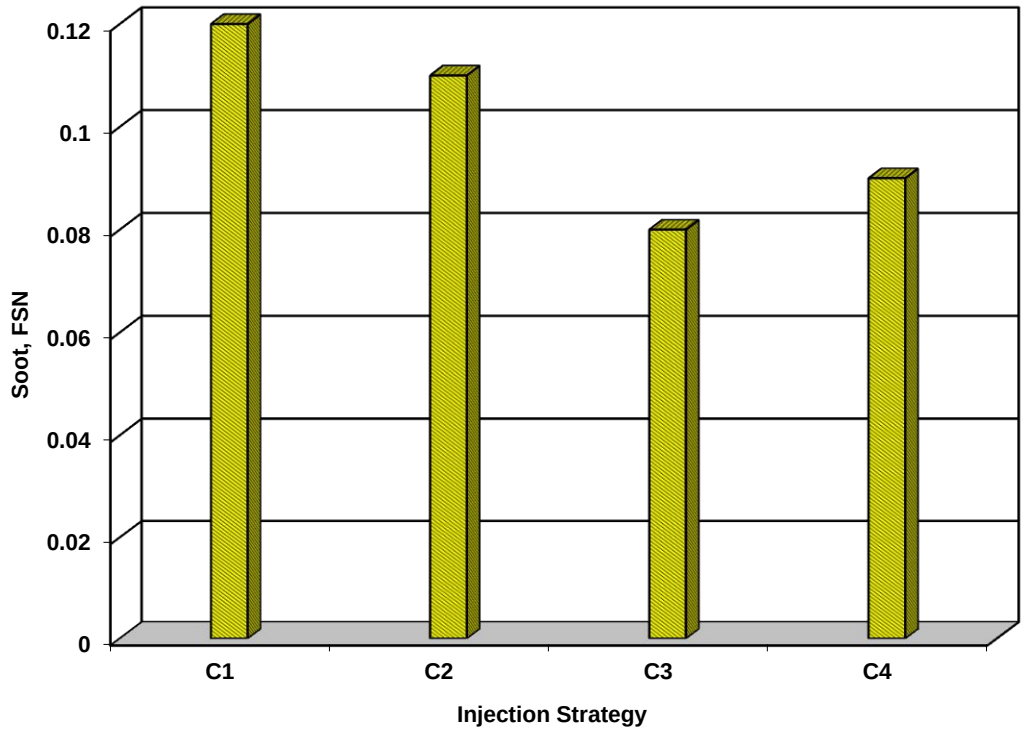

Figure 6.24 Soot Concentration for Strategy C at 1200 bar

The NOx emission for C2 strategy was slightly higher than C1. The NOx emission produced by C3 strategy was almost identical to that of C2 strategy since the in-cylinder conditions were approximately the same. The NOx emission produced by C4 strategy was lower than all the other strategies since combustion took place during the expansion stroke as shown in Figure 6.18, which limited the maximum combustion temperature.

The uHC emission for C2 and C3 strategies were lower than C1 strategy which was mainly due to improved fuel evaporation and mixing processes as the first injection

timing was retarded. Thus, more fuel was burned during the combustion process. On the other hand, C4 strategy produced high level of uHC emission since the first injection timing was further retarded which in turn limited the time available during the premixed and combustion phases. Consequently, high level of unburned fuel remained inside the cylinder upon the completion of the combustion process.

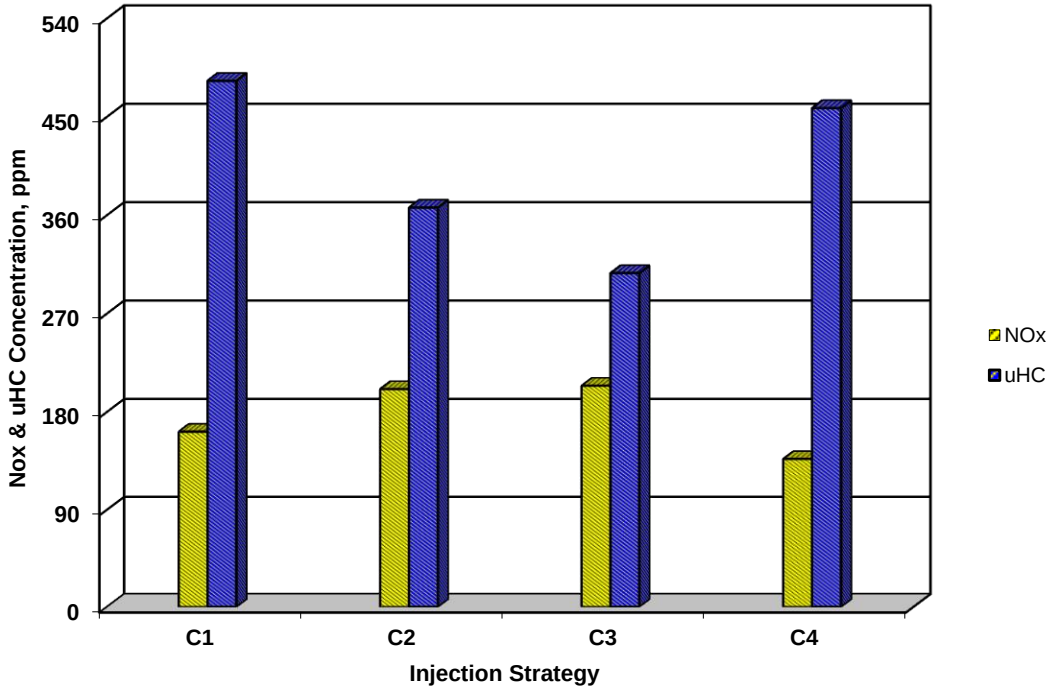

Figure 6.25 NOx and uHC Concentration for Strategy C at 1200 bar

The IMEP values obtained through all the strategies tested with fixed dwell angle of 10^{o} CA were considerably lower in comparison to the strategies with variable dwell angle as shown in Table 6.4. Therefore, the subsequent sections will focus merely on the strategies with variable dwell timing, nevertheless the in-cylinder pressure traces, heat release rate and emissions results for the remaining strategies with fixed dwell angle of 10^{o} CA are presented in Appendix D.

6.5 Results of 30:70 Split Injection Strategy

6.5.1 Strategy D (Low load, 30:70 split injection with fixed 2nd injection at TDC)

This strategy involves analysis of injection timing with variable dwell angle between injections on the combustion and emissions characteristics of a four-stroke HSDI diesel engine through 30:70 split injection strategies. The total fuel demand is 10 mm^3.

6.5.1.1 In-Cylinder Pressure and Heat Release Rate Analysis

The in-cylinder pressure data for strategies D1, D2, D3 and D4 averaged over 20 consecutive cycles are shown in Figure 6.26. The in-cylinder pressure trace for D1 strategy followed the line of motoring pressure until -6.6^o CA ATDC where it progressively increased and reached its peak value of 32.5 bar at 3.6^o CA ATDC. The in-cylinder pressure remained almost constant until 10.8^o CA ATDC where it steadily decreased from this point during the expansion stroke. The fuel injections took place at -20^o CA ATDC and TDC which resulted an IMEP value of 0.96 bar.

The in-cylinder pressure trace for D2 strategy followed the line of motoring pressure until -3.4^o CA ATDC where it suddenly increased and reached its peak value of 40.9 bar at 12.2^o CA ATDC, 8.6^o CA after D1 strategy. This delay was due to retarded injection timing of the first injection. The peak in-cylinder pressure value was considerably higher in comparison to D1 strategy due to the difference in the fuel injection quantity as the dwell angle between the two injections changed as shown in Figure 5.15. The in-cylinder pressure steadily decreased after the peak during the expansion stroke, though remained higher compared to D1 strategy. The fuel was injected at -15^o CA ATDC and TDC which led to an IMEP value of 3.17 bar.

The in-cylinder pressure trace for D3 strategy followed the line of motoring pressure until 1.6^o CA ATDC where it progressively increased and reached its maximum value of 33.1 bar at 8.8^o CA ATDC, 5.2^o CA after D1 strategy. This delay was due to retarded injection timing of the first injection whereby the combustion process took place late in the expansion stroke. The peak in-cylinder pressure was considerably

lower than D2 strategy since the total fuel injection quantity with 10^o CA dwell timing was considerably lower in comparison to D2 strategy where the dwell angle was 15^o CA as shown in Figure 5.15. The in-cylinder pressure after the peak steadily decreased following almost the same line as D1 strategy. The fuel was injected at -10^o CA ATDC and TDC which resulted an IMEP value of 0.79 bar.

The in-cylinder pressure trace for D4 strategy followed the line of motoring pressure until 4.2^o CA ATDC since the thermodynamic conditions under this strategy were almost identical to those of motoring up to this point. After this point, the in-cylinder pressure experienced a rapid increase, reaching its maximum value of 36.4 bar at 14.6^o CA ATDC, 11.0^o CA after D1 strategy. As previously stated, this delay was due to further retarded injection timing of the first injection. The dwell angle for this strategy was 5^o CA which was not sufficient for the injector to fully close prior to the onset of the second injection; thus, higher fuel quantity was injected. However, this effect was less paramount for D4 strategy in comparison to B4 and BB4 strategies as shown in Figure 5.15 since the injection duration of the first injection was shorter in comparison to 50:50 strategies. The peak in-cylinder pressure was higher than D1 and D3 strategies due to the greater fuel quantity injected, yet remained lower than D2 strategy due to the limited time available during the premixed and combustion phases with D4 strategy. The in-cylinder pressure after the peak steadily decreased during the expansion stroke. The fuel was injected at -5^o CA ATDC and TDC which led to an IMEP value of 2.26 bar.

The heat release rate for strategies D1, D2, D3 and D4 are presented in Figure 6.27 which follow the same pattern as those of strategy B. The heat release rate for D1 strategy exhibited a minor decrease at -17.8^o CA ATDC due to charge cooling shortly after the onset of the first fuel injection and the heat transfer effects during the compression stroke which lasted until -16.2^o CA ATDC. The charge cooling effect was less noticeable since the fuel quantity injected during the first injection was considerably lower in comparison to B and BB strategies. After this point, the rate of heat release progressively increased until 2.8^o CA ATDC where it rapidly increased following the start of the second injection at TDC. The maximum heat release rate occurred at 10.6^o CA ATDC, due to premixed combustion. This phase of combustion

lasted until the end of the combustion process with no evidence of diffusion combustion taking place for this strategy based on the heat release rate data presented in Figure 6.27. The heat release gradually decreased after the peak during the expansion stroke.

The heat release rate for D2 strategy experienced a sudden decrease at -10.6^{o} CA ATDC due to charge cooling shortly after the onset of the first fuel injection and the heat transfer effects during the compression stroke which lasted until -7.6^{o} CA ATDC. After this point, the rate of heat release sharply increased until 2.8^{o} CA ATDC due to the first fuel injection. At this point the heat release rate sharply increased for the second time following the onset of the second injection at TDC. The maximum heat release rate due to premixed combustion occurred at 7.6^{o} CA ATDC, 2.2^{o} CA before D1 strategy, which was greater than D1 strategy. This was mainly attributed to improved fuel evaporation and mixing effects given that the first fuel injection took place closer to TDC where the in-cylinder temperature was higher. In addition, the ignition delay was longer in comparison to D1 strategy due to the greater total fuel injection quantity for this strategy. Therefore, more fuel and air was mixed during the premixed phase of combustion which led to greater heat release rate during the first phase of combustion. In this case the end of premixed combustion and the start of diffusion combustion were mixed and difficult to distinguish.

The heat release rate for D3 strategy rapidly increased after the start of the first injection, reaching its peak value at 8.6^{o} CA ATDC, 2.0^{o} CA before D1 strategy, due to premixed combustion. The peak heat release rate was lower than D2 strategy since the time available for the combustion process to complete was more limited due to further retarded injection timing of the first injection. In addition, less fuel was injected due to the dwell angle used as shown in Figure 5.15. After this point, the heat release rate steadily decreased during the expansion stroke with no noticeable signs of diffusion combustion taking place based on the heat release rate data shown in Figure 6.27.

As previously stated, the dwell timing of 5^{o} CA led to total fuel injection quantity

considerably higher than intended. The heat release rate for D4 strategy gradually increased following the onset of the first injection until 2.8^{o} CA ATDC where the rate of heat release rapidly increased, reaching its maximum value at 11.4^{o} CA ATDC, 0.8^{o} CA after D1 strategy, due to premixed combustion. This strategy produced the maximum heat release rate due to premixed combustion in comparison to the

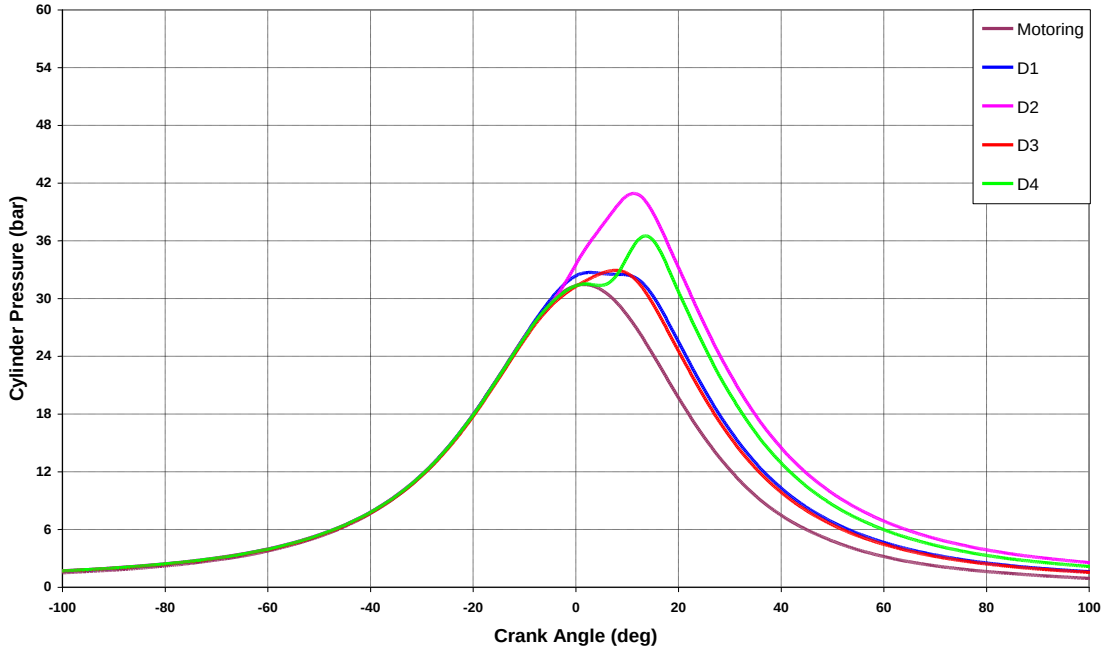

Figure 6.26 In-Cylinder Pressure Data for Strategy D at 1200 bar

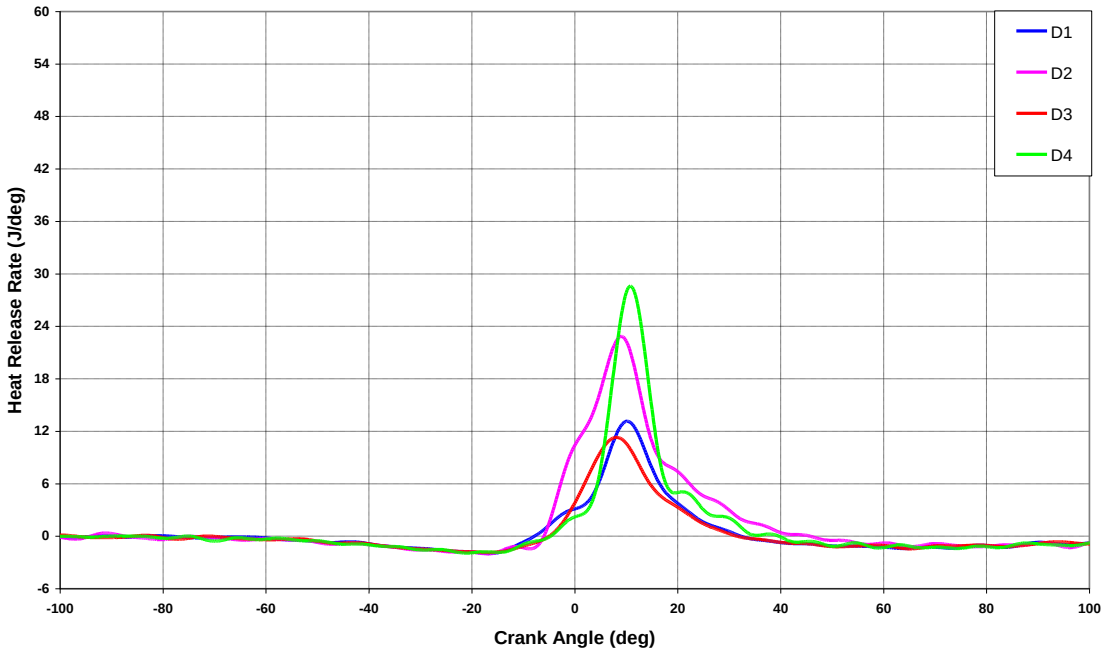

Figure 6.27 Heat Release Rate Traces for Strategy D at 1200 bar

other strategies as shown in Figure 6.27. This was due to greater total fuel injection quantity as a consequence of the dwell angle used as well as improved fuel evaporation effect as the first fuel injection took place closer to TDC where the in-cylinder temperature was higher. This phase of combustion lasted until 19.6^{o} CA ATDC where the second phase of combustion started. The maximum heat release rate due to diffusion combustion occurred at 21.8^{o} CA ATDC and progressively decreased after this point.

6.5.1.2 Fuel Injection and Combustion Visualisation

Figure 6.28 shows the image sequence obtained for D2 strategy through high speed video imaging technique.

As previously mentioned, although D4 strategy produced the maximum heat release rate, high speed imaging was carried out for D2 strategy since the actual total fuel injection quantity for D4 strategy was much greater than 10 mm^{3}. The first three frames in Figure 6.28 show the fuel sprays development from the start to the end of the first injection where in the last frame fuel sprays were almost fully evaporated. The fuel sprays in these images were not fully developed which was due to short injection duration of the first injection since 30% of total fuel quantity was injected at this stage. The subsequent four frames show the image sequence from the start to the end of the second injection. From this image sequence it is evident that the fuel sprays reached the piston wall. This was due to longer injection duration used during the second injection as 70% of total fuel quantity was injected at this point.

The first combustion phase apparent from the heat release rate data at -7.6^{o} CA ATDC, Figure 6.27, resulted in no visible combustion until TDC where the first visible combustion was observed. Flame was propagated in the same manner as that of B2 strategy, starting at the tip of the fuel sprays where fuel vapour was highly concentrated and spread along the periphery of the fuel sprays where fuel evaporation rate was considerably higher as shown in frames five, six and seven at 1.8^{o} CA ATDC, 2.7^{o} CA ATDC and 3.6^{o} CA ATDC respectively. In the last two frames, flame spread to the outer regions of the sprays tip due to fuel sprays impingement on the piston wall, creating a mushroom like structure. In the next frame at 8.1^{o} CA ATDC,

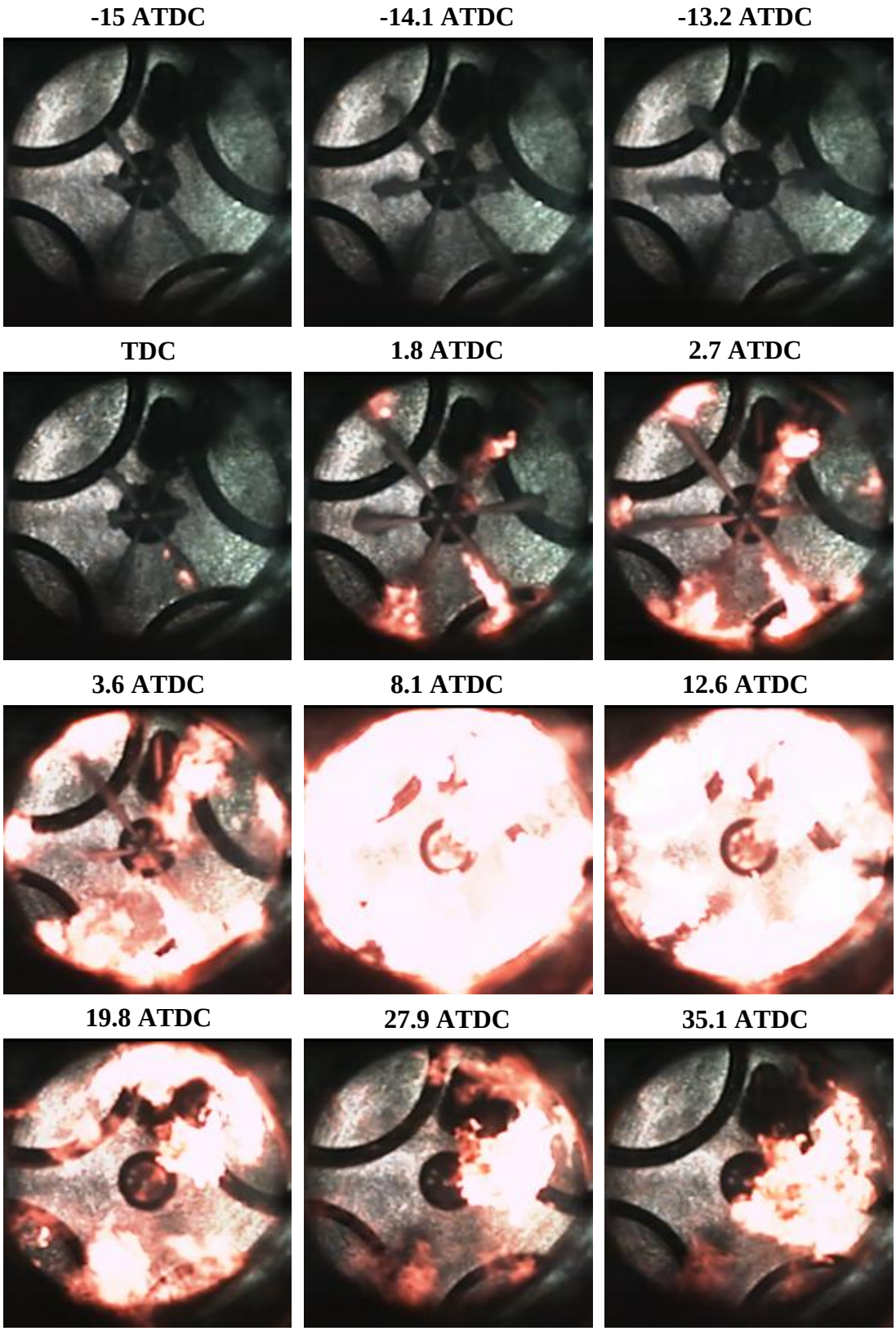

Figure 6.28 Combustion Image Sequence for D2 Strategy at 1200 bar

where approximately the maximum heat release rate occurred during premixed combustion, intense flame propagation took place spreading to the periphery of the piston wall where the majority of premixed fuel and air was concentrated. The same trend exists at 12.6^{o} CA ATDC where fuel was burning in the same manner during the first phase of combustion. Although the end of premixed combustion and the start of diffusion combustion for this strategy were mixed as shown in Figure 6.27, several combustion sites are present indicating the presence of some diffusion combustion corresponding to the second phase of combustion at 19.8^{o} CA ATDC, 27.9^{o} CA ATDC and 35.1^{o} CA ATDC. Flame was moved in the clockwise direction due to the swirl motion as the combustion process evolved.

6.5.1.3 Soot and Exhaust Emissions

The soot and gaseous exhaust emissions results for strategy D are depicted in Figures 6.29 and 6.30 respectively.

The soot level produced by D2 strategy was considerably higher compared to D1 strategy; this was mainly due to the greater total fuel injection quantity for this strategy as a result of the dwell angle used. In contrast, the soot concentration for D3 strategy was lower than D1 and D2 strategies since the total injected fuel quantity was much lower than the other two strategies as shown in Figure 5.15. D4 strategy produced high level of soot since dwell timing between the two injections was not sufficient for the injector to fully close prior to the onset of the second injection; thus, replicating a single injection strategy with total injected fuel quantity considerably higher than intended. However, the soot produced by D4 strategy remained lower than D2 strategy since the premixed combustion was more intense which resulted in improved soot oxidation as indicated by the in-cylinder pressure and heat release curves.

The NOx and uHC emissions follow the same pattern as those of strategy B. The NOx emission produced by D2 strategy was considerably higher than D1 strategy since greater fuel quantity was injected for D2 strategy due to the injection timings used which led to higher temperature combustion. In contrast, D3 strategy produced lower

NOx emission compared to D2 strategy since the injected fuel quantity was less for D3 strategy as shown in Figure 5.15. Nevertheless, NOx emission produced by D3 was higher than D2 even though less fuel was injected, this was due to improved fuel evaporation and mixing processes since the first injection took place closer to TDC where the in-cylinder temperature was higher. The NOx emission produced by D4 strategy was substantially higher than the other strategies since the dwell timing was not sufficient for the injector to fully close prior to the onset of the second injection. Thus, greater total fuel quantity was injected than intended, Figure 5.15, which resulted in higher temperature combustion.

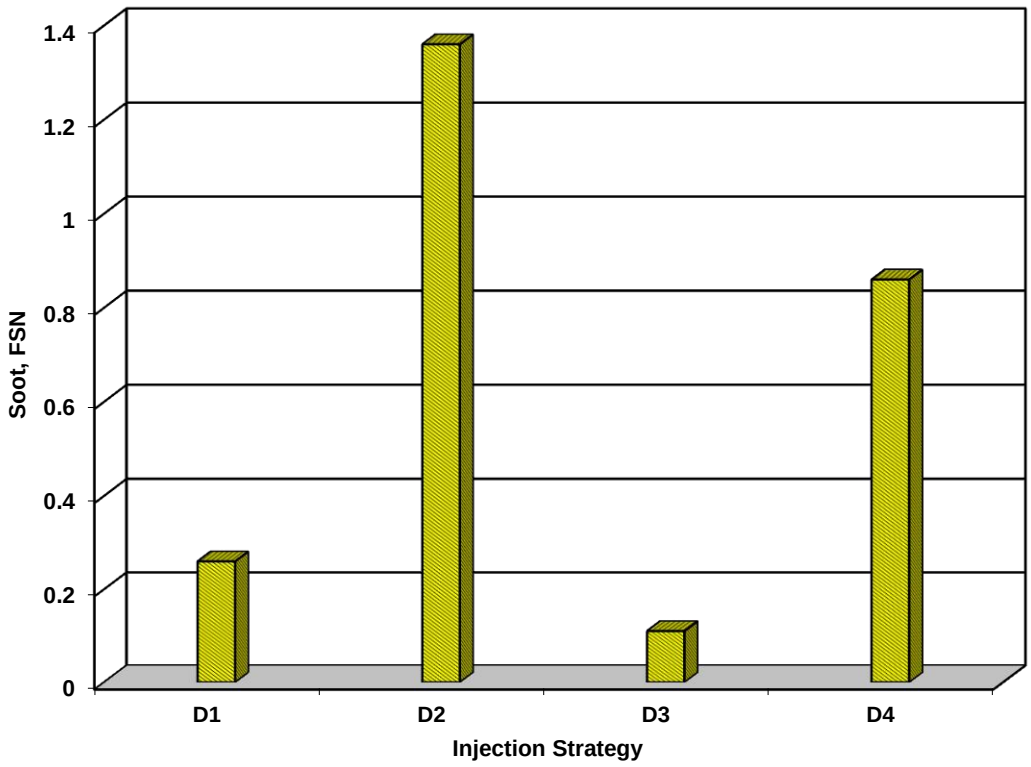

Figure 6.29 Soot Concentration for Strategy D at 1200 bar

The uHC emission for D2 strategy was lower compared to D1 strategy, this was due to improved fuel evaporation and mixing processes since the first fuel injection took place closer to TDC. In addition, the ignition delay for this strategy was longer in comparison to D1 strategy indicating greater fuel and air mixing during the premixed phase of combustion which in turn led to lower uHC emission. D3 strategy produced

higher uHC emission in comparison to D2 strategy; this was mainly due to limited time available during the premixed and combustion phases as the injection timing of the first injection was further retarded. D4 strategy produced higher uHC emission in comparison to all the other strategies, this was due to the dwell timing used for this strategy whereby the two injections interacted with each other, resulting in a single injection with much longer injection duration in comparison to the other dwell timings used in this study as shown in Figure 5.15. In addition, limited time was available during the premixed and combustion phases due to the retarded injection timing of the first injection. Therefore, high level of unburned fuel remained inside the cylinder upon the completion of the combustion process.

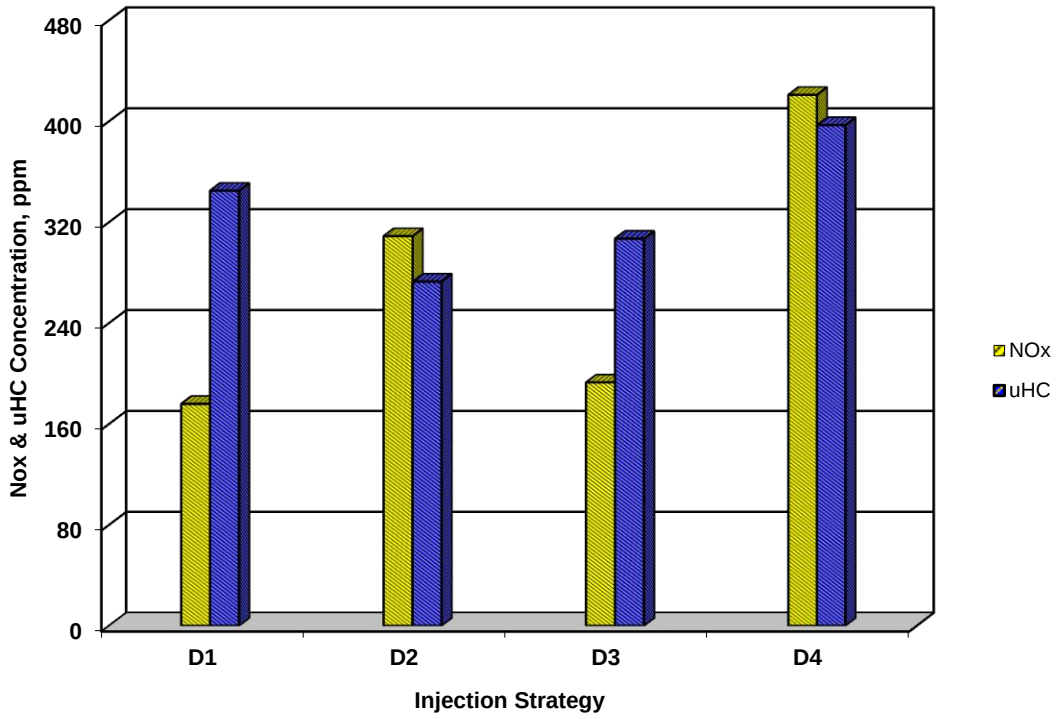

Figure 6.30 NOx and uHC Concentration for Strategy D at 1200 bar

6.5.2 Strategy DD (High load, 30:70 split injection with fixed 2nd injection at TDC)

This strategy involved analysis of injection timing with variable dwell angle on the combustion and emissions characteristics of a four-stroke HSDI diesel engine through 30:70 split injection strategies. The total fuel demand was 20 mm^3.

6.5.2.1 In-Cylinder Pressure and Heat Release Rate Analysis

The in-cylinder pressure data for strategies DD1, DD2, DD3 and DD4 averaged over 20 consecutive cycles are shown in Figure 6.31. The in-cylinder pressure trace for DD1 strategy followed the line of motoring pressure until -5.8^{o} CA ATDC where it rapidly increased, reaching its peak value of 38.7 bar at 4.2^{o} CA ATDC due to the first fuel injection. The in-cylinder pressure experienced a second peak with the value of 41.3 bar at 11.8^{o} CA ATDC. The in-cylinder pressure steadily decreased from this point during the expansion stroke. The fuel injections took places at -20^{o} CA ATDC and TDC which resulted an IMEP value of 3.56 bar.

The in-cylinder pressure trace for DD2 strategy followed the line of motoring pressure until -4.6^{o} CA ATDC where it suddenly increased and reached its peak value of 43.2 bar at 12.6^{o} CA ATDC, 8.4^{o} CA after DD1 strategy. This delay was due to retarded injection timing of the first injection. The peak in-cylinder pressure value was higher in comparison to DD1 strategy due to the difference in the fuel quantity injected as the dwell angle between the two injections changed as shown in Figure 5.16. The in-cylinder pressure steadily decreased after the peak during the expansion stroke. The fuel was injected at -15^{o} CA ATDC and TDC which led to an IMEP value of 4.28 bar.

The in-cylinder pressure trace for DD3 strategy followed the line of motoring pressure until -6.8^{o} CA ATDC where it progressively increased until 1.2^{o} CA ATDC. The in-cylinder pressure suddenly increased at this point, reaching its maximum value of 40.2 bar at 11.4^{o} CA ATDC, 7.2^{o} CA after DD1 strategy. As previously stated, this delay was due to retarded injection timing of the first injection whereby the combustion process took place later in the expansion stroke. The peak in-cylinder pressure was considerably lower than DD2 strategy since the fuel quantity injected with 10^{o} CA dwell timing was considerably lower compared to DD2 strategy where the dwell angle of 15^{o} CA was used as shown in Figure 5.16. The in-cylinder pressure after the peak steadily decreased during the expansion stroke. The fuel was injected at -10^{o} CA ATDC and TDC which resulted an IMEP value of 2.86 bar.

The in-cylinder pressure trace for DD4 strategy followed the line of motoring pressure

until 6.8^{o} CA ATDC where it experienced a rapid increase in pressure, reaching its maximum value of 45.7 bar at 15.8^{o} CA ATDC, 11.6^{o} CA after DD1 strategy. This delay was attributed to late initiation of combustion due to retarded injection timing of the first injection. The dwell angle between the two injections for this strategy was 5^{o} CA which was not sufficient for the injector to fully close prior to the onset of the second injection; thus, resulting in higher injected fuel quantity as shown in Figure 5.16. The peak in-cylinder pressure was the highest which was due to the greater fuel quantity injected. The in-cylinder pressure after the peak steadily decreased during the expansion stroke, yet remained higher than all other strategies. The fuel was injected at -5^{o} CA ATDC and TDC which led to an IMEP value of 5.42 bar.

The heat release rate for strategies DD1, DD2, DD3 and DD4 are presented in Figure 6.32. The heat release rate for DD1 strategy exhibited a minor decrease at -18.4^{o} CA ATDC due to charge cooling shortly after the onset of the first fuel injection and the hest transfer effects during the compression stroke which lasted until -16.4^{o} CA ATDC. The charge cooling effect was less noticeable since the fuel quantity injected during the first injection was considerably lower in comparison to 50:50 injection strategies. After this point, the rate of heat release progressively increased until -8.6^{o} CA ATDC where it rapidly increased, reaching its maximum value at -1.4^{o} CA ATDC, due to premixed combustion. This phase of combustion lasted until 3.6^{o} CA ATDC where the second phase of combustion started. The maximum heat release rate due to diffusion combustion occurred at 10.6^{o} CA ATDC and progressively decreased after this point. The heat released during this phase of combustion following the onset of the second injection was considerably higher than the maximum heat release rate due to premixed combustion. This was mainly due to the greater fuel quantity injected during the second injection. The heat release gradually decreased after the peak during the expansion stroke.

The heat release rate for DD2 strategy experienced a sudden decrease at -11.2^{o} CA ATDC due to charge cooling shortly after the onset of the first fuel injection and the heat transfer effects during the compression stroke which lasted until -7.8^{o} CA ATDC. After this point, the rate of heat release sharply increased until 2.4^{o} CA ATDC due to the first injection. At this point, the heat release rate rapidly increased for the second

time following the onset of the second fuel injection at TDC. The maximum heat release rate occurred at 10.6^{o} CA ATDC, 12.0^{o} CA after DD1 strategy, due to premixed combustion. This delay was due to retarded injection timing of the first injection in comparison to DD1 strategy. Subsequently, the heat release rate steadily decreased during the expansion stroke with no noticeable signs of diffusion combustion taking place based on the heat release rate data shown in Figure 6.32.

The heat release rate for DD3 strategy exhibited a minor decrease at -7.2^{o} CA ATDC due to charge cooling shortly after the onset of the first fuel injection and also the heat transfer effects during the compression stroke which lasted until -5.4^{o} CA ATDC. After this point, the rate of heat release rapidly increased, reaching its maximum value at 7.2^{o} CA ATDC, 8.6^{o} CA after DD1 strategy, due to premixed combustion. The peak heat release rate was lower than DD2 strategy since the time available for the combustion process to complete was more limited due to further retarded injection timing of the first injection. In addition, less fuel was injected due to the dwell angle used as shown in Figure 5.16. In this case the end of premixed combustion and the start of diffusion combustion were mixed and difficult to distinguish. The heat release gradually decreased after the peak during the expansion stroke.

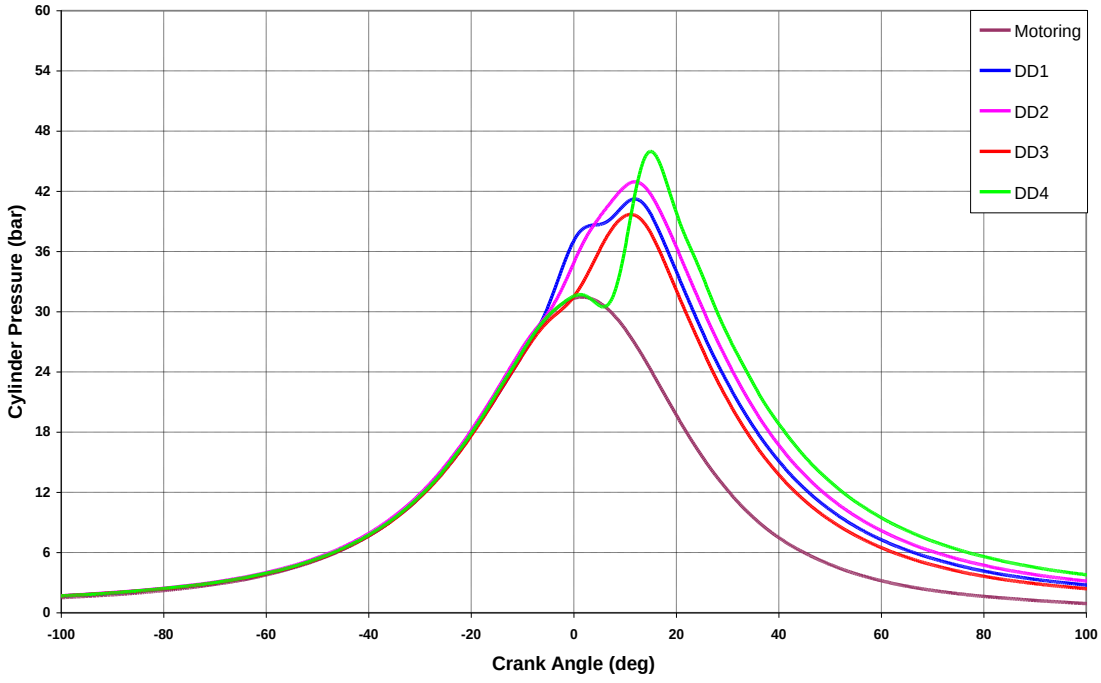

Figure 6.31 In-Cylinder Pressure Data for Strategy DD at 1200 bar

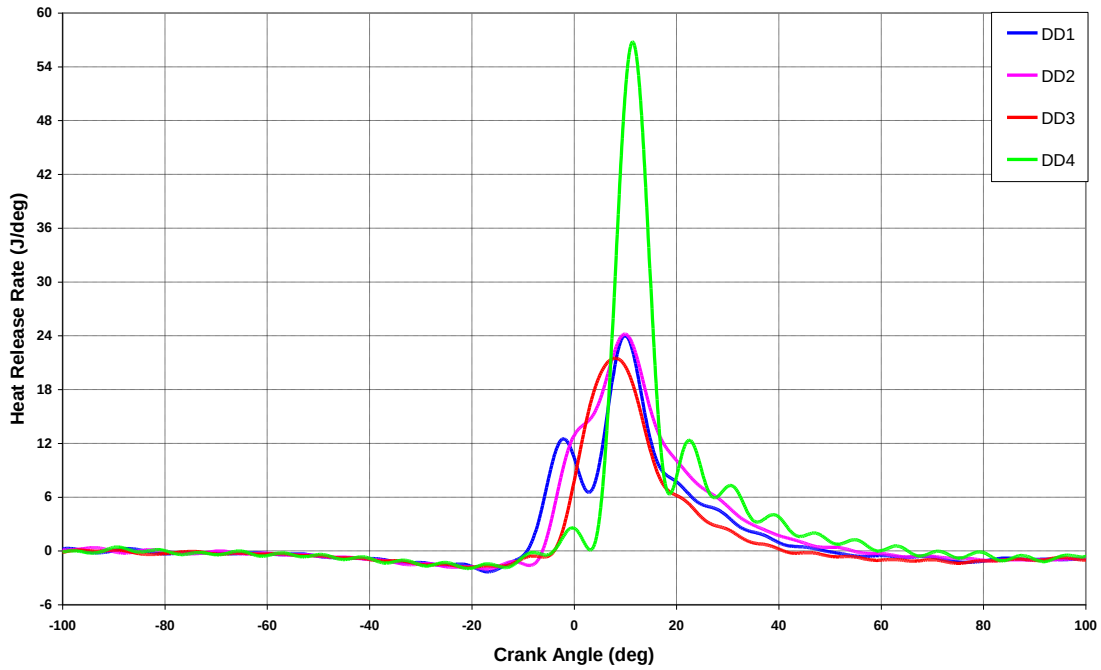

Figure 6.32 Heat Release Rate Traces for Strategy DD at 1200 bar

As previously stated, the dwell timing of 5^{o} CA resulted in total injected fuel quantity considerably higher than intended. The heat release rate for DD4 strategy experienced a sudden decrease at 0.4^{o} CA ATDC due to charge cooling effects which lasted until 3.6^{o} CA ATDC. After this point, the rate of heat release rapidly increased, reaching its maximum value at 11.8^{o} CA ATDC, 13.2^{o} CA after DD1 strategy, due to premixed combustion. This strategy produced the maximum heat release rate due to premixed combustion in comparison to the other strategies as shown in Figure 6.32. This was due to the greater fuel quantity injected as a consequence of the dwell angle used as well as longer ignition delay, indicating prolonged premixed phase, Table 6.4. Consequently, more fuel and air was mixed which led to greater heat release during the first phase of combustion. This phase of combustion lasted until 19.2^{o} CA ATDC where the second phase of combustion started. The maximum heat release rate due to diffusion combustion occurred at 23.2^{o} CA ATDC and progressively decreased after this point.

6.5.2.2 Fuel Injection and Combustion Visualisation

Figure 6.33 shows the image sequence obtained for DD2 strategy through high speed video imaging technique.

As previously mentioned, although DD4 strategy produced the maximum heat release rate, high speed imaging was carried out for DD2 strategy since the actual fuel quantity injected for DD4 strategy was much greater than 20 mm^3. The first three frames in Figure 6.33 show the fuel spray jets development from the start to the end of the first injection where in the last frame fuel sprays were almost fully evaporated. The fuel sprays in these images were not fully developed which was due to short injection duration of the first injection since 30% of total fuel quantity was injected at this stage. The frames presented at TDC, 1.8^o CA ATDC, 3.6 ^{o} CA ATDC and 5.4 ^{o} CA ATDC show the image sequence from the start to the end of the second injection. From the image sequence presented it is evident that the fuel sprays reached the piston wall. This was due to longer injection duration used during the second injection as 70% of total fuel quantity was injected at this stage.

The first combustion phase apparent from the heat release rate data at -7.8^o CA ATDC, Figure 6.32, resulted in no visible combustion until -2.7^o CA ATDC where the first visible combustion was observed. Flame was propagated in the same manner as that of D2 strategy, starting at the tip of the fuel sprays where fuel vapour was highly concentrated and spread along the periphery of the fuel sprays where fuel evaporation rate was considerably higher as shown in frames six and seven at 1.8^o CA ATDC and 3.6^o CA ATDC respectively. The flame spread to the outer regions of the sprays tip due to the fuel sprays impingement on the piston wall, creating a mushroom like structure. In the image sequence at 10.8^o CA ATDC, where approximately the maximum heat release rate occurred during premixed combustion, flame was almost fully propagated, covering the entire combustion chamber. From the image sequence at 23.4^o CA ATDC, 31.5^o CA ATDC and 42.3^o CA ATDC, it is evident that the flame intensity was diminishing during the expansion stroke. Although no diffusion combustion was detected for this strategy from the heat release rata data as shown in Figure 6.32, several combustion sites were present in the last two images, indicating the presence of some diffusion combustion corresponding to the second phase of combustion. Flame was moved in the clockwise direction due to the swirl motion as the combustion process evolved.

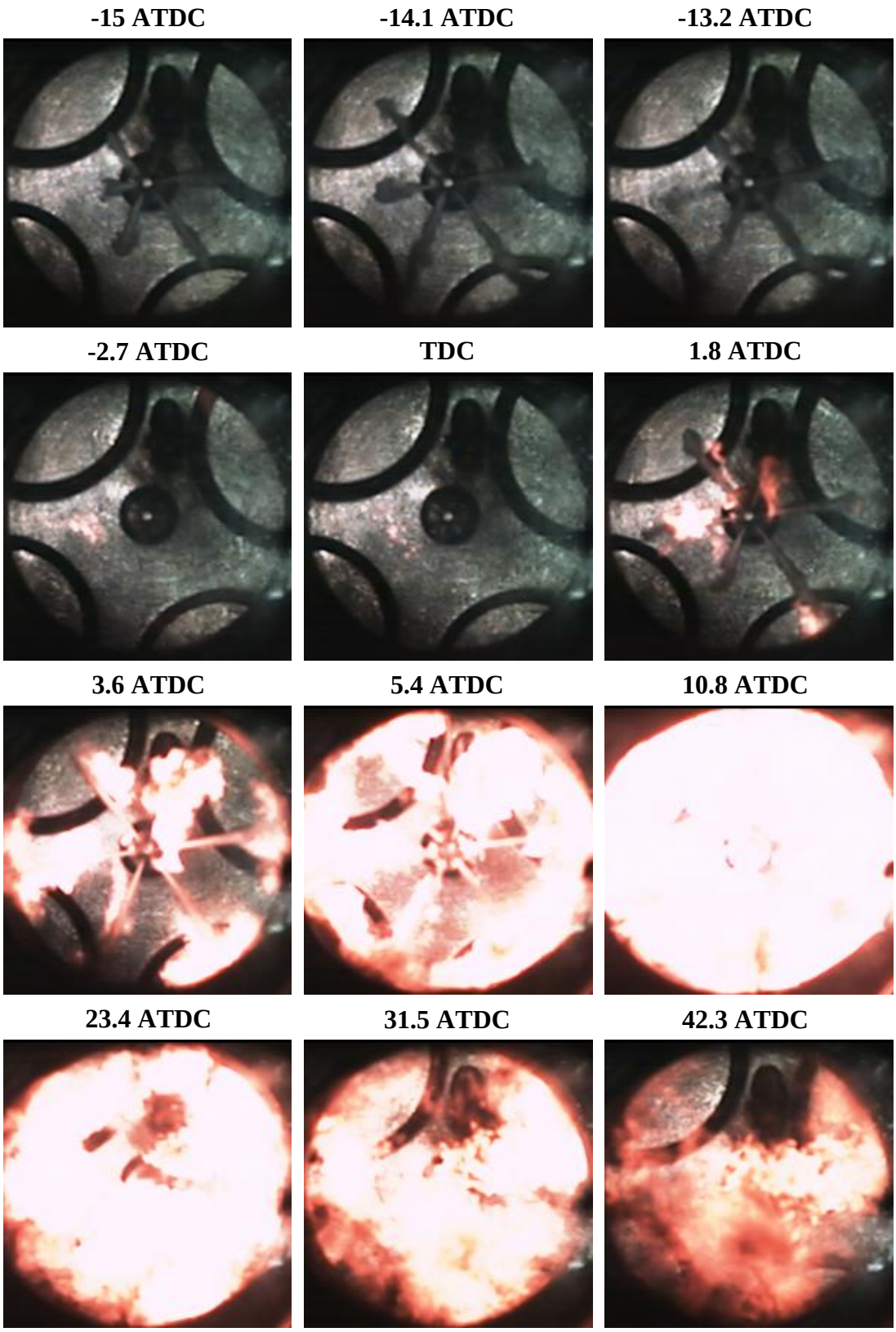

Figure 6.33 Combustion Image Sequence for DD2 Strategy at 1200 bar

6.5.2.3 Soot and Exhaust Emissions

The soot and gaseous exhaust emissions results for strategy DD are depicted in Figures 6.34 and 6.35 respectively.

The soot emission produced by DD strategies followed the same trend as those of D strategies. The soot level produced by DD2 strategy was considerably higher compared to DD1 strategy; this was mainly due to the greater fuel quantity injected for this strategy as a result of the dwell angle used. In contrast, the soot concentration for DD3 strategy was lower than DD1 and DD2 strategies since the fuel quantity injected was much lower than the other two strategies as shown in Figure 5.16.

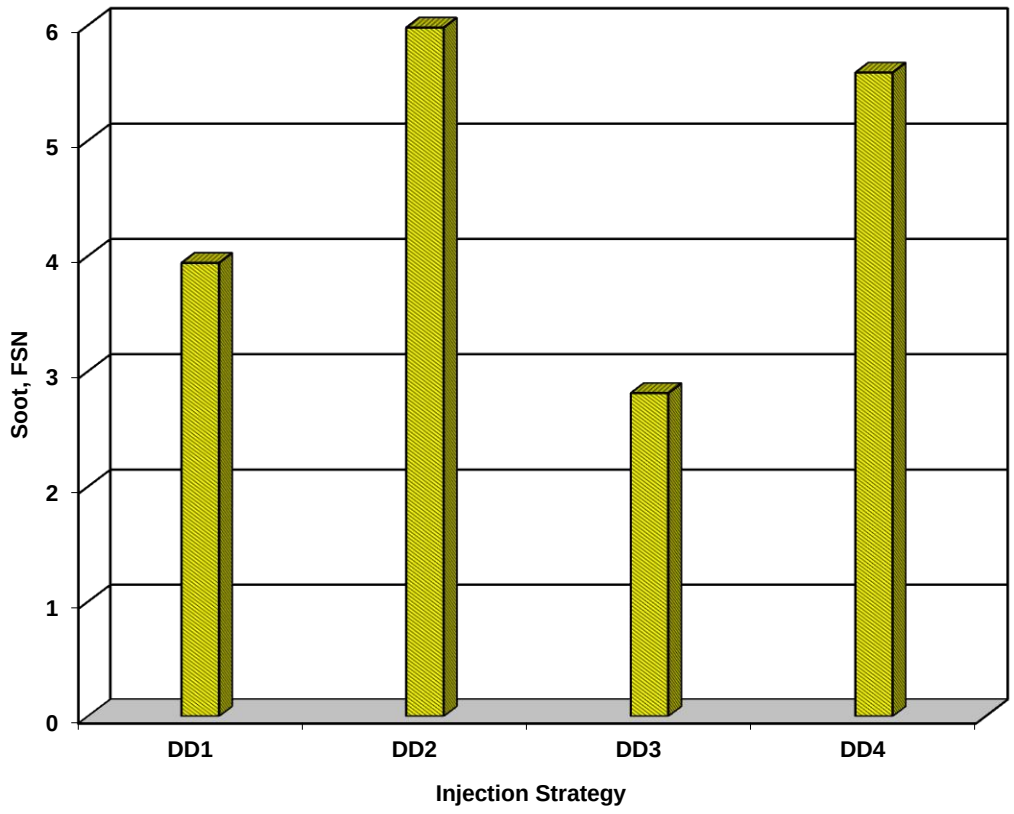

Figure 6.34 Soot Concentration for Strategy DD at 1200 bar

DD4 strategy produced high level of soot since the dwell timing between the two injections was not sufficient for the injector to fully close prior to the onset of the second injection; thus, replicating a single injection strategy with total injected fuel

quantity considerably higher than intended. Though, the soot produced by DD4 strategy remained lower than DD2 strategy due to the limited time available for the complete combustion.

The NOx and uHC emissions followed the same pattern as those of strategy BB. The NOx emission for DD2 strategy was almost identical to DD1 strategy since combustion took place in two stages for DD2 strategy which lowered the combustion temperature in comparison to DD1 strategy. In addition, more fuel was injected for this strategy due to the dwell timing used as shown in Figure 5.16, which led to lower in-cylinder temperatures as a result of latent heat of evaporation of fuel. The NOx emission produced by DD3 strategy was higher than DD1 and DD2 strategies since the fuel quantity injected was substantially higher for this strategy. In contrast, DD4 strategy produced lower NOx emission compared to DD3 strategy even though more fuel was injected; this was mainly due to the limited time available during the premixed and combustion phases.

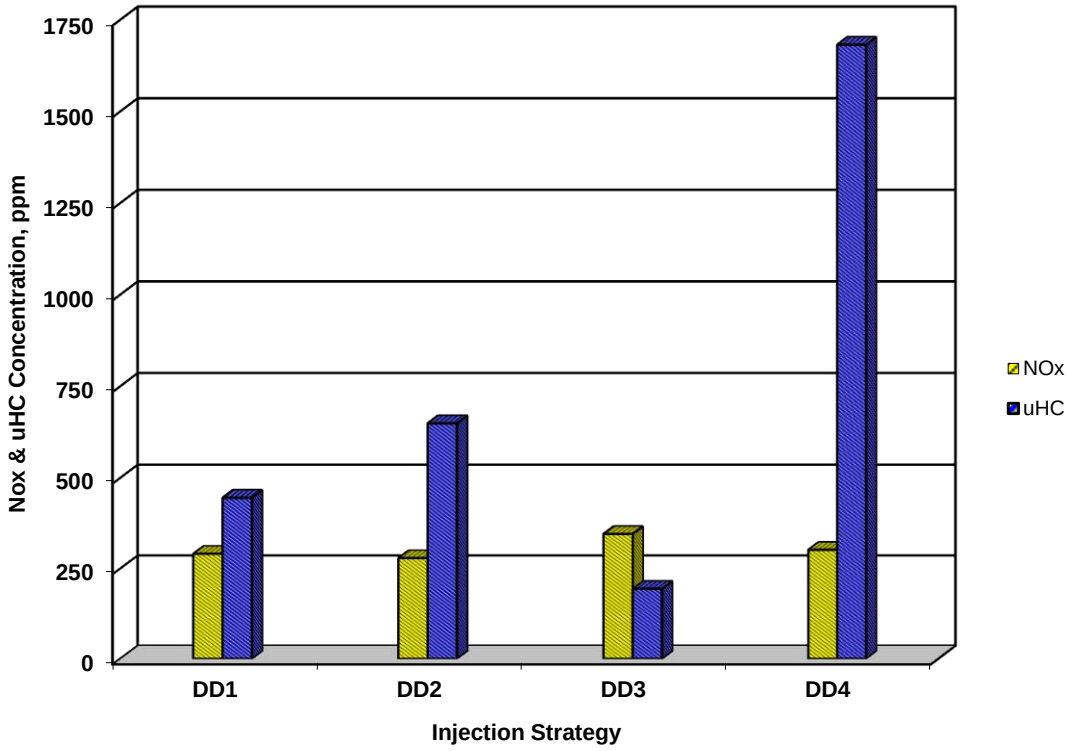

Figure 6.35 NOx and uHC Concentration for Strategy DD at 1200 bar

The uHC emission for DD2 strategy was higher compared to DD1 strategy; this was due to the greater fuel quantity injected for this strategy. In contrast, DD3 strategy produced less uHC emissions since the least fuel quantity was injected for this strategy; thus, low levels of unburned fuel remained inside the cylinder upon the completion of the combustion process. Moreover, fuel evaporation process was improved since the first fuel injection took place closer to TDC. DD4 strategies produced considerably higher uHC emission in comparison to all the other strategies, this was due to the dwell timing used for this strategy whereby the two injections interacted with each other, resulting in a single injection with much longer injection duration in comparison to the other dwell timings used in this study. In addition, the time available during the premixed and combustion phases was limited as the injection timing was further retarded. Therefore, high levels of unburned fuel remained inside the cylinder upon the completion of the combustion process.

6.6 Results of 70:30 Split Injection Strategy

6.6.1 Strategy F (Low load, 70:30 split injection with fixed 2nd injection at TDC)

This strategy involved analysis of injection timing with variable dwell angle between injections on the combustion and emissions characteristics of a four-stroke HSDI diesel engine through 70:30 split injection strategies. The total fuel demand was 10 mm^3.

6.6.1.1 In-Cylinder Pressure and Heat Release Rate Analysis

The in-cylinder pressure data for strategies F1, F2, F3 and F4 averaged over 20 consecutive cycles are shown in Figure 6.36. The in-cylinder pressure trace for F1 strategy followed the line of motoring pressure until -6.2^o CA ATDC where it rapidly increased, reaching its peak value of 37.1 bar at 4.4^o CA ATDC following the onset of the second injection at TDC. The in-cylinder pressure steadily decreased from this point during the expansion stroke. The fuel injections took place at -20^o CA ATDC and TDC which resulted an IMEP value of 1.01 bar.

The in-cylinder pressure trace for F2 strategy followed the line of motoring pressure

until -3.4^{o} CA ATDC where it suddenly increased and reached its peak value of 41.0 bar at 9.6^{o} CA ATDC, 5.2^{o} CA after F1 strategy. This delay was due to retarded injection timing of the first injection. The peak in-cylinder pressure was approximately 10% higher compared to F1 strategy mainly due to the difference in fuel quantity injected as the dwell timing changed as shown in Figure 5.15. The in-cylinder pressure steadily decreased after the peak during the expansion stroke. The fuel was injected at -15^{o} CA ATDC and TDC which led to an IMEP value of 2.33 bar.

The in-cylinder pressure trace for F3 strategy followed the line of motoring pressure until -3.8^{o} CA ATDC where it progressively increased until 1.2^{o} CA ATDC. The in-cylinder pressure suddenly increased at this point, reaching its maximum value of 36.3 bar at 7.8^{o} CA ATDC, 3.4^{o} CA after F1 strategy. This delay was due to retarded injection timing of the first injection whereby the combustion process took place later in the expansion stroke. The peak in-cylinder pressure was considerably lower than F2 strategy since the fuel quantity injected with 10^{o} CA dwell timing was considerably lower in comparison to F2 strategy where the dwell angle between the injections was 15^{o} CA as shown in Figure 5.15. The in-cylinder pressure after the peak steadily decreased during the expansion stroke. The fuel was injected at -10^{o} CA ATDC and TDC which resulted an IMEP value of 0.84 bar.

The in-cylinder pressure trace for F4 strategy followed the line of motoring pressure until 0.6^{o} CA ATDC where it progressively increased until 4.8^{o} CA ATDC. After this point, the in-cylinder pressure increased rapidly, reaching its maximum value of 40.8 bar at 13.8^{o} CA ATDC, 9.4^{o} CA after F1 strategy. As previously stated, this delay was due to further retarded injection timing of the first injection. The dwell angle between the two injections for this strategy was 5^{o} CA which was not sufficient for the injector to fully close prior to the onset of the second injection; thus, resulting in higher injected fuel quantity as shown in Figure 5.15. Consequently, the peak in-cylinder pressure was similar to F2 strategy even though combustion took place later in the expansion stroke where the time available for the combustion process to complete was more limited. The in-cylinder pressure after the peak steadily decreased during the expansion stroke, yet remained higher than all the other strategies. The fuel was injected at -5^{o} CA ATDC and TDC which led to an IMEP value of 3.06 bar.

The heat release rate for strategies F1, F2, F3 and F4 are presented in Figure 6.37. The heat release rate for F1 strategy exhibited a sudden decrease at -14.8^{o} CA ATDC due to charge cooling shortly after the onset of the first fuel injection and the heat transfer effects during the compression stroke which lasted until -12.2^{o} CA ATDC. After this point, the rate of heat release rapidly increased, reaching its maximum value at -2.4^{o} CA ATDC, due to premixed combustion. This phase of combustion lasted until 3.2^{o} CA ATDC where the second phase of combustion started. The maximum heat release rate due to diffusion combustion occurred at 8.2^{o} CA ATDC and progressively decreased after this point during the expansion stroke.

The heat release rate for F2 strategy experienced a sudden decrease at -10.8^{o} CA ATDC due to charge cooling shortly after the onset of the first fuel injection and the heat transfer effects during the compression stroke which lasted until -7.8^{o} CA ATDC. After this point, the rate of heat release sharply increased, reaching its peak value at 3.2^{o} CA ATDC, due to first injection. The heat release rate remained constant until 4.4^{o} CA ATDC where it increased for the second time, due to the second injection. The second peak due to premixed combustion occurred at 8.4^{o} CA ATDC, 10.8^{o} CA after F1 strategy. This delay was due to retarded injection timing of the first injection compared to F1 strategy. The maximum heat release was higher than F1 strategy mainly due to improved fuel evaporation and mixing effects given that the first fuel injection took place closer to TDC where the in-cylinder temperature was higher. In this case the end of premixed combustion and the start of diffusion combustion were mixed and difficult to distinguish. The heat release gradually decreased after the peak during the expansion stroke.

The heat release rate for F3 strategy exhibited a minor decrease at -6.8^{o} CA ATDC due to charge cooling shortly after the onset of the first fuel injection and the heat transfer effects during the compression stroke which lasted until -5.6^{o} CA ATDC. After this point, the rate of heat release rapidly increased, reaching its maximum value at 4.6^{o} CA ATDC, 7.0^{o} CA after F1 strategy, due to premixed combustion. The peak heat release rate was lower than F2 strategy since the time available for the combustion process to complete was more limited due to further retarded injection timing of the first injection. In addition, less fuel was injected due to the dwell angle

used between the two injections as shown in Figure 5.15. This phase of combustion lasted until 12.2^{o} CA ATDC where the second phase of combustion started. The heat released during the second phase of combustion was relatively lower than other strategies as evident in Figure 6.37. The heat release gradually decreased during the expansion stroke.

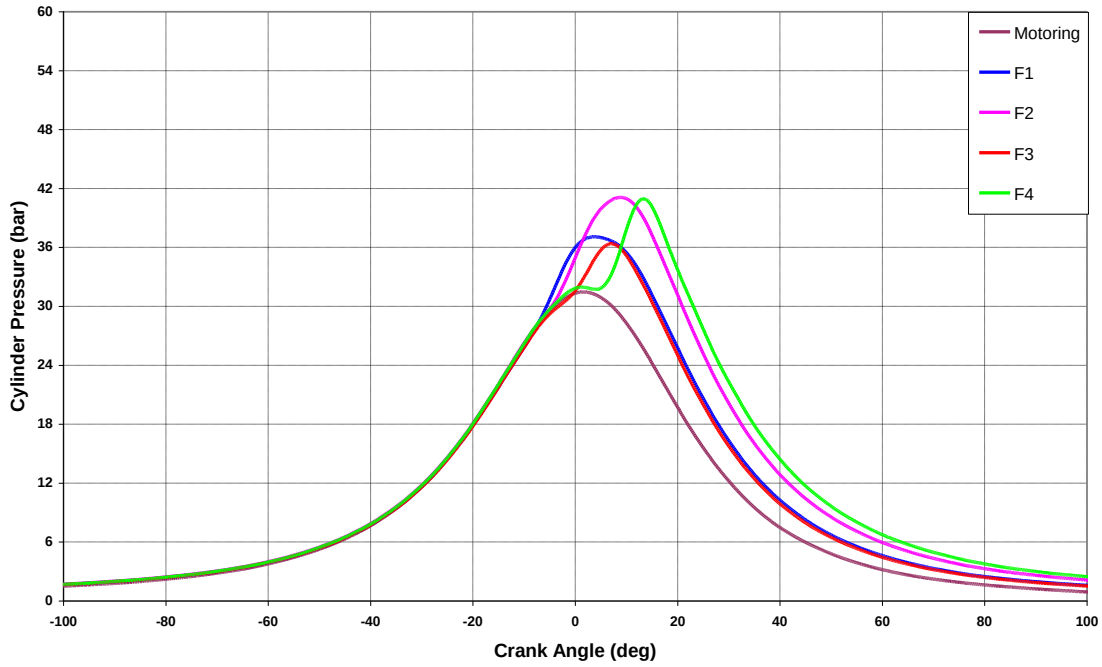

Figure 6.36 In-Cylinder Pressure Data for Strategy F at 1200 bar

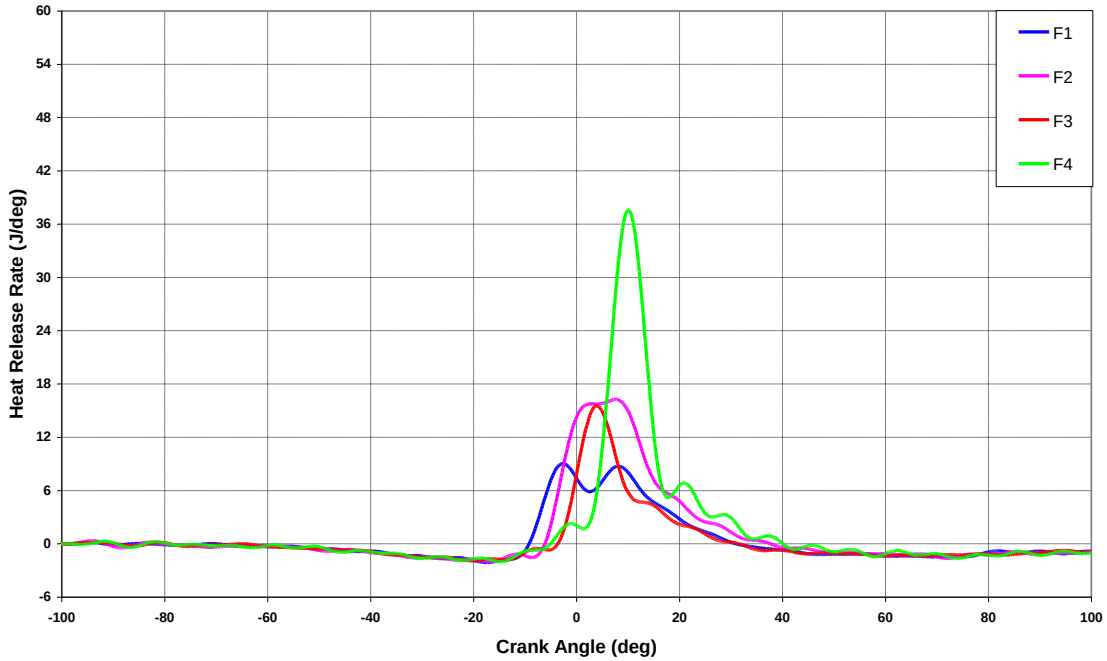

Figure 6.37 Heat Release Rate Traces for Strategy F at 1200 bar

As previously stated, the dwell timing of 5^{o} CA resulted in total injected fuel quantity considerably higher than intended. The heat release rate for F4 strategy experienced a sudden decrease at 0.6^{o} CA ATDC due to charge cooling effects which lasted until 2.2^{o} CA ATDC. After this point, the rate of heat release rapidly increased, reaching its maximum value at 10.4^{o} CA ATDC, 12.8^{o} CA after F1 strategy, due to premixed combustion. This strategy produced the maximum heat release rate due to premixed combustion in comparison to the other strategies as shown in Figure 6.37. This was due to the greater fuel quantity injected as a consequence of the dwell angle used as well as improved fuel evaporation effects as the first injection took place closer to TDC where the in-cylinder temperature was higher. This phase of combustion lasted until 18.2^{o} CA ATDC where the second phase of combustion started. The maximum heat release rate due to diffusion combustion occurred at 21.6^{o} CA ATDC and progressively decreased after this point during the expansion stroke.

6.6.1.2 Fuel Injection and Combustion Visualisation

Figure 6.38 shows the image sequence obtained for F2 strategy through high speed video imaging technique.

As previously mentioned, although F4 strategy produced the maximum heat release rate, high speed imaging was carried out for F2 strategy since the actual fuel quantity injected for F4 strategy was much greater than 10 mm^3. The first three frames in Figure 6.38 show the fuel spray jets development from the start to the end of the first injection where in the last frame, fuel sprays were almost fully evaporated. The fuel sprays in these images were not fully developed which was due to short injection duration of the first injection. The frames presented at TDC, 0.9^{o} CA ATDC, 1.8^{o} CA ATDC and 2.7^{o} CA ATDC show the image sequence from the start to the end of the second injection. From the image sequence presented it is evident that the fuel sprays reached the piston wall.

The first combustion phase apparent from the heat release rate data at -7.8^{o} CA ATDC, Figure 6.37, resulted in no visible combustion until -1.8^{o} CA ATDC where the first visible combustion was observed. Flame is propagated in the same manner as

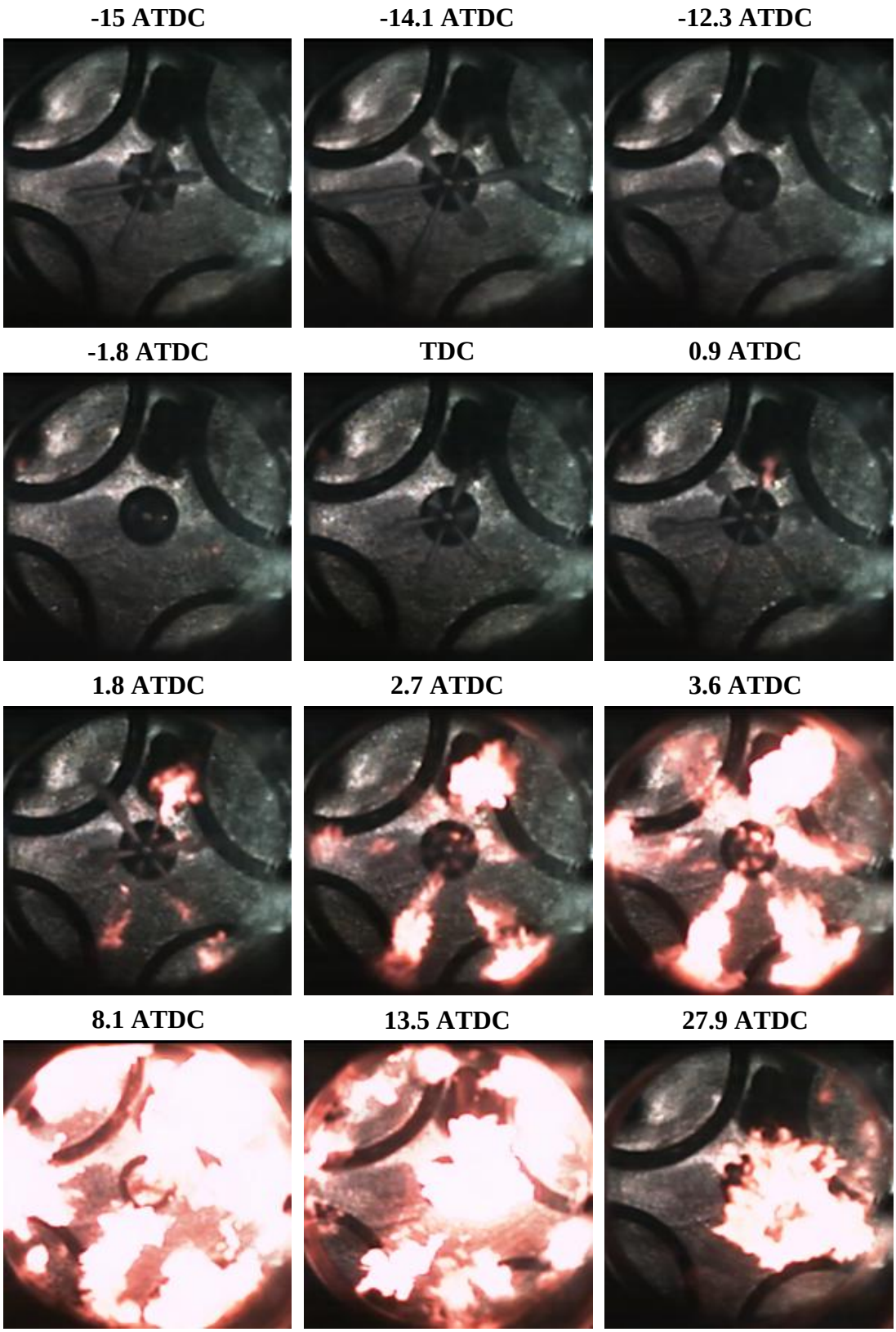

Figure 6.38 Combustion Image Sequence for F2 Strategy at 1200 bar

that of B2 strategy, starting at the tip of the fuel sprays where fuel vapour was highly concentrated and spread along the periphery of the fuel sprays where fuel evaporation rate was considerably higher than the core region as shown in frames seven and eight at 1.8^{o} CA ATDC and 2.7^{o} CA ATDC respectively. The flame spread to the outer regions of the sprays tip due to the fuel sprays impingement on the piston wall, creating a mushroom like structure as shown in frame nine at 3.6^{o} CA ATDC. In the next frame at 8.1^{o} CA ATDC, where approximately the maximum heat release rate occurred during premixed combustion, intense flame propagation took place spreading to the periphery of the piston wall where the majority of premixed fuel and air was concentrated. From the image sequence at 13.5^{o} CA ATDC it is evident that the flame intensity was diminishing during the expansion stroke as the combustion process advanced. Although the end of premixed combustion and the start of diffusion combustion for this strategy were mixed as shown in Figure 6.37, several combustion sites are present in the last frame at 27.9^{o} CA ATDC, indicating the presence of some diffusion combustion. Flame was moved in the clockwise direction as the combustion process evolved due to the swirl motion.

6.6.1.3 Flame Temperature and Soot Concentration Measurement

For this injection strategy, the high-speed two-colour method was used to measure the combustion temperature and soot loading. The flame temperature and *KL* factor image sequence for strategy F2 are shown in Figure 6.39.

Minor combustion at relatively low temperature was detected in the first frame at 0.9^{o} CA ATDC. The subsequent frames at 1.8 ^{o} CA ATDC and 2.7^{o} CA ATDC show flame propagation around the tip and periphery of the sprays where high concentration of premixed fuel vapour and air was present. As the combustion process evolved, the flame temperature increased as evident in the next frame at 8.1 ^{o} CA ATDC where high temperature flame was detected around the periphery of the piston bowl, the same trend was observed in high speed image sequence. This crank angle approximately corresponds to where the maximum heat release due to premixed combustion occurred. Once the maximum heat release due to premixed combustion was reached, the flame temperature steadily decreased as it progressed during the

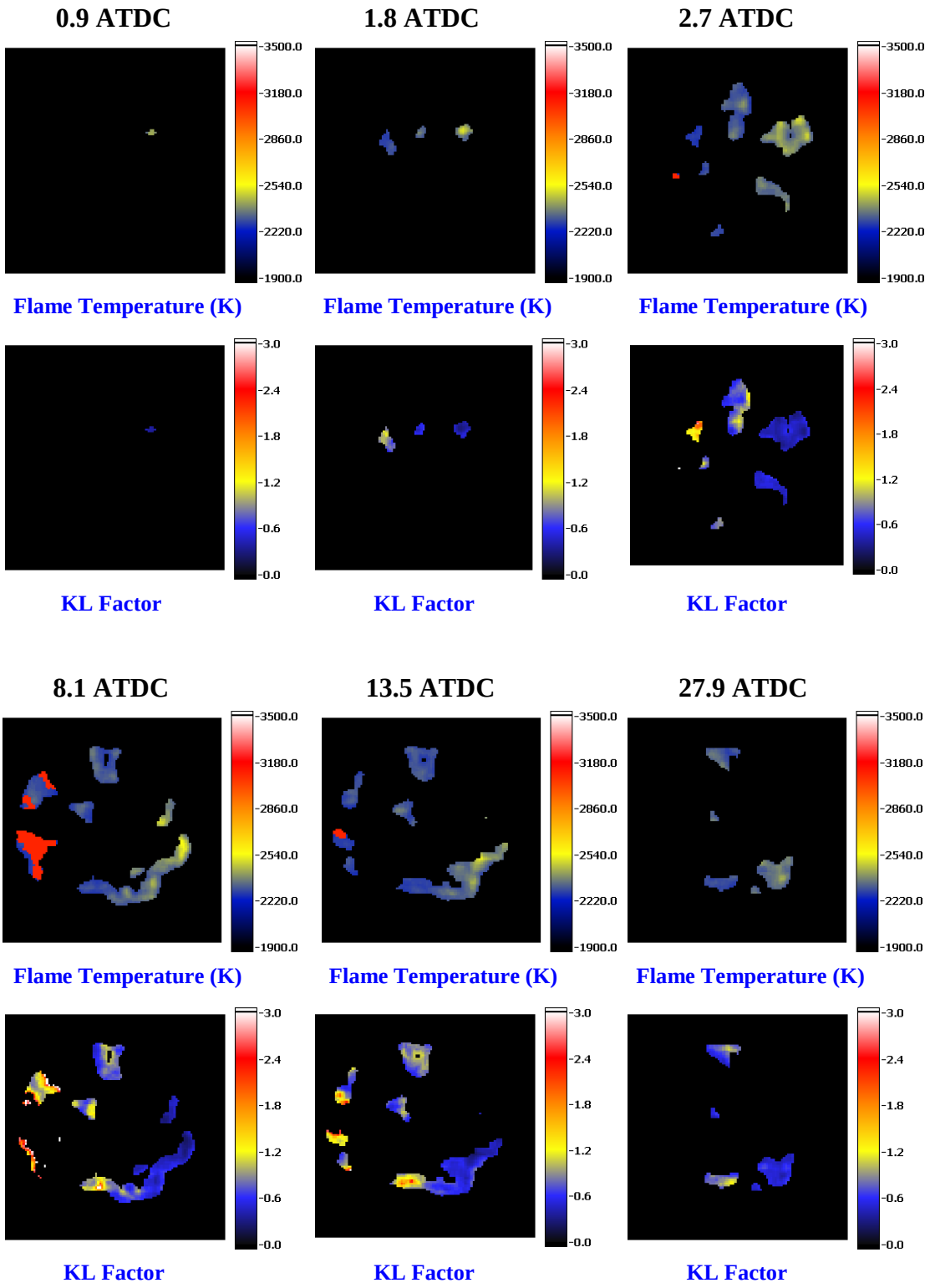

Figure 6.39 Flame Temperature and *KL* Factor Images for F2 Strategy at 1200 bar

expansion stroke as shown in the images at 13.5 ^{o} CA ATDC and 27.9^{o} CA ATDC respectively. Although luminous flame was detected through high speed imaging at crank angles later in the expansion stroke, no information could be detected at these crank angles due to inadequate sensitivity of the detection system at the preselected wavelengths in this investigation (i.e. 550 nm and 750 nm). The intensifier gain cannot be further increased due to image saturation at crank angles where highly luminous flame was present. Therefore, the first few frames at the initial and final stages of combustion were neglected as previously stated in Section 4.6.

The soot concentration profiles shown in Figure 6.39 followed the same pattern as that of flame temperature image sequence as expected. As shown by the *KL* factor images at 0.9 ^{o} CA ATDC and 1.8 ^{o} CA ATDC during initial stages of visible flame propagation during premixed combustion, soot concentration was very low. During this phase of combustion, soot was formed around the tip of the sprays. In the next two frames, soot concentration increased as the combustion process progressed during the expansion stroke. Soot was mainly concentrated at the tip of the sprays and the periphery of the piston bowl where the flame temperature was considerably high due to high concentration of premixed fuel vapour and air. Soot concentration decreased in the remaining image sequence mainly due to oxidation.

Soot concentration profiles depicted in these images suffer from low signal to noise ratio caused by low sensitivity of the detection system. Thus, although the trend in soot formation and oxidation could be determined from these images, care must be taken in quantitative analysis of these images. This strategy produced relatively high level of soot emission due to the greater fuel quantity injected which was caused by the injection timing used for this strategy as previously stated. This was further confirmed by the soot emission results presented in the next section.

6.6.1.4 Soot and Exhaust emissions

The soot and gaseous exhaust emissions results for strategy F are depicted in Figures 6.40 and 6.41 respectively.

The soot level produced by F2 strategy was considerably higher compared to F1 strategy; this was mainly due to the greater fuel quantity injected for this strategy as a

result of the dwell angle used. In contrast, the soot concentration for F3 strategy was lower than F1 and F2 strategies since the fuel quantity injected was much lower than the other two strategies as shown in Figure 5.15. Moreover, the ignition delay for this strategy was shorter in comparison to F1 and F2 strategies as shown in Table 6.4; thus, fuel and air mixing rate was limited during the premixed phase of combustion which led to low intensity combustion accompanied by lower soot emission. F4 strategy produced the highest soot emission due to the greater fuel quantity injected. In addition, less time was available for soot oxidation due to retarded injection timing of the first injection.

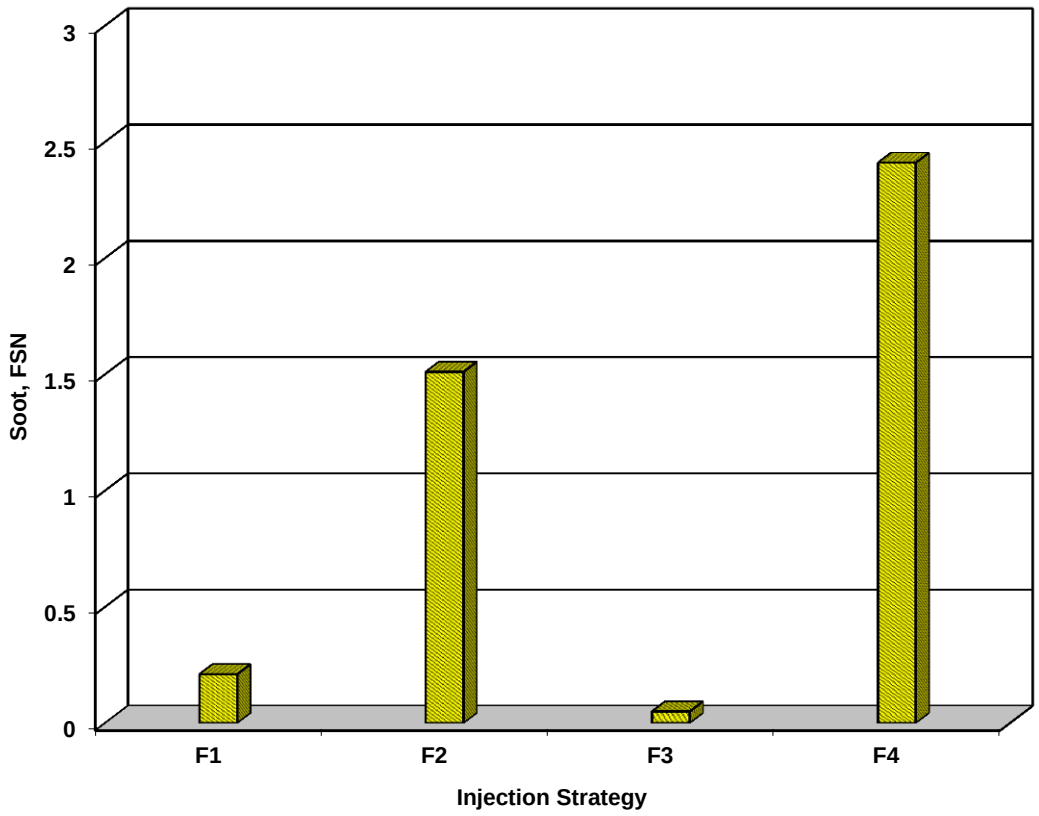

Figure 6.40 Soot Concentration for Strategy F at 1200 bar

The NOx and uHC emissions followed the same pattern as those of strategy D. The NOx emission produced by F2 strategy was considerably higher than F1 strategy since greater fuel quantity was injected for F2 strategy due to the dwell timing used as shown in Figure 5.15, which resulted in higher temperature combustion. In contrast, F3 strategy produced lower NOx emission compared to F2 strategy since the injected

fuel quantity was less for F3 strategy as shown in Figure 5.15. Nevertheless, NOx emission produced by F3 was higher than F2 even though less fuel was injected, this was due to improved fuel evaporation and mixing processes since the first injection took place closer to TDC where the in-cylinder temperature was higher. The NOx emission produced by F4 strategy was the highest in comparison to the other strategies since the dwell timing between the two injections was not sufficient for the injector to fully close prior to the onset of the second injection which resulted in greater total fuel quantity injected than intended.

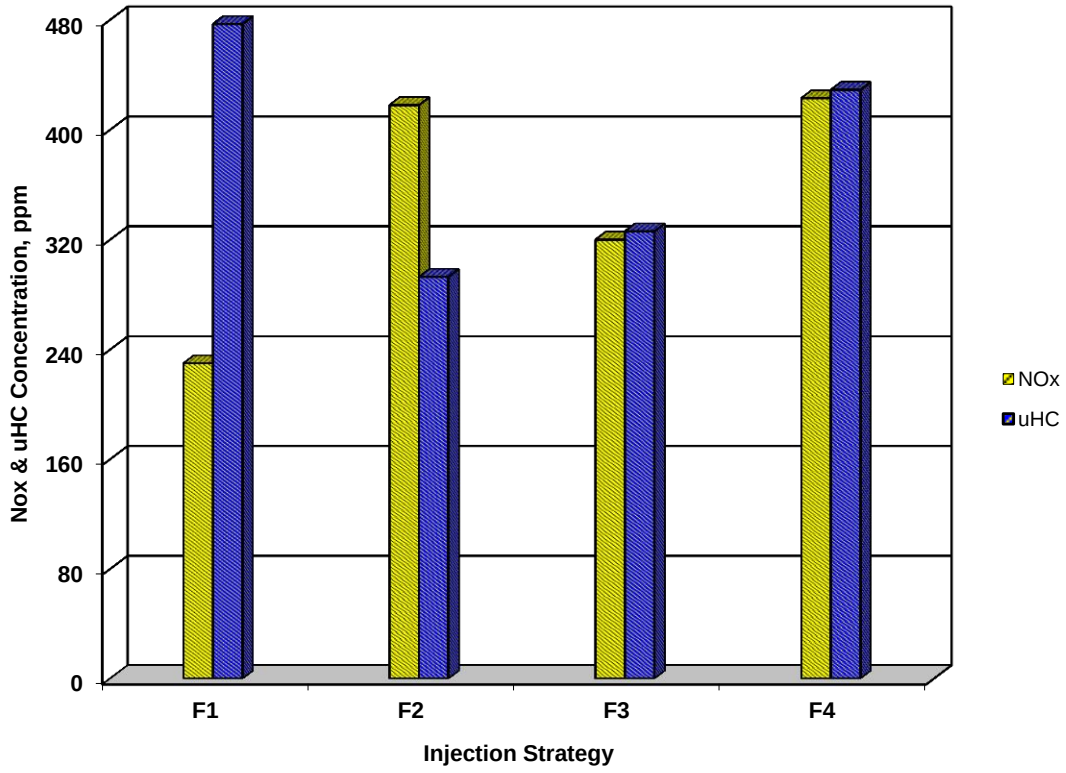

Figure 6.41 NOx and uHC Concentration for Strategy F at 1200 bar

The uHC emission for F2 strategy was lower in comparison to F1 strategy, this was due to improved fuel evaporation and mixing processes since the first fuel injection took place closer to TDC. F3 strategy produced higher uHC emission in comparison to F2 strategy mainly due to the limited time available during the premixed and combustion phases as the injection timing of the first injection was further retarded. F4 strategy produced the highest uHC emission in comparison to all the other

strategies, this was due to the dwell timing used for this strategy whereby the two injections interacted with each other, resulting in a single injection with much longer injection duration in comparison to the other dwell timings used in this study as shown in Figure 5.15. In addition, the time available during the premixed and combustion phases was limited as the injection timing was further retarded. Therefore, high level of unburned fuel remained inside the cylinder upon the completion of the combustion process.

6.6.2 Strategy FF (High load, 70:30 split injection with fixed 2nd injection at TDC)

This strategy involved analysis of injection timing with variable dwell angle between injections on the combustion and emissions characteristics of a four-stroke HSDI diesel engine through 70:30 split injection strategies whereby 70% of total fuel quantity was injected during the first injection and the remaining during the second. The total fuel demand was 20 mm^3.

6.6.2.1 In-Cylinder Pressure and Heat Release Rate Analysis

The in-cylinder pressure data for strategies FF1, FF2, FF3 and FF4 averaged over 20 consecutive cycles are shown in Figure 6.42. The in-cylinder pressure trace for FF1 strategy followed the line of the motoring pressure until -18.8^o CA ATDC where it progressively increased until -6.2^o CA ATDC. After this point, the in-cylinder pressure rapidly increased, reaching its peak value of 37.9 bar at 3.2^o CA ATDC following the onset of the second injection. The in-cylinder pressure steadily decreased from this point during the expansion stroke. The fuel injections took place at -20^o CA ATDC and TDC which resulted an IMEP value of 1.54 bar.

The in-cylinder pressure trace for FF2 strategy followed the line of motoring pressure until -3.6^o CA ATDC where it suddenly increased and reached its peak value of 48.9 bar at 6.6^o CA ATDC, 3.4^o CA after FF1 strategy. This delay was due to retarded injection timing of the first injection. The peak in-cylinder pressure value was higher in comparison to FF1 strategy. This was mainly due to the difference in the fuel quantity injected as the dwell angle between the two injections changed as shown in

Figure 5.16. The in-cylinder pressure steadily decreased after the peak during the expansion stroke. The fuel was injected at -15^{o} CA ATDC and TDC which led to an IMEP value of 3.71 bar.

The in-cylinder pressure trace for FF3 strategy followed the line of motoring pressure until -1.2^{o} CA ATDC where it suddenly increased, reaching its maximum value of 47.3 bar at 8.4^{o} CA ATDC, 5.2^{o} CA after FF1 strategy. As previously mentioned, this delay was due to retarded injection timing of the first injection whereby the combustion process took place later in the expansion stroke. The peak in-cylinder pressure was lower than FF2 strategy since the fuel quantity injected with 10^{o} CA dwell timing between the two injections was lower compared to FF2 strategy where the dwell angle between the injections was 15^{o} CA as shown in Figure 5.16. The in-cylinder pressure after the peak steadily decreased during the expansion stroke. The fuel was injected at -10^{o} CA ATDC and TDC which led to an IMEP value of 2.62 bar.

The in-cylinder pressure trace for FF4 strategy followed the line of motoring pressure until 6.6^{o} CA ATDC where it experienced a rapid increase in pressure, reaching its maximum value of 48.8 bar at 15.8^{o} CA ATDC, 12.6^{o} CA after FF1 strategy. This delay was attributed to late initiation of combustion due to further retarded injection timing of the first injection. The dwell angle between the two injections for this strategy was 5^{o} CA which was not sufficient for the injector to fully close prior to the onset of the second injection; thus, greater fuel quantity was injected as shown in Figure 5.16. The peak in-cylinder pressure was identical to that of FF2 strategy even though greater fuel quantity was injected for this strategy. This was due to the limited time available during the premixed and combustion phases for FF4 strategy since the timing of the first injection was further retarded in comparison to FF2 strategy. The in-cylinder pressure after the peak steadily decreased during the expansion cycle, yet remained higher than all the other strategies. The fuel was injected at -5^{o} CA ATDC and TDC which resulted an IMEP value of 5.74 bar.

The heat release rate for strategies FF1, FF2, FF3 and FF4 are presented in Figure 6.43. The heat release rate for FF1 strategy exhibited a sudden decrease at -18.6^{o} CA ATDC due to charge cooling shortly after the onset of the first injection and the heat

transfer effects during the compression stroke which lasted until -9.8^{o} CA ATDC. The charge cooling effect was much more significant in comparison to all the other strategies presented in previous sections. This was due to the greater fuel quantity injected during the first injection. After this point, the rate of heat release rapidly increased, reaching its peak value at -0.4^{o} CA ATDC, due to premixed combustion. This phase of combustion lasted until 5.4^{o} CA ATDC where the heat release rate sharply increased, reaching its second peak at 10.6^{o} CA ATDC, due to diffusion combustion following the start of the second injection. The heat release gradually decreased after the peak during the expansion stroke.

The heat release rate for FF2 strategy experienced a sudden decrease at -10.8^{o} CA ATDC due to charge cooling shortly after the onset of the first fuel injection and the heat transfer effects during the compression stroke which lasted until -6.8^{o} CA ATDC. After this point, the rate of heat release rapidly increased until 0.8^{o} CA ATDC where the maximum heat release due to premixed combustion occurred, 1.2^{o} CA after FF1 strategy. This delay was due retarded injection timing of the fist injection in comparison to FF1 strategy. This phase of combustion lasted until 7.8^{o} CA ATDC where the heat release rate exhibited a second peak at 11.4^{o} CA ATDC, due to diffusion combustion. The heat release gradually decreased after the peak during the expansion stroke.

The heat release rate for FF3 strategy experienced a sudden decrease at -7.6^{o} CA ATDC due to charge cooling shortly after the onset of the first fuel injection and also the heat transfer effects during the compression stroke which lasted until -3.4^{o} CA ATDC. After this point, the rate of heat release rapidly increased until 4.4^{o} CA where the maximum heat release due to premixed combustion occurred, 4.8^{o} CA after FF1 strategy. The peak heat release rate was higher than FF2 strategy due to improved fuel evaporation since the first injection took place closer to TDC where the in-cylinder temperature was higher. This phase of combustion lasted until 11.8^{o} CA ATDC where the heat release rate exhibited a second peak at 16.2^{o} CA ATDC, due to diffusion combustion. The heat release gradually decreased after the peak during the expansion stroke.

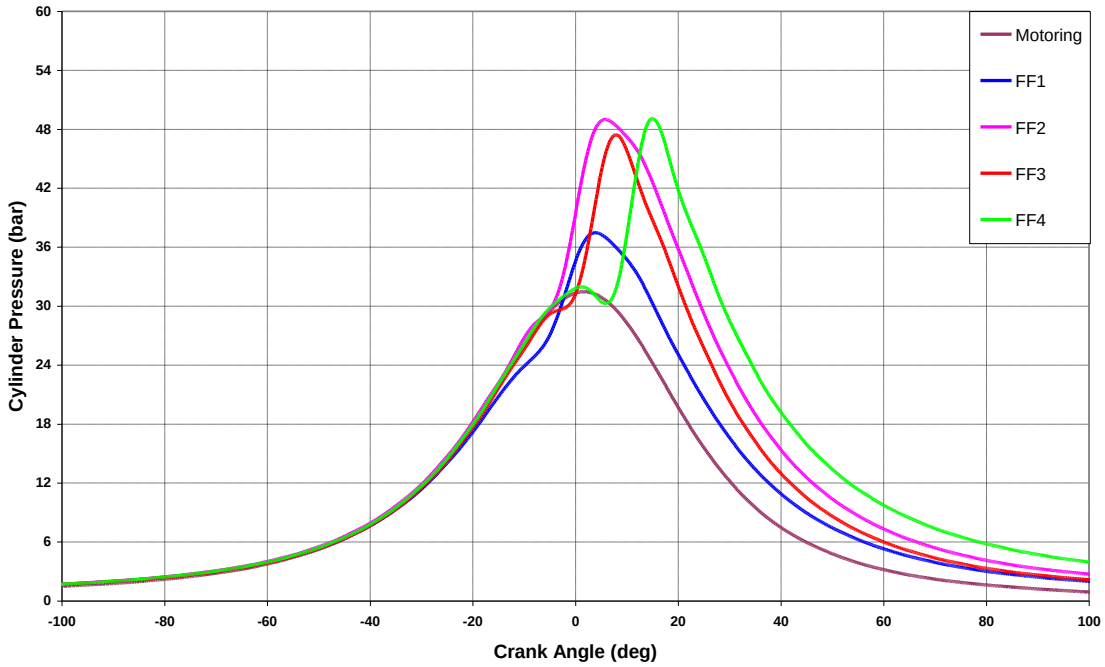

Figure 6.42 In-Cylinder Pressure Data for Strategy FF at 1200 bar

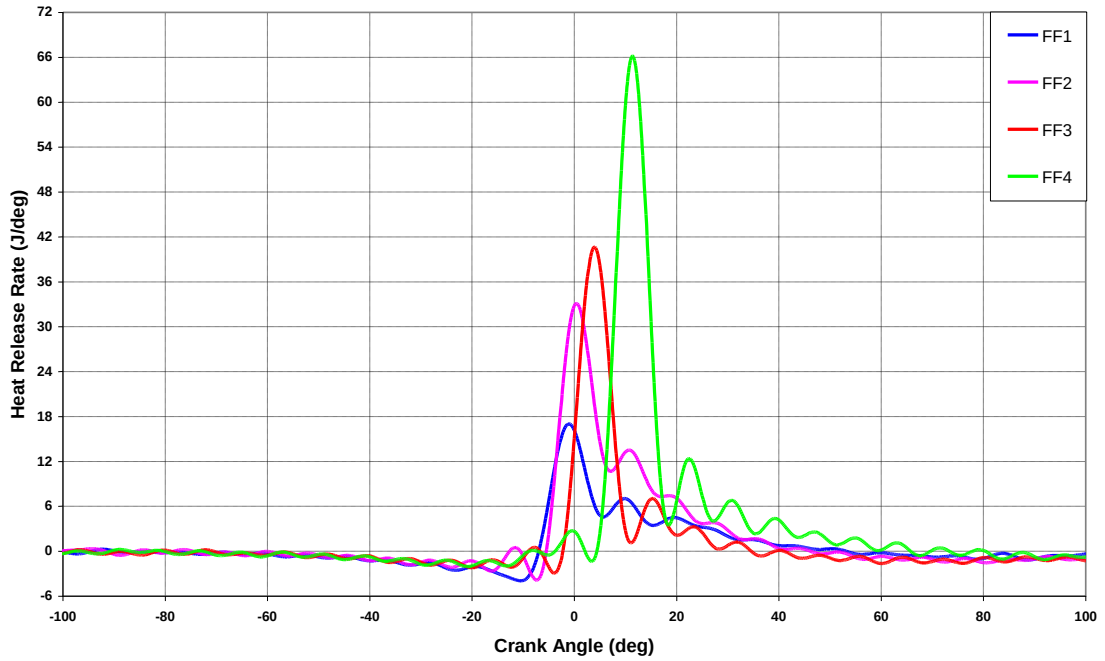

Figure 6.43 Heat Release Rate Traces for Strategy FF at 1200 bar

As previously stated, 5^{o} CA dwell timing between the two injections was not sufficient for the injector to fully close prior to the onset of the second injection which resulted in the total injected fuel quantity considerably higher than intended. The heat release rate for FF4 strategy experienced a sudden decrease at 0.4^{o} CA ATDC due to

charge cooling shortly after the onset of the second injection which lasted until 3.8^{o} CA ATDC. After this point, the rate of heat release rapidly increased, reaching its maximum value at 11.6^{o} CA ATDC, 12.0^{o} CA after FF1 strategy, due to premixed combustion. This strategy produced the maximum heat release rate due to premixed combustion in comparison to the other strategies as shown in Figure 6.43. This was due to the greater fuel quantity injected as a consequence of the dwell angle used as shown in Figure 5.16. This phase of combustion lasted until 18.8^{o} CA ATDC where the second phase of combustion started. The maximum heat release rate due to diffusion combustion occurred at 23.2^{o} CA ATDC and progressively decreased after this point.

6.6.2.2 Fuel Injection and Combustion Visualisation

Figure 6.44 shows the image sequence obtained for FF2 strategy through high speed video imaging technique.

As previously stated, although FF4 strategy produced the maximum heat release rate, high speed imaging was carried out for FF2 strategy since the actual fuel quantity injected for FF4 strategy was much greater than 20 mm^{3}. The first four frames in Figure 6.44 show the fuel spray jets development from the start to the end of the first injection where in the last frame fuel sprays were almost fully evaporated. The fuel sprays in frames three and four were fully developed due to long injection duration of the first injection since 70% of total fuel quantity was injected at this stage. The fuel sprays impingement on the piston wall is evident from these images where the tip of fuel sprays spread along the piston wall upon impact, generating a mushroom type structure. The frames presented at TDC, 0.9^{o} CA ATDC, 1.8 ^{o} CA ATDC and 3.6 ^{o} CA ATDC show the image sequence from the start to the end of the second injection. From the image sequence presented it is evident that the fuel sprays reached the piston wall during the second injection.

The first combustion phase apparent from the heat release rate data at -6.8^{o} CA ATDC, Figure 6.43, resulted in no visible combustion until -3.6^{o} CA ATDC where the first visible combustion was observed. Flame was propagated in the same manner as that of BB2 strategy, starting at the tip of the fuel sprays where fuel vapour was highly

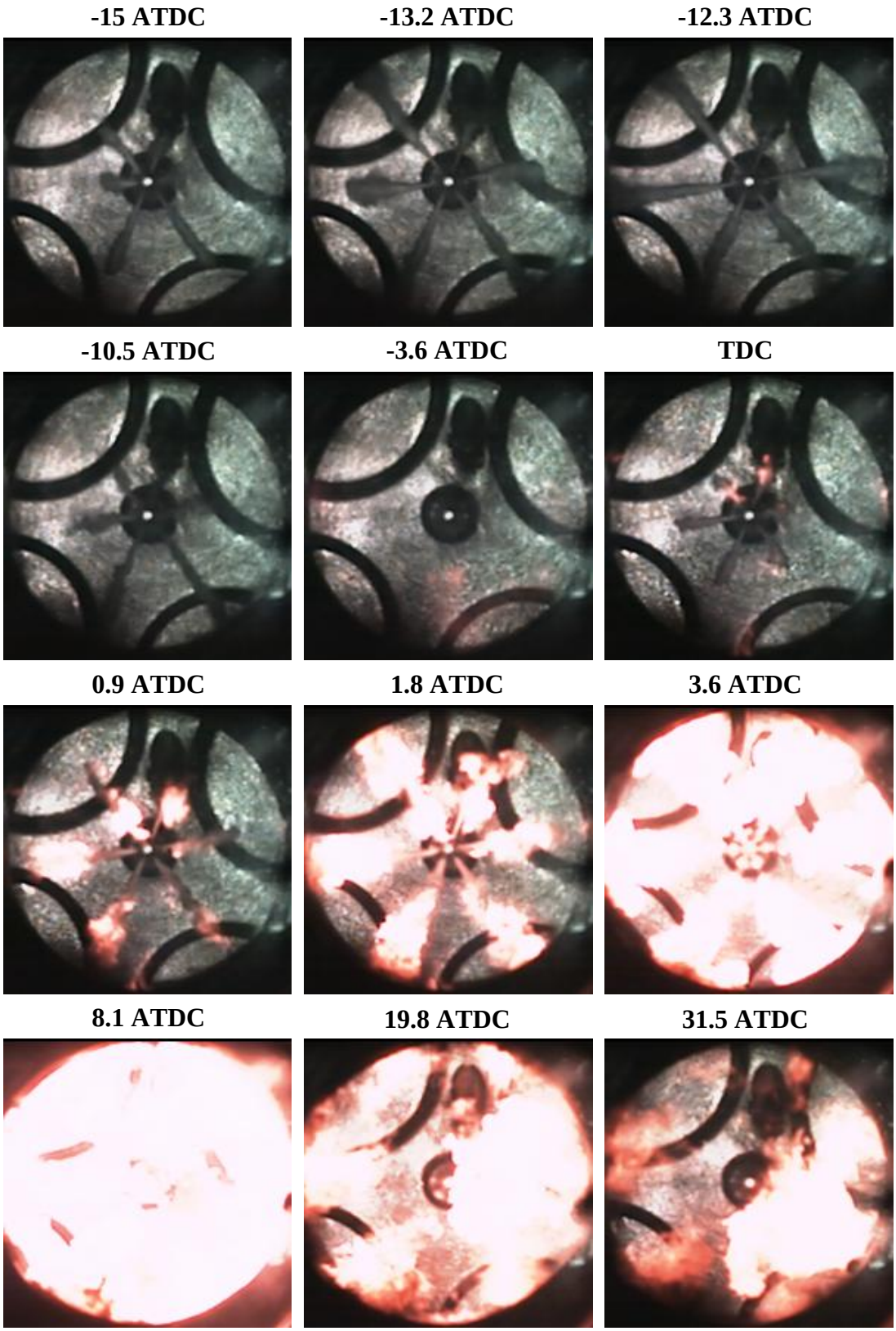

Figure 6.44 Combustion Image Sequence for FF2 Strategy at 1200 bar

concentrated and spread along the periphery of the fuel sprays where fuel evaporation rate was considerably higher as shown in frames seven and eight at 0.9^{o} CA ATDC and 1.8^{o} CA ATDC respectively. In the next frame at 3.6^{o} CA ATDC, the flame spread to the outer regions of the sprays tip due to the fuel sprays impingement on the piston wall, following the mushroom like structure previously created due to fuel spray impingement. In the subsequent frame at 8.1^{o} CA ATDC, flame was fully propagated covering the entire combustion chamber. From the image sequence at 19.8^{o} CA ATDC and 31.5^{o} CA ATDC, it is evident that the flame intensity was diminishing during the expansion stroke. Several combustion sites are present in the last two images, indicating the presence of diffusion combustion corresponding to the second phase of combustion. Flame was moved in the clockwise direction due to the swirl motion as the combustion process evolved.

6.6.2.3 Flame Temperature and Soot Concentration Measurement

The flame temperature and *KL* factor image sequence for strategy FF2 are shown in Figure 6.45.

Minor combustion at relatively low temperature was detected in the first frame at 0.9^{o} CA ATDC, which was in good agreement with the high speed image taken at this crank angle, Figure 6.44, which indicated minor combustion at the same location. The subsequent frames at 1.8 ^{o} CA ATDC and 3.6^{o} CA ATDC show flame propagation around the tip and periphery of the sprays where high concentration of premixed fuel vapour and air was present. As the combustion process evolved, the flame temperature increased as evident in the next frame at 8.1 ^{o} CA ATDC where high temperature flame was detected around the periphery of the piston bowl, the same trend was observed in high speed image sequence. This crank angle approximately corresponded to where the maximum heat release due to premixed combustion occurred. Once the maximum heat release due to premixed combustion was reached, the flame temperature steadily decreased as it progressed during the expansion stroke as shown in image sequence at 19.8 ^{o} CA ATDC and 31.5^{o} CA ATDC respectively. Although luminous flame was detected through high speed imaging at crank angles later in the expansion stroke, no information could be detected at these crank angles due to

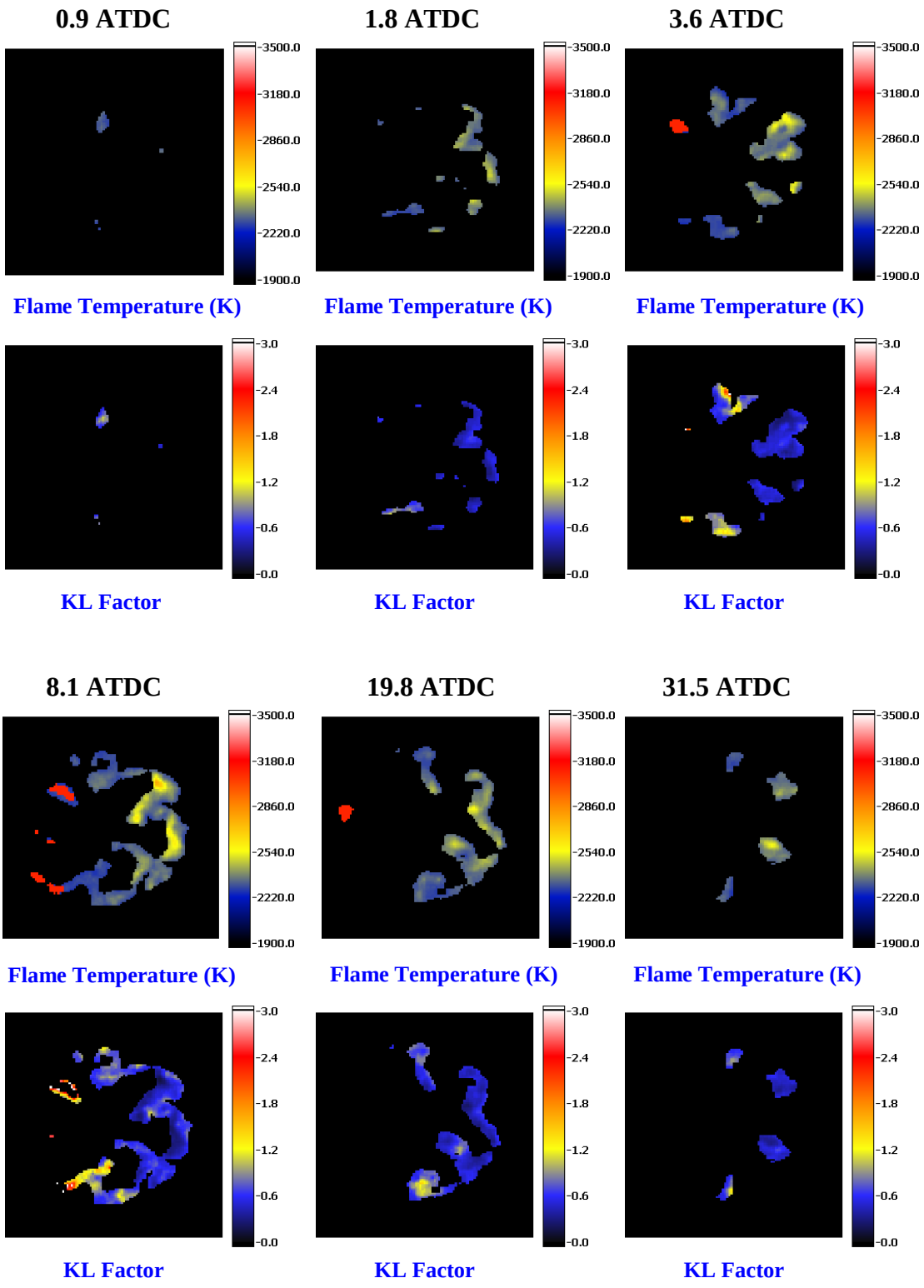

Figure 6.45 Flame Temperature and *KL* Factor Images for FF2 Strategy at 1200 bar

inadequate sensitivity of the detection system at the preselected wavelengths in this investigation (i.e. 550nm and 750nm). The intensifier gain cannot be further increased due to image saturation at crank angles where highly luminous flame was present. Therefore, the first few frames at the initial and final stages of combustion were neglected as previously mentioned.

The soot concentration profile shown in Figure 6.45 followed the same pattern as that of flame temperature image sequence as expected. As shown by the *KL* factor images at 0.9^{o} CA ATDC and 1.8^{o} CA ATDC during initial stages of visible flame propagation, soot concentration was very low. During this phase of combustion soot was formed around the tip and periphery of the sprays. In the next two frames at 3.6^{o} CA ATDC and 8.1^{o} CA ATDC, soot concentration increased, spreading to the periphery of the combustion bowl as the combustion process progressed during the expansion stroke. Soot was mainly concentrated around the tip of the fuel sprays and the periphery of the piston bowl where the flame temperature was considerably high due to high concentration of premixed fuel vapour and air. Soot concentration decreased in the remaining image sequence mainly due to oxidation. Soot concentration was higher in comparison to F2 strategy since the total fuel quantity injected was twice that of F2 strategy.

The same explanation regarding low signal to noise ratio of the results obtained holds true in this case, though its effect was less paramount since the flame intensity was considerably higher than F2 strategy. Thus, although the trend in soot formation and oxidation could be determined from these images, care must be taken in quantitative analysis of these images. This strategy produced exceedingly high level of soot emission due to greater total fuel demand for this strategy (20 mm^3). This was further confirmed by the soot emission results presented in the next section.

6.6.2.4 Soot and Exhaust Emissions

The soot and gaseous exhaust emissions results for strategy FF are depicted in Figures 6.46 and 6.47 respectively.

The soot emission produced by FF strategies followed the same trend as that of DD strategies. The soot level produced by FF2 strategy was considerably higher compared to FF1 strategy; this was mainly due to the greater fuel quantity injected for this strategy as a result of the dwell angle used. In contrast, the soot concentration for FF3 strategy was lower than FF1 and FF2 strategies since the fuel quantity injected was much lower than the other two strategies as shown in Figure 5.16. In addition the time available for soot formation was more limited due to retarded injection timing of the first injection. FF4 strategy produced high level of soot since the dwell timing between the two injections was not sufficient for the injector to fully close prior to the onset of the second injection which resulted in total injected fuel quantity considerably higher than intended. However, the soot produced by FF4 strategy remained lower than FF2 strategy due to the limited time available during the premixed and combustion phases for FF4 strategy which in turn limited the time available for soot formation.

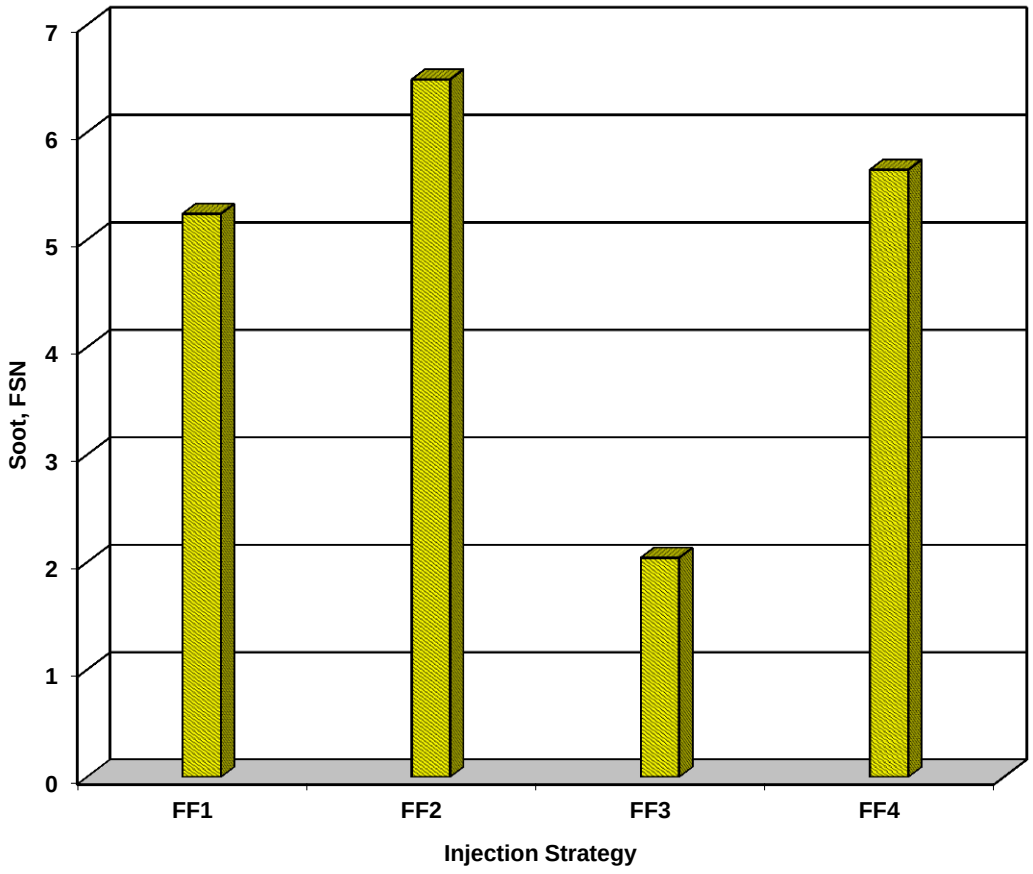

Figure 6.46 Soot Concentration for Strategy FF at 1200 bar

The NOx and uHC emissions followed the same pattern as those of strategy DD. The NOx emission for FF2 strategy was less than FF1 strategy since less time was available during the premixed and combustion phases due to retarded injection timing of the first injection. In addition more fuel was injected for this strategy due to the dwell timing used as shown in Figure 5.16 which led to lower in-cylinder temperatures as a result of latent heat of evaporation of the fuel. Moreover, the ignition delay was shorter compared to FF1 strategy; thus, less time was available during the premixed phase of combustion which in turn resulted in lower temperature combustion. The NOx emission produced by FF3 strategy was less than FF1 strategy since less fuel was injected in comparison to FF1 strategy as shown in Figure 5.16. FF4 strategy produced the lowest NOx emission compared to all the other strategies since combustion took place during the expansion stroke as shown in Figure 6.43 which limited the maximum combustion temperature. In addition, the fuel quantity injected was substantially higher for this strategy as shown in Figure 5.16 which led to lower in-cylinder temperature due to latent heat of evaporation of the fuel.

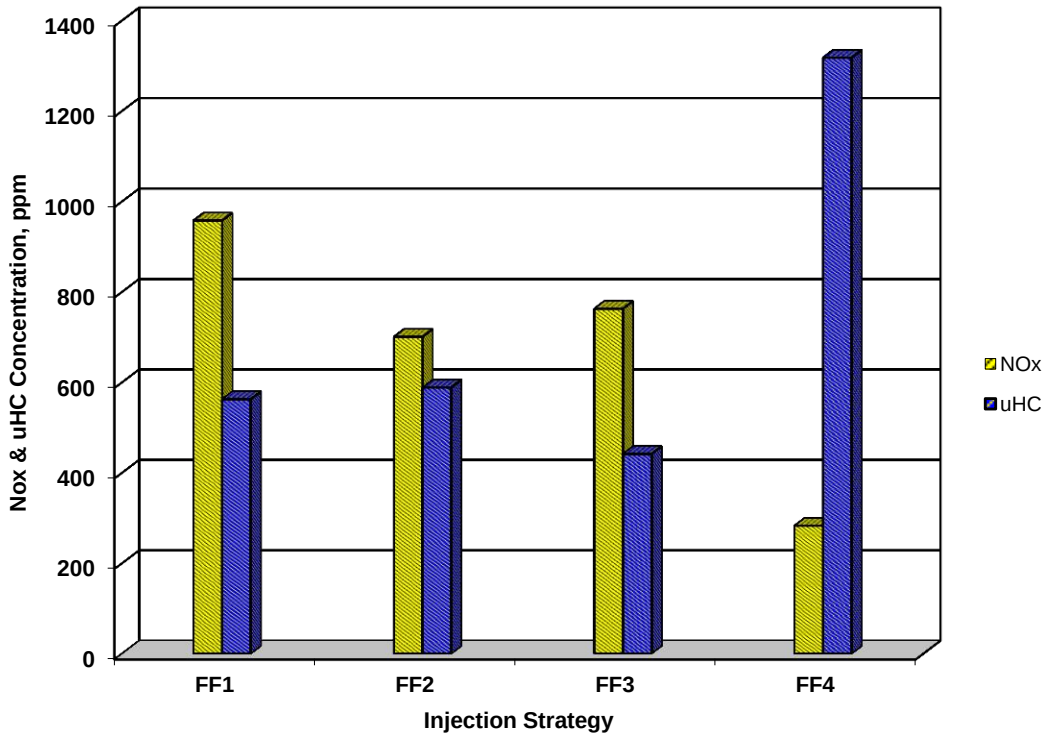

Figure 6.47 NOx and uHC Concentration for Strategy FF at 1200 bar

The uHC emission for FF2 strategy was higher in comparison to FF1 strategy; this was due to the greater fuel quantity injected for this strategy as a result of the dwell angle used. In addition, the ignition delay for this strategy was shorter which minimised the time available during the premixed phase of combustion which led to higher uHC emission. In contrast, FF3 strategy produced less uHC emissions since the least fuel quantity was injected for this strategy as shown in Figure 5.16; thus, lower level of unburned fuel remained inside the cylinder upon the completion of the combustion process. Moreover, fuel evaporation process was improved since the first injection took place closer to TDC where the in-cylinder temperature was higher. FF4 strategy produced considerably higher uHC emission in comparison to all the other strategies, this was due to the dwell timing used for this strategy whereby the two injections interacted with each other and resulted in a single injection with much longer injection duration in comparison to the other dwell timings used in this study. In addition, the time available during the premixed and combustion phases was limited as the injection timing of the first injection was further retarded. Therefore, high level of unburned fuel remained inside the cylinder upon the completion of the combustion process.

6.6.3 Strategy G (Low load, 70:30 split injection with 1st injection fixed at -10^{o} CA ATDC)

This strategy involved analysis of injection timing with variable dwell angle between injections on the combustion and emissions characteristics of a four-stroke HSDI diesel engine through 70:30 split injection strategies whereby 70% of total fuel quantity was injected during the first injection and the remaining during the second. The timing of the first injection was kept constant while the dwell timing between the two injections was changed in order to identify the effect of late injection on the level of soot produced. The total fuel demand was 10 mm^3.

6.6.3.1 In-Cylinder Pressure and Heat Release Rate Analysis

The in-cylinder pressure data for strategies G1, G2 and G3 averaged over 20 consecutive cycles are shown in Figure 6.48. The in-cylinder pressure trace for G1 strategy followed the line of the motoring pressure until 0.8^{o} CA ATDC where it

sharply increased and reached its peak value of 38.2 bar at 9.4^{o} CA ATDC. The in-cylinder pressure steadily decreased from this point during the expansion stroke. The fuel injections took place at -10^{o} CA ATDC and 5^{o} CA ATDC which resulted an IMEP value of 2.61 bar.

The in-cylinder pressure trace for G2 strategy followed the line of motoring pressure until 0.8^{o} CA ATDC where it rapidly increased and reached its peak value of 35.9 bar at 8.8^{o} CA ATDC, 0.6^{o} CA after G1 strategy. The peak in-cylinder pressure value was less than G1 strategy since the second injection took place later in the expansion stroke which limited the time available for the combustion process to complete. The in-cylinder pressure decreased after the peak during the expansion stroke until 15.8^{o} CA ATDC where it exhibited a minor increase due to the second fuel injection. The in-cylinder pressure steadily decreased after this point. The fuel was injected at -10^{o} CA ATDC and -10^{o} CA ATDC which led to an IMEP value of 1.24 bar.

The in-cylinder pressure trace for G3 strategy followed the line of motoring pressure until 0.8^{o} CA ATDC where it rapidly increased and reached its peak value of 35.4 bar at 8.8^{o} CA ATDC, 0.6^{o} CA after G1 strategy. The peak in-cylinder pressure occurred at the same crank angle as G2 strategy and was almost identical in magnitude since the injection timing and quantity of the first injection was identical for both cases. In addition, since the second injection took place late in the expansion stroke, it did not affect the peak in-cylinder pressure as shown in Figure 6.49. The in-cylinder pressure decreased after the peak during the expansion stroke until 23.2^{o} CA ATDC where it exhibited a minor increase due to the second fuel injection. The in-cylinder pressure steadily decreased after this point. The fuel injections took place at -10^{o} CA ATDC and -15^{o} CA ATDC which led to an IMEP value of 1.68 bar.

The heat release rate for strategies G1, G2 and G3 are presented in Figure 6.49. The heat release rate for G1 strategy exhibited a decrease at -6.6^{o} CA ATDC due to charge cooling shortly after the onset of the first injection and the heat transfer effects during the compression stroke which lasted until -3.6^{o} CA ATDC. The charge cooling effect for this strategy was less paramount since the first injection took place close to TDC where the in-cylinder temperature was higher. After this point, the rate of heat release

suddenly increased, reaching its peak value at 5.4^{o} CA ATDC, due to premixed combustion. This phase of combustion lasted until 10.2^{o} CA ATDC where the second phase of combustion started. The maximum heat release rate due to diffusion combustion occurred at 14.2^{o} CA ATDC and progressively decreased after this point during the expansion stroke. This strategy produced the maximum heat release due to premixed and diffusion combustion compared to all the other strategies. This was mainly due to the dwell timing used for this strategy which led to much greater fuel quantity injected as shown in Figure 5.15. In addition, the second injection took place earlier in the expansion stroke in comparison to G2 and G3 strategies which resulted in improved fuel evaporation.

The heat release rate for G2 strategy experienced a minor decrease at -6.6^{o} CA ATDC due to charge cooling shortly after the onset of the first fuel injection and the heat transfer effects during the compression stroke which lasted until -3.6^{o} CA ATDC. In this case the charge cooling effect was less dominant due to lower fuel quantity injected with the selected dwell timing as shown in Figure 5.15. After this point, the rate of heat rapidly increased until 5.4^{o} CA ATDC where the maximum heat release due to premixed combustion occurred. The maximum heat release due to this phase of combustion occurred at the same crank angle as that of G1 strategy since the timing of the first injection was kept constant. This phase of combustion lasted until 13.6^{o} CA ATDC where the second phase of combustion started. The maximum heat release rate due to diffusion combustion occurred at 17.6^{o} CA ATDC and progressively decreased after this point during the expansion stroke. The maximum heat release due to the second phase of combustion was lower for this strategy compared to G1 strategy; this was mainly due to the dwell timing used for this strategy which resulted in lower injected fuel quantity as shown in Figure 5.15.

The heat release rate for G3 strategy followed the same trend as that of G2 strategy. It experienced a small decrease at -6.6^{o} CA ATDC due to charge cooling shortly after the onset of the first fuel injection and the heat transfer effects during the compression stroke which lasted until -3.6^{o} CA ATDC. After this point, the rate of heat sharply increased, reaching its maximum at 5.4^{o} CA ATDC, due to premixed combustion. The maximum heat release due to this phase of combustion occurred at the same crank

angle as those of G1 and G2 strategies since the timing of the first injection remained unaltered. This phase of combustion lasted until 17.8^{o} CA ATDC where the second phase of combustion started. The maximum heat release rate due to diffusion combustion occurred at 25.2^{o} CA ATDC and progressively decreased after this point during the expansion stroke. The maximum heat release due to the second phase of combustion was higher than G2 strategy; this was mainly due to the dwell timing used

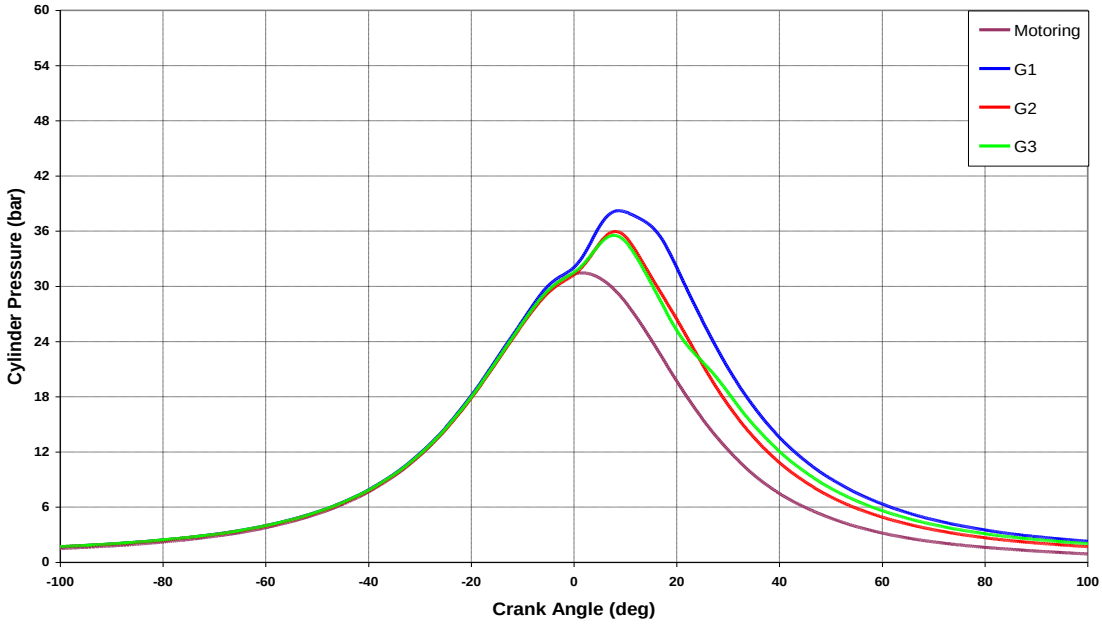

Figure 6.48 In-Cylinder Pressure Data for Strategy G at 1200 bar

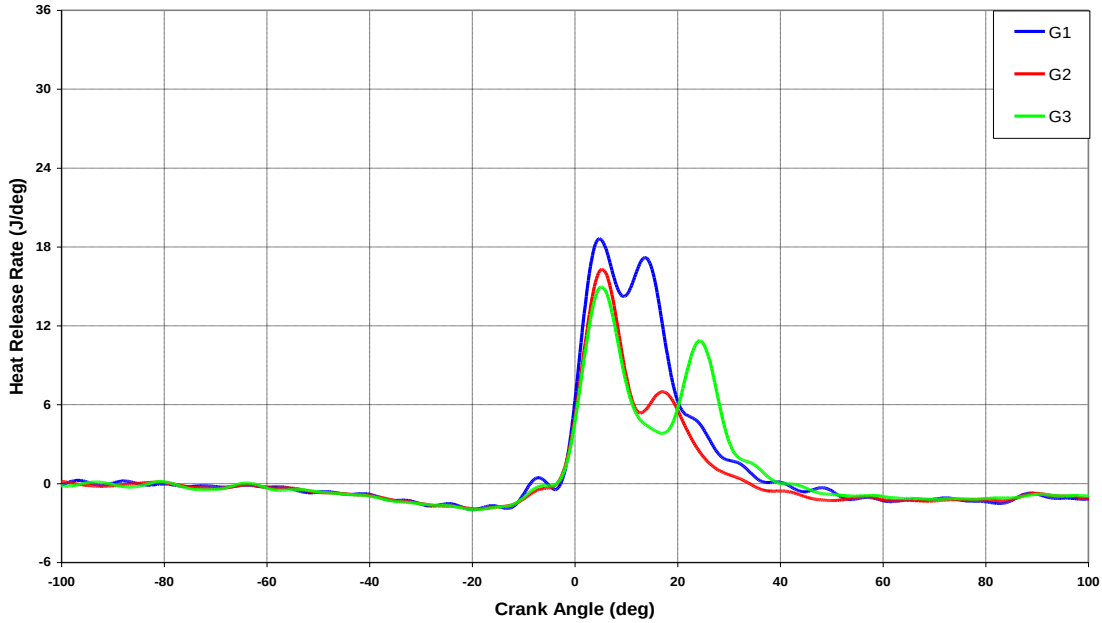

Figure 6.49 Heat Release Rate Traces for Strategy G at 1200 bar

which resulted in higher injected fuel quantity as shown in Figure 5.15. Though, the heat release due to diffusion combustion for G3 strategy was lower than G1 strategy mainly due to the injection timing of the second injection.

6.6.3.2 Fuel Injection and Combustion Visualisation

Figure 6.50 shows the image sequence obtained for G1 strategy through high speed video imaging technique.

The high speed imaging was carried out for this strategy since it produced the highest IMEP value. The first three frames in Figure 6.50 show the fuel spray jets development from the start to the end of the first injection where in the last frame fuel sprays were almost fully evaporated. The fuel sprays in these images were not fully developed due to short injection duration of the first injection as well as improved fuel evaporation due to the injection timings used for this strategy. The frames presented at 5^{o} CA ATDC, 6.3 ^{o} CA ATDC, 7.2 ^{o} CA ATDC and 8.1 ^{o} CA ATDC show the image sequence from the start to the end of the second injection. From the image sequence presented it is evident that some of the fuel sprays reached the piston wall. The asymmetry of fuel sprays in these images was due to the inherent characteristic of VCO injector used in this study as previously reported in Section 6.3.1.2.

The first combustion phase apparent from the heat release rate data at -3.6^{o} CA ATDC, Figure 6.49, resulted in no visible combustion until -0.9^{o} CA ATDC where the first visible combustion was observed. Flame was propagated in the same manner as that of F2 strategy, starting at the tip of the fuel sprays where fuel vapour was highly concentrated and spread along the periphery of the fuel sprays where fuel evaporation rate was considerably higher as shown in frames six, seven and eight at 6.3^{o} CA ATDC, 7.2^{o} CA ATDC and 8.1^{o} CA ATDC respectively. In the next frame at 9.9^{o} CA ATDC, intense flame propagation took place, spreading to the periphery of the piston wall where the majority of premixed fuel and air was concentrated. In this frame, flame spread to the outer regions of the sprays tip due to the fuel sprays impingement on the piston wall, creating a mushroom like structure. The same trend existed at 14.4^{o} CA ATDC where fuel was burning in the same manner during the first phase of combustion.

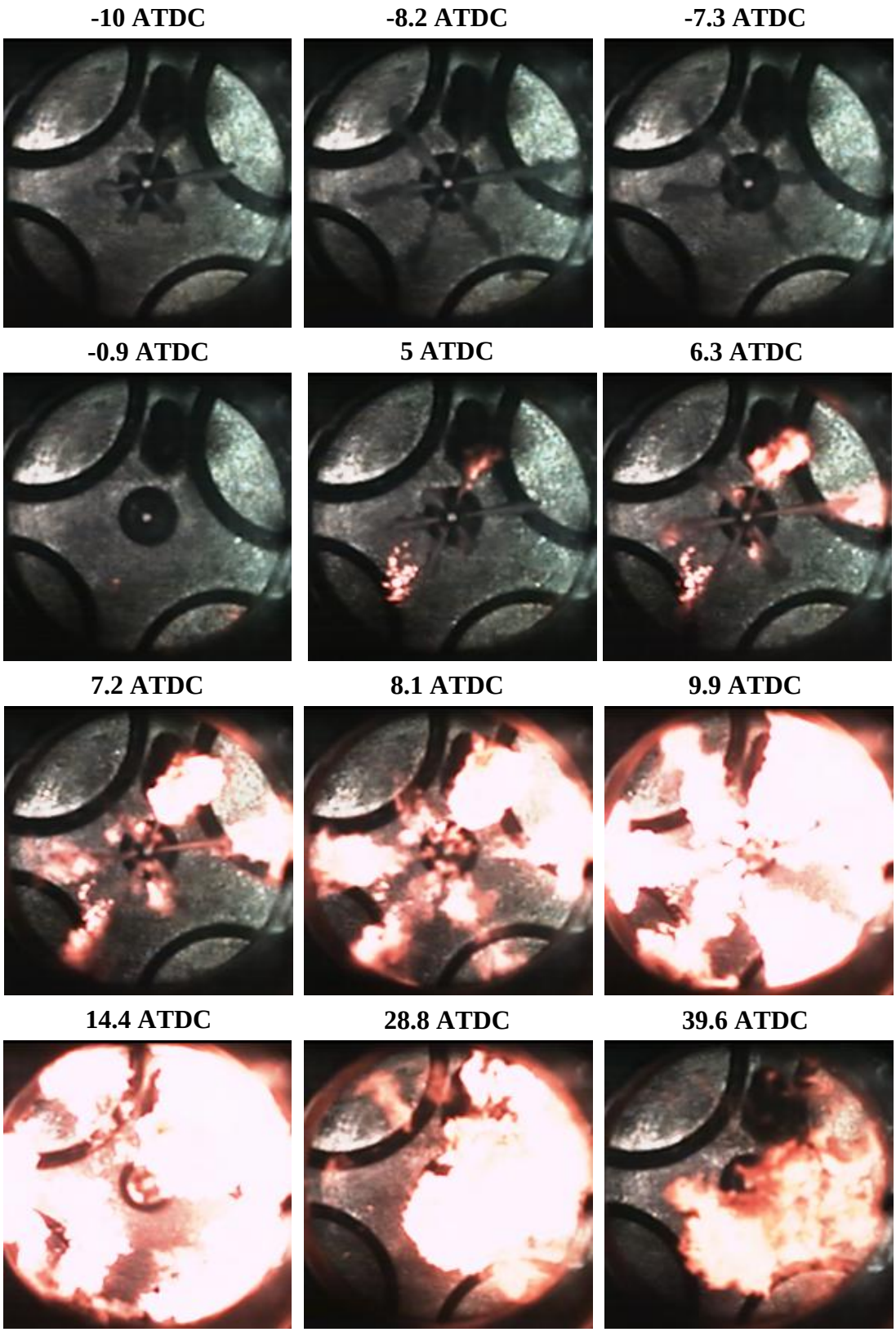

Figure 6.50 Combustion Image Sequence for G1 Strategy at 1200 bar

Based on the image sequence at 9.9^{o} CA ATDC and 14.4^{o} CA ATDC, it is evident that flame was more intense on the right side of the cylinder; this was due to uneven distribution of fuel vapour within the cylinder. In the last two frames several combustion sites are present, indicating the presence of some diffusion combustion corresponding to the second phase of combustion. Flame was moved in the clockwise direction due to the swirl motion as the combustion process evolved.

6.6.3.3 Flame Temperature and Soot Concentration Measurement

The flame temperature and *KL* factor image sequence for strategy G1 are shown in Figure 6.51.

Minor combustion at relatively low temperature was detected in the first frame at 5^{o} CA ATDC which was in good agreement with the high speed image taken at this crank angle, Figure 6.50. The first visible flame was detected later in the expansion stroke in comparison to F2 and FF2 strategies due to retarded injection timing of the first injection for this strategy. The subsequent frame at 6.3 ^{o} CA ATDC, 0.9^{o} CA after the occurrence of maximum heat release due to premixed combustion, shows relatively small flame propagation around the tip of the fuel sprays where high concentration of premixed fuel vapour and air was present. The same trend was observed in the next frame at 9.9 ^{o} CA ATDC. In the subsequent frame at 14.4^{o} CA ATDC, combustion flame was detected around the periphery of the piston bowl where the premixed fuel and air was concentrated due to sprays impingement on the piston bowl. As the combustion process evolved, the flame temperature increased as seen in the second, third and fourth frames. The flame temperature was lower than F2 strategy due to late initiation of the combustion. Once the maximum heat release due to premixed combustion was reached, the flame temperature steadily decreased as it progressed during the expansion stroke as shown in image sequence at 28.8 ^{o} CA ATDC and 39.6^{o} CA ATDC respectively. Luminous flame was detected through high speed imaging at crank angles later in the expansion stroke, yet no information could be detected at these crank angles due to inadequate sensitivity of the detection system.

The soot concentration profile shown in Figure 6.51 followed the same pattern as that of flame temperature image sequence as expected. As shown by the *KL* factor image

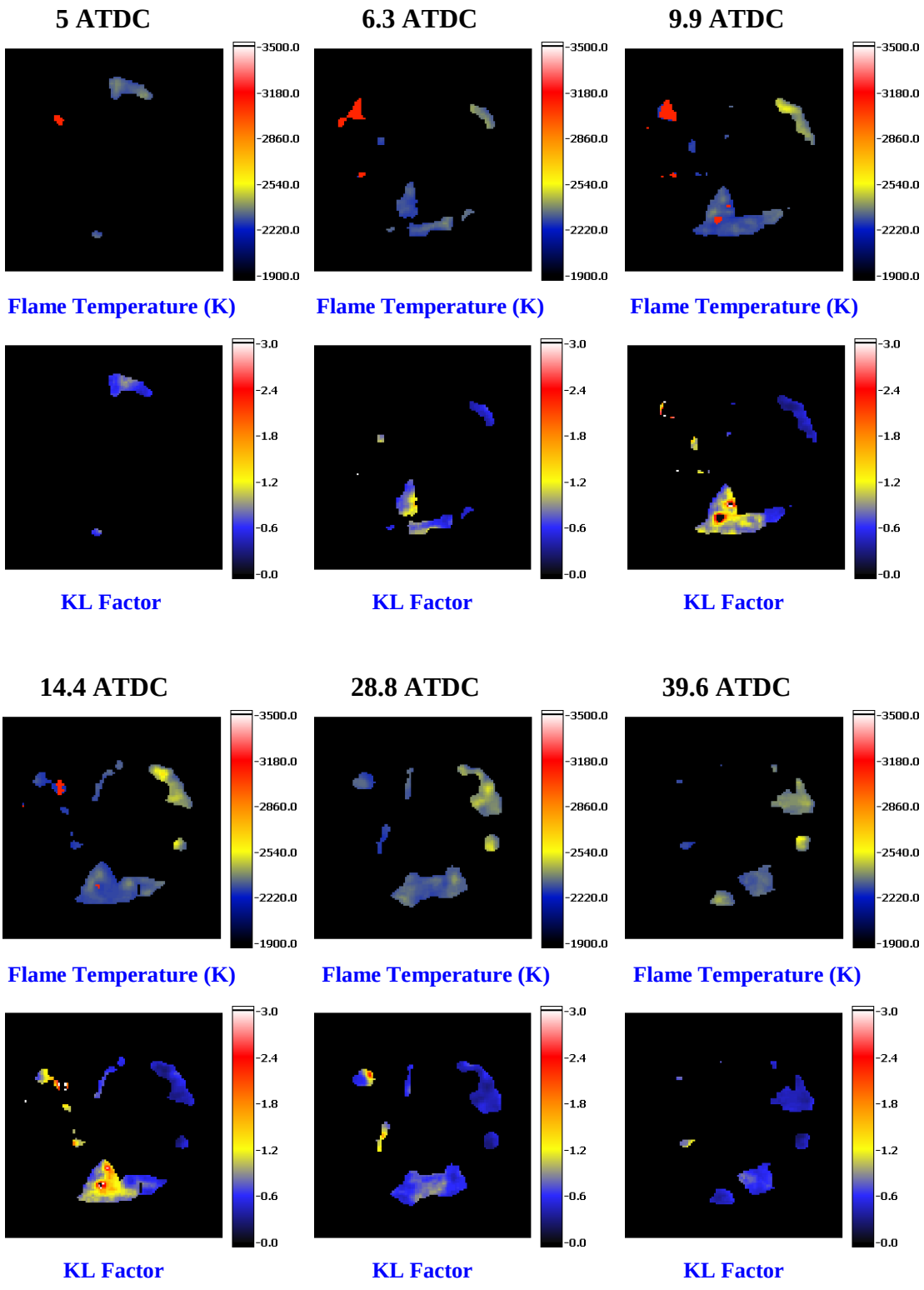

Figure 6.51 Flame Temperature and *KL* Factor Images for G1 Strategy at 1200 bar

at 5^o CA ATDC, during initial stage of visible flame propagation, soot concentration was very low. In the next frame at 6.3^o CA ATDC, 0.9^o CA after the maximum heat release rate due to premixed combustion, soot was formed around the tip and periphery of the piston bowl where flame temperature was considerably high due to high concentration of premixed fuel vapour and air. Soot concentration increased as the combustion process progressed during the premixed combustion phase as shown in frames two, three and four. Soot concentration decreased later in the expansion stroke mainly due to oxidation as shown in the image sequence at 28.8^o CA ATDC and 39.6^o CA ATDC, though remained higher than F2 strategy due to retarded injection timing of the first injection whereby limited time was available for soot particles to oxidise. This was further confirmed by the soot emission results presented in the next section.

6.6.3.4 Soot and Exhaust emissions

The soot and gaseous exhaust emissions results for strategy G are depicted in Figures 6.52 and 6.53 respectively.

The soot level produced by G1 strategy is considerably higher compared to G2 strategy; this is mainly due to the greater fuel quantity injected for this strategy as a result of the dwell angle used. In contrast, the soot concentration for G2 strategy is lower since the fuel quantity injected is much lower than the other two strategies as shown in Figure 5.15. Moreover, the time available for soot formation is more limited due to advanced injection timing of the second injection. G3 strategy produces higher soot emission in comparison to G2 strategy; this is due to the greater fuel quantity injected for this strategy as shown in Figure 5.15. This is further validated by the heat release data shown in Figure 6.49 whereby the heat release due to the second phase of combustion is greater than G2 strategy. Nevertheless, the soot level produced by G3 strategy remains lower than G1 strategy since the time available for soot formation is limited due to further advancement of the second injection timing.

The NOx emission for G2 strategy was higher than G1 since greater percentage of premixed combustion took place for G2 strategy. However, G3 strategy produced the least NOx emission since the second injection took place late in the expansion stroke.

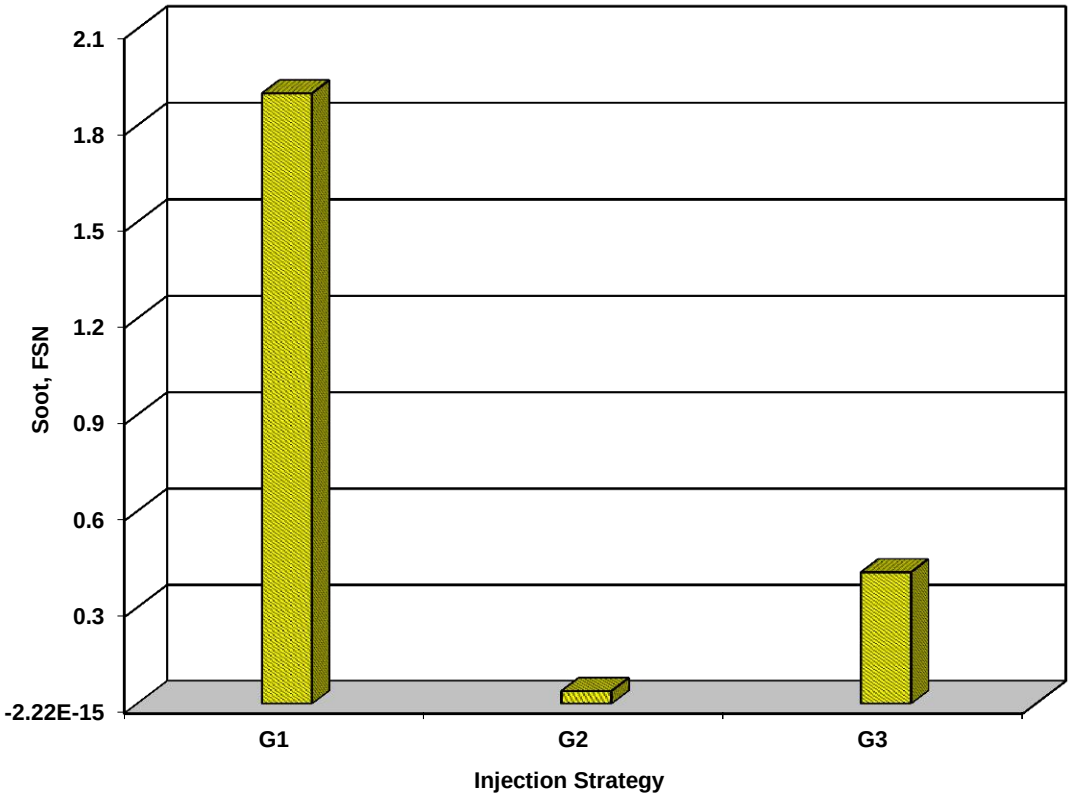

Figure 6.52 Soot Concentration for Strategy G at 1200 bar

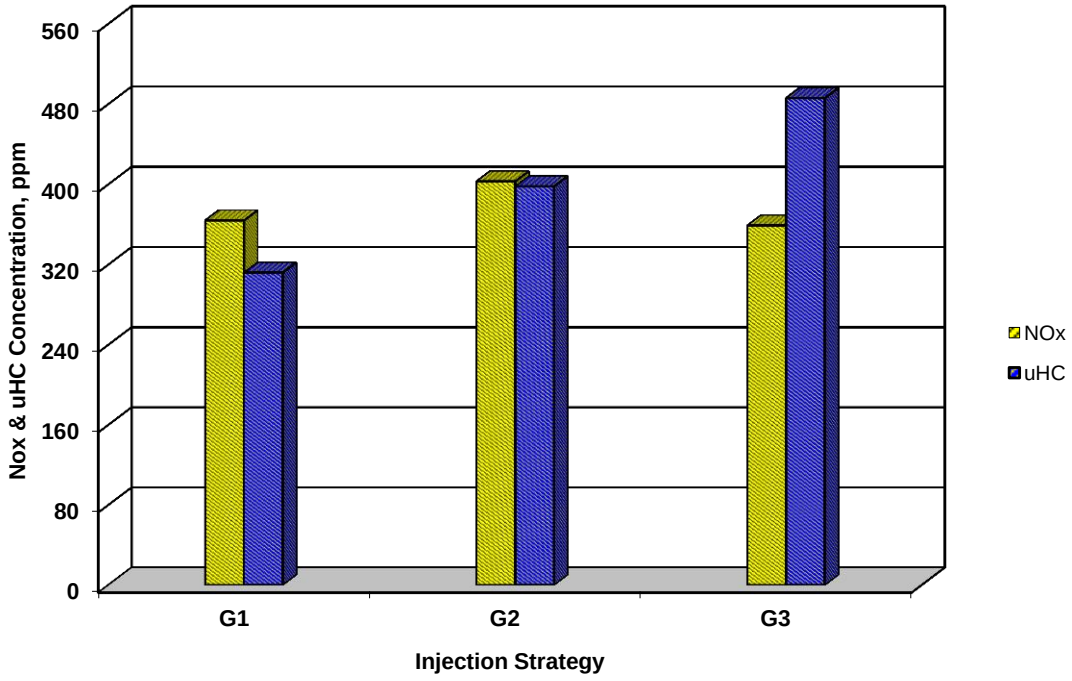

Figure 6.53 NOx and uHC Concentration for Strategy G at 1200 bar

The uHC emission increased as the dwell timing between the two injections was further increased as shown in Figure 6.53. This was mainly attributed to the limited time available during the premixed and combustion phases as the dwell timing was increased. Therefore, high level of unburned fuel remained inside the cylinder upon the completion of the combustion process.

6.7 Summary

In this chapter, experimental procedure and results were presented for different injection strategies. Detailed analyses were performed on the in-cylinder pressure, heat release rate, combustion images, exhaust emissions, flame temperature and soot loading distributions for selected cases. The results were interpreted with regard to the injection timings, dwell angles and in particular the interaction of split injections. The results obtained using fuel quantities of 10 and 20 mm^3 with single fuel injection showed that the IMEP values increased as the injection was further retarded. This was mainly due to improved fuel evaporation and mixing processes.

In the case of split injection strategies, the dwell angle of 5^o CA produced the highest IMEP value due to the greater fuel quantity injected which was caused by the interaction between the two injections almost replicating a single injection. The second highest IMEP was achieved with the dwell timing of 15^o CA, as stated earlier the total injected fuel quantity for these strategies was higher that all the other dwell timings utilised in this investigation, excluding 5^o CA dwell timing. The highest soot production was produced by the strategies with the aforementioned dwell timings. However, the trend in NOx emission was different in the case of 10 mm^3 and 20 mm^3 fuel demand. In the former case, the highest NOx emission was produced by 5^o CA and 15^o CA dwell timings due to higher gas temperature. However, the opposite was observed in the latter case, this was mainly attributed to the effect of latent heat of evaporation of fuel due to considerably higher fuel quantities injected in comparison to the former case. Although NOx emission in the latter case was considerably lower than the former, severe penalty in terms of uHC emission was incurred. In comparison, the 50:50 split injection strategies produced relatively high IMEP values with significantly lower exhaust emissions in relation to 30:70 and 70:30 strategies

with the total fuel demand of 10 mm^3. However, in the case of strategies with total fuel demand of 20 mm^3, although similar IMEP values were produced by all three split injection strategies, significantly lower exhaust emissions were produced by the 30:70 strategies.

In the case of fixed dwell angle, the injection quantity was constant while the timing of the first injection was altered. The soot and NOx emissions reduced for almost all the strategies with retarded injection. This was attributed to late initiation of the combustion during the expansion stroke. Furthermore, the effect of late injection on soot formation and oxidation was investigated. The results indicated that although reduction in soot concentration was achieved with these strategies, it remained almost the same and in some cases higher that those using variable dwell timing. However, considerable increase in uHC emission incurred using fixed dwell timing.

7

CHAPTER 7

Development of Laser Induced Exciplex Fluorescence Technique

7.1 Introduction

In IC engines, fuel spray injected into a high temperature gaseous atmosphere evaporates due to heat transfer from its surroundings. The combustion characteristics and exhaust emissions are directly influenced by the fuel evaporation process, fuel/air mixing rate, ignition delay and the location of initial combustion. However, these parameters are all functions of the spatial and temporal distribution of liquid droplets and fuel vapour within the combustion chamber. The fuel distribution is influenced by the thermodynamic conditions of the gaseous medium in which fuel is injected to (i.e. gas density, temperature, pressure, etc.), the characteristics of the fuel injection system (i.e. nozzle geometry, injection pressure, injection rate, etc.) and the geometrical configuration of the piston bowl and the combustion chamber. Therefore, advancement in engine design requires good understanding of fuel evaporation and mixing processes inside the combustion chamber. During the past two decades, the development of non-intrusive laser based optical diagnostic techniques including Raman Scattering (RS) [174, 175], photography [176, 177], Laser Light Scattering (LLS) [178] and two-wavelength laser absorption/scattering [179] have facilitated in depth analysis of fuel sprays both in macroscopic and macroscopic levels. These techniques are capable of providing information at physically inaccessible locations. However, these methods are not capable of simultaneous and discrete measurement of liquid and vapour phases. This is mainly due to insufficient distinctive spectroscopic characteristics of soluble organic molecules in a polar solvent in both phases.

However, recent advancements in laser based optical diagnostic techniques yielded the development of a unique technique by Melton [124, 180], known as Laser Induced

Exciplex Fluorescence (LIEF), capable of simultaneous visualisation of liquid and vapour phases at spectrally separated wavelengths with potential for quantification. This chapter includes detailed explanation of the principle of this technique, its implementation and calibration in an optical engine.

7.2 Principle of LIEF Technique

LIEF is a unique technique which is based on the addition of organic dopants to the base fuel with similar chemical and physical properties to that of standard diesel fuel. This technique allows for the measurement of macroscopic features of a fuel spray such as liquid/vapour penetration length and cone angle as well as microscopic characteristics including local air-fuel ratio and spray Sauter Mean Diameter (SMD), provided that appropriate dopants are selected.

7.2.1 Photophysical Reaction

The absorption and emission spectra of organic molecules dissolved in non-polar solvents, such as decane, are almost identical to that of the same molecule in the vapour phase. However, an organic molecule M can absorb light to form an excited molecule M^* with an average lifetime of 10-100 ns. The excited molecule may undergo several different processes [124].

$$M^* \rightleftharpoons M + h_{\nu M} \quad (1)$$

$$G + h_{\nu} \rightleftharpoons G^* \quad (2)$$

$$M^* + G \overset{K}{\rightleftharpoons} E^* + h_{\nu E} \quad (3)$$

$$E^* \rightleftharpoons M + G + h_{\nu M} \quad (4)$$

1. M^* may return to the ground state without light emission referred to as fluorescence quenching
2. M^* may transfer part of its energy to excite another molecule G, referred to as partner, due to reactive collision. The newly formed excite molecule G^* could

subsequently fluoresce, provided that G has an adequate energy level prior to collision.

3. M^* may bind reversibly with G to form an Excited State Complex (Exciplex) molecule $(E)^*$ which could subsequently fluoresce.
4. E^* may fluoresce and return to the ground state

Therefore, in favourable cases it is possible to react an excited fluorescent monomer, M^*, with an appropriate partner, G, to form new species in an excited state, E^*. The reaction between M^* and G is reversible; therefore the concentration of the latter can be adjusted so that the fluorescent emission produced by liquid and vapour phases are dominated by E^* at longer wavelengths and M^* at shorter wavelengths respectively as shown in Figure 7.1.

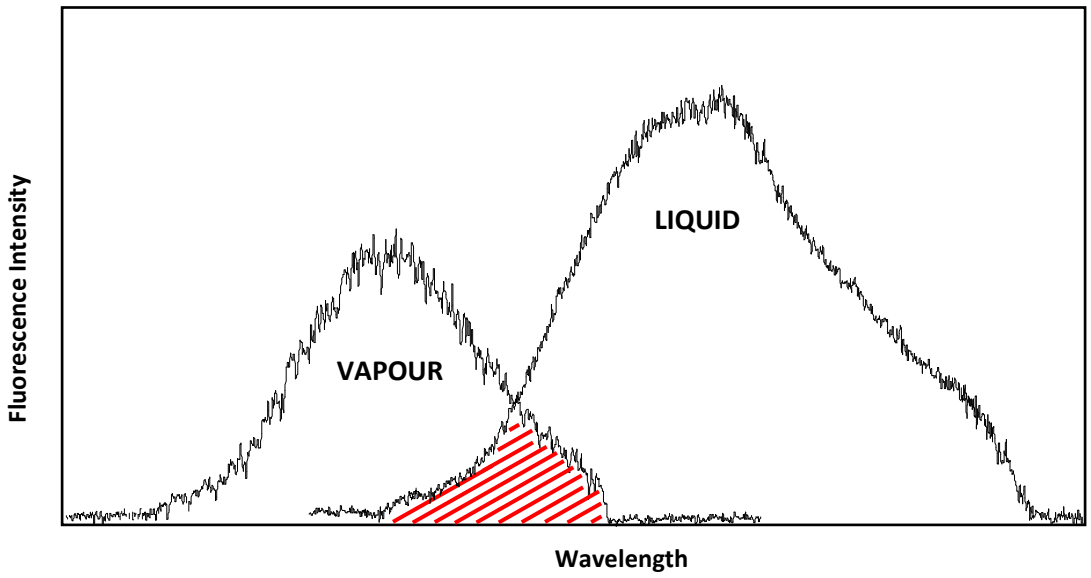

Figure 7.1 Schematic Diagram of Liquid and Vapour Fluorescence Spectra

The understanding of the formation and dissociation processes involved in an exciplex system is multifaceted since the exciplexes are formed in a reversible equilibrium with a reaction constant *K* whose value is highly temperature dependent.

The dashed area in Figure 7.1, marked in red, represents the region in the emission spectrum whereby both liquid and vapour phases produce fluorescence emission. This is known as cross-talk which is a major concern when quantitatively analysing the

LIEF results. This phenomenon is more paramount at elevated temperatures whereby the fluorescence spectrum of the exciplex molecules is blue-shifted (i.e. the liquid signal peaks at lower wavelengths) resulting in higher cross-talk between liquid and vapour signals. In contrast, the influence of vapour signal in the liquid phase is relatively small since the measured fluorescence intensity is proportional to the mass of the excited molecules in the measuring volume.

The binding energy in the excited state may be as much as 20-30% of a normal chemical bond. Thus, the emission spectrum of these newly formed species is red-shifted with respect to that of the fluorescent monomer, M^*, since the exciplex formation is an energy depleting process as shown in Figure 7.2.

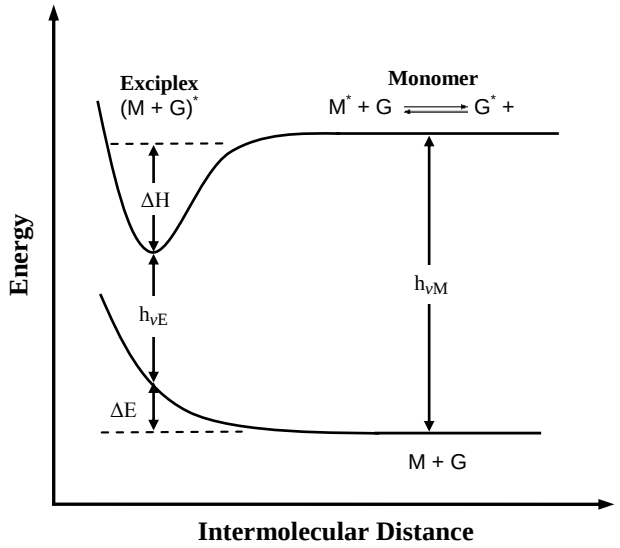

Figure 7.2 Schematic Diagram of Potential Energy for an Exciplex System

Where h_{vE} and h_{vM} are the photon energies at maximum exciplex fluorescence intensity and maximum monomer fluorescence intensity respectively. ΔE is the Coulomb repulsion potential of the two ground state molecules which is defined by the following expression:

$$\Delta E = h_{\nu M} - \left(h_{\nu E} + \Delta H\right) \qquad \text{Equation 7.1}$$

Therefore, the binding energy of the exciplex species can be evaluated, provided that h_{vE} and h_{vM} values are known.

7.2.2 Exciplex System

In order to spectrally separate the emission spectra of liquid and vapour phases of an evaporating fuel spray, appropriate exciplex system must be selected. There are several exciplex systems which are capable of visualising the spray structure. The exciplex system is selected based on the criteria listed below.

- Volatility of organic molecules
- Boiling point
- Exciplex binding energy
- Spectral shift

The solvent is often an alkane due to its nonfluorescent characteristics and the organic molecule M is carefully selected such that it coevaporates with the solvent, capable of forming exciplexes, and fluoresces when excited. Thus, the organic molecules which satisfy these criteria are exceptionally limited which makes the selection process very challenging. The most commonly applied and best suited system for the investigation of diesel fuel sprays is 0.5-1 % (w/w) N,N,N',N'-tetramethyl-p-phenylenediamine (TMPD), 10% (w/w) α-methyl-naphthalene and balance alkane (decane, tetradecane, or hexadecane) [124, 125, 180]. In this system α-methyl-naphthalene serves as the partner and TMPD as the monomer while decane is utilised as the solvent as shown in Figure 7.3.

The exciplex species are formed due to reactive collision of the excited monomer with the reacting partner in a dense region such as the liquid phase where the reaction probability is much higher [181, 182]. Therefore, by careful adjustment of the concentration of M and G, the fluorescence emission from the exciplex species and the excited monomer serve as the markers of the liquid and vapour phases respectively.

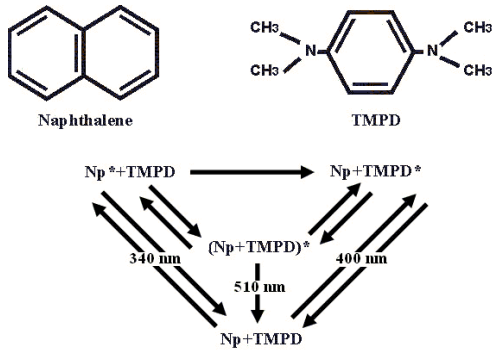

Figure 7.3 Schematic Diagram of Photophysical Processes in an Exciplex System (Melton, [124])

The boiling point of TMPD, α-methyl-naphthalene and decane are 260^{o}C, 244.8^{o}C and 214.5^{o}C respectively, thus the overall boiling point of TMPD/ α-methyl-naphthalene exciplex system lies within the range of 200 to 300^{o}C which is comparable to that of standard diesel fuel. Thus, it is assumed that the mixture of decane, α-methyl-naphthalene and TMPD coevaporates at approximately the same rate as that of standard diesel fuel which is crucial when analysing macroscopic and microscopic characteristics of evaporating diesel sprays.

The bonding energy required for exciplex formation typically lies within the range of 4-20 kcal/mol [183, 184], this range holds true for the aforementioned exciplex system which results in the emission spectrum of the exciplex molecules being red-shifted about 90nm in comparison to that of the fluorescent monomer [181]. This spectral shift is sufficient for the segregation of the liquid and vapour signals. Furthermore, high quantum yield of this exciplex system is another factor in promoting these organic dopants as a common choice in studying diesel sprays [185].

Decane is photophysically inert at the excitation wavelength used in this study, 308nm, thus organic dopants are added to this base fuel in order to trace the liquid and vapour phases [186]. The exciplex systems used in this investigation consist of 89% decane, 10% α-methyl-naphthalene and 1% TMPD; and 88% decane, 10% α-methyl-naphthalene and 2% TMPD respectively. These exciplex systems are commonly adopted for the analysis of diesel sprays since the boiling points of the dopants are comparable to that of the base fuel, ensuring accurate measurement of the evaporation process.

7.3 Quantitative Analysis

The fluorescence intensities obtained from the LIEF technique can be made quantitative, provided that the spray is optically thin, laser sheet/beam is spatially uniform and the monomer coevaporates with the exciplex species. Under these conditions, the fluorescence intensity from each phase is proportional to the mass concentration. In addition, the collection efficiency of the detection system and the quenching effects due to oxygen molecules must be evaluated in order to include their effects.

7.3.1 Calibration

Melton [183] developed a calibration method which involved analysis of several photophysical parameters including light absorption and the quantum yield of the exciplex system. The former is dependent on the local concentration of the liquid and vapour phases while the latter is dependent on the composition and structure of the monomer and the colliding partner as well as the ambient pressure of the gaseous medium within which the calibration process is performed. The quantum yield of the exciplex system is highly temperature dependent, increasing with temperature up to 600 K and decreasing nearly linearly with temperature with further increases in temperature; this further complicates the calibration procedure [135, 185]. Therefore, the overall accuracy of the calibration method depends on the accuracy of individual calibration procedures involved. Thus, small inaccuracy in each calibration process results in considerable error in the calibration data. Consequently, Rotunno et al. [131] developed a direct calibration technique based on the measurement of fluorescence intensities of known quantities of liquid and vapour, eliminating the problems associated with Melton's calibration method. The direct calibration technique discussed in the following sections is based on the method originally proposed by Rotunno et al. [131].

7.3.1.1 Vapour Phase Calibration

The relationship between the vapour concentration and the fluorescence intensity is established in two stages. The first step is to measure the vapour pressure with respect

to temperature, subsequently the molar concentration (*n/V*) can be obtained from the equation of state (*PV* = *nRT*). The second step is to measure the vapour fluorescence intensity with respect to temperature. The combination of the results from these two steps relates the fluorescence intensity to vapour mass concentration.

Vapour concentration can also be determined by absorption measurement. However, the molar extinction coefficient (ε) is dependent on the wavelength of the light source, the solvent and the surrounding temperature.

The fluorescence signal per laser pulse and unit volume collected by each pixel of the detector can be defined as:

$$S_f = \left[\frac{\eta\beta\Omega}{4\pi}\right]\left[\Phi_f^0\right]\left[b^{-1}\left(1-\exp\left[-\varepsilon cb\right]\right)\right]I_0 \qquad \text{Equation 7.2}$$

Where η Collection efficiency of the optics

β Detector efficiency

Ω Solid angle of light collection

Φ Quantum yield of fluorescent monomer

b Path length

ε Molar absorption coefficient

c Unknown mass concentration of fluorescent monomer

I_o Incident photon intensity

The first part of the equation represents the overall efficiency of the optics and the detector, whereas the second and third terms embody the quantum efficiency and the total number of species per unit volume. The normalised fluorescence intensity is merely a function of the species concentration, provided that quantum efficiency of the monomer is constant and all excitation and detection parameters are identical for all the experiments as depicted below:

$$S_f \propto 1-\exp\left[-\varepsilon cb\right] \qquad \text{Equation 7.3}$$

If $\varepsilon cb << 1$, the fluorescence intensity can be written as:

$$S_f \propto \varepsilon cb$$ Equation 7.4

Consequently, at low concentration of the fluorescent monomer, the relationship between normalised fluorescence intensities and species concentration follows a linear trend. However, these relationships hold true, provided that fluorescence quenching of the vapour signal is not experienced. Furthermore, the intense fluorescence of the monomer is attenuated by the addition of exciplex forming dopant into the fuel mixture, decreasing as the concentration of G increases. Moreover, the fluorescence intensity of the vapour phase is temperature dependent; decreasing with increase in temperature which is known as temperature quenching. This quenching process could be caused as a result of either dissipation of the excited molecules into thermal energy or due to collision with other molecules [134]. However, it is very difficult to identify which process has instigated the thermal quenching of the excited fluorescent monomers. Thus, different dopant concentrations must be tested in order to obtain an optimum fuel mixture whereby comparable fluorescence intensities from both phases can be obtained.

7.3.1.2 Fluorescence Quenching

Quenching is defined as a process which decreases the fluorescence intensity of a matter. Quenching could occur through several mechanisms as listed below,

- Dynamic quenching
- Static quenching
- Quenching through energy transfer
- Quenching due to charge transfer reaction or photochemistry

Although there are several mechanisms through which fluorophores can experience quenching, dynamic or collisional quenching is only discussed in this section. Quenching is often highly dependent on the pressure and temperature of the surrounding environment. This phenomenon poses a problem when applying spectroscopic techniques such as LIEF to IC engines whereby elevated pressures and temperatures exist at the time of fuel injection. Furthermore, molecular oxygen is one of the best-known collisional quenchers for all fluorophores [187]. Oxygen molecules

deactivate the excited state species, precluding fluorescence emission. The reduction in fluorescence intensity is directly proportional to the decay in fluorescence lifetime of the quenched species. The fluorescence intensity of a molecule is directly proportional to the quencher concentration through the Stern-Volmer relationship, Equation 7.5 [187].

$$\frac{F_0}{F} = \frac{T_0}{T} = 1 + k_q T_0 Q \qquad \text{Equation 7.5}$$

Where F Fluorescent intensity (Quenched)

F_0 Fluorescent intensity (Normal)

T Fluorescent lifetime (Quenched)

T_0 Fluorescent lifetime (Normal)

Q Quencher concentration

k_q Quencher rate coefficient

The quencher rate coefficient under diffusion-limited quenching condition can be defined as:

$$k_q = \frac{8RT}{3\eta} \qquad \text{Equation 7.6}$$

Where R Ideal gas constant

T Absolute temperature (K)

η Viscosity of the solution

The term $k_q T_0$ is also known as Stern-Volmer constant, K_{SV}. The fluorescence quenching of the liquid phase is insignificant since the liquid droplet lifetime is relatively short prohibiting the diffusion of oxygen molecules into droplets. In addition, dissolved oxygen molecules present in the fuel can be purged prior to testing. In contrast, dynamic quenching is a major concern in the vapour phase in particular when performing quantitative analysis. Therefore all the experiments must be carried out in a nitrogen environment to avoid collisional quenching by oxygen molecules.

7.3.1.3 Liquid Phase Calibration

The fluorescence images of exciplex droplets of a known size are taken with an ICCD camera. The fluorescence intensity of the droplets are then calculated and plotted versus droplet mass. This procedure is carried out for droplets of different sizes in order to generate a calibration map. The volume of a droplet can be calculated by:

$$V_d = \frac{F}{f} \qquad \text{Equation 7.7}$$

Where F Bulk flow rate

f Production frequency

The droplet radius can be defined as:

$$r_d = \left(\frac{3F}{4\pi f} \right)^{\frac{1}{3}} \qquad \text{Equation 7.8}$$

The intensity of individual droplets is established by summing the intensity values of the pixels containing the droplet. The fluorescence from the droplets of different size should be proportional to the droplet mass or volume as long as the droplets are optically thin. Otherwise, a decrease in the fluorescence collection efficiency is expected as the optical density of the droplets increases except when the excitation level is high (i.e. fluorescence saturation) where a linear relation exists. The relationship between the detected fluorescence signal and the incident irradiance is given by the following expression:

$$E_f \propto ck_f \left[1 + \frac{k_f}{\sigma(\lambda)(E_P)_0 \Phi_f} \right]^{-1} \qquad \text{Equation 7.9}$$

Where k_f Rate constant (s^{-1})

$\sigma(\lambda)$ Absorption cross section (cm^{-2})

$(E_P)_0$ Incident irradiance (photon cm^{-2} s^{-1})

The absorption cross section can be expressed as:

$$\sigma(\lambda) = \frac{2.303\varepsilon(\lambda)}{N} = 3.82 \times 10^{-21}\,\varepsilon(\lambda) \qquad \text{Equation 7.9}$$

Where N Avogadro's number

It is evident from Equation 7.9 that a plot of E_f versus incident irradiance reaches a plateau. However, care must be taken when quantitatively analysing the liquid phase of an evaporating diesel spray, since the liquid core of a diesel spray is very dense whereby liquid droplets in this region scatter the incident light rather than absorbing it. The loss of intensity due to this phenomenon must be considered when performing quantitative analysis. Furthermore, the cross-talk between the two phases must be measured and compensated for when quantifying the results.

It is important to note that the fluorescence intensities produced by both liquid and vapour phases are dependent on the mass concentration as well as the thermodynamic conditions of the surrounding gaseous medium. Thus, direct calibration techniques developed under ambient conditions such as those presented by Rotunno et al. [131] and Kim et al. [188] are not valid for quantitative analysis in IC engines where elevated temperatures and pressures are experienced. Therefore, the same procedure must be applied at elevated pressures and temperatures in order to accurately quantify the selected exciplex and detection systems. Furthermore, the effect of laser beam non-uniformity must be accounted for, since the fluorescence intensity is directly proportional to the laser intensity.

7.4 Limitations of LIEF Technique

The inherent limitations in the application of this technique are associated with the accuracy of the calibration process as well as the disparity in the physical and chemical properties of the model fuel compared to standard diesel fuel as listed below,

- The TMPD serves as a marker for the fuel but is not the fuel itself

- The volatility of the individual components of the mixture is distinct which could result in varying evaporation rates at different regions of the spray which may lead to inaccurate estimation of the fuel quantity
- The quantum yield of the exciplex system is temperature dependent

In addition, LIEF technique is based on the detection of fluorescence emitted by single component molecules, thus impurities in the fuel mixture could lead to erroneous results. Furthermore, this technique suffers from dynamic or collisional quenching by oxygen molecules, as previously stated in Section 7.3.1.2, thus the experiments are to be carried out in a nitrogen environment. Therefore, fuel evaporation during initial stages of combustion cannot be studied. Thus, although this technique enables detailed microscopic and macroscopic analysis of evaporating fuel sprays, care must be taken when quantifying and comparing these results to those obtained in normal engine operating conditions.

7.5 Experimental Setup

This section includes detailed explanation of the experimental setup employed, outlining the characteristics of the detection system utilised.

7.5.1 Excitation Source

In order to visualise the fuel spray, an excimer XeCl laser; COMPex 102 Lambda Physik; operating at 308nm was utilised. The specifications of the excimer laser are listed in Table 7.1.

Table 7.1 Excimer Laser Specifications

XeCl Excimer Laser **Type: COMPex 102 Lambda Physik**	
Wavelength (nm)	308
Maximum Power (W)	12
Pulses Width (ns)	10-15
Maximum Pulse Repetition Rate (Hz)	20

7.5.2 ICCD Camera

An Oriel InstaSpec V was used in this study to capture still images of the fuel sprays. This was an intensified camera with a monochrome CCD sensor, Figure 7.4. The camera was connected to a camera control unit for triggering purposes and to a data acquisition card installed in a PC to transfer the recorded image, Figure 7.4. The gain was set from zero to nine via a switch on the camera.

The software used with the ICCD camera was Andor MCD by Andor Technologies. The camera and acquisition software were triggered internally for focusing purposes and externally for fuel spray measurements. Due to inherent long acquisition time of the imaging system, the ICCD image acquisition rate was limited to 0.2 Hz or 1 frame per five seconds.

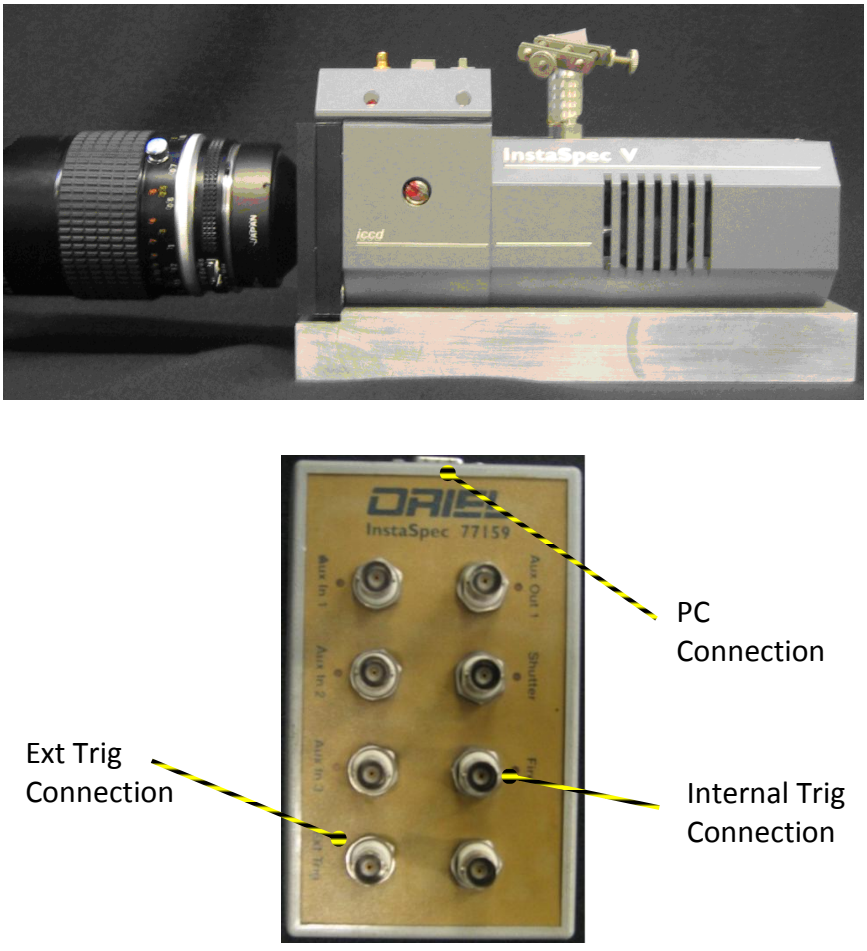

Figure 7.4 ICCD Camera (Top), Control Unit (Bottom)

The camera control unit provided the interface between the PC, camera and the external trigger signal. The external trigger signal was connected to the 'Ext Trig' connection point during the measurements whilst the 'Fire' connection was used for focusing purposes whereby an internal trigger was generated by the software. The software was set accordingly.

7.5.3 Nitrogen System

As previously stated in Section 7.3.1.2, oxygen molecules severely quench the vapour signal, as a result the experiments were carried out in a nitrogen environment in order to minimise such an effect. The surge tank, as previously shown in Figure 3.10, was filled with nitrogen prior to each test. A pneumatic actuator was installed on the intake manifold which controlled the opening and closing of the surge tank.

7.5.4 Synchronisation

In order to perform the LIEF measurement, it was critical to synchronise the laser, ICCD camera, fuel injection and nitrogen filling events. As the camera had an update time of approximately five seconds between frames (0.2 Hz), it was necessary to run the engine in the skip-fire mode to prevent unnecessary window fouling. This was achieved by a specially designed synchronisation unit in combination with a SRS DG535 delay generator unit.

The synchronisation unit shown in Figure 7.5 used the shaft encoder reference signal as the input signal. The minimum time required between injections was determined by the time required for the camera to update, in this case 63 cycles, equating to approximately five seconds at the engine speed of 1500 rpm. Therefore, two output signals at a preset crank angle were produced for every 63 cycles, upon the detection of an input signal from a shaft encoder box. One output signal was connected to EXT TRIG of the delay generator from which injection, laser and camera trigger signals were generated in sequence as shown in Figure 7.6 and the other was connected to the nitrogen filling system.

The injection control unit by EmTroniX had an 'Enable' input added by EmTroniX to allow injections to be enabled or disabled by the injection enable signal received from

the delay generator (T_o). The start of injection took place 510 µs after the injection signal was transmitted to the injector and the laser had an internal delay of 950 ns. Thus, laser was triggered 509 µs after the injection signal was sent to the EmTroniX while the camera was triggered 950 ns after the laser, as shown in Figure 7.6. The gate width of the ICCD camera was set to 200 ns by a TTL pulse generated by the C/D output of the delay generator to minimise the background light. The fluorescence lifetime of the exciplex system was found within the range of 10 to 100 ns.

Figure 7.5 Synchronisation Unit

The laser and the camera trigger signals were further delayed in order to obtain fuel spray images at different timings. The delay was set depending on the tested engine speed, the increment of 50 µs was used which corresponds to approximately 0.5^o CA at the engine speed of 1500rpm.

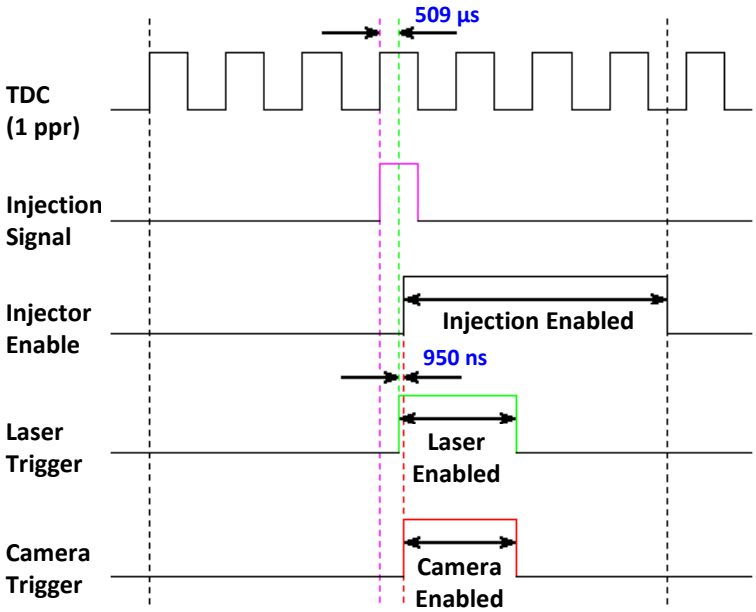

Figure 7.6 LIEF Control System Timing Diagram

The second output was used to trigger the actuator of the nitrogen supply system. Through several experiments with different nitrogen tank pressures, it was found that the surge tank should be filled with nitrogen at the pressure of 2 bar in order to completely flush the engine with nitrogen prior to the onset of the fuel injection. Figure 7.7 shows the intake manifold pressure as a function of actuator injection timing and the start of injection. The synchronisation unit was set so that the pneumatic actuator was triggered five cycles prior to the onset of the fuel injection and closed upon the start of the fuel injection as evident in Figure 7.7. In addition, the actuator timing was set such that fuel injection took place when the intake manifold and the combustion chamber were completely flushed with nitrogen. Due to the pressure drop between the surge tank and the intake, the intake manifold pressure at the time of injection was 1.5 bar (i.e. 0.5 bar boost). The intake heating system was not used since nitrogen entered the intake manifold at high speed, limiting the time available for heating. Consequently, all the experiments were carried out at ambient intake temperature.

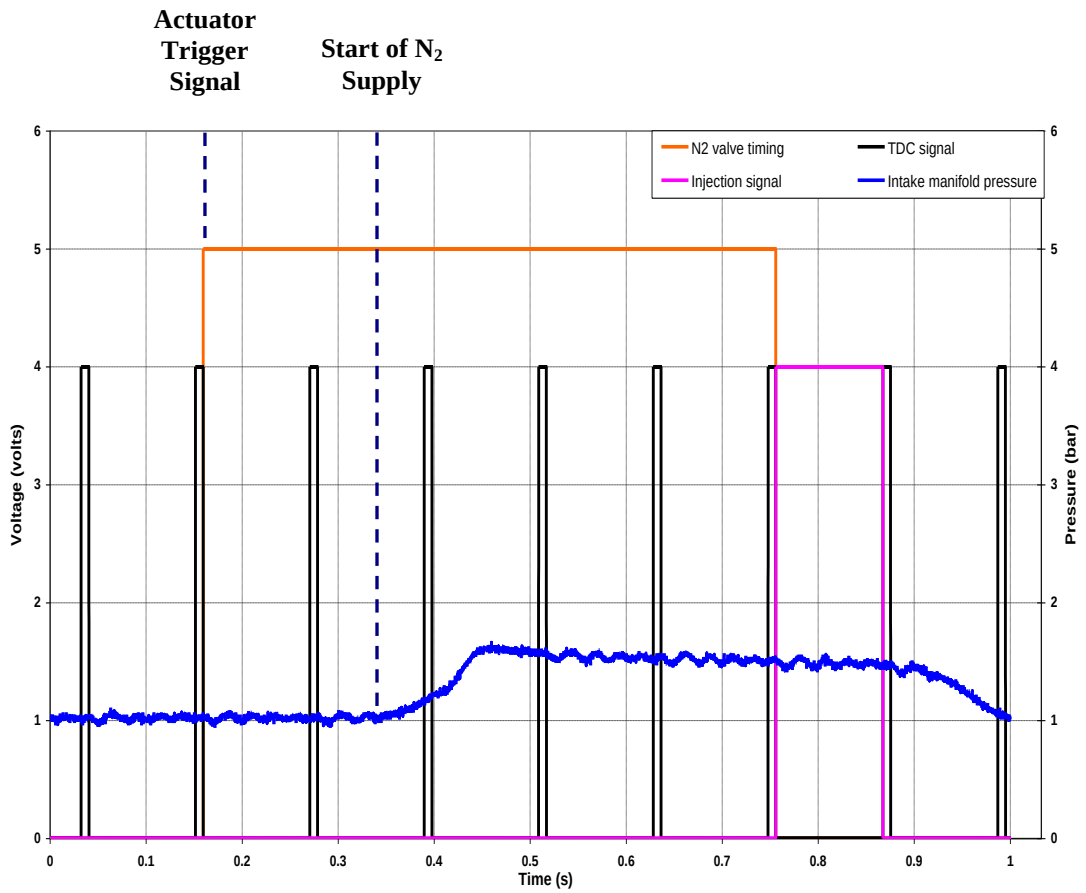

Figure 7.7 Nitrogen System Synchronisation Diagram

7.5.5 Optical Setup

Appropriate optical filters must be selected in order to allow discrete measurement of liquid and vapour phases; therefore it was essential to obtain the fluorescence spectra of the selected exciplex systems. The spectra of liquid and vapour phases were obtained using a constant volume chamber. The pressure and temperature inside the chamber were set at 5 bar and 500 K respectively when measuring vapour phase spectrum while pressure and temperature were set to 5 bar and 300 K respectively when measuring the liquid phase spectrum. The fuel was placed in a cuvette while measuring the liquid phase spectrum which was placed in the centre of the chamber. The XeCl Excimer laser operating at 308nm was used as the excitation source. The spectrum plotted in Figure 7.8 was obtained for the exciplex system consisting of 88% decane, 10% α-methyl-naphthalene and 2% TMPD using an Oriel MS127i spectrograph with spectral resolution of 0.22nm scanning over a wavelength range from 200 to 640nm.

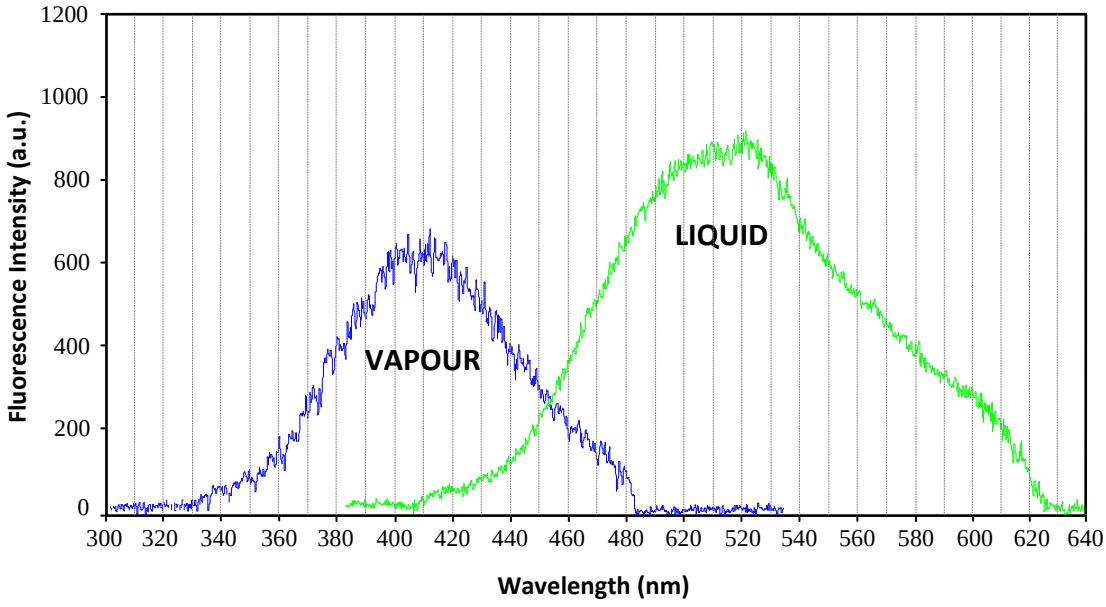

Figure 7.8 Fluorescence Emission Spectra of 88% decane, 10% α-methyl-naphthalene and 2% TMPD

The spectrum plotted in Figure 7.9 was obtained using 89% decane, 10% α-methyl-naphthalene and 1% TMPD under the same thermodynamic conditions as previously stated.

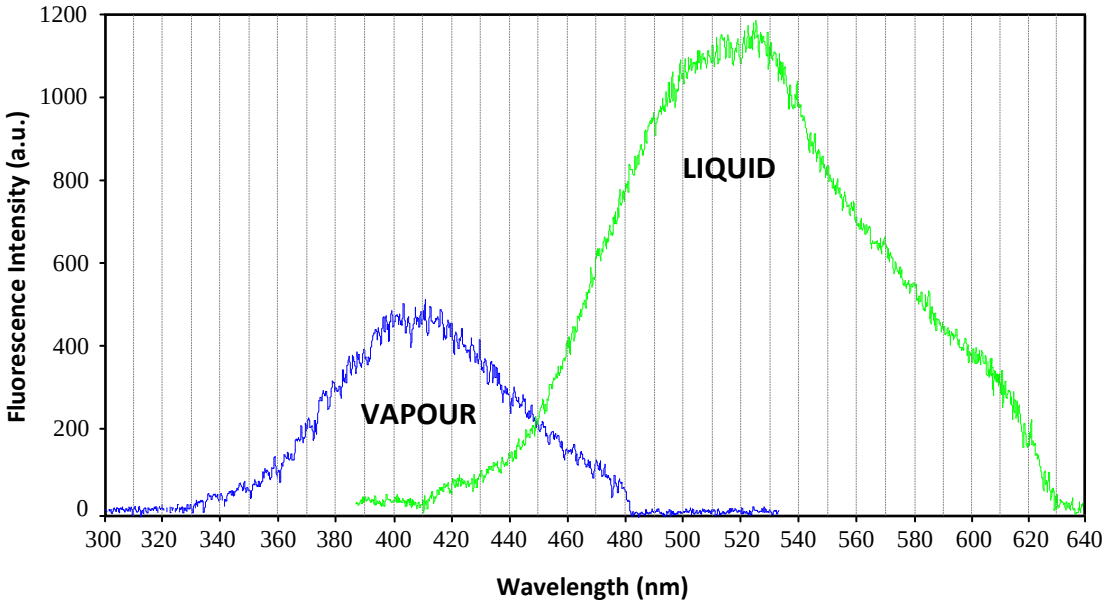

Figure 7.9 Fluorescence Emission Spectra of 89% decane, 10% α-methyl-naphthalene and 1% TMPD

The setup used for the application of LIEF technique on the single cylinder optical research engine is shown in Figure 7.10.

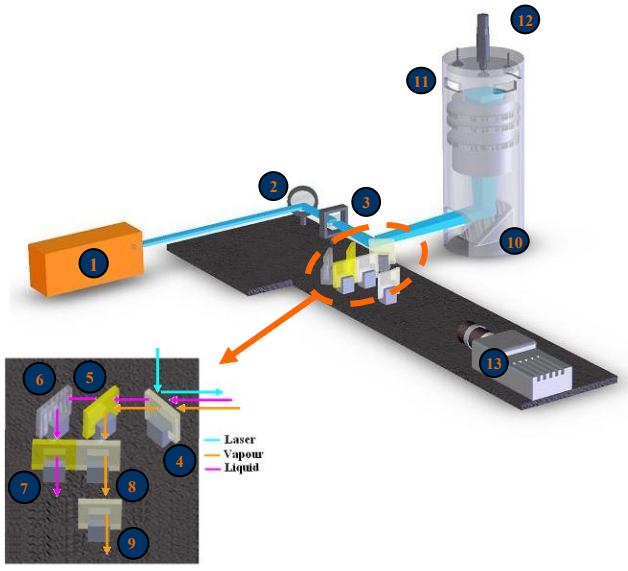

1. 308 nm Excimer (XeCl) Laser
2. Mirror
3. Diverging Cylindrical Lens
4. 330 nm Dichroic Filter
5. 420 nm Dichroic Filter
6. Mirror
7. 475 nm Longpass Filter
8. 360 nm Longpass Filter
9. 400 nm Shortpass Filter
10. Mirror (Bottom Access)
11. Optical Windows
12. Fuel Injector
13. ICCD Camera

Figure 7.10 Schematic Diagram of LIEF Setup

The laser beam was expanded using a cylindrical lens with a focal length of 150 mm and subsequently reflected onto a 330nm Dichroic Filter (DCF) positioned at 45^{o}. The laser was reflected to the bottom access mirror which was also positioned at 45^{o} and was subsequently reflected into the combustion chamber. Thus, combustion chamber was flooded with laser light, illuminating the entire combustion chamber. In such a configuration, laser extinction effects were substantially minimised. The liquid and vapour signals were transmitted by the dichroic filter since the excited monomer and exciplex species fluoresced at wavelengths longer than 330nm as shown in Figures 7.8 and 7.9. Based on the recorded fluorescence spectra with different dopant concentrations, a 420nm dichroic filter was selected and positioned in the path of the transmitted signal in order to separate the liquid and vapour signals, as shown in Figure 7.10. The vapour signal was reflected by this filter while the liquid signal was transmitted and subsequently reflected by a normal mirror. Details of the optical filters utilised are given in Appendix E.

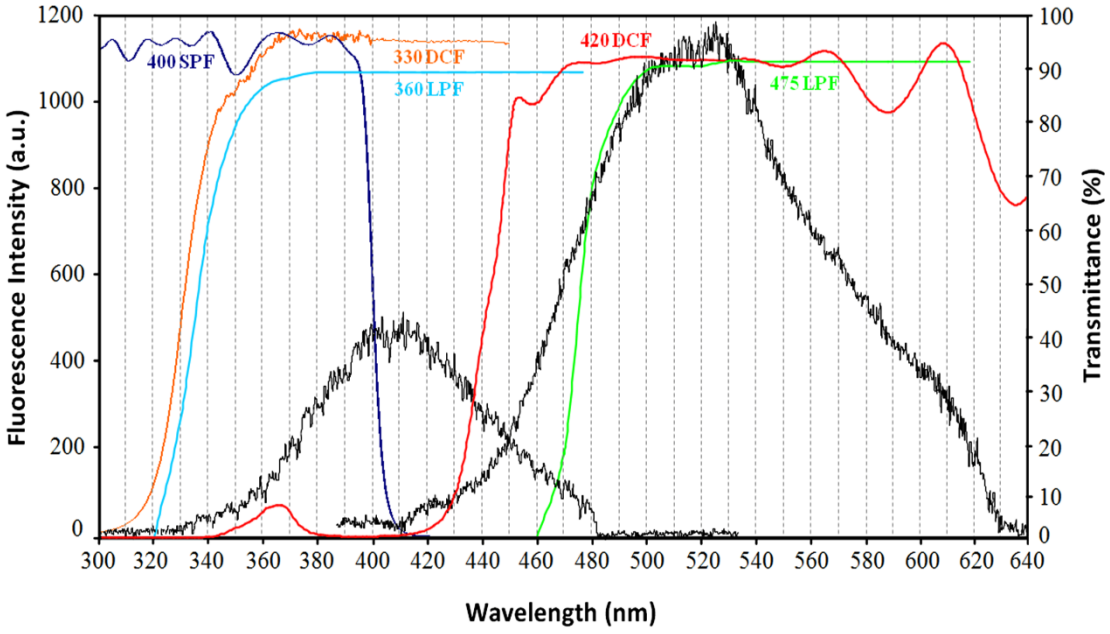

Figure 7.11 Spectral Transmission Response of Optical Filters

The vapour signal was then passed through a 360nm Longpass Filter (LPF) in order to eliminate the remnant light scattering and background noise signals which had not been filtered by the 330nm dichroic filter. The vapour signal was finally passed through an additional 400nm Shortpass Filter (SPF) in order to minimise the cross-talk

effect due to the liquid phase as evident in Figures 7.8 and 7.9. On the other hand, the liquid signal was passed through a 475nm LPF in order to isolate the liquid signal, as shown in Figure 7.11.

In addition, the absorption band of TMPD and α-methyl-naphthalene are also present at 370 and 320nm respectively [131, 125], therefore a 360nm LPF in conjunction with a 420nm DCF ensured the minimisation of the interference between the vapour and liquid signals, which further justifies the optical filters utilised.

7.6 Complications

There were three main difficulties associated with the application of this technique to the optical diesel engine utilised in this study as listed below,

- Laser light scattering
- Oil splashing
- Premature failure of fuel injection equipment

The following sections include detailed explanation of the aforementioned difficulties and their respective solutions.

7.6.1 Laser Light Scattering

The laser light had an initial dimension of 25 x 10 mm^2 which was expanded using a cylindrical lens, as previously stated in Section 7.5.5, in order to illuminate the entire combustion chamber. The expanded beam was almost the same size as the original 330nm DCF which resulted in high level of background noise due to laser light scattering. In addition, laser light reflections due to the cylinder head surface resulted in additional background noise as shown in Figure 7.12.

This issue was resolved through the use of a 100 x 100 mm^2 DCF which was sufficiently large in comparison to the dimension of the expanded laser beam, thus substantially minimising laser light scattering due to laser beam expansion as shown in Figure 7.12.

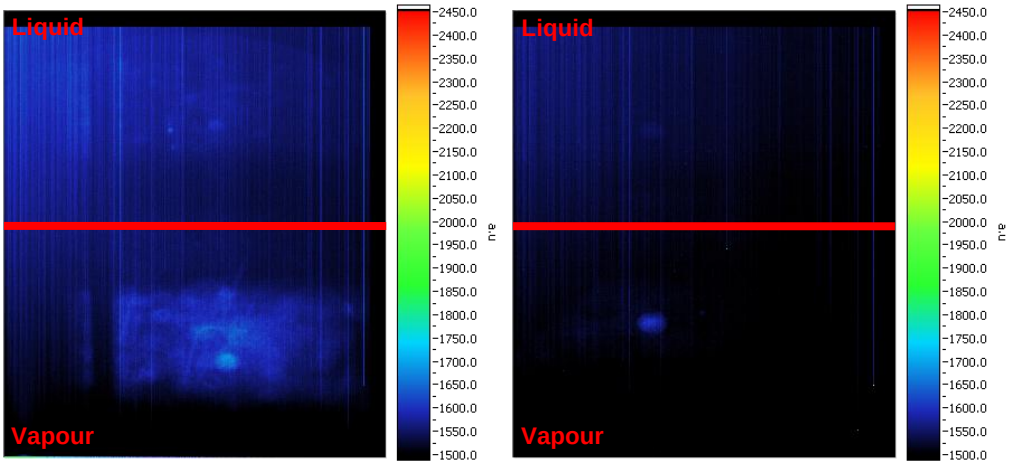

Figure 7.12 Original Laser Background (Left), Improved Laser Background (Right)

The reflection from the cylinder head was also minimised by thoroughly cleaning the soot deposits from the surface of the cylinder head during each engine rebuild and painting the surface with a matt black paint. Consequently, the background intensity was considerably reduced as depicted in Figure 7.12.

7.6.2 Oil Splashing

The oil in the crankcase splashed on the surface of the 45^{o} angled mirror due to the vacuum created in the crankcase as a result of the upward motion of the piston during the compression and exhaust strokes. Although the level of oil splashing was minimal and not visible in the high speed movies, it was easily detected by the LIEF detection system when illuminated with the UV excitation source, Figure 7.13.

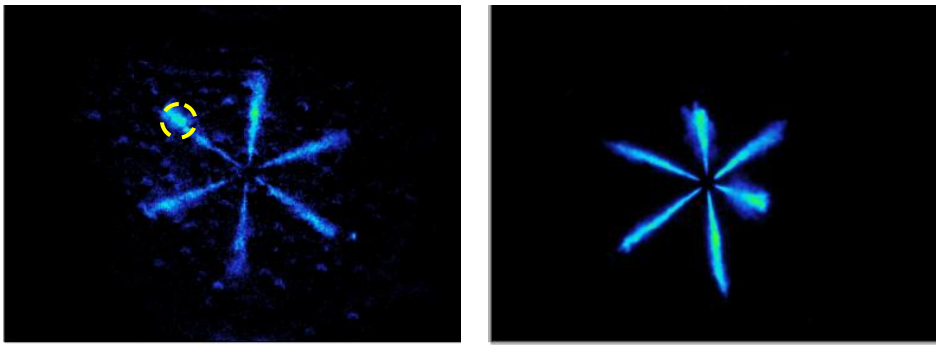

Figure 7.13 Background Noise in Vapour Phase Signal with Standard Engine Oil (Left) and Nonfluorescent Synthetic Oil (Right)

This phenomenon was more paramount in the vapour phase signal, since the vapour signal intensity was relatively weaker in comparison to that of the liquid phase as shown in Figures 7.8 and 7.9. The background noise intensity depended on the size of the splashed oil droplets, thus larger droplets interfered with the vapour signal, generating erroneous results, as highlighted in Figure 7.13. This issue was resolved by using high performance nonfluorescent synthetic oil, provided by British Petroleum, as the lubricating medium instead of standard engine oil. Consequently, the background noise due to oil splashing was eliminated as shown in Figure 7.13.

7.6.3 Premature Failure of Fuel Injection Equipment

The lubricity of the model fuel used for the application of LIEF technique was considerably lower than the standard diesel fuel. Although, α-methyl-naphthalene was not a good lubricant, the overall lubricity of the model fuel was highly dependent on the concentration of TMPD. The lubricity of the model fuel decreases as the concentration of TMPD increases. Furthermore, TMPD is in powder form and must be dissolved in the mixture of decane and α-methyl-naphthalene. However, the solubility of TMPD is relatively poor which results in the emulsion of TMPD residues in the fuel mixture even though the solution is mixed with a hotplate magnetic stirrer.

Current high pressure diesel pumps and fuel injectors in the market are designed for use with filtered standard diesel fuel with relatively high lubricity. Thus, the use of the model fuel with TMPD deposits and low lubricity led to premature failure of the fuel injection system. In the setup employed, a pneumatic pump was utilised in order to avoid premature failure of the pump, however, no solution was found for the fuel injectors. With hindsight, it may prove useful to have a fuel filter installed upstream of the injector, nevertheless, this may lead to alterations in the absolute TMPD concentration from measurement to measurement. Several fuel injectors were used in order to obtain the data presented in this Chapter.

7.7 Data Analysis

The image post processing was performed using a LabVIEW program written by the author in which the average background signal was subtracted from the measured liquid and vapour signals and the contours of spatial distribution of the liquid and

vapour phases were displayed as shown in Figure 7.14. Subsequently, the “LIEF.vi” program outputted the contours of spatial distribution of the liquid and vapour phases in Bitmap (.bmp) format.

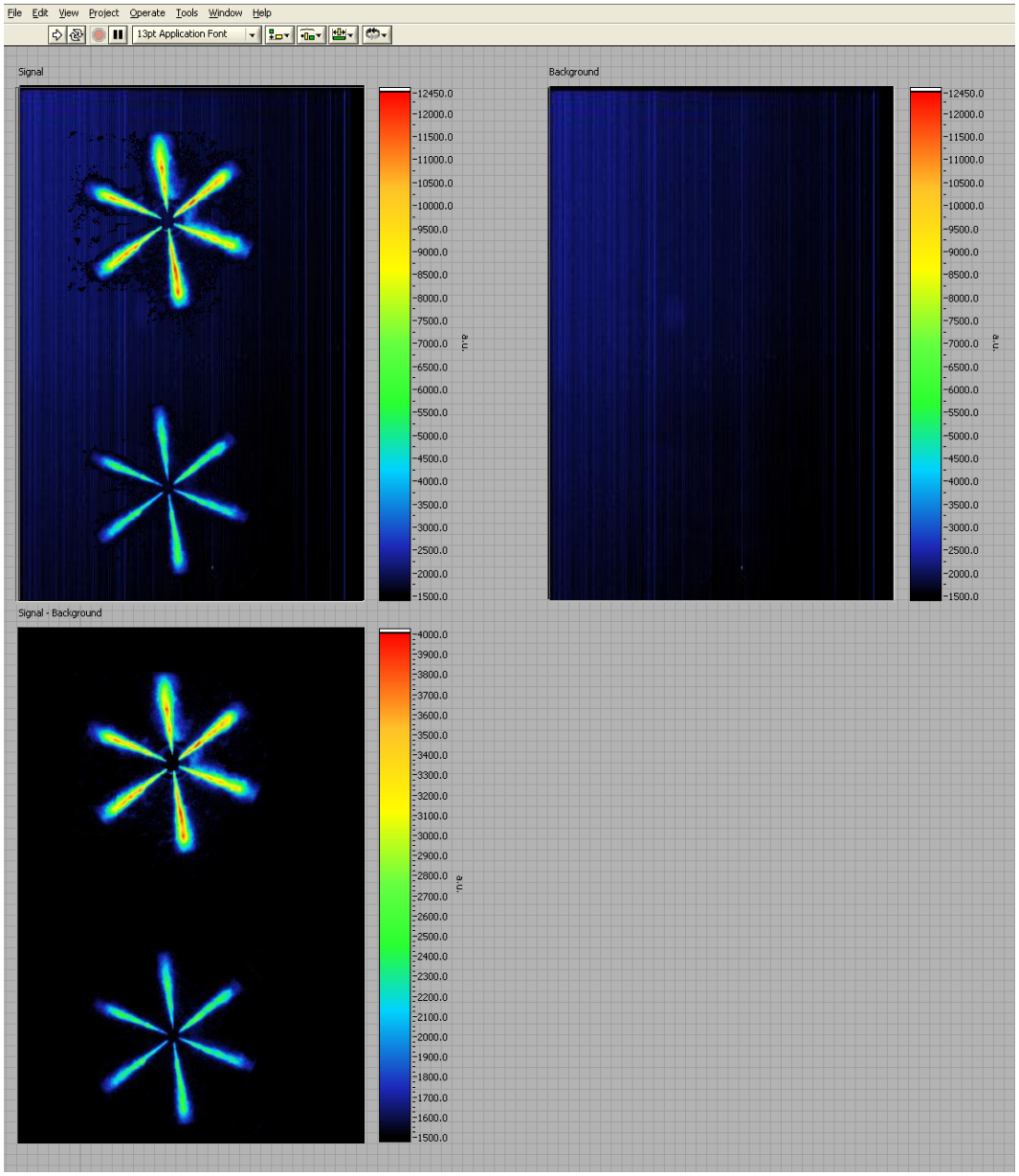

Figure 7.14 Front Panel of LIEF.vi Program

Two background images were obtained for each image sequence, one with the laser while fuel injection was deactivated and the other without the laser and fuel injection. Although the average background signal was removed by the program, the remnant of

the background noise may be present in the processed images due to statistical fluctuations in the background signal.

7.8 Results

LIEF images of evaporating diesel sprays using the single injection strategy are presented in the following sections using TMPD/α-methyl-naphthalene exciplex system with the following dopant concentrations,

- **Strategy 1 -** 89% decane, 10% α-methyl-naphthalene and 1% TMPD
- **Strategy 2 -** 88% decane, 10% α-methyl-naphthalene and 2% TMPD

The engine operating conditions, fuel injection timing, optical setup and laser energy level were identical in both cases. The experimental conditions employed for strategies 1 and 2 are shown in Table 7.2.

Table 7.2 Experimental Conditions for Strategies 1 and 2

Excitation Source	Excimer 308nm (XeCl)
Laser Pulse Duration	25 ns
Average Energy	100 mJ
Laser Beam Dimension	47x47 mm^2
ICCD Camera Array Size	389 x 579
Image Resolution	123 µm x 123 µm per pixel
Injection Timing	25^o CA BTDC
Injection Quantity	10 mm^3
Injection Pressure	1200 bar
Intake Temperature	40^o C
Intake Pressure	1.5 bar
Engine Speed	1500 rpm

7.8.1 Strategy 1

The fuel spray images at different timings After the Start of Injection (ASOI) using 89% decane, 10% α-methyl-naphthalene and 1% TMPD are illustrated in Figure 7.15.

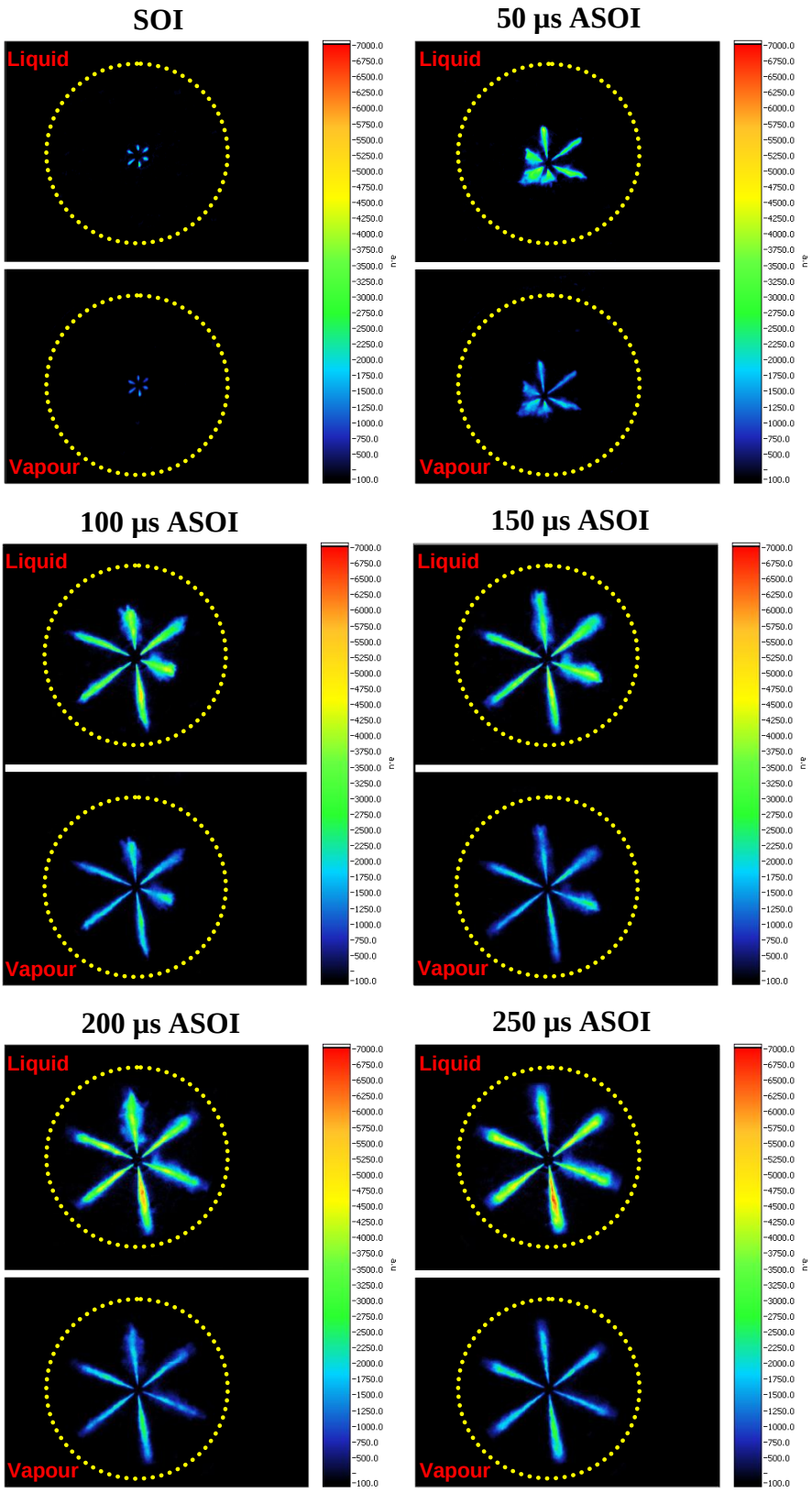

Figure 7.15 Contour Maps of Spatial Distribution of Liquid and Vapour Phases of Evaporating Diesel Fuel Sprays, Strategy 1

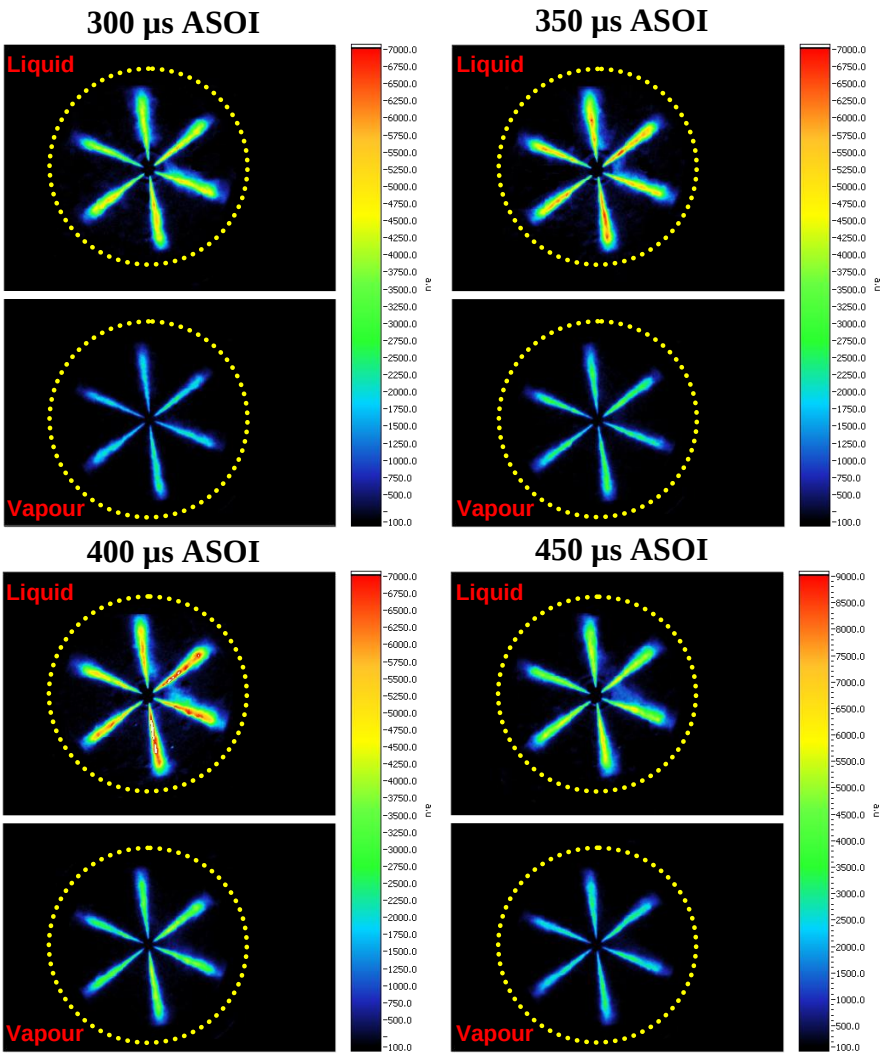

Figure 7.15 Contour Maps of Spatial Distribution of Liquid and Vapour Phases of Evaporating Diesel Fuel Sprays (cont'd)

Since the laser pulse lasted 10-20 ns and the fluorescence lifetime of the exciplex system lied within the range of 10 to 100 ns, frozen flow images of the fuel sprays were obtained. From the image sequence presented in Figure 7.15 at 50, 100 and 150 µs ASOI, the asymmetry of the fuel sprays is evident, this is an inherent characteristic of VCO injectors utilised in this study as previously discussed in Section 5.2.1. This result was in good agreement with the high speed images presented in Chapter 6. This phenomenon exists at the initial stages of the fuel injection and diminishes once the injector needle is fully open as evident in Figure 7.15. The liquid and vapour concentrations increased in the image sequence at 200, 250, 300, 350 and 400 µs ASOI as more fuel was injected. The fuel sprays in these images are almost fully

developed with the liquid length almost impinging on the piston wall. However, the penetration seen in the images is in the radial direction, since the fuel sprays were illuminated using a laser beam through the piston crown. Thus the real penetration should be calculated using the cone angle of the injector utilised. The vapour fuel distribution almost followed the same pattern as that of the liquid phase which was not expected, this may be attributed to the cross-talk in the vapour signal due to the liquid phase. This phenomenon must be further investigated by acquiring the fluorescence spectra of the exciplex system at elevated pressures and temperatures.

7.8.2 Strategy 2

The fuel spray images at different timings after the start of injection using 88% decane, 10% α-methyl-naphthalene and 2% TMPD are illustrated in Figure 7.16.

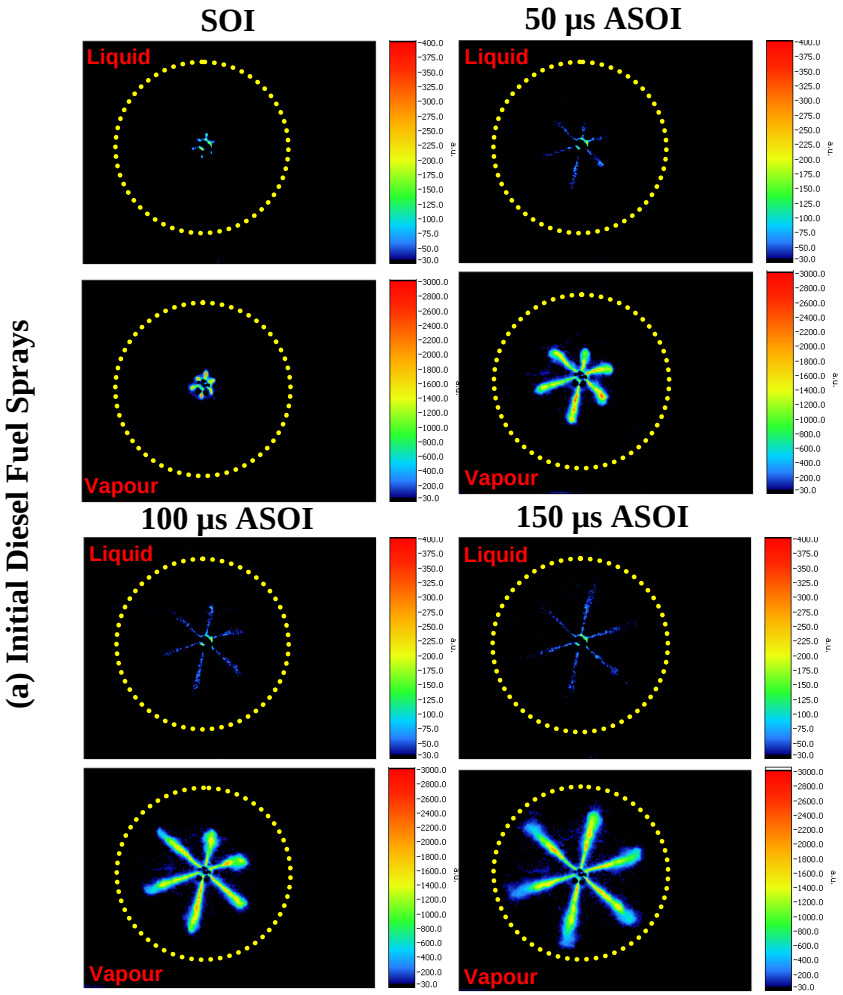

Figure 7.16 Contour Maps of Spatial Distribution of Liquid and Vapour Phases of Evaporating Diesel Fuel Sprays, Strategy 2; (a) Initial Diesel Fuel Sprays, (b) Diesel Fuel Sprays at Later Stages

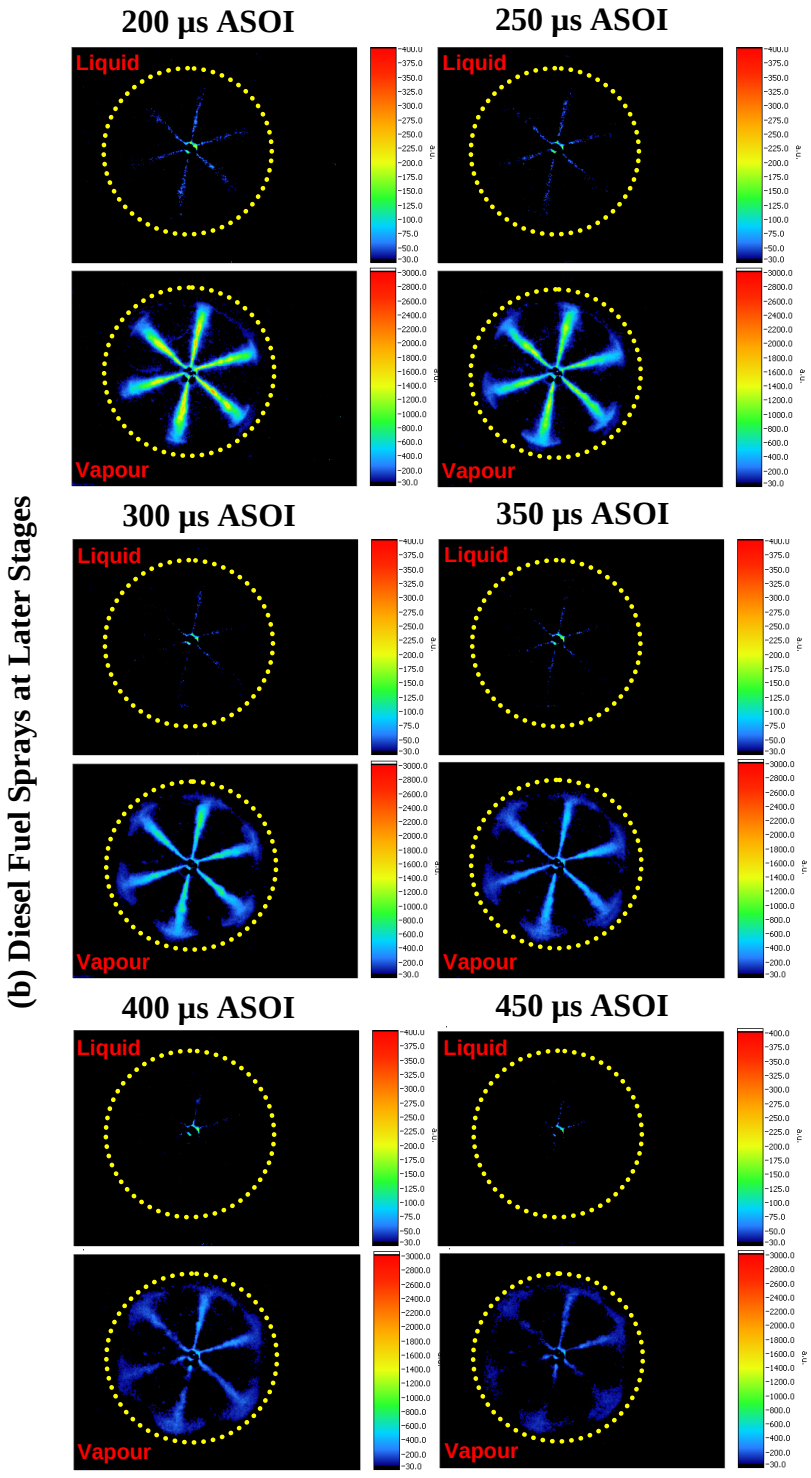

Figure 7.16 Contour Maps of Spatial Distribution of Liquid and Vapour Phases of Evaporating Diesel Fuel Sprays, Strategy 2; (a) Initial Diesel Fuel Sprays, (b) Diesel Fuel Sprays at Later Stages (cont'd)

From the image sequence presented in Figure 7.16 at 50 and 100 µs ASOI, the asymmetry of fuel sprays is evident, the same explanation holds true as that of strategy 1. The liquid signal intensity was substantially lower than the vapour phase; this may be due to the spectral shift of the exciplex species at elevated pressures and temperatures with the fuel mixture used and/or TMPD decomposition at such pressures and temperatures. In contrast, increase in TMPD concentration resulted in much improved vapour signal. The spatial distribution of the vapour phase is clearly observed in the image sequence at 150, 200, 250, 300, 350, 400 and 450 µs ASOI. In these images, the mushroom structure observed in high speed images due to spray impingement on the piston wall is clearly shown. This fuel mixture resulted in clear indication of the vapour phase while the fuel mixture used for strategy 1 led to clear exhibition of the liquid phase. Therefore, an optimum fuel mixture must be developed in order to balance the signal intensities in both liquid and vapour phases. As previously stated in Section 7.8.1, the fluorescence spectra of the tested fuel mixtures must be further examined at elevated pressures and temperatures similar to those experienced in HSDI diesel engines under motoring conditions using a CVC. A new CVC was designed by the author, capable of operating at such pressures and temperatures, which is currently being manufactured at Brunel University. The schematic diagram of the setup is shown in Figure 7.17.

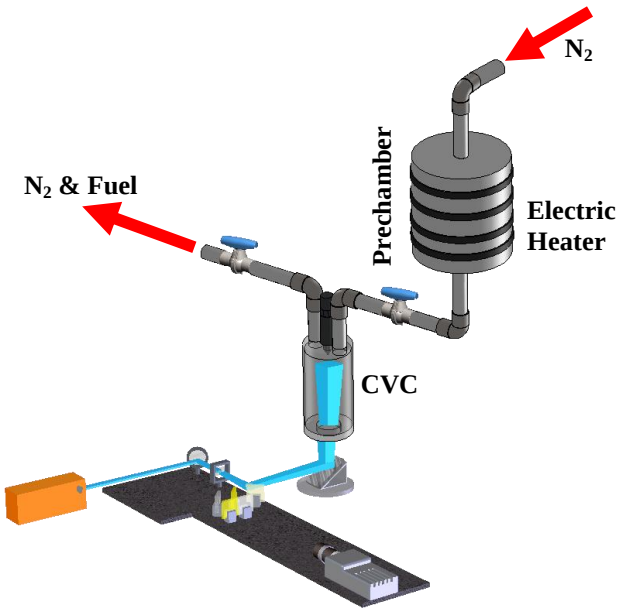

Figure 7.17 Schematic Diagram of Newly Designed Constant Volume Chamber

In this setup nitrogen is pressurised and heated in the prechamber. The preheated nitrogen is then transferred to the CVC once the desired temperature is reached. Subsequently, fuel is injected into the CVC and the fluorescence intensities of liquid and vapour phases are recorded.

7.9 Summary

This chapter included detailed explanation of the principle of the LIEF technique, its implementation and calibration in an optical diesel engine. The specification of the equipment, optical components, the control systems and the data acquisition system were explained. The spatial distribution of liquid and vapour phases were presented and analysed using TMPD/α-methyl-naphthalene exciplex system with different dopant concentrations. In addition, current research being conducted on further development of the technique was discussed.

CHAPTER 8

8

Conclusions and Recommendations for Future Work

8.1 Conclusions

This study investigated the in-cylinder fuel injection, mixing and combustion using a VCO solenoid injector in an optical single cylinder diesel engine. The in-cylinder mixing and combustion processes and exhaust emissions were studied through the development and implementation of a range of optical techniques as well as utilisation of emission analysers. In addition, the in-cylinder pressure measurement was employed for the characterisation of the combustion process through heat release rate analysis. The first investigation involved the characterisation of the FIE for single and split injection strategies while the second investigation was carried out on the in-cylinder fuel injection, mixing and combustion of split injection using commercially available diesel fuel. The third study involved the development and application of the LIEF technique for fuel evaporation and mixing studies under the motored engine operations.

8.1.1 Fuel Injection Equipment Characterisation

The following conclusions were drawn from the first investigation performed, detailed in Chapter 5.

- A constant volume chamber based fuel injection rig has shown to be capable of accurate measurement of the rate of injection and the quantity for both single and split injections.

- The split injection with 5^{o} CA dwell angle resulted in interaction between the first and the second injections for all the injection strategies tested. This was

identified to be due to the mechanical limitations of the injector utilised. In the case of 10^o CA, 15^o CA, 20^o CA and 25^o CA dwell timings the injection quantity of the first injection remained almost constant for all the tested strategies, though the quantity of the second injection varied depending on the dwell timing used. This was mainly attributed to the negative effect of pressure waves in the high pressure fuel line which was due to the first injection, as depicted in Chapter 5.

- In the case of 10^o CA dwell angle, fuel line pressure was declining at the start of the second injection which resulted in reduced injected fuel quantity during this phase of injection. Although fuel line pressure was lower than set in the case of 15^o CA, it was higher in comparison to the former case which led to the increase in the injected fuel quantity for this strategy. In the case of 20^o CA the fuel quantity during the second injection was lower than expected; however, its effect was less paramount in comparison to 10^o CA case since the fuel line pressure was relatively higher at the start of the second injection. The same trend held true in the case of 25^o CA, though the reduction in fuel line pressure due to the pressure waves was less in comparison to the former case which explained the increase in injected fuel quantity for this strategy.

- In addition to the critical information on fuel injection quantity delivered during the split injection process, the fuel injection results highlighted the negative effect of multiple injections on the injector's performance and the additional care required in the application of such injection strategies to diesel engines.

8.1.2 In-Cylinder Studies of Fuel Injection, Mixing and Combustion

Fuel injection, mixture formation, autoignition, combustion and emission characteristics of single and split investigation strategies using commercially available diesel fuel were investigated. The effects of injection timing, quantity and dwell angle in split injection strategies were investigated. Three different split injection strategies including 30:70, 50:50 and 70:30 were studied. Additionally, the effect of total fuel demand using 10 mm^3 and 20 mm^3 total fuel quantities were investigated. Moreover,

the effect of variable and fixed dwell angle in split injections were examined, five different values between 5^o CA and 25^o CA in the case of variable and 10^o CA in the case of fixed dwell timing. The last parameter investigated was the injection timing, nine injection timings were tested for each of the strategies.

The following conclusions were reached as detailed in Chapter 6:

- The results obtained using 10 mm^3 single fuel injection showed that the IMEP values increased as the injection was further retarded. This was mainly due to improved fuel evaporation and mixing processes. The same trend held true for strategies with total fuel demand of 20 mm^3, however considerably higher soot and NOx emissions were produced in comparison to the former case.

- In all cases of split injection strategies, the dwell angle of 5^o CA produced the highest IMEP value due to greater total fuel injection quantity whereby the interaction between the two injections almost replicated a single injection with prolonged injection duration. The second highest IMEP was achieved with the dwell timing of 15^o CA, as stated earlier the total injected fuel quantity for these strategies was higher that all the other dwell timings utilised in this investigation, excluding 5^o CA dwell timing. The same trend was observed in terms of soot emission whereby the highest soot production was produced by the strategies with the aforementioned dwell timings. However, the trend in NOx emission was different in the case of 10 mm^3 and 20 mm^3 fuel demand. In the former case, the highest NOx emission was produced by 5^o CA and 15^o CA dwell timings due to the higher gas temperature caused by the greater fuel quantity injected. However, the opposite was observed in the latter case, this was mainly attributed to the effect of latent heat of evaporation of fuel due to considerably higher total fuel injection quantity in comparison to the former case. Although NOx emission in the latter case was considerably lower than the former, severe penalty in terms of uHC emission incurred.

- In the case of fixed dwell angle, the injection quantity remained constant while the timing of the first injection was altered. The soot and NOx emissions were reduced for almost all the strategies with retarded injection due to late

initiation of the combustion during the expansion stroke. However, very low IMEP values were produced for all the tested strategies, consequently, one set of data was analysed and the remnant were presented in the Appendices.

- The effect of late injection on soot formation and oxidation was investigated. The results revealed that although reduction in soot concentration was achieved with these strategies, it remained almost the same and in some cases higher that those using variable dwell timing. Though, considerable increase in uHC emission incurred using fixed dwell timing.

8.1.3 Laser Induced Exciplex Fluorescence Technique

The LIEF technique was developed and implemented in the optical single cylinder diesel engine utilised in this study. Two TMPD/naphthalene exciplex systems were tested: one consisted of 89% decane, 10% α-methyl-naphthalene and 1% TMPD and the other 88% decane, 10% α-methyl-naphthalene and 2% TMPD. The fluorescence emissions spectra of these two exciplex systems were acquired based on which appropriate optical filters were used. A single injection strategy with 10 mm^3 total fuel injection quantity was used. The liquid and vapour phases of evaporating diesel sprays were simultaneously measured using the aforementioned exciplex systems. The results showed that:

- The exciplex system containing 1% TMPD resulted in satisfactory visualisation of the liquid phase though the cross-talk in the vapour phase avoided accurate detection of the vapour phase.

- In contrast, the exciplex system containing 2% TMPD resulted in satisfactory visualisation of the vapour phase, replicating similar features observed in the high speed movies, though the intensity of the liquid phase was compromised as a result. This was mainly attributed to TMPD decomposition at elevated temperatures.

8.2 Recommendations for Future Work

The soot loading measured by the two-colour method suffered from low sensitivity of the detection system, thus it is recommended to measure the soot concentration using the LII technique in order to verify the accuracy of the results.

The use of split injection strategy with variable dwell timing has shown the potential for simultaneous reduction of NOx and soot emissions in diesel engines. Although the absolute values of exhaust emissions were higher than those of the single strategies, the IMEP values obtained through the former strategies were considerably higher. This implies that the same engine performance can be achieved through the use of split injection strategies with lower exhaust emissions and reduced fuel consumption. However, optimisation of injection timing, quantity and dwell angle plays a crucial role in the application of split injection strategies. Therefore, further investigation of this mode of injection using Design of Experiments (DoE) technique is suggested, aimed at optimisation of the aforementioned FIE features for different loads and speeds. In addition, further characterisation of the fuel injection system is recommended in order to achieve the desired rate of fuel injection for a given injection pressure and duration such that true effect of split injection strategy can be exposed. Further, piezoelectric injectors are known for their accuracy and tolerance, thus the use of such injectors is recommended for the investigation of split injection strategies.

The combustion efficiency and the level of exhaust emissions is a function of spatial and temporal distributions of premixed fuel within the combustion chamber of diesel engines. Thus, the application of nonintrusive laser based optical diagnostic techniques such as LIEF are beneficial in better understanding of the processes involved. The LIEF technique has been developed and implemented in the single cylinder optical diesel engine utilised in this study aimed at detailed analysis of fuel evaporation and mixing processes. The system utilised a blend of special dopants referred to as exciplex system, the fluorescence spectra of which forms the basis of its application. Thus, it is recommended to study the fluorescence spectra of exciplex systems with various dopant concentrations aimed at the optimisation of the liquid and vapour signals. In addition, detailed analysis of the characteristics of such exciplex systems at elevated pressures and temperatures is highly recommended. Furthermore,

high speed visualisation technique can be performed in conjunction with the LIEF technique in order to further validate the results using the latter technique.

Appendix A

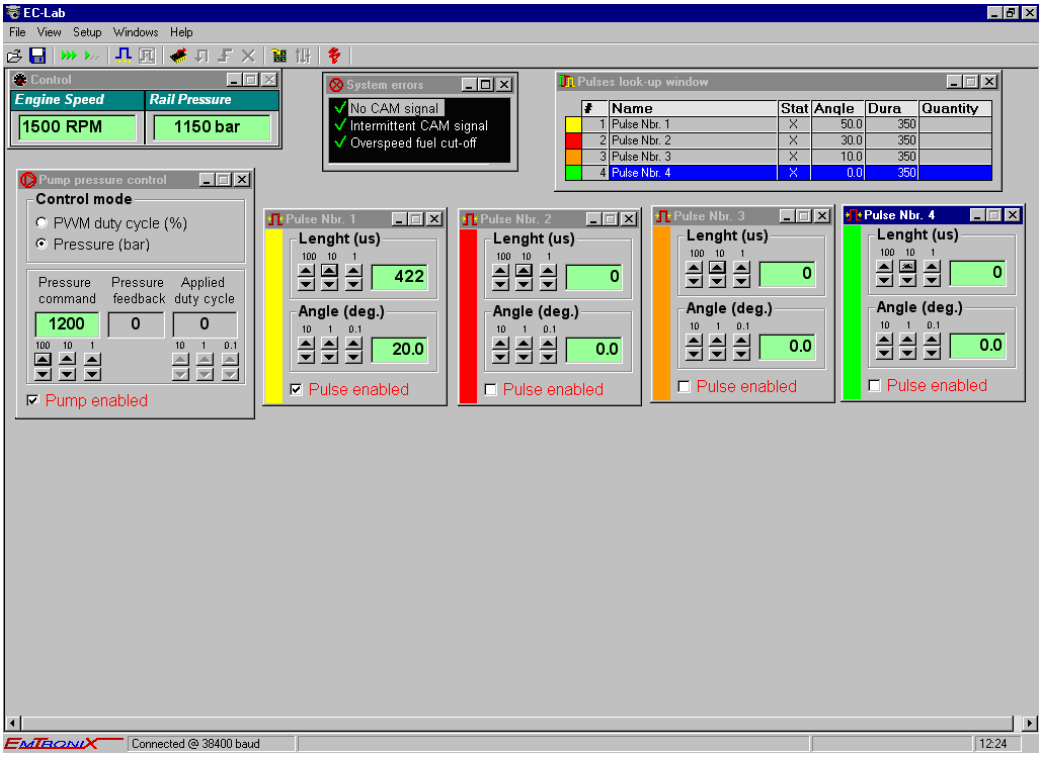

Figure A1 Screenshot of EC-Lab Software

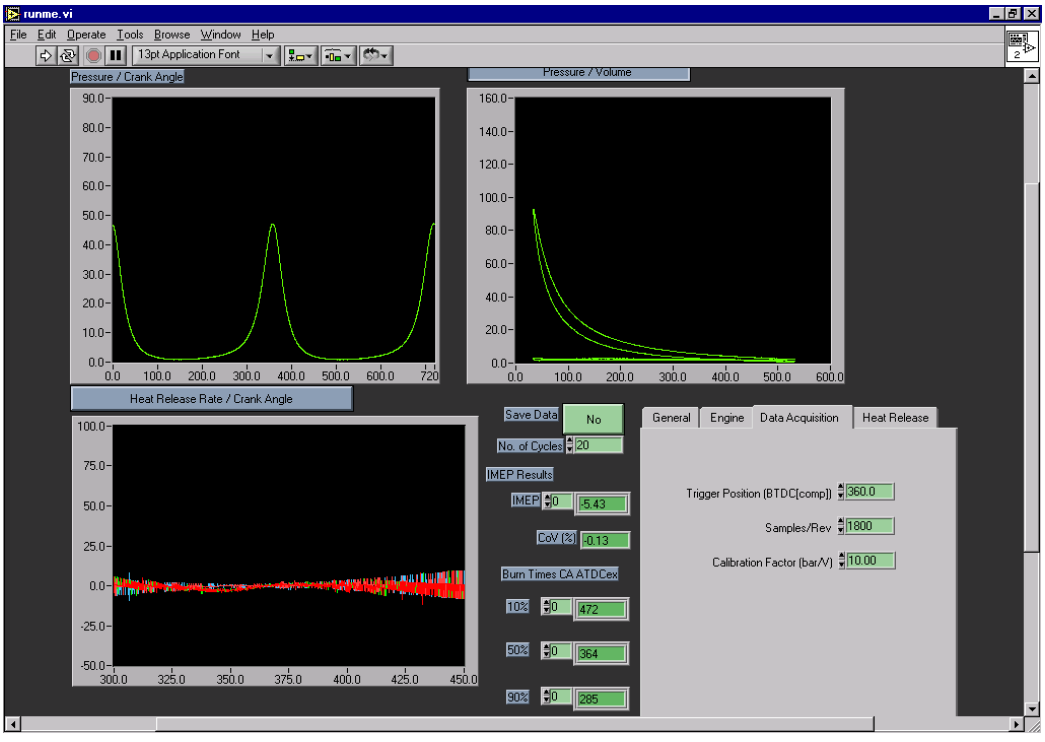

Figure A2 Screenshot of Data Acquisition Software

Appendix B

Table B1 Tungsten Lamp Calibration Matrix

Temp [K]	Current [A]	Temp [K]	Current [A]	Temp [K]	Current [A]
973	6.52	1313	10.83	1653	17.71
983	6.60	1323	11.01	1663	17.94
993	6.68	1333	11.18	1673	18.17
1003	6.77	1343	11.36	1683	18.40
1013	6.86	1353	11.54	1693	18.63
1023	6.95	1363	11.72	1703	18.86
1033	7.04	1373	11.91	1713	19.09
1043	7.14	1383	12.09	1723	19.33
1053	7.24	1393	12.28	1733	19.56
1063	7.34	1403	12.47	1743	19.80
1073	7.45	1413	12.66	1753	20.03
1083	7.56	1423	12.86	1763	20.27
1093	7.67	1433	13.05	1773	20.51
1103	7.78	1443	13.25	1783	20.75
1113	7.90	1453	13.45	1793	21.00
1123	8.02	1463	13.65	1803	21.24
1133	8.14	1473	13.85	1813	21.48
1143	8.27	1483	14.05	1823	21.73
1153	8.40	1493	14.26	1833	21.98
1163	8.53	1503	14.46	1843	22.22
1173	8.66	1513	14.67	1853	22.47
1183	8.80	1523	14.88	1863	22.72
1193	8.94	1533	15.09	1873	22.97
1203	9.08	1543	15.30	1883	23.23
1213	9.23	1553	15.52	1893	23.48
1223	9.38	1563	15.73	1903	23.73
1233	9.53	1573	15.95	1913	23.99
1243	9.68	1583	16.16	1923	24.25
1253	9.84	1593	16.38	1933	24.50
1263	10.00	1603	16.60	1943	24.76
1273	10.16	1613	16.82	1953	25.02
1283	10.33	1623	17.04	1963	25.28
1293	10.49	1633	17.27	1973	-
1303	10.66	1643	17.49		

Table B2 The Relation between the Pixel Intensity Values and the Apparent Temperatures

Aperture Position	Gain (%)	Apparent Temperature Equations	Cut-off Pixel Values
f 4	90	Ta1 = 6E-05(pv) + 2153.5	< 1,600,000
		Ta2 = 7E-05(pv) + 2043.6	< 1,650,000

Appendix C

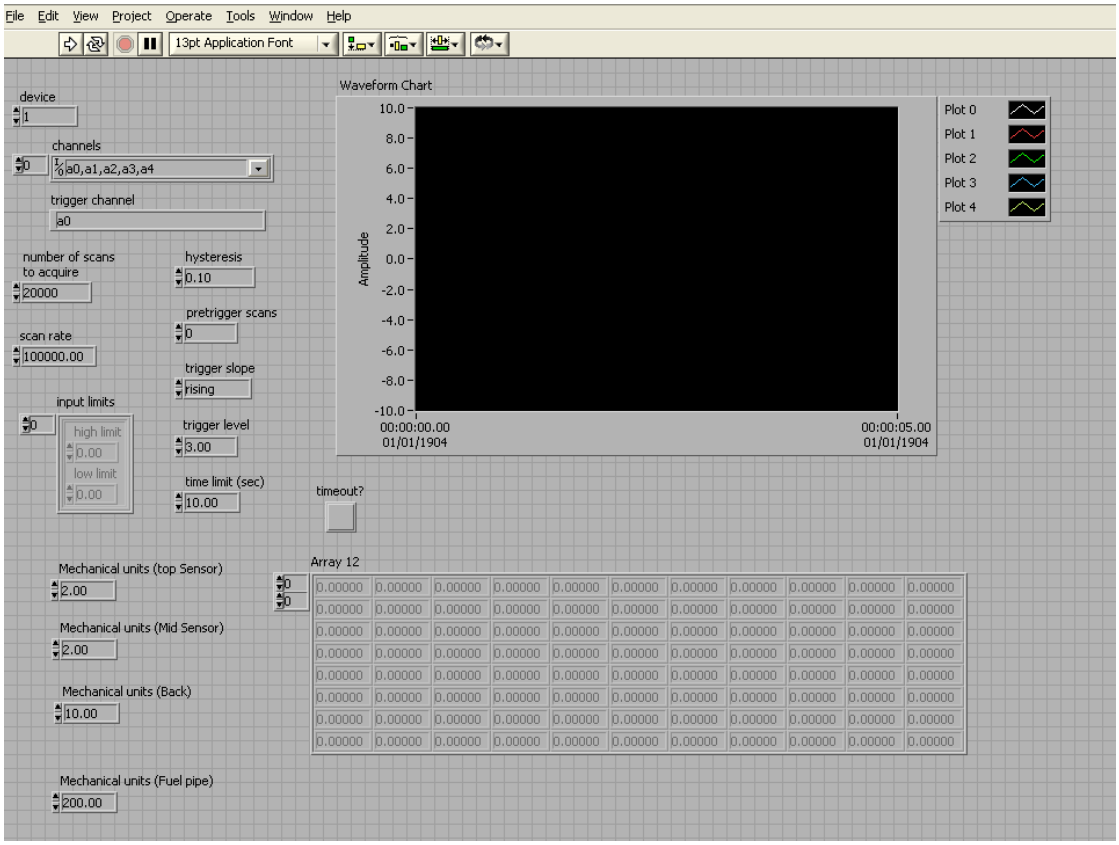

Figure C1 Screenshot of Injection Rate Test Rig Data Acquisition Software

Appendix D

Strategy CC

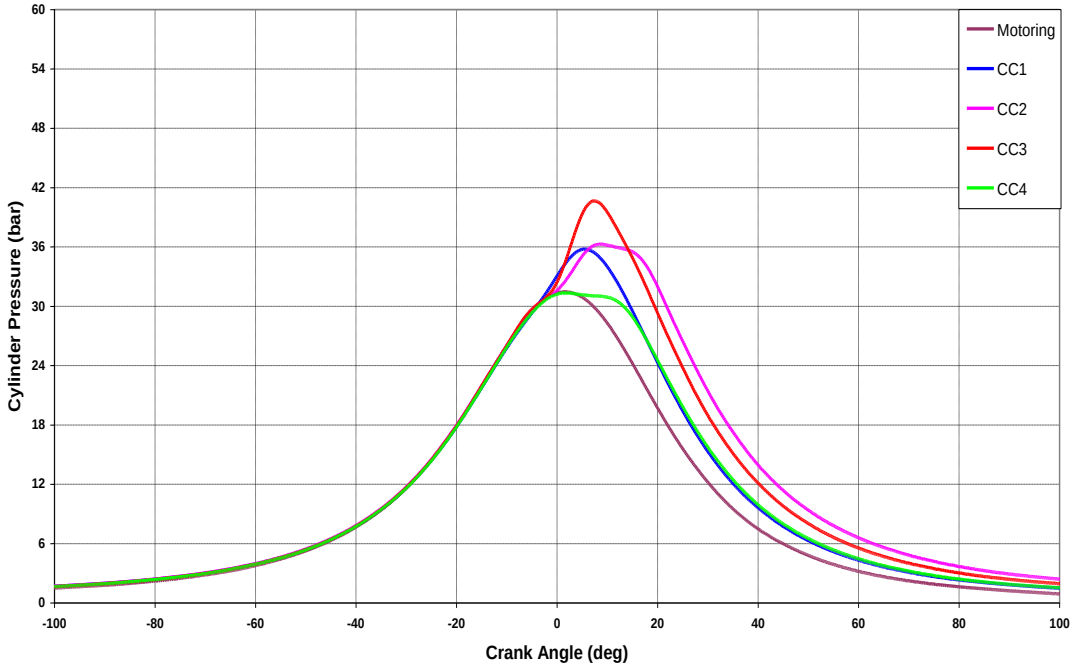

Figure D1 In-Cylinder Pressure Data for Strategy CC at 1200 bar

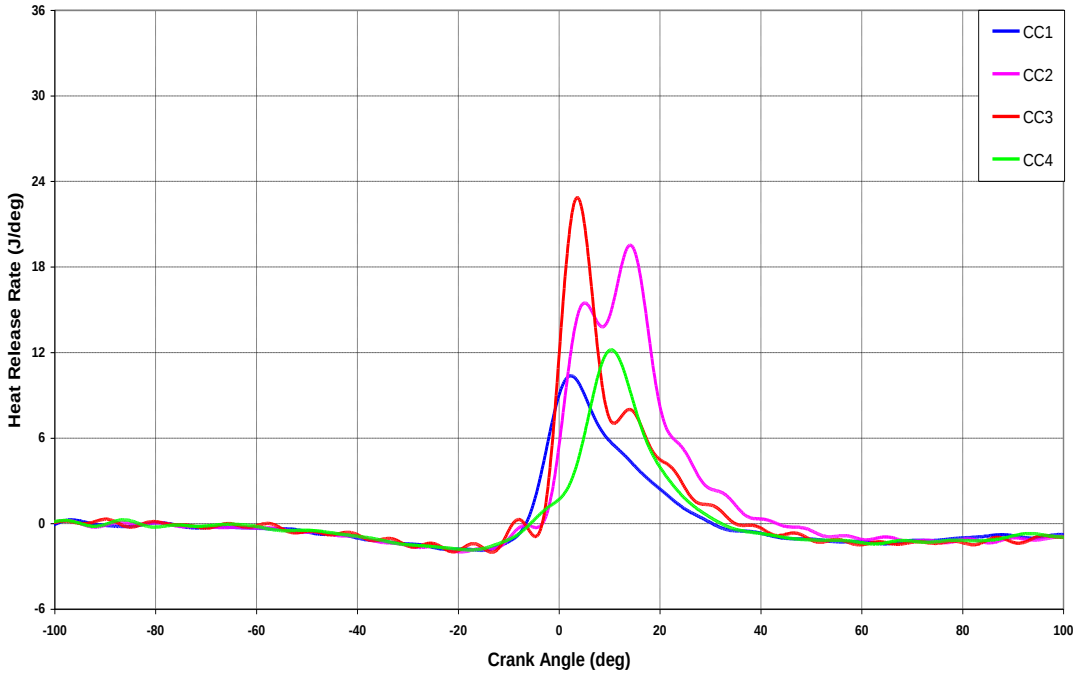

Figure D2 Heat Release Rate Traces for Strategy CC at 1200 bar

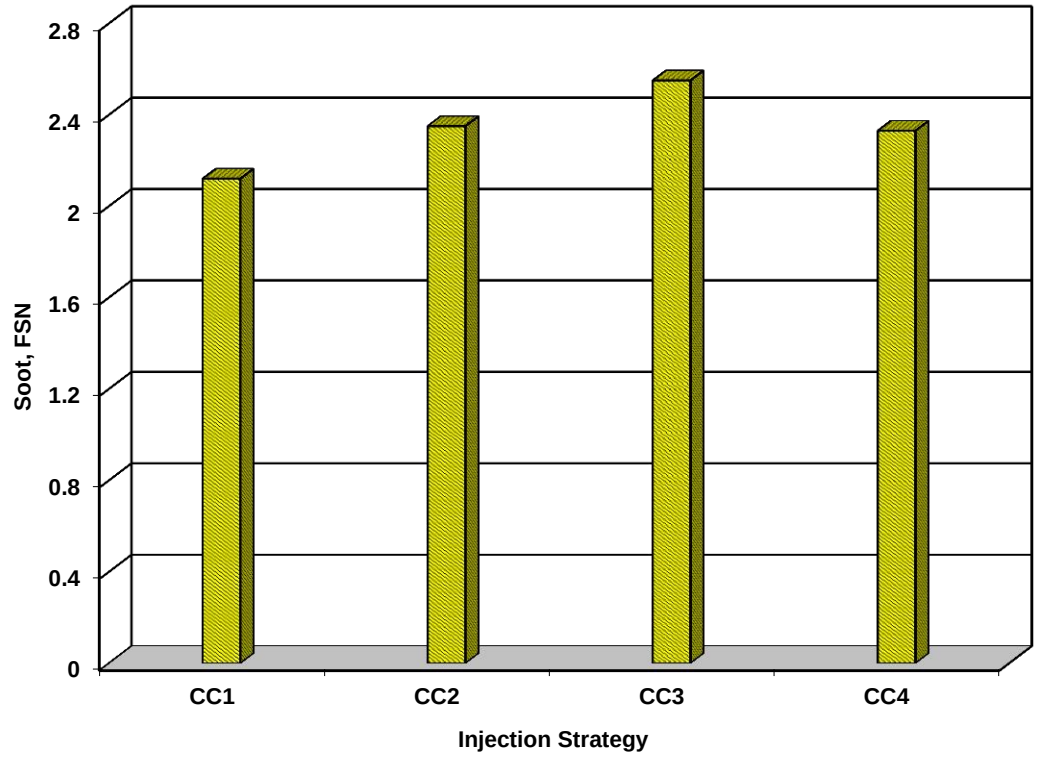

Figure D3 Soot Concentration for Strategy CC at 1200 bar

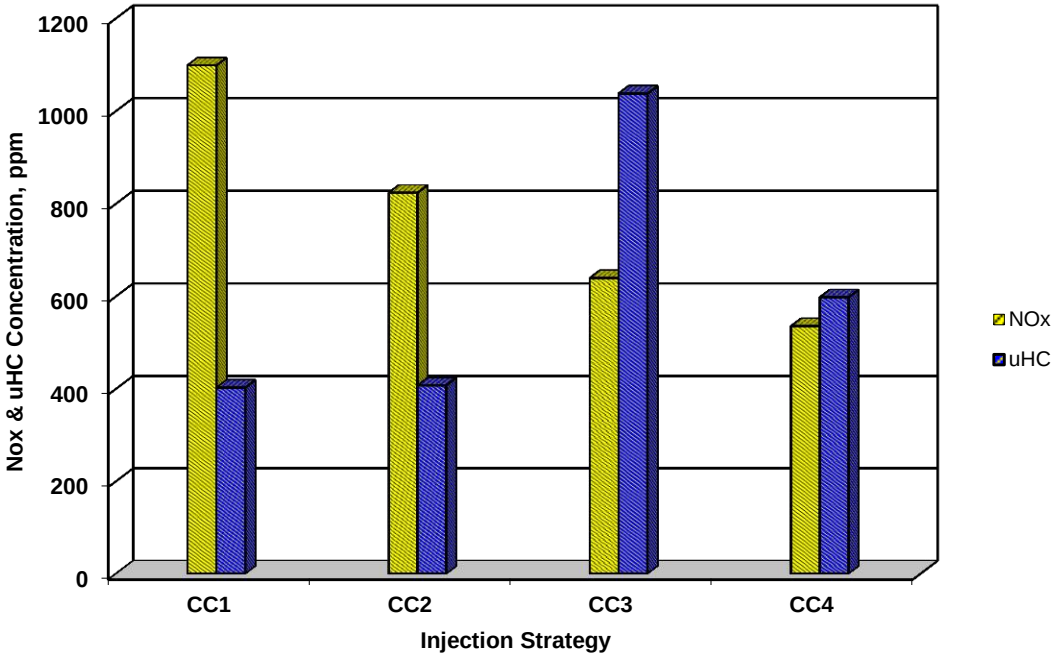

Figure D4 NOx and uHC Concentration for Strategy CC at 1200 bar

Strategy E

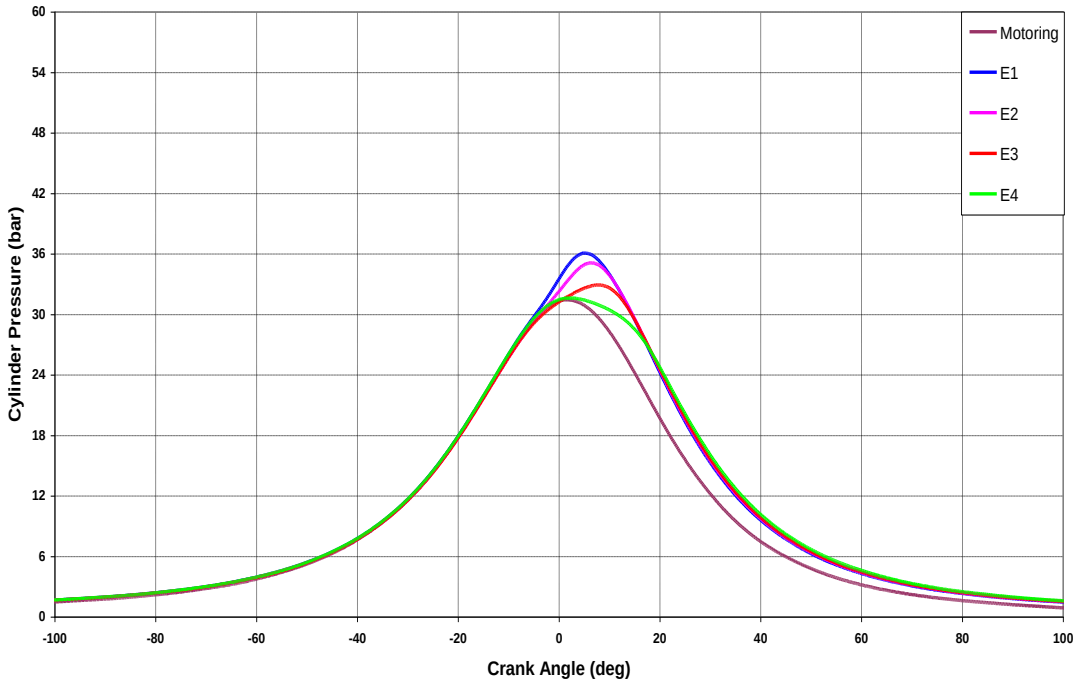

Figure D5 In-Cylinder Pressure Data for Strategy E at 1200 bar

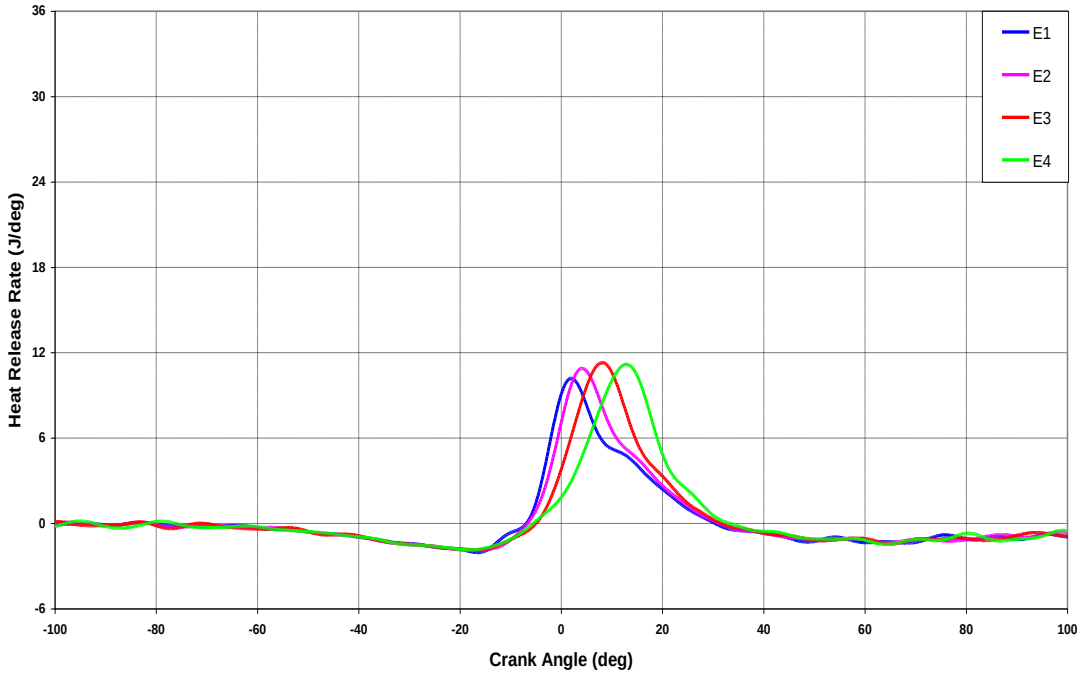

Figure D6 Heat Release Rate Traces for Strategy E at 1200 bar

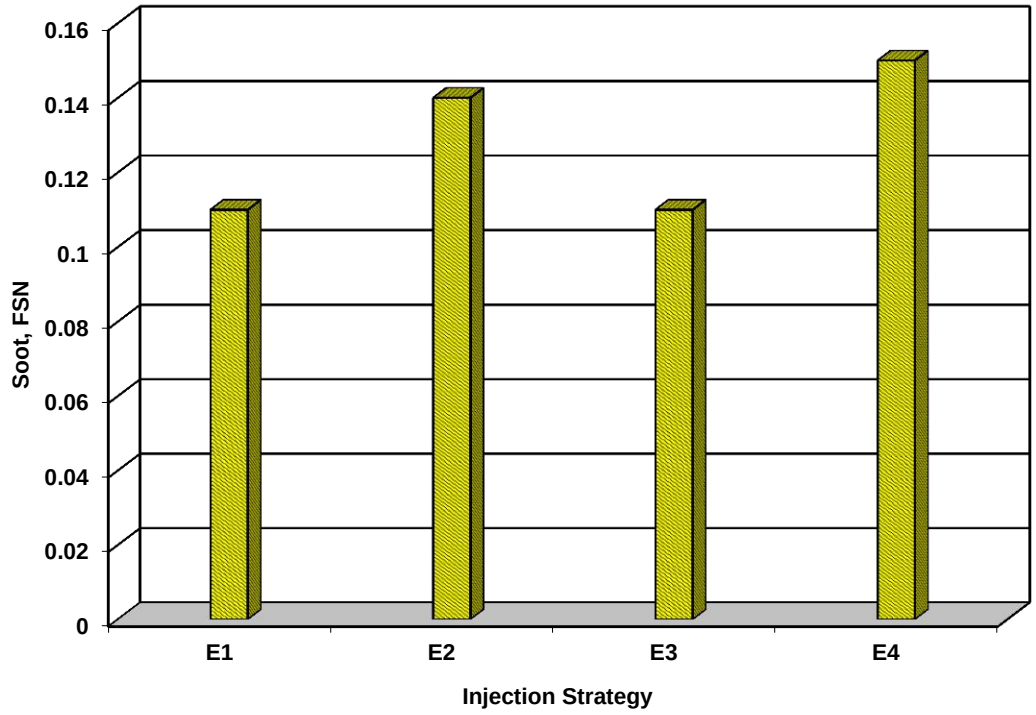

Figure D7 Soot Concentration for Strategy E at 1200 bar

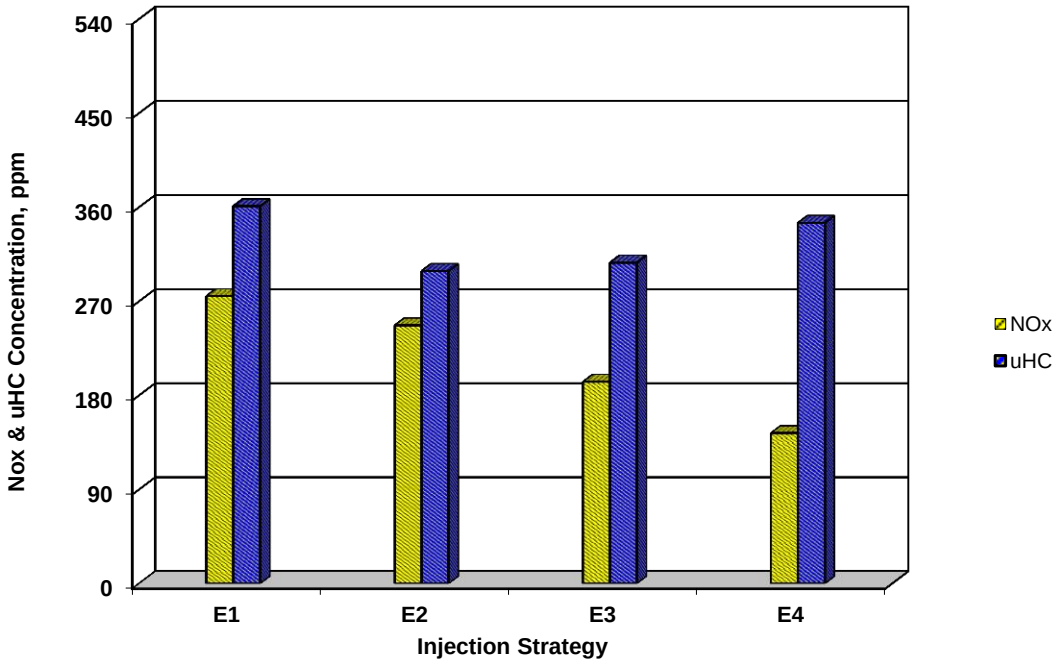

Figure D8 NOx and uHC Concentration for Strategy E at 1200 bar

Strategy EE

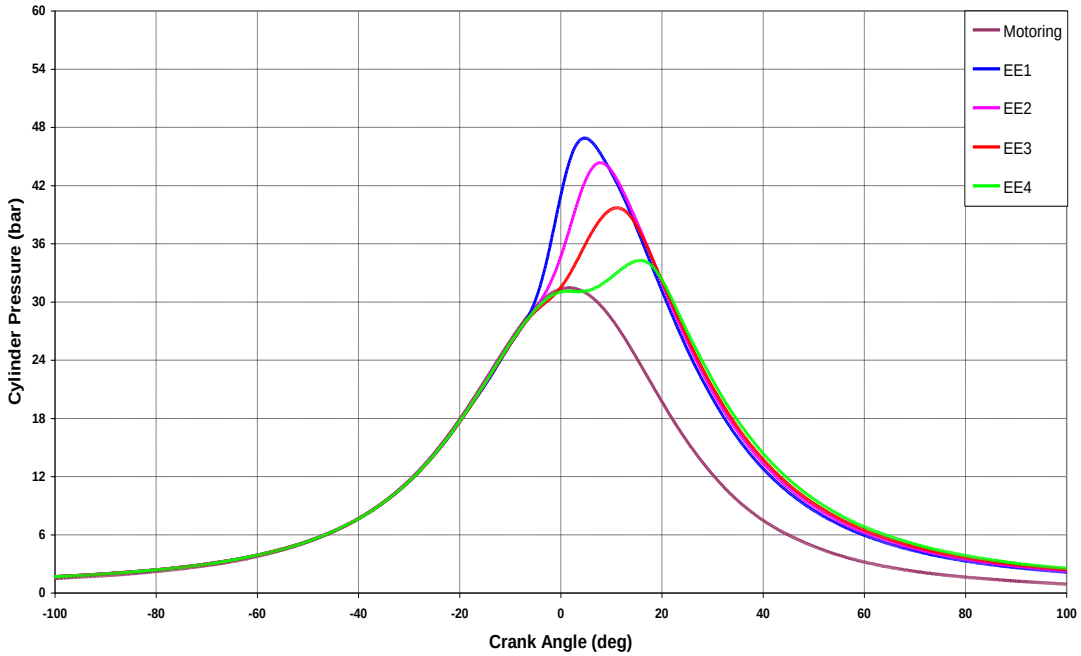

Figure D9 In-Cylinder Pressure Data for Strategy EE at 1200 bar

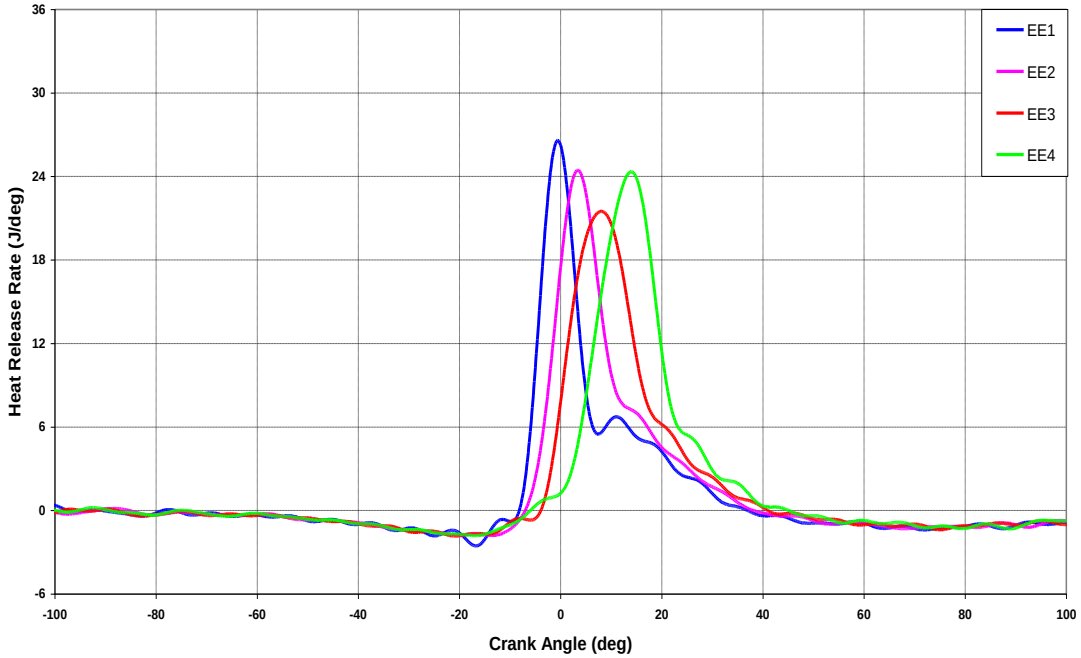

Figure D10 Heat Release Rate Traces for Strategy EE at 1200 bar

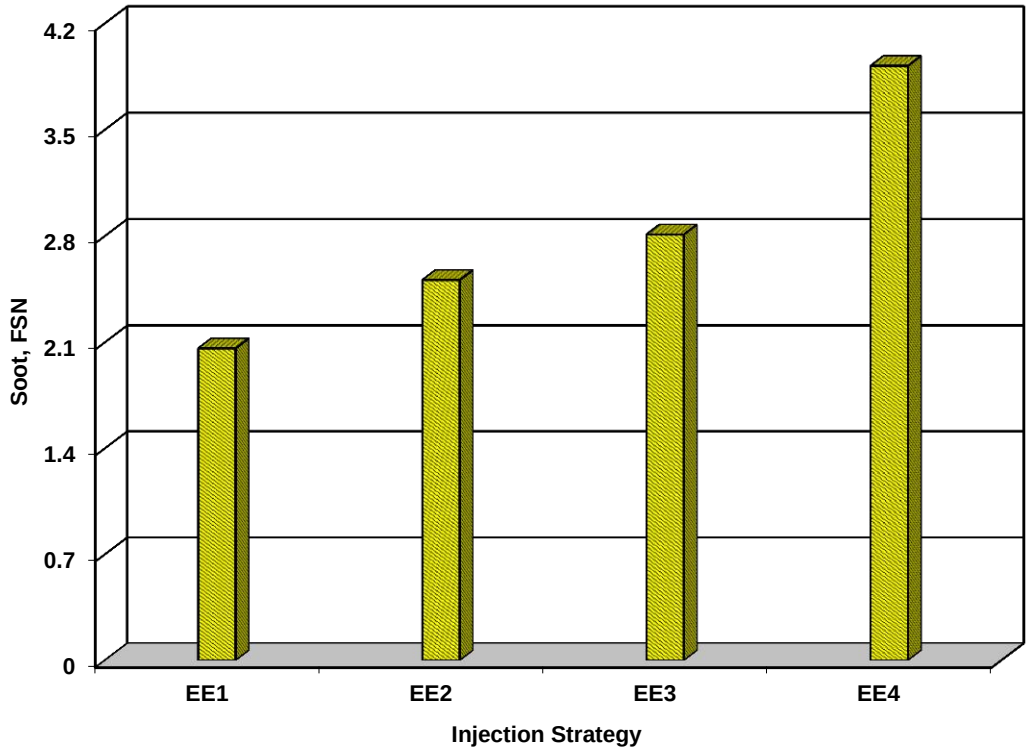

Figure D11 Soot Concentration for Strategy EE at 1200 bar

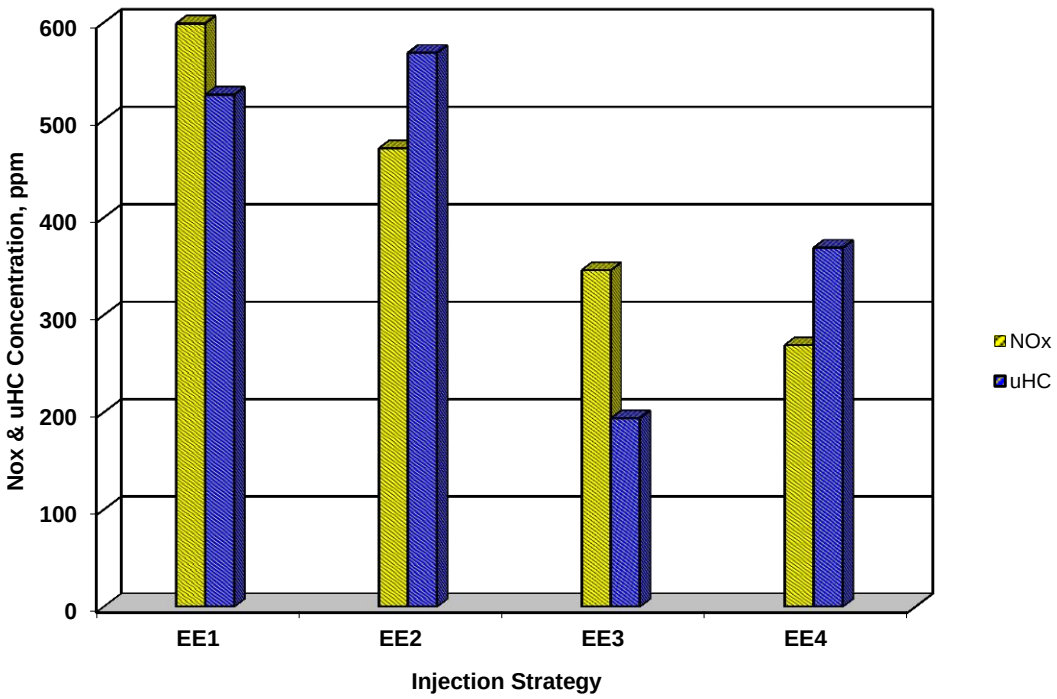

Figure D12 NOx and uHC Concentration for Strategy EE at 1200 bar

Strategy H

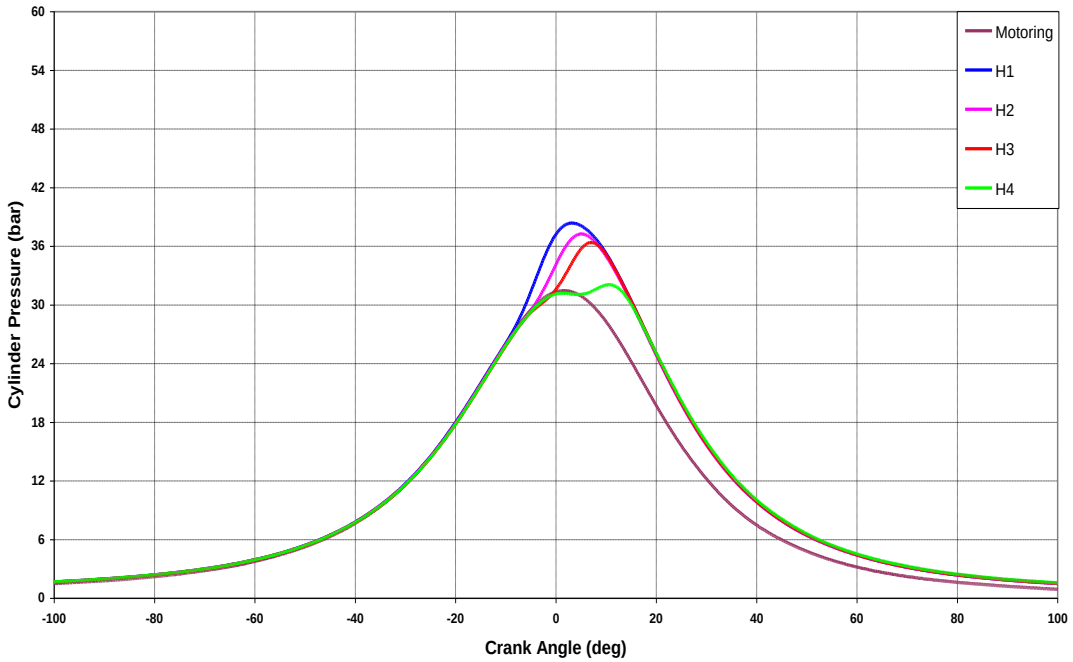

Figure D13 In-Cylinder Pressure Data for Strategy H at 1200 bar

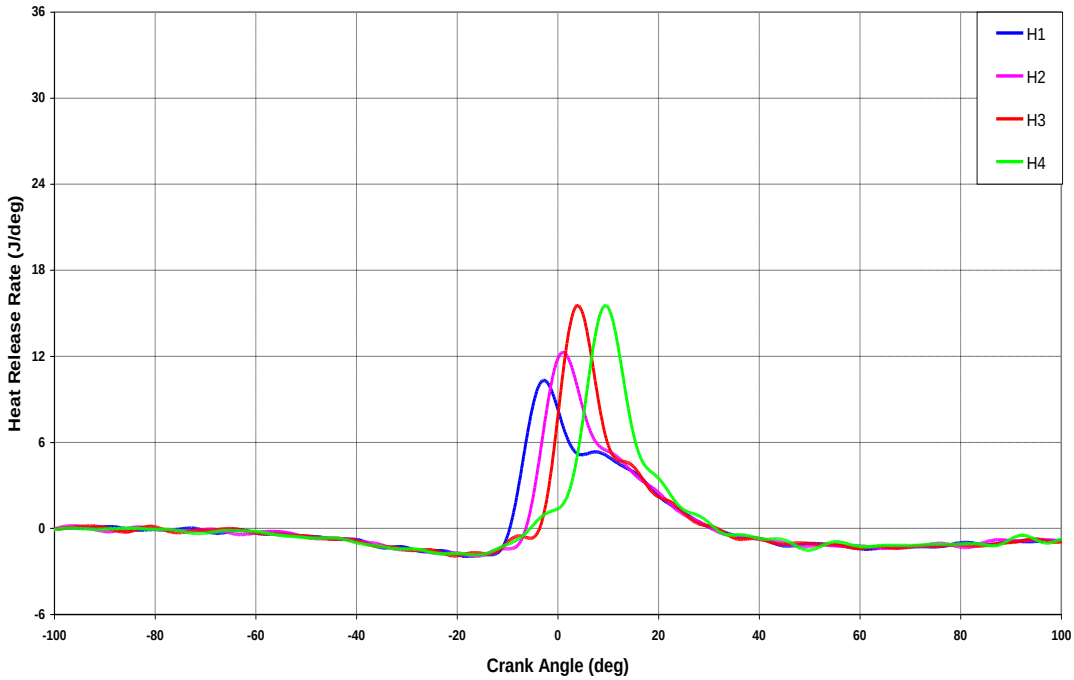

Figure D14 Heat Release Rate Traces for Strategy H at 1200 bar

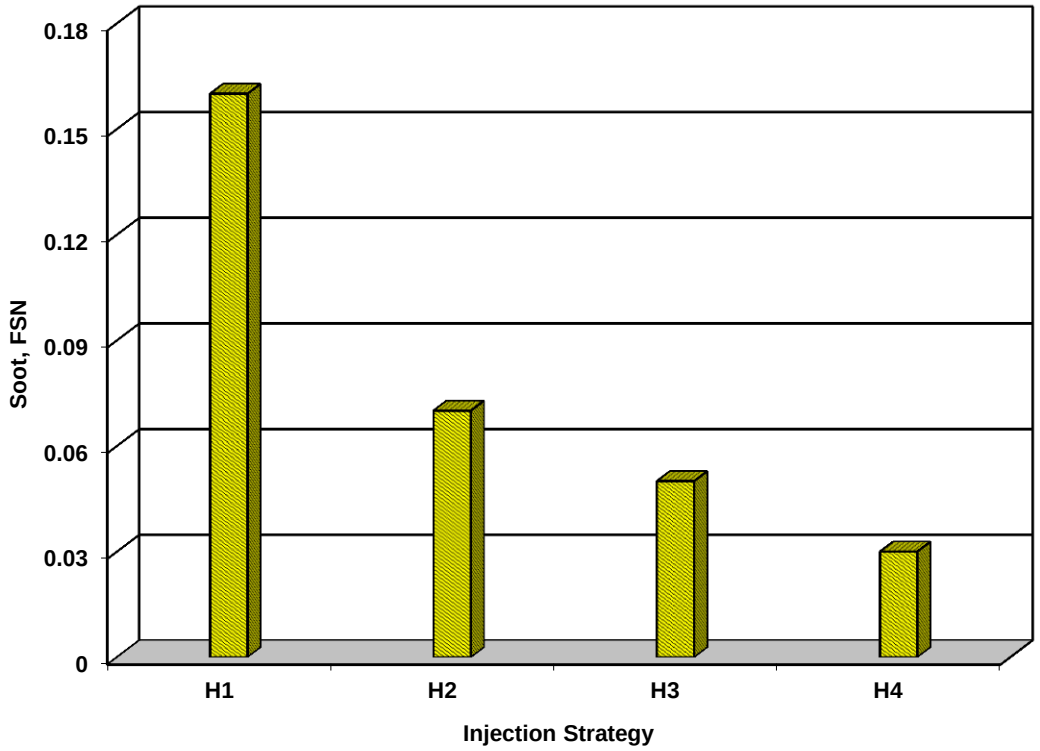

Figure D15 Soot Concentration for Strategy H at 1200 bar

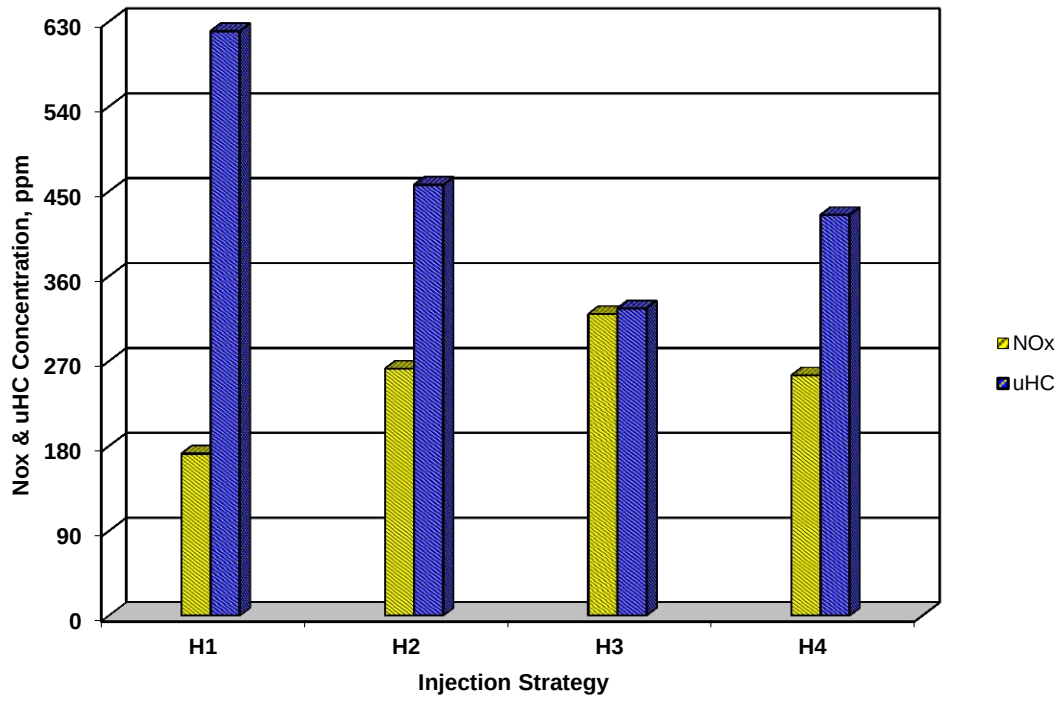

Figure D16 NOx and uHC Concentration for Strategy H at 1200 bar

Strategy HH

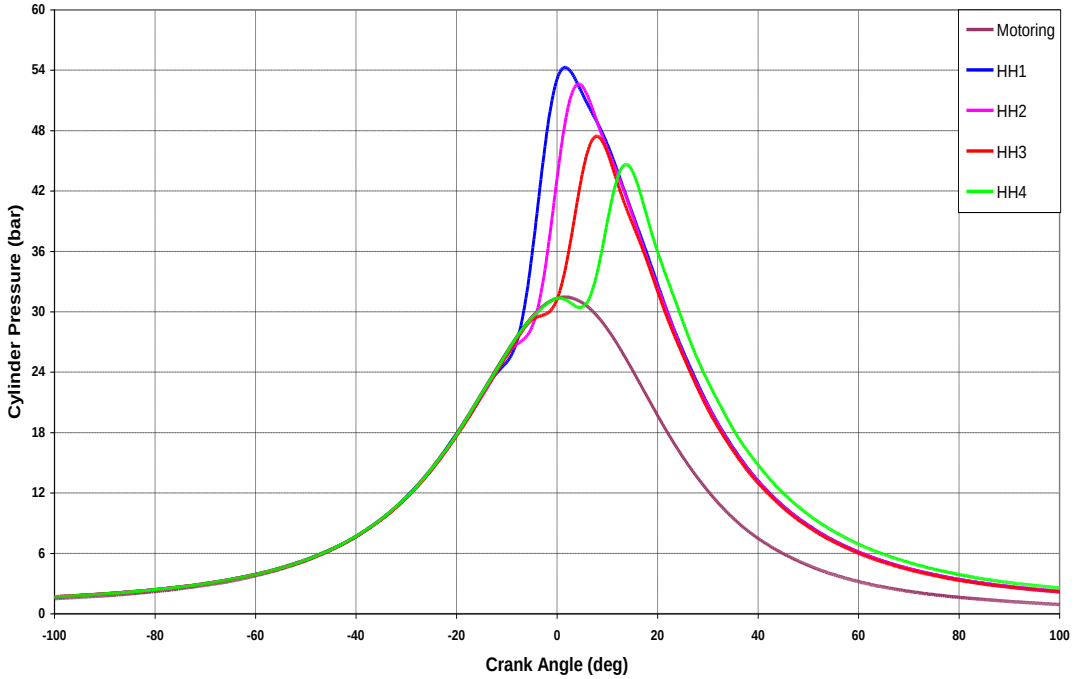

Figure D17 In-Cylinder Pressure Data for Strategy HH at 1200 bar

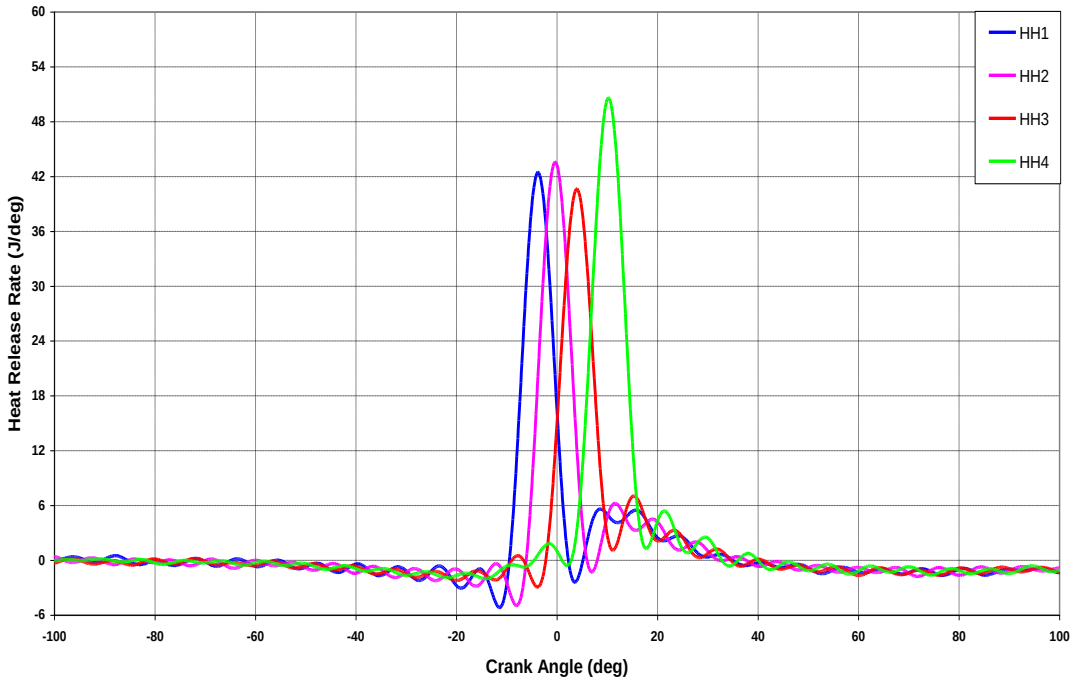

Figure D18 Heat Release Rate Traces for Strategy HH at 1200 bar

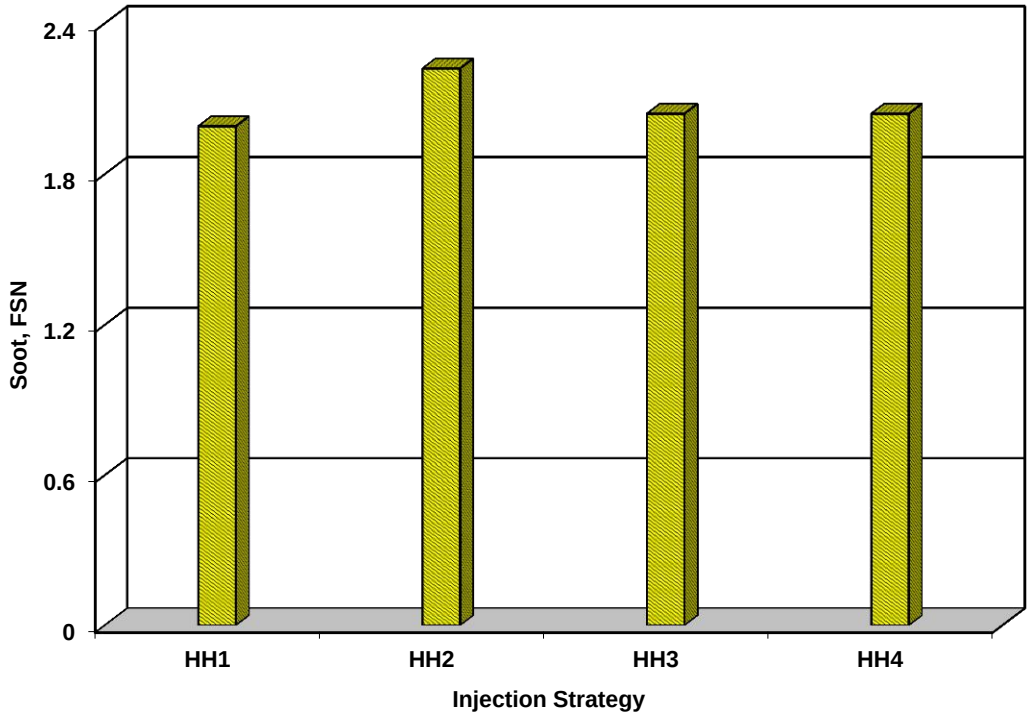

Figure D19 Soot Concentration for Strategy HH at 1200 bar

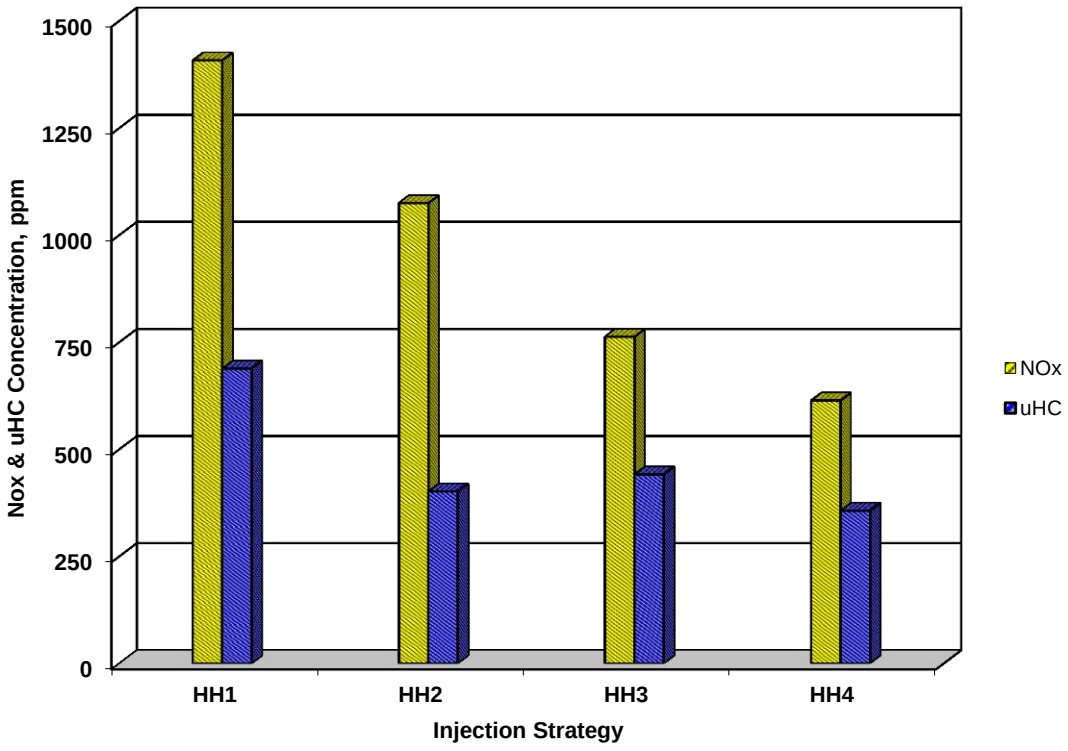

Figure D20 NOx and uHC Concentration for Strategy HH at 1200 bar

Appendix E

Table E1 Specifications of Optical Filters

	360 LPF	400 SPF	475 LPF
Make	Schott	Asahi	Schott
Model	WG360	ZUS0400	GG475
CWL	360 +/- 6nm	400 +/- 5nm	475 +/- 6nm
Size	50x50mm^2	50x50mm^2	50x50mm^2
Thickness	3mm	1mm	3mm
AOI	0 degrees	0 degrees	0 degrees

Table E2 Specifications of Dichroic Filers

	330 DCF	420 DCF
Make	Horiba	Horiba
Model	330DCLP	420DCLP
Transmission	>=90% @peak	>=90% @peak
Size	100x100mm^2	50x50mm^2
Thickness	3.0 +/- 0.2mm	1mm
AOI	45 degrees	45 degrees

References

1. Heywood, J.B., 1988. Internal Combustion Engine Fundamentals McGraw-Hill Science Engineering

2. MAN Diesel and Turbo. [Cited on 15/03/2010; Available from: http://www.manbw.dk/]

3. European Automobile Manufacturers' Association. [Cited on 15/03/2010; Available from: http://www.acea.be/]

4. California Air Resource Board. [Cited on 16/03/2010; Available from: http://www.arb.ca.gov/homepage.htm]

5. Environmental Protection Agency. [Cited on 20/03/2010; Available from: http://www.epa.gov/]

6. European Commission. [Cited on 29/03/2010; Available from: http://ec.europa.eu/]

7. Stanmore, B.R., Brilhac, J.F., Gilot, P., 2001. The oxidation of soot: a review of experiments, mechanisms and models. Carbon. Vol. 39, PP 2247

8. Kittelson, D.B., 1998. Engines and nanoparticles: a review. Journal of Aerosol Society, Vol. 29, No. 5

9. Kittelson, D.B., Watts, W.F., Johnson, J.P., Rowntree, C.J., Goodier, S.P., Payne, M.J., Preston, W.H., Warrens, C.P., Ortiz, M., Zink, U., Goersmann, C., Twigg, M.V., Walker, A.P., 2006. Driving Down On-Highway Particulate Emissions. SAE Paper 2006-01-0916

10. Xi, J., and Zhong, B., 2006. Soot in Diesel Combustion Systems. Chemical Engineering Technology, Vol. 29, No. 6

11. Bockhorn, H., 1994. Soot Formation in Combustion (Bockhorn, H. Ed.). Springer, Berlin, Vol. 59

12. Dobbin, R.A., Subramaniasivam, H., 1994. Soot Formation in Combustion: Mechanism and models (Bockhorn, H. Ed.). Springer, Berlin, Vol. 59

13. Shigeki, D., Yoshitada K., Takayuki I., Naohisa O., Toshihisa S., 2000. Analysis of soot accumulation inside diesel engines. JSAE Review, Vol. 21, No. 3, PP 303-308

14. Suzuki, H., Koike, N., Ishii, H., Odaka, M., 1997. Exhaust Purification of Diesel Engines by Homogeneous Charge with Compression Ignition Part 1: Experimental Investigation of Combustion and Exhaust Emission Behavior

Under Pre-Mixed Homogeneous Charge Compression Ignition Method. SAE Paper 970313

15. Suzuki, H., Koike, N., Ishii, H., Odaka, M., 1997. Exhaust Purification of Diesel Engines by Homogeneous Charge with Compression Ignition Part 2: Analysis of Combustion Phenomena and NOx Formation by Numerical Simulation with Experiment. SAE Paper 970315

16. Senda, J., Ikeda, M., Yamamoto, M., Kawaguchi, B., Fujimoto, H., 1999. Low Emission Diesel Combustion System by Use of Reformulated Fuel with liquefied CO2 and n-Tridecane. SAE Paper 1999-01-1136

17. Kawano, D., Senda, J., Kawakami, K., Shimada, A., Fujimoto, H., 2001. Fuel Design Concept for Low Emission in Engine Systems -2nd report Analysis of Combustion Characteristics for the mixed fuels. SAE Paper 2001-01-1071

18. Adomeit, P., Pischinger, S., Becker, M., Rohs, H., Greis, A., Grünefeld, G., 2006. Potential Soot and CO Reduction for HSDI Diesel Combustion Systems. SAE Paper 2006-01-1417

19. Miyamoto, N., Ogawa, H., Nurun, N.M., Obata, K., Arima, T., 1998. Smokeless, Low NOx, High Thermal Efficiency, and Low Noise Diesel Combustion with Oxygenated Agents as Main Fuel. SAE Paper 98-05-06

20. Kitamura, T., Ito, T., Senda, J., and Fujimoto, H., 2001. Detailed Chemical Kinetic Modeling of Diesel Spray Combustion with Oxygenated Fuels. SAE Paper 2001-01-1262

21. Xu, Y., Lee, C.F., 2006. Study of Soot Formation of Oxygenated Diesel Fuels Using Forward Illumination Light Extinction (FILE) Technique. SAE Paper 2006-01-1415

22. Dec, J.E., Espey, C., 1995. Ignition and Early Soot Formation in a DI Diesel Engine Using Multiple 2-D Imaging Diagnostics. SAE Paper 950456

23. Dec, J.E., 1992. Soot Distribution in a DI Diesel Engine Using 2-D Imaging of Laser-Induced Incandescence, Elastic Scattering, and Flame Luminosity. SAE Paper 920115

24. Espey, C., Dec, J.E., 1993. Diesel Engine Combustion Studies in a Newly Designed Optical-Access Engine Using High-Speed Visualization and 2-D Laser Imaging. SAE Paper 930971

25. Asai, G., Kurata, K., Yokoyama, T., Senda, J., Fujimoto, H., 1997. Soot Diagnostics in Diesel Combustion by means of Laser-Induced Scattering and Laser-Induced Incandescence Method. SAE Transaction, Vol. 28, No. 3, SAE Paper 9736636

26. Dec, J.E., Espey, C., 1992. Soot and Fuel Distributions in a D.I. Diesel Engine via 2-D Imaging. SAE Transactions, Vol. 101, Sec. 4, pp 1642-1651, SAE Paper 922307

27. Zur Loye, A.O., Siebers, D.L., Dec, J.E., 1990. 2-D Soot Imaging in a Direct-Injection Diesel Engine Using Laser-Induced Incandescence," Proceedings of the International Symposium on Diagnostics and Modelling of Combustion in Internal Combustion Engines. COMO-DIA, vol. 90, PP 523-528

28. Dec, J.E., 1997. A Conceptual Model of DI Diesel Combustion Based on Laser-Sheet Imaging. SAE Paper 970873

29. Senda, J., Choi, D., Iwamuro, M., Fujimoto, H., Asai G., 2002. Experimental Analysis on Soot Formation Process in DI Diesel Combustion Chamber by Use of Optical Diagnostics. SAE Paper 2002-01-0893

30. Inagaki, K., Takasu, S., Nakakita, K., Watanabe, S., 2003. Quantitative Analysis of Soot Formation and Oxidation Process using Laser-Induced Incandescence. SAE Paper 2003-01-1795

31. Xu, Y., Lee, C.F., 2004. Investigation of Soot Formation in Diesel Combustion Using Forward Illumination Light Extinction (FILE) Technique. SAE Paper 2004-01-1411

32. Xu, Y., Lee, C.F., 2004. Effects of Ambient Temperature and Oxygen Concentration on Soot Evolution in Diesel Spray Combustion. Proceedings of 2004 ASME Heat Transfer/Fluids Engineering Summer Conference HT-FED2004-56433

33. Han, Z., Uludogan, A.N., Hampson, G.J., Reitz, R.D., 1996. Mechanism of Soot and NOx Emission Reduction Using Multiple-Injection in a Diesel Engine. SAE Paper 960633

34. Xu, Y., Lee, C.F., 2005. Investigation of Fuel Effects on Soot Formation Using Forward Illumination Light Extinction (FILE) Technique. SAE Paper 2005-01-0365

35. Fujimoto, H., Kurata, K., Asai, G., Senda, J., 1998. OH Radical Generation and Soot Formation / Oxidation in DI Diesel Engine. SAE Paper 982630

36. Choi, D., Enami, M., Kurata, K., Asai, G., Senda, J., Fujimoto, H., 1999. Soot Formation and Oxidation Process in a DI Diesel Engine by Use of LII/LIS Technique. The 15th Internal Combustion Engine Symposium (Intl.) in Seoul, Paper No. 9935590, PP 315-320

37. Hiroyasu, H., Kadota, T., 1976. Models for Combustion and Formation of Nitric Oxide and Soot in DI Diesel Engines. SAE Paper 760129

38. Fusco, A., Knox-Kelecy, A.L., Foster, D.E., 1994. Application of a Phenomenological Soot Model for Diesel Engine Combustion. The 3rd International Symposium on Diagnostics and Modeling of Combustion in Internal Combustion Engines, COMODIA 94, PP 571-576

39. Kazakov, A. Foster, D.E., 1998. Modeling of Soot Formation During DI Diesel Combustion Using A Multi-Step Phenomenological Model. SAE Paper 982463

40. Tao, F., Reitz, R.D., Foster, D.E., Liu, Y., 2009. Nine-step phenomenological diesel soot model validated over a wide range of engine conditions. International Journal of Thermal Sciences, Vol. 48, PP 1223-1234

41. Fujimoto, H.G., Senda, J., Komemushi, Y., Kuge, T., 2006. Soot Generation in Spray of Oxygenated Fuel. SAE Paper 2006-01-3371

42. Janssen, A., Muether, M., Kolbeck, A., Lamping, M., Pischinger, S., 2010.The Impact of Different Biofuel Components in Diesel Blends on Engine Efficiency and Emission Performance. SAE Paper 2010-01-2119

43. Karavalakis, G., Bakeas, E., Stournas, S., 2010. An Experimental Study on the Impact of Biodiesel Origin and Type on the Exhaust Emissions from a Euro 4 Pick-up Truck. SAE Paper 2010-01-2273

44. Kawano, D., Mizushima, N., Ishii, H., Goto, Y., Iwasa, K., 2010. Exhaust Emission Characteristics of Commercial Vehicles Fuelled with Biodiesel. SAE Paper 2010-01-2276

45. Kuhnert, S., Wagner, U., Spicher, U., Haas, S.F., Gabel , K., Kutschera, I., 2010. Influence of Injection Nozzle Hole Diameter on Highly Premixed and Low Temperature Diesel Combustion and Full Load Behavior. SAE Paper 2010-01-2109

46. Morgan, R.E., Gold, M.R., Laguitton, O., Crua, C., Heikal, M.R., 2003. Characterisation of the Soot Formation Processes in a High Pressure Combusting Diesel Fuel Spray. SAE Paper 2003-01-3086

47. Bergin, M., Reitz, R.D., Oh, S., Miles, P.C., Hildingsson, L., Hultqvist, A., 2007. Fuel Injection and Mean Swirl Effects on Combustion and Soot Formation in Heavy Duty Diesel Engines with EGR. SAE Paper 2007-01-0912

48. Ehleskog, R., Ochoterena, R.L., 2008. Soot Evolution in Multiple Injection Diesel Flames. SAE Paper 2008-01-2470

49. Roberts, C.E., Naegeli, D., Chadwell, C., 2005. The Effect of Water on Soot Formation Chemistry. SAE Paper 2005-01-3850

50. Alriksson, M., Gjirja, S., Denbratt, I., 2007. The Effect of Charge Air and Fuel Injection Parameters on Combustion With High Levels of EGR in a HDDI Single-Cylinder Diesel Engine. SAE Paper 2007-01-0914

51. Huestis, E., Erickson, P.A., Musculus, M.P.B., 2007. In-Cylinder and Exhaust Soot in Low-Temperature Combustion Using a Wide-Range of EGR in a Heavy-Duty Diesel Engine. SAE Paper 2007-01-4017

52. Aronsson, U., Chartier, C., Andersson, O., Johansson, B., Sjöholm, J., Wellander,R., Richter,M., Alden, M., Miles, P., 2010. Analysis of EGR Effects on the Soot Distribution in a Heavy Duty Diesel Engine using Time-Resolved Laser Induced Incandescence. SAE Paper 2010-01-2104

53. Mauderly, J., Health Effects of Diesel Emissions: A Toxicological Viewpoint. National Environmental Respiratory Centre. [Cited on 20/06/2010; Available from: http://www.hc-sc.gc.ca/ewh-semt/air/out-ext/effe/diesel/exsum-sommaire-eng.php]

54. Kennedy, I.M., 2007. The health effects of combustion-generated aerosols. Proceedings of the Combustion Institute, Vol. 31, PP 2757-2770

55. Stöber, W., Abel, U.R., 1996. Lung cancer due to diesel soot particles in ambient air? A critical appraisal of epidemiological studies addressing this question. Int. Arch. Occup. Environ Health, Vol.68, No. 3

56. Schwartz, J., 1994. Air pollution and daily mortality: a review and meta analysis. Environ Res., Vol. 64, No. 1, PP 36–52

57. Schwartz, J., Norris, G., Larson, T., Sheppard, L., Claiborne, C., Koenig, J.Q., 1999. Episodes of high coarse particle concentrations are not associated with increased mortality. Environ Health Perspect, Vol. 107, No. 5, PP 339-342

58. Miller, F.J., Gardner, D.E., Graham, J.A., Lee, R.E., Wilson, W.E., Bachmann, J.D., 1979. Size considerations for establishing a standard for inhalable particles. J. Air Poll Control Assoc, Vol. 29, PP 610-615

59. Majewski, W.A., Khair, M.K., 2006. Diesel Emissions and Their Control. SAE International

60. Shundoh, S., Komori, M., Tsujimura, K., Kobayashi, S., 1992. NOx Reduction from Diesel Combustion Using Pilot Injection with High Pressure Fuel Injection. SAE Paper 920461

61. Nehmer, D., Reitz, R., 1994. Measurement of the Effect of Injection Rate and Split Injections on Diesel Engine Soot and NOx Emissions. SAE Paper 940668

62. Ropke, S., Schweimer, G.W., Strauss, T.S., 1995. NOx Formation in Diesel Engines for Various Fuels and Intake Gases. SAE Paper 950213

63. Shundoh, S., Kakegawa, T., Tsujimura, K., Kobayashi, S., 1991. The Effect of Injection Parameters and Swirl on Diesel Combustion with High Pressure Fuel Injection. SAE Paper 910489

64. Alriksson, M., Rente, T., Denbratt, I., 2005. Low Soot, Low NOx in a Heavy Duty Diesel Engine Using High Levels of EGR. SAE Paper 2005-01-3836

65. Nakano, K., Kinji, T., Yokota, K., Okino, H., Satou, D., 2004. Research of the Exhaust Gas With the Recirculation of NOx in IDI Diesel Engine. Vol. 108, No. 4, PP 9-12

66. Sarangi, A.K., McTaggart-Cowan, G.P., Garner, C.P., 2010. The Effects of Intake Pressure on High EGR Low Temperature Diesel Engine Combustion. SAE Paper 2010-01-2145

67. Brakora, J., Reitz, R., 2010. Investigation of NOx Predictions from Biodiesel-fueled HCCI Engine Simulations Using a Reduced Kinetic Mechanism. SAE Paper 2010-01-0577

68. Hountalas, D.T., Mavropoulos, G.C., Zannis, T.C., 2006. Mamalis, S.D., Use of Water Emulsion and Intake Water Injection as NOx Reduction Techniques for Heavy Duty Diesel Engines. SAE Paper 2006-01-1414

69. National Aeronautics and Space Administration. [Cited on 15/07/2010; Available from: http://www.nasa.gov/]

70. Zhao, H., 2007. Overview of CAI/HCCI Gasoline Engines / HCCI and CAI Engines for the Automotive Industry. Woodhead Publishing Limited, PP 21-42

71. Kaiser, E.W., Yang, J., Culp, T., Xu, N., Maricq, M.M., 2002. Homogeneous charge compression ignition engine-out emissions- does flame propagation occur in homogeneous charge compression ignition? Int. J. Engine Research, Vol. 3, No. 4

72. Hultqvist, A., Christensen, M., Johansson, B., Franke, A., Richter, M., Alden, M., 1999. A Study of the Homogeneous Charge Compression Ignition Combustion Process by Chemiluminescence Imaging. SAE Paper 1999-01-3680

73. Aceves, S.M., Flowers, D.L., Martinez-Frias, J., Smith, J.R., Dibble, R., Au, M., Girard, J., 2001. HCCI Combustion: Analysis and Experiments. SAE Paper 2001-01-2077

74. Docquier, N., 2003. Influence of Fresh Charge Preparation and Composition on Auto-Ignition Delays and Combustion Development in an Optical HCCI Direct Injection Diesel Engine. SAE Paper 2003-01-3174

75. Kashdan, J.T., Docquier, N., Bruneaux, G., 2004. Mixture Preparation and Combustion via LIEF and LIF of Combustion Radicals in a Direct-Injection, HCCI Diesel Engine. SAE Paper 2004-01-2945

76. Stanglmaier, R.H., Roberts, C.E., 1999. Homogeneous Charge Compression Ignition (HCCI); Benefits, Compromises and Future Engine Applications. SAE Paper 1999-01-3682

77. Strålin, P., Wåhlin F. and Ångström H., 2003. Effects of Injection Timing on the Conditions at Top Dead Center for Direct Injected HCCI. SAE Paper 2003-01-3219

78. Ra, Y., Reitz, R.D., 2005. The Use of Variable Geometry Sprays With Low Pressure Injection for Optimization of Diesel HCCI Engine Combustion. SAE Paper 2005-01-0148

79. Komninos, N.P., Hountalas, D.T., Kouremenos, D.A., 2005. Description of in-Cylinder Combustion Processes in HCCI Engines Using a Multi-Zone Model. SAE Paper 2005-01-0171

80. Kawano, D., Suzuki, H., Ishii, H., Goto, Y., Odaka, M., Murata, Y., Kusaka, J., Daisho, Y., 2005. Ignition and Combustion Control of Diesel HCCI. SAE Paper 2005-01-2132

81. Bression, G., Soleri, D., Savy, S., Dehoux, S., Azoulay, D., Hamouda, H.B., Doradoux, L., Guerrassi, N., Lawrence, N., 2008. A Study of Methods to Lower HC and CO Emissions in Diesel HCCI. SAE Paper 2008-01-0034

82. Takeda, Y., Keiichi, N., Keiichi, N., 1996. Emission Characteristics of Premixed Lean Diesel Combustion with Extremely Early Staged Fuel Injection. SAE Paper 961163

83. Akagawa, H., Miyamoto, T., Harada, A., Sasaki, S., Shimazaki, N., Hashizume, T., Tsujimura, K., 1999. Approaches to Solve Problems of the Premixed Lean Diesel Combustion. SAE Paper 1999-01-0183

84. Kimura, S., Aoki, O., Kitahara, Y., Aiyoshizawa, E., 2001. Ultra Clean Combustion Technology Combining a Low-Temp & Premixed Combustion Concept for Meeting Future Emission Standards. SAE Paper 2001-01-0200

85. Simescu, S., Ryan III, T.W., Neely, G.D., Matheaus, A.C., Surampudi, B., 2002. Partial Pre-Mixed Combustion with Cooled and Uncooled EGR in a Heavy-Duty Diesel Engine. SAE Paper 2002-01-0963

86. Simescu, S., Fiveland, S.B., Dodge, L.G., 2003. An Experimental Investigation of PCCI-DI Combustion and Emissions in a Heavy-Duty Diesel Engine. SAE Paper 2003-01-0345

87. Kook, S., Bae, C., 2004. Combustion Control Using Two-Stage Diesel Fuel Injection in a Single-Cylinder PCCI Engine. SAE Paper 2004-01-0938

88. Hardy, W.L., Reitz, R.D., 2006. A Study of the Effects of High EGR, High Equivalence Ratio, and Mixing Time on Emissions Levels in a Heavy-Duty Diesel Engine for PCCI Combustion. SAE Paper 2006-01-0026

89. Hardy, W.L., Reitz, R.D., 2006. An Experimental Investigation of Partially Premixed Combustion Strategies Using Multiple Injections in a Heavy-Duty Diesel Engine. SAE Paper 2006-01-0917

90. Nevin, R.M., Sun, Y., Gonzalez, M.A., Reitz, R.D., 2007. PCCI Investigation Using Variable Intake Valve Closing in a Heavy Duty Diesel Engine. SAE Paper 2007-01-0903

91. Kanda, T., Hakozaki, T., Uchimoto, T., Hatano, J., Kitayama, N., Sono, H., 2005. PCCI Operation with Early Injection of Conventional Diesel Fuel. SAE Paper 2005-01-378

92. Kanda, T., Hakozaki, T., Uchimoto, T., Hatano, J., Kitayama, N., Sono, H., 2006. PCCI Operation with Fuel Injection Timing Set Close to TDC. SAE Paper 2006-01-0920

93. Lee, S., Reitz, R.D., 2006. Spray Targeting to Minimize Soot and CO Formation in Premixed Charge Compression Ignition (PCCI) Combustion with a HSDI Diesel Engine. SAE Paper 2006-01-0918

94. Murata, Y., Kusaka, J., Odaka, M., Daisho, Y., Kawano, D., Suzuki, H., Ishii, H., Goto, Y., 2006. Achievement of Medium Engine Speed and Load Premixed Diesel Combustion with Variable Valve Timing. SAE Paper 2006-01-0203

95. Neely, G.D., Sasaki, S., Huang, Y., Leet, J.A., Stewart, D.W., 2005. New Diesel Emission Control Strategy to Meet US Tier 2 Emissions Regulations. SAE Paper 2005-01-1091

96. Alriksson, M., Denbratt, I., 2006. Low Temperature Combustion in a Heavy Duty Diesel Engine Using High Levels of EGR. SAE Paper 2006-01-0075

97. Dolenc, A., 1990. The injection equipment of future high speed DI diesel engine with respect to power and pollution requirement. I.Mech.E lecture, London, Uinited Kingdom

98. Nehmer, D., Reitz, R., 1994. Measurement of the Effect of Injection Rate and Split Injections on Diesel Engine Soot and NOx Emissions. SAE Paper 940668

99. Zambare, V.V., Winterbone, D.E., 1999. Photographic Investigation of Multi-Stage Fuel Injection in Single Cylinder DI Diesel Engine. SAE Paper 1999-01-1501

100. Koyanagi, K., Oing, H., Renner, G., Maly, R., 1999. Optimizing Common Rail-Injection by Optical Diagnostics in a Transparent Production Type Diesel Engine. SAE Paper 1999-01-3646

101. Juneja, H., Ra, Y., Reitz, R.D., 2004. Optimization of Injection Rate Shape Using Active Control of Fuel Injection. SAE Paper 2004-01-0530

102. Tanabe, K., Kohketsu, S., Nakayama, S., 2005. Effect of Fuel Injection Rate Control on Reduction of Emissions and Fuel Consumption in a Heavy Duty DI Diesel Engine. SAE Paper 2005-01-0907

103. Tow, T.C., Pierpont, D.A., Reitz, R.D., 1994. Reducing Particulate and NOdx Emissions by Using Multiple Injections in a Heavy; Duty D.I. Diesel Engine. SAE Paper 940897

104. Minami, T., Takeuchi, K., Shimazaki, N., 1995. Reduction of Diesel Engine NOx Using Pilot Injection. SAE Paper 950611

105. Pierpont, D.A., Montgomery, D.T., Reitz, R.D., 1995. Reducing Particulate and NOdx Using Multiple Injections and EGR in a D.I. Diesel. SAE Paper 950217

106. Farrell, P.V., Chang, C.T., Su, T.F., 1996. High Pressure Multiple Injection Spray Characteristics. SAE Paper 960860

107. Montgomery, D.T., Reitz, R.D., 2001. Effects of Multiple Injections and Flexible Control of Boost and EGR on Emissions and Fuel Consumption of a Heavy-Duty Diesel Engine. SAE Paper 2001-01-0195

108. Shayler, P.J., Brooks, T.D., Pugh, G.J., Gambrill, R., 2005. The Influence of Pilot and Split-Main Injection Parameters on Diesel Emissions and Fuel Consumption. SAE Paper 2005-01-0375

109. Zhang, Y., Ito, T., Nishida, K., 2001. Characterization of Mixture Formation in Split-Injection Diesel Sprays via Laser Absorption-Scattering (LAS) Technique. SAE Paper 2001-01-3498

110. Zhang, Y., Nishida, K., 2003. Vapor/Liquid Behavior in Split Injection D.I. Diesel Engine Sprays in a 2-D Model Combustion Chamber. SAE Paper 2003-01-1837

111. Shayler, P.J., Ng, H.K., 2004. Simulation Studies of the Effect of Fuel Injection Pattern on NO and Soot Formation in Diesel Engines. SAE Paper 2004-01-0116

112. Liu, Y., Reitz, R.D., 2005. Optimizing HSDI Diesel Combustion and Emissions Using Multiple Injection Strategies. SAE Paper 2005-01-0212

113. Ricaud, J.C., Lavoisier, F., 2002. Optimizing the Multiple Injection Settings on an HSDI Diesel Engine. THIESEL 2002 Conference

114. Gill, K., Zhao, H., 2008. In-cylinder Studies of Fuel Injection and Combustion from a Narrow Cone Fuel Injector in a High Speed Single Cylinder Optical Engine. SAE Paper 2008-01-1789

115. Lee, S., Choi H., Chung J., 2010. The Effects of Injection Timing and Piston Bowl Shape on PHCCI Combustion with Split injections. SAE Paper 2010-01-0359

116. Yamaguchi, I., Nakahira, T., Komori, M., Kobayashi, S., 1990. An Image Analysis of High Speed Combustion Photographs for D.I. Diesel Engine with High Pressure Fuel Injection. SAE Transactions, Vol. 99, Sec. 3, pp 1836-1848, SAE Paper 901577

117. Werlberger, P., Cartellieri, W., 1987. Fuel Injection & Combustion Phenomena in High Speed DI Diesel Engine Observed by Means of Endoscopic High Speed Photography. SAE Paper 870097

118. Arcoumanis, C., Hadjiapostolou, A., Whitelaw, J., 1991. Flow and Combustion in a Hydra Direct-Injection Diesel Engine. SAE Paper 910177

119. Arcoumanis, C., Whitelaw, J., Hentschel, W., Schindler, K.P., 1994. Flow and Combustion in a transparent 1.9 litre direct injection diesel engine. Proceedings of the Institute of Mechanical Engineers, Vol. 208, PP 191-205

120. Lai, M., Henein, N.A., Xie, X., Chue, T., Itoh, Y., Bryzik, W., 1995. Diesel Cold-Starting Study Using Optically Accessible Engines. SAE Paper 952366

121. Shimazaki, N., Hatanaka, H., Yokota, K., Nakahira, T., 1996. A Study of Diesel Combustion Process Under the Condition of EGR and High Pressure Fuel Injection with Gas Sampling Method. SAE Paper 960030

122. Lefebvre, A.H., 1989. Atomisation and spray. Hemisphere Publishing Corporation, New York

123. Settles, G.S., 2001. Schlieren and shadowgraph techniques: visualizing phenomena in transparent media

124. Melton, L.A., 1983. Spectrally separated fluorescence emissions for diesel fuel droplets and vapour. Applied Optics, Vol. 21, No. 14, PP 2224-2226

125. Melton, L.A., Verdieck, J.F., 1985. Vapor/Liquid Visualization for Fuel Sprays, Combustion Science and Technology. Vol. 42, PP 217-222

126. Bardsley, M.E.A., Felton, P.G., Bracco , F.V., 1988. 2-D Visualization of Liquid and Vapor Fuel in an I.C. Engine. SAE Paper 880521

127. Bardsley, M.E.A., Felton, P.G., Bracco, F.V., 1989. 2-D Visualization of a Hollow-Cone Spray in a Cup-in-Head, Ported, I.C. Engine. SAE Paper 890315

128. Diwakar, R., Fansler, T.D., French, D.T., Ghandhi, J.B., Dasch, C.J., Heffelfinger, D.M., 1992. Liquid and Vapor Fuel Distributions from an Air-Assist Injector - An Experimental and Computational Study. SAE Paper 920422

129. Bower, G.R., Foster, D.E.,The Effect of Split Injection on Fuel Distribution in an Engine-Fed Combustion Chamber. SAE Paper 930864

130. Melton, L.A., 1988. Final Report of Army Research Office contract. DAAL 03-86-k-0082

131. Rotunno, A., Winter, M., Dobbs, G., and Melton, L., 1990. Direct Calibration Procedures for Exciplex-Based Vapor/Liquid Visualization of Fuel Sprays.Combust. Sci. and Tech., Vol. 71, pp 247-261

132. Felton, P., Bracco, F., Bardsley, M., 1993. On the Quantitative Application of Exciplex Fluorescence to Engine Sprays. SAE Paper 930870

133. Yeh, C., Kamimoto, T., Kosaka, H., Kobori, S., 1994. Quntitative Measurement of 2-D Fuel Vapor Concentration in a Transient Spray via Laser-Induced Fluorescence Technique. SAE Paper 941953

134. Senda, J., Kanda, T., Kobayashi, M., Fujimoto, H., 1997. Quantitative analysis of fuel vapor concentration in diesel spray by exciplex fluorescence method. SAE Paper 970796

135. Ghandhi, J.B., Kim, T., 2001. Quantitative 2-D Fuel Vapor Concentration Measurements in an Evaporating Diesel Spray using the Exciplex Fluorescence Method. SAE Paper 2001-01-3495

136. Yamashita, H., Suzuki, T., Matsuoka, H., Mashida, M., Kitano, K., 2007. Research of the DI Diesel Spray Characteristics at High Temperature and High Pressure Ambient. SAE Paper 2007-01-0665

137. Bruneaux, G., Maligne, D., 2009. Study of the Mixing and Combustion Processes of Consecutive Short Double Diesel Injections. SAE Paper 2009-01-1352

138. Hottel, H.G., Broughton, F.P., 1932. Determination of true temperature and total radiation from luminous gas flames. Ind. and Engng Chem., Vol. 4, No. 2, PP 166-175

139. Matsui, Y., Kamimoto, T., Matsuoka, S., 1979. A study of the time and space resolved measurement of flame temperature and soot concentration in a DI diesel engine by the two-colour method. SAE Paper 790491

140. Matsui, Y., Kamimoto, T., Matsuoka, S., 1980. A study on the application of the two-colour method to the measurement of flame temperature and soot concentration in diesel engines. SAE Paper 800970

141. Matsui, Y., Kamimoto, T., Matsuoka, S., 1982. Formation and oxidation processes of soot particulates in a DI diesel engine – an experimental study via the two-colour method. SAE Paper 820464

142. Zhao, H., Ladommatos, N., 1994. A Guide to Measurement of Flame Temperature and Soot Concentration in Diesel Engines Using the Two-Colour Method Part 1: Theory. SAE Paper 941956

143. Zhao, H., and Ladommatos, N., 1994. A Guide to Measurement of Flame Temperature and Soot Concentration in Diesel Engines Using the Two-Colour Method Part 2: Implementation. SAE Paper 941957

144. Arcoumanis, C., Bae, C., Nagwaney, A., Whitelaw, J.H., 1995. Effect of EGR on Combustion Development in a 1.9L DI Diesel Optical Engine. SAE Paper 950850

145. Quoc, H.X., Vignon, J.M., Brun, M., 1991. A New Approach of the Two-Colour Method for Determining Local Instantaneous Soot Concentration and Temperature in a D.I. Diesel Combustion Chamber. SAE Paper 910736

146. Shakal, J.S., Martin, J.K., 1994. Imaging and Spatially Resolved Two-Colour Temperature Measurements through a Coherent Fiber Optic: Observation of Auxiliary Fuel Injection Effects on Combustion in a Two-Stroke DI Diesel. SAE Paper 940903

147. Bakenhus, M., Reitz, R.D., 1999. Two-Colour Combustion Visualization of Single And Split Injections in a Single-Cylinder Heavy-Duty DI Diesel Engine Using and Endoscope-Based Imaging System. SAE Paper 1999-01-112

148. Hampson, G.J., Reitz, R.D., 1998. Two-Colour Imaging of In-Cylinder Soot Concentration and Temperature in a Heavy-Duty DI Diesel Engine with Comparison to Multidimensional Modeling for Single and Split Injections. SAE Paper 980524

149. Tominaga, Y., Tajima, H., Strom, A., Uno, K., 2005. Flame Temperature Measurement in Diesel Engine on Two Colour Method utilizing CMOS Camera. Journal of the Visualization Society of Japan, Vol. 25, No. 2, PP 97-98

150. Gill, K., 2007. Investigation of Multiple Injections and Fuel Properties on Diesel Combustion and Emission. Brunel University PhD Thesis

151. Díez Rodríguez, A., 2009. Investigation of Split Injection in a Single Cylinder Optical Diesel Engine. Brunel University PhD Thesis

152. Joel, R., 2008. Basic Engineering Thermodynamics. Pearson

153. Zhao, H., Ladommatos, N., 2001. Engine Combustion Instrumentation and Diagnostics. Society of Automotive Engineers, Inc., PP 337-394

154. Gomes, P., Yates, D.A., 1998. Analysis of the Influence of Injection Timing on Diesel Combustion by the Two-Colour Method. SAE Paper 982890

155. Pastor, J.V., García, J.M., Pastor, J.M., Buitrago, J.E., 2005. Analysis Methodology of Diesel Combustion by Using Flame Luminosity, Two-Colour Method and Laser-Induced Incandescence. SAE Paper 2005-24-012

156. Payri, F., Pastor, J.V., García, J.M., Pastor, J.M., 2007. Contribution to the application of two-colour imaging to diesel combustion. Measurement Science and Technology, Vol. 18, PP 2579–2598

157. Pöttker, S., Eckert, P., Delebinski, T., Baumgarten, C., Oehlert, K., Merker, G. P., Wagner, U., Spicher, U., 2004. Investigations of HCCI Combustion Using Multi-Stage Direct-Injection with Synthetic Fuels. SAE Paper 2004-01-2946

158. Merkel, S., Eckert, P., Wagner, U., Velji, A., Spicher, U., 2008. Investigation of a New Injection Strategy for Simultaneous Soot and NOx Reduction in a Diesel Engine with Direct Injection. SAE Paper 2008-01-1790

159. Sison, K., 2006. In-cylinder Studies of Diesel Combustion with Oxygenated Fuels and Multiple Injections. Brunel University PhD Thesis

160. Larrabee, R.D., 1959. Spectral emissivity of tungsten. Journal of the Optical Society of America, Vol. 49, PP 619-625

161. Yan, J., Borman, G.L., 1988. Analysis and In-Cylinder Measurement of Particulate Radiant Emissions and Temperature in a Direct Injection Diesel Engine. SAE Paper 881315

162. Bower, R.G., Foster, D., 1991. A Comparison of the Bosch and Zuech rate of injection meters. SAE Paper 910724

163. Baniasad, M.S., 1994. Analysis of fuel injection rate in diesel injection systems. Imperial College, University of London PhD Thesis

164. Baumgarten, C., 2006. Mixture Formation in Internal Combustion Engines: Heat and Mass Transfer (Mewes, D., Mayinger, F. Ed.). Springer, Berlin, 1st Edition

165. Bae, C., Yu, J., Kang, J., Kong, J., Lee, K.O., 2002. Effect of Nozzle Geometry on the Common-Rail Diesel Spray. SAE Paper 2002-01-1625

166. Ganser, M.A., 2000. Common rail injectors for 2000 bar and beyond. SAE Paper 2000-01-0706

167. Birch, S., 2004. New fuel injector technology from Delphi. Automotive Engineering International Magazine, Vol. 112, No. 2, PP 36 and 111

168. Ishikawa, S., Ohmori, Y., Fukushima, S., Suzuki, T., Takamura, A., Kamimoto, T., 2000. Measurement of Rate of Multiple-Injection in CDI Diesel Engines. SAE Paper 2000-01-1257

169. Desantes, J., Benajes, J., Molina, S., Gonzales, C., 2004. The modification of fuel injection rate in heavy-duty engines Part 2: Effects of combustion. Applied Thermal Engineering, Vol. 24, PP 2715−2726

170. Arcoumanis, C., Baniasad, M.S., Gibbins, J.R., 1992. Measurement and analysis of injection rate variations in diesel engines. I.Mech.E seminar, Diesel fuel injection system

171. Kohketsu, S., Tanabe, K., Mori, K., 2000, Flexibly Controlled Injection Rate Shape with Next Generation Common Rail System for Heavy Duty DI Diesel Engines. SAE Paper 2000-01-0705

172. Aronsson, U., Chartier, C., Horn, U., Andersson, Ö., Johansson, B., Egnell, R., 2008. Heat Release Comparison Between Optical and All-Metal HSDI Diesel Engines. SAE Paper 2008-01-1062

173. Kashdan, J.T., Thirouard, B., 2009. A Comparison of Combustion and Emissions Behaviour in Optical and Metal Single-Cylinder Diesel Engines. SAE Paper 2009-01-1963

174. Johnson, S.C., 1981. In Fluid Mechanics of Combustion systems: Proceedings of ASME Fluids Engineering Conference (Morell, T. Ed.). Boulder, Colo., PP 107-118

175. Johnson, S.C., 1981. Raman spectroscopy and flow visualization study of stratified charge engine combustion. SAE Paper 800136

176. Hussein, G.A., Jasuja, A.K., Fletcher, R.S., 1982. Penetration and break-up studies of discrete liquid jets in cross flowing airstreams. American Society of Mechanical Engineers, International Gas Turbine Conference and Exhibit, 27th, London, England, Paper 82-GT-25

177. Sangiovanni, J.J., 1980. United Technologies Research Center Report. R80-954424

178. Yule, A.J., Seng, C.A., Felton, P.G., Ungut, A., Chigier, N.A., 1981. Eighteenth Symposium (International) on Combustion, The Combustion Institute, Pittsburgh, PP 1501-1509

179. Chraplyvy, A.R., 1981. NONINTRUSIVE MEASUREMENTS OF VAPOR CONCENTRATIONS INSIDE SPRAYS. Appl. Opt., Vol. 20, No. 15, PP 2620-2624

180. Melton, L.A., Verdieck, J.F., 1984. Vapor/Liquid Visualization in Fuel Sprays. Twentieth Symposium (International) on Combustion, The Combustion Institute, PP 1283-1290

181. Fujimoto, H., Choi, D., Shima, Y., Senda, J., 2002. Two-dimensional imaging of fuel-vapour concentration by use of LIEF technique during mixture formation process in a DI diesel engine. Measurement Science and Technology, Vol. 13, PP 391-400

182. Zhao, H., Ladommatos, N., 1998. Optical Diagnostics for In-cylinder Mixture Formation Measurements in IC engines. Progress in energy & combustion science, PP 297-336

183. Melton, L.A., 1996. Planar Liquid and Gas Visualization. AT-Process, Journal of Process Analytical Chemistry

184. Yeh, C.N., Kamimoto, T., Kobori, S., Kosaka, H., 1993. 2-D Imaging of Fuel Vapor Concentration in a Diesel Spray via Exciplex-Based Fluorescence Technique. SAE Paper 932652

185. Hale, S.J., Melton, L.A., 1990. Absolute Quantum Yields for Exciplex Fluorescence. Applied Spectroscopy, Vol. 44, No. 1

186. Le Coz, J.F., Hermant, L., 2001. Quantification of Fuel Concentrations and Estimation of Liquid/Vapor Ratios in Direct Injection Gasoline Sprays by Laser-Induced Fluorescence. SAE Paper 2001-01-0916

187. Lakowicz, J.R., 1999. Principles of fluorescence spectroscopy. 2nd Edition, Springer, PP 367–394

188. Kim, J.U., Hong, J., 2001. Quantitative vapour–liquid visualization using laser-induced exciplex fluorescence. J. Opt. A: Pure Appl. Opt., Vol. 3, PP 338-345